People's Democratic Republic of Algeria
Ministry of Higher Education and Scientific Research

Higher Normal School of Technological Education of Skikda



Department of : Physics and Chemistry

THESIS

Submitted in fulfillment of the requirements for the degree of

Doctorate

Domain:	Materials Sciences
Field of study :	Physics
Speciality:	Condensed Matter Physics

Presented by :

Ms. Louati Nesrine

Title:

Ab-initio study of the structural, electronic, optical, thermal properties and structural stability of III-V ternary semiconductors and double perovskites by the FP-LAPW method.

Publicly defended on: / /

before the Jury composed of:

Full name	Academic rank	Establishment	Role
Mr. Chebli Abdelhak	Professor	ENSET Skikda	Chair
Mr. Oumelaz Fayçal	MCA	ENSET Skikda	Supervisor
Mme. Nemiri Ouarda	MCA	ENSET Skikda	Co-supervisor
Mme. Triki Houria	Professor	University Badji Mokhtar–Annaba	Examiner
Mme. Drablia Samia	Professor	University Badji Mokhtar–Annaba	Examiner
Mr. Boubekri Hani	MCA	ENSET Skikda	Examiner
Mme. Benredouane Rabab	MCB	ENSET Skikda	Invited

Academic Year : 2025/2026

République Algérienne Démocratique et Populaire
Ministère de l'Enseignement Supérieur et de la Recherche Scientifique

École Normale Supérieure de l'Enseignement Technologique de Skikda

Département de : Physique et chimie

THÈSE

Présentée en vue de l'obtention du diplôme de

Doctorat

Domaine : Sciences de la matière
Filière : Physique
Spécialité : Physique de la matière condensée

Présentée par

M^me^ : Louati Nesrine

Thème :

Etude ab-initio des propriétés structurales, électroniques, optiques, thermiques et stabilité structurale des semi-conducteurs ternaires III-V et des doubles pérovskites par la méthode FP-LAPW

Soutenue publiquement le : / /

devant le jury composé de :

Nom	Grade	Établissement	Qualité
Mr. Chebli Abdelhak	Professeur	ENSET Skikda	Président
Mr. Oumelaz Fayçal	MCA	ENSET Skikda	Directeur de thèse
Mme. Nemiri Ouarda	MCA	ENSET Skikda	Co-directrice
Mme. Triki Houria	Professeur	Université Badji Mokhtar–Annaba	Examinatrice
Mme. Drablia Samia	Professeur	Université Badji Mokhtar–Annaba	Examinatrice
Mr. Boubekri Hani	MCA	ENSET Skikda	Examinateur
Mme. Benredouane Rabab	MCB	ENSET Skikda	Invitée

Année Universitaire : 2025/2026

Acknowledgments

First and foremost, I would like to thank almighty God, to whom I express my gratitude, for granting me health, courage, and strength to successfully complete this work until the end.

This dissertation would not have been possible without the guidance and support of numerous individuals who in one way or another contributed and extended their valuable assistance in the completion of this study. It is with deep gratitude that I take this moment to extend my sincere thanks to those who made it a possibility.

I would like to express my deepest gratitude and sincere appreciation to my supervisor, ***Dr. Oumelaz Fayçal****, for his invaluable guidance, unwavering support, and inspiring mentorship throughout the entire course of this work. His expertise, insightful advice, and continuous encouragement were fundamental to the successful completion of this thesis.*

I am equally and profoundly grateful to my co-supervisor, ***Dr. Nemiri Ouarda****, for her remarkable dedication, constructive feedback, and constant support. Her thoughtful guidance and commitment greatly enriched this research.*

I would also like to express my sincere and heartfelt gratitude to ***Dr. Boujaadar Djamel,*** *who guided as both as a professor and as the director of the Higher Normal School of Technological Education of Skikda, for his continuous support, encouragement, and for fostering an environment that promotes academic excellence and research development.*

My sincere appreciation goes to the members of the jury: ***Prof. Chebli Abdelhak****,* ***Prof. Triki Houria****,* ***Prof. Drablia Samia****,* ***Dr. Boubekri Hani****, and* ***Dr. Benredouane Rabab****, for the honor they have given me by evaluating this work and for their valuable comments and insightful remarks.*

I would like to express my special thanks to future doctors, my colleagues and dear friends, ***Gouasmia Wissam*** *and* ***Chebouki Sonia****, for their moral support, encouragement, and companionship throughout this journey.*

*Finally, behind every achievement stands a family whose unwavering support forms its true foundation, and I am deeply blessed to have such a family. I express my heartfelt gratitude to all my family members, especially my parents, my husband **Atef**, and my sisters **Nour**, **Khaoula**, and **Yousra**, for their endless love, constant support, and encouragement throughout this journey. I also extend my sincere thanks to my brothers **Aymen**, **Saad El Din**, and **El Omda** for their continuous motivation and presence. I express my deep affection and appreciation to my grandfathers, as well as to my aunts, uncles, and cousins, for their kindness, encouragement, and support.*

It is impossible to mention everyone individually without the risk of omission; however, all those who supported me, directly or indirectly, are sincerely acknowledged and associated with this achievement, with my profound gratitude for their invaluable contribution.

Louati. N

Dedication

‘To my parents, whose love and wisdom light my path,

to my husband, whose support lifts me every day,

and to my little one, not yet born, who already inspires my heart with hope and joy.’

Louati. N

Abstract

Through our work, we investigate the properties of $YN_{1-x}Sb_x$ternary alloys in which (Y: B, Al and Ga) while x represent the Sb concentration (x=0, 0.25, 0.5, 0.75 and 1) in addition to Sr_2NaXO_6 (X = Cl, Br, and I) double perovskites thought the Wien2k code package based on Density Functional Theory (DFT). This is achieved by full potential linearized augmented plane wave (FP-LAPW) method. A detailed and systematic analysis of the structural, electronic, optical, elastic and thermal properties in addition to thermoelectric properties for double oxide perovskite has been carried. Structural optimization, transition phase, thermal and elastic constant calculations were performed using the WC-GGA potential for $YN_{1-x}Sb_x$ alloys and PBEsol exchange–correlation functional forSr_2NaXO_6 (X = Cl, Br, and I) double perovskites. While the KTB-mBJ potential was employed to accurately, describe the electronic, thermoelectric, and optical properties. In addition, the WC-GGA and TB-mBJ scheme was used to further validate and refine the electronic band structure analysis. The elastic constants were calculated to verify the mechanical stability and determine the mechanical properties.The effect of temperature on the lattice constant, bulk modulus, heat capacity, and Debye temperature was also investigated. Our work demonstrates a high consistency between our calculated results and both available experimental data and previous theoretical studies. Therefore, we expect this research to represent a significant scientific contribution providing a valuable reference for future studies, as well as inspiring and facilitating subsequent experimental investigations

Keywords: Wien2k, DFT, FP-LAPW, semiconductor, alloys, double perovskites, band gap.

Résumé

Dans ce travail, nous étudions les propriétés des alliages $YN_{1-x}Sb_x$ (Y : B, Al et Ga) où x représente la concentration (x = 0, 0,25, 0,5, 0,75 et 1), ainsi que des double pérovskites Sr_2NaXO_6 (X = Cl, Br et I), à l'aide du code WIEN2k basé sur la théorie de la fonctionnelle de densité (DFT). L'étude a été réalisée par la méthode des ondes planes augmentées et linéarisées avec un potentiel complet. Une analyse détaillée et systématique des propriétés structurales, électroniques, optiques, élastiques et thermiques, ainsi que les propriétés thermoélectriques a été effectuée dans le cadre de la DFT. L'optimisation structurale, l'étude des transitions de phases, les propriétés thermiques et élastiques ont été réalisés en utilisant le potentiel WC-GGA pour les alliages $YN_{1-x}Sb_x$ et l'approximation PBEsol pour les double pérovskites Sr_2NaXO_6. Le potentiel KTB-mBJ a été employé pour décrire avec précision les propriétés électroniques, optiques et thermoélectriques. De plus, nous avons utilisé les méthodes WC-GGA et TB-mBJ pour confirmer et perfectionner l'analyse de la structure de bandes électroniques. Les constantes élastiques ont été calculées afin de vérifier la stabilité mécanique et de déterminer les propriétés mécaniques. L'effet de la température sur le paramètre de maille, module de compressibilité, la capacité thermique et la température de Debye a également été examiné et interprété. Nos résultats montrent une grande cohérence entre nos calculs et les données expérimentales disponibles ainsi que les études théoriques précédentes. Par conséquent, nous estimons que cette recherche représente une contribution scientifique significative et servira de référence fondamentale pour les futures recherches, tout en guidant et en renforçant les investigations expérimentales à venir.

Mots-clés :, Wien2k, DFT, FP-LAPW, semi-conducteur, alliages, double pérovskite, bande interdite.

ملخص

نهتم في هذا البحث بدراسة خصائص سبائك $YN_{1-x}Sb_x$ حيث (Y يمثل B، Al و Ga) و x يمثل التركيز ويأخذ القيم (0، 0.25، 0.5، 0.75 و 1) بالإضافة إلى البيروفسكيت المزدوج Sr_2NaXO_6 حيث (X يمثل Cl، Br و I) باستخدام برنامج المحاكاة Wien2k المستند إلى نظرية دالة الكثافة الوظيفية (DFT). تم تنفيذ الدراسة بواسطة طريقة الامواج المستوية المتزايدة خطيًا ذات الكمون الكامل (FP-LAPW) .تم إجراء تحليل مفصل ومنهجي للخصائص البنيوية والإلكترونية والبصرية والمرنة والحرارية، بالإضافة إلى الخصائص الكهروحرارية للبيروفسكيت المزدوج . تمت دراسة الخصائص البنيوية، تحول الطور وحساب الثوابت الحرارية والمرنة باستخدام تقريبWC-GGA لسبائك YN1-xSbx و التقريب PBEsol للبيروفسكيت المزدوج Sr_2NaXO_6.في حين تم استخدام تقريب KTB-mBJ لوصف الخصائص الإلكترونية والكهربائية والبصرية بدقة. بالإضافة إلى ذلك، تم استخدام كل من WC-GGA و K TB-mBJتم حساب ثوابت المرونة للتحقق من الاستقرار الميكانيكي وايضا لتحديد الخصائص الميكانيكية للمواد المدروسة. كما تم دراسة تأثير درجة الحرارة على ثابت الشبكة، معامل الصلابة، السعة الحرارية و كذا درجة حرارة ديباي. تظهر النتائج المتحصل عليها في بحثنا اتساقًا عاليًا بين الحسابات التي أجريناها والبيانات التجريبية المتاحة والدراسات النظرية السابقة. لذلك، نتوقع أن يمثل هذا البحث إسهامًا علميًا مهمًا ويكون مرجعًا أساسيًا للدراسات المستقبلية، كما أنه يحفز ويدعم البحوث التجريبية القادمة.

الكلمات المفتاحية: DFT Wien2k، FP-LAPW ، نظرية الكثافة الوظيفية، أشباه الموصلات، السبائك، البيروفسكيت المزدوج ، فجوة الطاقة.

Content

General introduction ……... 1

References ……..... 6

Chapter1: Fundamental Physical Properties of Semiconductors

I.1. Introduction:.....10

I.2. Structural properties: 11

I.2.1. General Concepts of Crystal Structures:.....11

I.2.1.a. Crystal structure: 12

I.2.1.b. Bravais Lattices:.....13

I.2.1.c. Reciprocal Lattice: 13

I.2.1.d. Wigner Seitz Cell : 14

I.2.1.e. First Brillouin Zone:.....15

I.2.1.f. High Symmetric Points and Lines:.....15

I.2.2. Basic Crystal Structures:.....16

I.2.2.a. Zinc Blende (ZB) Structure:.....16

I.2.2.b. Wurtzite (WZ) Structure: 17

I.2.2.c. Sodium chloride (NaCl) structure: 18

I.2.2.d. Cesium Chloride (Cscl) Structure:.....19

I.2.2.e. Cubic Double Perovskite Structure :.....20

I.2.3. Ground State structure and Transition Phase:.....21

I.3. Electronic properties:.....21

I.3.1. Band structure in Solids:.....21

I.3.2. Direct and Indirect Band Gap Semiconductors: **23**
I.4. Optical properties: **24**
I.4.1. Dielectric Function: **24**
I.4.2. Refractive Index: **25**
I.4.3. Absorption Coefficient: **25**
I.4.4. Normal Incidence Reflectivity: **25**
I.4.5. Optical Conductivity: **26**
I.5. Elastic Properties: **26**
I.5.1. Elastic Stability Criteria: **27**
I.5.2. Mechanical Modulus: **27**
I.5.3. Ductile and Brittle Nature: **28**
I.5.4. Elastic anisotropy: **29**
I.5.5. Acoustic behavior: **30**
I.6. Thermal properties **31**
I.7. Applications of Advanced Semiconductor Materials: III–V Compounds and Double Perovskites **31**
References: **34**

Chapter2: Fundamentals of Density Functional Theory (DFT)

II.1. The DFT Foundations **39**
II.1.1. Many-Body Schrodinger Equation Problem **39**
II.1.2. Born Oppenheimer Approximation: **40**
II.1.3. Reduction to Single - Particle Problem **41**
II.1.3.a. Pauli Exclusion Principle **41**
II.1.3.b. Hartree Approximation **42**
II.1.3.c. Hartree-Fock Approximation **43**
II.2. Density Functional Theory **46**
II.2.1. The Thomas-Fermi-Dirac Model **46**
II.2.2. Hohenberg-Kohn Theorems **49**

II.2.3. Kohn-Sham Equations 52

II.2.4. Exchange Correlation Functionals 55

II.2.4.a. Local Density Approximation (LDA) 56

II.2.4.b. Generalized Gradient Approximations (GGA) 58

II.2.4.b.1. Gradient-Expansion Approximation (GEA) 58

II.2.4.b.2. Generalized Gradient Approximations (GGA) 59

II.2.4.b.3. The Improved Modified Becke-Johnson (K-Mbj) Potential 64

II.2.4.b.4. Hybrid Functional 66

II.3. Solving the Kohn–Sham equations 68

References 71

Chapter III: Full Potential Linearized Augmented Plane Wave method

III.1. Introduction 78

III.2. Plane-Waves 79

III.2.1. Translational Symmetry in Crystals 79

III.2.2. Bloch's Theorem: 80

III.2.3. Sampling the Brillouin-zone and K-points: 81

III.3. Augmented Plane Wave (APW) approaches 82

III.3.1. The Muffin-Tin (MT) Approximation 82

III.3.2. APW Method: 84

III.4. Linearized Augmented Plane Wave (LAPW) 87

III.5. Semi-Core States Problem: 88

III.5.1. LAPW with Local Orbital (LAPW+LO): 90

III.5.2. APW with Local Orbital (APW+lo): 90

III.6. The Full Potential Linearized Augmented Plane Wave (FP-LAPW) method: 92

III.7. WIEN2k Code: 92

III.7.1. WIEN2K Computational Code: 92

III.7.2. Core Components of the WIEN2k Code: 93

III.7.2.a. Initialization of the calculation: 95

III.7.2.b. Self-Consistency Cycle (SCF) Calculation: 97

III.7.3. Calculating properties: 99

III.7.3.a. Volume Optimization: 100

III.7.3.b. Band structure: 100

III.7.3.c. Density of States (DOS): 101

III.7.3.d. Optical properties: 103

References: 105

Chapter 4: Results and discussions

IV.1. Introduction 109

IV.2. Methodology 109

IV.3. Properties of $YN_{1-x}Sb_x$ (Y = B, Al and Ga) Alloys (x = 0, 0.25, 0.50, 0.75 and 1) 110

***IV.3.1.* Structural properties 110**

***IV.3.2.* Structural transition phase 118**

***IV.3.3.* Electronic properties 124**

***IV.3.4.* Optical properties 137**

***IV.3.5.* Elastic properties 147**

***IV.3.6.* Thermal properties 161**

IV.4. Properties of Sr_2NaXO_6 (X = Cl, Br and I) Double Perovskite semiconductors 167

***IV.4.1.* Structural properties 167**

***IV.4.2.* Electronic properties 168**

IV.4.3. **Optical properties** **172**

IV.4.4. **Elastic properties** **176**

IV.4.5. **Thermoelectric properties** **184**

References: **189**

General Conclusion **199**

List of Figures

Figure	Title	Page
Chapter1: Fundamental Physical Properties of Semiconductors		
Figure I. 1	Schematic diagram of the path difference in two-center scattering	11
Figure I. 2	Combination of basis and lattice forms crystal structure	12
Figure I. 3	Crystal structures: (a) simple cubic (SC), (b) body-centered cubic (BCC), and (c) face-centered cubic (FCC)	13
Figure I. 4	Real and reciprocal space of graphene showing lattice vectors $\overrightarrow{a_1}, \overrightarrow{a_2}$ and reciprocal vectors $\overrightarrow{b_1}, \overrightarrow{b_2}$	14
Figure I. 5	Brillouin zone (a) for simple cubic (SC), (b) for body-centered cubic (BCC), and (c) for face-centered cubic (FCC)	15
Figure I. 6	Zinc blende structure	17
Figure I. 7	Wurtzite structure	18
Figure I. 8	Sodium chloride structure	18
Figure I. 9	Cesium chloride crystal structure.	19
Figure I. 10	The crystal structure of the double perovskite unit cell for Cs_2BiCuI_6	20
Figure I. 11	Schematic Diagram of Energy Gap Formation	22
Figure I. 12	Energy band schematics for (a) insulator, (b) semiconductor, and (c) conductor	23
Figure I. 13	Direct and Indirect bandgap in semiconductor	24
Chapter2: Fundamentals of Density Functional Theory (DFT)		
Figure II. 1	Visual depiction of the Kohn–Sham method	55
Figure II. 2	Jacob's Ladder of Exchange–Correlation Functionals in DFT.	56
Figure II. 3	Self-Consistent Kohn–Sham Density Functional Theory (DFT) Workflow	70
Chapter III: Full Potential Linearized Augmented Plane Wave method		
Figure III. 1	Smallest wedge of the 1st BZ such that any wave-vector k in the 1^{st} BZ can be obtained from a wave-vector k in the IBZ	82
Figure III. 2	Schematic representation of unit cell Volume partitioned into muffin-tin and interstitial regions.	83
Figure III. 2	Muffin-tin and interstitial regions with APWs (red) matched to plane waves (blue) at sphere boundaries.	85
Figure III. 4	The w2web server	94

Figure III. 3	*The creation of a new session and directory*	*94*
Figure III. 6	*Creating the master input file (struct file)*	*95*
Figure III. 4	*Initialization with w2web*	*96*
Figure III. 8	*Flowchart illustrating workflow of a WIEN2k calculation, covering the initialization phase and the SCF cycle[32].*	*99*
Figure III. 9	*w2web window for Calculating the band structure*	*101*
Figure III. 10	*w2web window for calculating the density of state*	*102*
Figure III. 5	*w2web window for calculating the optical properties*	*103*
Chapter 4:Results and discussions		
Figure IV.1	*The total energy volume curves for $BN_{1-x}Sb_x$ x=0, 0.25, 0.50, 0.75 and 1) alloys*	*111*
Figure IV.2	*The total energy volume curves for $AlN_{1-x}Sb_x$(x=0, 0.25, 0.50, 0.75 and 1) alloys.*	*112*
Figure IV.3	*The energy versus volume curve of $GaN_{1-x}Sb_x$ alloys with x = {0, 0.25, 0.50, 0.75 and 1}*	*113*
Figure IV. 4	*Lattice Parameter and Bulk Modulus Variation with Sb Concentration in $YN_{1-x}Sb_x$ (Y=B, Al and Ga) (x=0, 0.25, 0.50, 0.75 and 1) alloys in zinc blende phase.*	*117*
Figure IV. 5	*Enthalpy (Ha) variation versus pressure (GPa) for ZB, NaCl, CsCl, WZ phases for $BN_{1-x}Sb_x$ (x=0, 0.25, 0.50, 0.75 and 1) alloys*	*119*
Figure IV. 6	*Enthalpy (Ha) variation versus pressure (GPa) for ZB, NaCl, CsCl, WZ phases for $AlN_{1-x}Sb_x$ (x=0, 0.25, 0.50, 0.75 and 1) alloys*	*120*
Figure IV. 7	*Enthalpy (Ha) variation versus pressure (GPa) for ZB, NaCl, CsCl, WZ phases for $GaN_{1-x}Sb_x$ (x=0, 0.25, 0.50, 0.75 and 1) alloys*	*121*
Figure IV. 8	*Energy band structure diagram of $BN_{1-x}Sb_x$ (x=0, 0.25, 0.50, 0.75 and 1) alloys using KTB potential scheme*	*126*
Figure IV. 9	*Energy band structure diagram of $AlN_{1-x}Sb_x$ (x=0, 0.25, 0.50, 0.75 and 1) alloys using KTB potential scheme*	*128*
Figure IV. 10	*Energy band structure diagram of $GaN_{1-x}Sb_x$ (x=0, 0.25, 0.50, 0.75 and 1) alloys using KTB potential scheme*	*129*
Figure IV. 11	*Calculated total and partial density of states for $BN_{1-x}Sb_x$ (x=0, 0.25, 0.50, 0.75 and 1) system using KTB-mBJ approximation.*	*134*

Figure IV. 12	*Calculated total and partial density of states for $AlN_{1-x}Sb_x$ (x=0, 0.25, 0.50, 0.75 and 1) system using KTB-mBJ approximation.*	*136*
Figure IV. 13	*Variation of the dielectric function, refractive index, and absorption versus energy of $BN_{1-x}Sb_x$ $(x = 0.0, 0.25, 0.5, 0.75\ and\ 1.0)$ alloys*	*138*
Figure IV. 14	*Variation of the dielectric function, refractive index, and absorption versus energy of $AlN_{1-x}Sb_x$ $(x = 0.0, 0.25, 0.5, 0.75\ and\ 1.0)$ alloys*	*139*
Figure IV. 15	*Variation of the dielectric function, refractive index, and absorption versus energy of $GaN_{1-x}Sb_x$ $(x = 0.0, 0.25, 0.5, 0.75\ and\ 1.0)$ alloys*	*140*
Figure IV. 16	*3D-directional dependence of the Bulk modulus (B in GPa) accompanied with its projections in different planes for $BN_{1-x}Sb_x$*	*152*
Figure IV. 17	*3D-directional dependence of the Shear modulus (B in GPa) accompanied with its projections in different planes for $BN_{1-x}Sb_x$*	*153*
Figure IV. 18	*3D-directional dependence of the Young modulus (B in GPa) accompanied with its projections in different planes for $BN_{1-x}Sb_x$*	*154*
Figure IV. 19	*3D-directional dependence of the Bulk modulus (B in GPa) accompanied with its projections in different planes for $AlN_{1-x}Sb_x$*	*155*
Figure IV. 20	*3D-directional dependence of the Shear modulus (B in GPa) accompanied with its projections in different planes for $AlN_{1-x}Sb_x$*	*156*
Figure IV. 21	*3D-directional dependence of the Young modulus (B in GPa) accompanied with its projections in different planes for $AlN_{1-x}Sb_x$*	*157*
Figure IV. 22	*3D surface of the bulk modulus in GPa and their 2D projections in (100), (010) and (001) planes for $GaN_{1-x}Sb_x$with x = (0, 0.25, 0.50, 0.75 and 1).*	*158*
Figure IV. 23	*3D surface of Shear modulus in GPa and their 2D projections in (100), (010) and (001) planes for $GaN_{1-x}Sb_x$with x = (0, 0.25, 0.50, 0.75 and 1).*	*159*
Figure IV. 24	*3D surface of Young's modulus in GPa and their 2D projections in (100), (010) and (001) planes for $GaN_{1-x}Sb_x$with x = (0, 0.25, 0.50, 0.75 and 1).*	*160*
Figure IV. 25	*variation of lattice parameter, bulk modulus, isochoric heat capacity C_V , isobaric heat capacity C_P and Debye temperature as*	*164*

	function of temperature for $BN_{1-x}Sb_x$ alloys with x = (0, 0.25, 0.50, 0.75 and 1).	
Figure IV. 26	*variation of lattice parameter, bulk modulus, isochoric heat capacity C_V , isobaric heat capacity C_P and Debye temperature as function of temperature for $AlN_{1-x}Sb_x$ alloys with x = (0, 0.25, 0.50, 0.75 and 1).*	*165*
Figure IV. 27	*variation of lattice parameter, bulk modulus, isochoric heat capacity C_V , isobaric heat capacity C_P and Debye temperature as function of temperature for $GaN_{1-x}Sb_x$ alloys with x = (0, 0.25, 0.50, 0.75 and 1).*	*166*
Figure IV. 28	*The total energy (in Ry) plotted against volume $(in(a.u.)^3)$ for Sr_2NaXO_6(X=Cl, Br and I) oxide double perovskite.*	*167*
Figure IV. 29	*The simulated band structures for Sr_2NaXO_6 (X = Cl, Br, and I) using KTB-mBJ approximation.*	*170*
Figure IV. 30	*TDOS and PDOS for Sr2NaXO6(X=Cl, Br and I) using KTB-mBJ potential scheme*	*171*
Figure IV. 31	*The energy dependence on the parts of dielectric function ($\varepsilon_1(\omega)$ and $\varepsilon_2(\omega)$) for Sr_2NaXO_6(X=Cl, Br and I) oxide double perovskite.*	*174*
Figure IV. 32	*the variation of absorption coefficient as function of energy for Sr_2NaXO_6(X=Cl, Br and I) oxide double perovskite*	*175*
Figure IV. 33	*Refractive index and Extinction coefficient as function of energy for Sr_2NaXO_6(X=Cl, Br and I) oxide double perovskite*	*176*
Figure IV. 34	*3D plotted of Bulk modulus and Young's modulus for Sr_2NaXO_6(X=Cl, Br and I)oxide double Perovskite*	*181*
Figure IV. 35	*3D plotted of Shear modulus and Poisson's ratio for Sr_2NaXO_6(X=Cl, Br and I) oxide double Perovskite*	*182*
Figure IV. 36	*3D plotted of Pugh's ratio and Hardness for Sr_2NaXO_6 (X=Cl, Br and I) oxide double Perovskite*	*183*
Figure IV. 37	*The variations of Seebeck coefficient as function of temperature for Sr2NaXO6(X=Cl, Br and I) oxide double perovskitse*	*185*
Figure IV. 38	*The variations of electronic conductivity per relaxation time as function of temperature for Sr2NaXO6(X = Cl, Br and I) oxide double perovskites*	*186*
Figure IV. 39	*The thermal conductivity, the electronic thermal conductivity and the lattice thermal conductivity per relaxation for Sr_2NaXO_6(X=Cl, Br and I) oxide double perovskite.*	*187*

Figure IV. 40	*The variations of power factor per relaxation time as function of temperature for Sr2NaXO6(X=Cl, Br and I) oxide double perovskites*	*188*
Figure IV. 41	*The variations of figure of merit as function of temperature for Sr_2NaXO_6(X=Cl, Br and I) oxide double perovskite*	*188*

List of Tables

Table	Title	Page
Chapter1: Fundamental Physical Properties of Semiconductors		
Table I. 1	High-Symmetry Points in the Brillouin Zone for Different Crystal Systems	16
Table I. 2	Comparison of Structural Characteristics of ZB, WZ, NaCl, and CsCl.	19
Chapter2: Fundamentals of Density Functional Theory (DFT)		
Table II. 1	KTB-mBJ potential parameters for different material classes	67
Chapter 4: Results and discussions		
Table IV. 1	Adopted values of the muffin-tin radius (R_{MT}) for YN1-xSbx (Y = B, Al and Ga) alloy at x=0.0, 0.25, 0.50, 0.75 and 1.0 s in ZB structure	110
Table IV. 2	Adopted values of the muffin-tin radius (R_{MT}) for Sr_2NaXO_6 (X=Cl, Br and I) double perovskites	110
Table IV. 3	Lattice constant and bulk modulus of $YN_{1-x}Sb_x$ (Y=B, Al and Ga) (x=0, 0.25, 0.50, 0.75 and 1) ternary alloys in the ZB phase	115
Table IV. 4	Lattice constant $a_0\ (°A)$ and bulk modulus $B_0(GPa)$ for $BN_{1-x}Sb_x$ (x = 0.25, 0.50 and 0.75) and $BSb_{1-x}N_x$ (x = 0.25, 0.50 and 0.75) alloys	116
Table IV. 5	Critical pressure for NaCl, CsCl, ZB, and WZ phases for $AlN_{1-x}Sb_x$ and $GaN_{1-x}Sb_x$ alloys	122
Table IV. 6	Energy band gaps (eV) of $YN_{1-x}Sb_x$ (Y = B, Al and Ga) alloys in the ZB phase	124
Table IV. 7	Values of zero-frequency limits $\varepsilon_1(0), n(0)$ and The critical points energies (eV) in $\varepsilon_2(\omega)$ of $YN_{1-x}Sb_x$ (Y=B, Al and Ga) alloys in the ZB phase using the KTB-mBJ scheme	145
Table IV. 8	The estimated elastic constants $C_{ij}\ (GPa)$, Cauchy pressure $C'\ (GPa)$ and Kleinman parameter ξ of $YN_{1-x}Sb_x$ (Y=B, Al and Ga) systems	147
Table IV. 9	The Estimated mechanical parameters $(B, G, E, v, H_v and\ B/G)$ elastic anisotropy parameters (A, A_G, A_B and A^U) for $YN_{1-x}Sb_x$ (Y=B, Al and Ga) systems in ZB phase	150

Table IV. 10	*Lattice parameter a_0, bulk modulus B_0, isochoric heat capacity C_V, isobaric heat capacity C_P and Debye temperature $\theta(K)$ at ambient conditions for $YN_{1-x}Sb_x$ (Y=B, Al and Ga) systems*	*163*
Table IV. 11	*Fundamental structural parameters(a_0, B_0, B'_0, E_0), formation energy (E_F), Goldschmidt's tolerance factor $(\tau)$and octahedral factor (μ) for Sr2NaXO6(X=Cl, Br and I)*	*168*
Table IV. 12	*Energy gap values (eV) of Sr2NaXO6$(X = Cl, Br\ and\ I)$*	*169*
Table IV. 13	*Elastic constants $C_{ij}(GPa)$, Elastic compliance constants $S_{ij}(GPa^{-1})$, Kleinman's parameter ξ and Cauchy pressure C'' (GPa) for Sr2NaXO6(X=Cl, Br and I) oxide double perovskites*	*177*
Table IV. 14	*Mechanical modulus (GPa) for Sr2NaXO6(X=Cl, Br and I) oxide double perovskites*	*178*
Table IV. 15	*The elastic anisotropy parameters(A^U, A, A_G, A_B, A_L) for Sr2NaXO6(X=Cl, Br and I) oxide double perovskites*	*179*

General introduction

Condensed matter physics is the largest and most multilateral branch of physics, dynamic and innovative field addresses a wide spectrum of challenging and fascinating concepts [1]. It study the characteristics of matter from the atomic scale to the macroscopic scale, by linking atomic-level interactions with bulk material behavior, thus offering essential foundations for both scientific understanding and technological innovation [2]. Where the technological innovation is interested and focused on discovering new materials with unique and tunable properties, such as semiconductors, which play a vital role in advancing renewable energy applications [3–5].

Semiconductors are solid material, characterized by a qualitative band gap placed between those of conductors and insulators [6]. This band gab can be varied with many factors like impurity content, temperature, excess charge carrier injection, and optical excitation, therefore, offers unique applications of these materials in various electronic devices[7]. Semiconductors are the heart of modern technology and industry, where the III–V semiconductors and double perovskite compounds are standing out as particularly powerful and promising classes of materials with promising roles in modern technology.

The III–V semiconductors are compounds formed by integrating of elements from group III (B, Al and Ga,…) and group V (N, Sb and As, …) of the periodic table resulting in binary semiconductor materials such as GaN, GaSb, AlN and AlSb. The usefulness of III–V semiconductors is greatly enhanced by their remarkable alloying flexibility, which arises from the possibility of substituting one group-III or group-V element with another of the same group. These partial substitutions lead to the formation of ternary alloys such as $GaN_{1-x}Sb_x$ and $AlN_{1-x}Sb_x$. The binary compounds (As: GaN, GaSb, AlN, AlSb) have a direct band gap [8,9] so electrons can recombine with holes without requiring intermediate steps, this allows for rapid radiative recombination and gives these materials the capability to efficiently generate light. Which makes them highly efficient for optoelectronic applications such as LEDs [10,11], electroluminescent diodes and laser diodes [12–14], high-frequency devices [15], and solar cells [16–18].

III – V nitride materials (like: GaN, AlN and their alloys) are especially notable and have attracted great interest due to their direct band gap transitions, along with their high thermal conductivity. The III-V ternary semiconductors like (Al, In)GaN system has therefore become a

key platform for high-power, high-temperature electronics and short-wavelength optoelectronics [10]. In particular, GaN, with its wide bandgap of 3.4 eV and robust crystal structure, supports technologies from violet laser diodes to blue and green LEDs, enabling full-color displays and advancing solid-state lighting [9,19]. Beyond optoelectronics, GaN is also emerging as a strong candidate to replace silicon in power devices[19,20]. Meanwhile, GaAs, favorable for its high electron mobility, remains essential for high-frequency integrated circuits and infrared optoelectronic devices [10].

Double perovskite compounds are quaternary compounds generally have the formula $A_2BB'X_6$, where A is a large cation (alkali or rare earth), and B, B' are transition metal cations. Owing to their structural flexibility and compositional versatility that allow a wide variety of cation compositions, double perovskites are drawing growing attention over simple perovskites, offering a rich variety of electronic, thermoelectrical, and optical behaviors. Their tunable band gaps, high charge carrier mobility and excellent stability, offer strong light absorption and tunable photoluminescence [21]. All this features make them strong candidates for photovoltaic applications [22,23], photo-detection materials for optical communication [24–26], X-ray detectors [27–29], memory storage devices [30], in addition to others. There are distinct classes of perovskite materials with different compositions and structural features as double oxide perovskites ($A_2BB'O_6$) and double halide perovskites ($A_2BB'X_6$) where X refer to halide inion.

The research for new semiconductor materials with specific physical or chemical properties is a major challenge for the current industry, and determining their properties is even more challenging, because require the synergy between experimental methods and computational simulations. In which based on computational simulation, it has become possible to determine the properties of materials with high precision based on quantum-mechanical calculations, these predictions guide experimental synthesis and characterization to validate performance and properties. Among computational techniques, Density Functional Theory (DFT)[31–33] combined with the Full-potential Linearized Augmented Plane Wave (FP-LAPW) method[34] stands out as a highly accurate approach for predicting and analyzing the structural, electronic, elastic and thermal properties….

DFT offers a quantum mechanical framework that treats the many-electron problem presented by Schrödinger equation and put a good reformulation of this problem by Kohn, Hohenberg, and Sham in the 1960 [32,33]. In which, reformulates the complex many-electron problem by replacing interacting electrons with non-interacting particles moving in an effective potential. Based on electron density rather than wave functions. DFT focuses on the electronic density depending only on three spatial coordinates. By solving single-electron Kohn-Sham equations self-consistently allowing tractable calculations of ground state properties. FP-LAPW enhances this by providing a full-potential treatment without shape approximations to the potential or charge density, enabling precise calculations of these properties. WIEN2k combines linearized augmented plane waves with full-potential methods within Density Functional Theory, allowing detailed and reliable modeling of complex crystal geometries and electronic properties that are essential for semiconductor research and material design.

A thesis organized into two main parts—a theoretical section with three chapters and a second section is for results and discussions—provides a clear, systematic framework for presenting research.

The first part establishes the foundational framework for the research:

- Chapter I titled '***Fundamental Physical Properties of Semiconductors'*** in which examine the main crystal structures and identify the basic characteristics of these crystals, in addition to explore the fundamental properties of semiconductors.
- Chapter II following the title '***Fundamentals of Density functional theory'*** offer a clear and concise introduction to the fundamental equations that are essential for understanding DFT.
- Chapter III following the title '***Full Potential Linearized Augmented Plane Wave method***' provide an overview for the computational methods in electronic structure calculations—from APW method to FP-LAPW approach and introduces the WIEN2k software.

The second part represent Chapter IV titled ***'Results and discussions'.*** Driven by the outstanding properties of gallium nitride alloys and double perovskites. We conduct a detailed study to investigate the stability, structural, electronic, optical, elastic, and thermal characteristics for $YN_{1-x}Sb_x$ ternary alloys in which (Y: B, Al and Ga) with x representing Sb concentration (x=0,

0.25, 0.5, 0.75 and 1) in addition to Sr_2NaXO_6 (X = Cl, Br, and I) double perovskite. These compounds are identified as emerging semiconductor materials with significant potential for future technological application.

References:

[1] Introduction, in: Encyclopedia of Condensed Matter Physics, Elsevier, 2024: pp. ix–xvii. https://doi.org/10.1016/B978-0-323-90800-9.09967-4.
[2] P. Willmott, Deposition of complex multielemental thin films, Progress in Surface Science 76 (2004) 163–217. https://doi.org/10.1016/j.progsurf.2004.06.001.
[3] H. Meddeb, M. Götz-Köhler, N. Neugebohrn, U. Banik, N. Osterthun, O. Sergeev, D. Berends, C. Lattyak, K. Gehrke, M. Vehse, Tunable Photovoltaics: Adapting Solar Cell Technologies to Versatile Applications, Advanced Energy Materials 12 (2022) 2200713. https://doi.org/10.1002/aenm.202200713.
[4] E. Kianfar, H. Koten, W.R. Kadhum, Investigating the properties of semiconductors solar cells technologies, efficiency for photovoltaic cells and application graphene for solar cells : A review, Solar Compass 16 (2025) 100147. https://doi.org/10.1016/j.solcom.2025.100147.
[5] A.A. Khan, I. Khan, I. Ahmad, Z. Ali, Thermoelectric studies of IV–VI semiconductors for renewable energy resources, Materials Science in Semiconductor Processing 48 (2016) 85–94. https://doi.org/10.1016/j.mssp.2016.03.012.
[6] II-VI Semiconductor Materials and their Applications, n.d. https://books.google.com/books/about/II_VI_Semiconductor_Materials_and_their.html?hl=fr&id=TRc9SmakXwYC (accessed October 19, 2025).
[7] Characterization of Semiconductors, in: Semiconductor Materials, Springer, Boston, MA, 2003: pp. 171–215. https://doi.org/10.1007/0-306-47942-7_7.
[8] D.V. Khanin, S.E. Kul'kova, Electronic Properties of III – V Semiconductors, Russ Phys J 48 (2005) 70–77. https://doi.org/10.1007/s11182-005-0086-1.
[9] Physical Properties of III-V Semiconductor Compounds - Sadao Adachi - Google Livres, (n.d.). https://books.google.dz/books?hl=fr&lr=&id=fpiSIdfAlz4C&oi=fnd&pg=PR15&dq=properties+of+iii+v+semiconductors&ots=ERPOa7R6RJ&sig=wOUjsgUjJqmVj-oPHOopprgo2N4&redir_esc=y#v=onepage&q=properties%20of%20iii%20v%20semiconductors&f=false (accessed October 20, 2025).
[10] III-V Semiconductors, Beneq (n.d.). https://beneq.com/led-photonics/iii-v-semiconductors/ (accessed October 20, 2025).
[11] J. Bruckbauer, Luminescence study of III-nitride semiconductor nanostructures and LEDs, (2013).
[12] T. Sadi, I. Radevici, P. Kivisaari, J. Oksanen, Electroluminescent cooling in III–V intracavity diodes: Efficiency bottlenecks, IEEE Transactions on Electron Devices 66 (2019) 2651–2656.
[13] R.H. Rediker, Semiconductor diode luminescence and lasers. A perspective, IEEE Journal of Selected Topics in Quantum Electronics 6 (2002) 1355–1362.
[14] N. Holonyak, The III–V alloy p–n diode laser and LED ultimate lamp, Proceedings of the IEEE 101 (2013) 2158–2169.

[15] S. Prasad, High-frequency compound SC devices, Materials Today 12 (2009) 34–37. https://doi.org/10.1016/S1369-7021(09)70111-7.
[16] Comparison of neutron conversion layers for GaN-based scintillators - Melton - 2012 - physica status solidi c - Wiley Online Library, (n.d.). https://onlinelibrary.wiley.com/doi/abs/10.1002/pssc.201100432 (accessed October 20, 2025).
[17] T. Kinoshita, T. Obata, T. Nagashima, H. Yanagi, B. Moody, S. Mita, S. Inoue, Y. Kumagai, A. Koukitu, Z. Sitar, Performance and Reliability of Deep-Ultraviolet Light-Emitting Diodes Fabricated on AlN Substrates Prepared by Hydride Vapor Phase Epitaxy, Appl. Phys. Express 6 (2013) 092103. https://doi.org/10.7567/APEX.6.092103.
[18] T. Kinoshita, K. Hironaka, T. Obata, T. Nagashima, R. Dalmau, R. Schlesser, B. Moody, J. Xie, S. Inoue, Y. Kumagai, A. Koukitu, Z. Sitar, Deep-Ultraviolet Light-Emitting Diodes Fabricated on AlN Substrates Prepared by Hydride Vapor Phase Epitaxy, Appl. Phys. Express 5 (2012) 122101. https://doi.org/10.1143/APEX.5.122101.
[19] a S. Strite, H. Morkoç, GaN, AlN, and InN: a review, Journal of Vacuum Science & Technology B: Microelectronics and Nanometer Structures Processing, Measurement, and Phenomena 10 (1992) 1237–1266.
[20] K. Kash, Optical properties of III–V semiconductor quantum wires and dots, Journal of Luminescence 46 (1990) 69–82. https://doi.org/10.1016/0022-2313(90)90009-Z.
[21] Advances in lead-free double perovskite nanocrystals, engineering band-gaps and enhancing stability through composition tunability - Nanoscale (RSC Publishing) DOI:10.1039/C9NR01031A, (n.d.). https://pubs.rsc.org/en/content/articlehtml/2019/nr/c9nr01031a (accessed October 20, 2025).
[22] M. Rani, P.K. Kamlesh, S. Kumawat, U. Rani, G. Arora, A.S. Verma, Rare earth-based oxides double perovskites A2NiMnO6 (A= La and Gd): applications in magneto-caloric, photo-catalytic and thermoelectric devices, Physica B: Condensed Matter 680 (2024) 415645.
[23] A. Aziz, N. Bibi, M. Usman, S. Noreen, First-Principles evaluation of Lead-Free X2NaIO6 (X=Sr, Ba) Double-Perovskite: For optoelectronic and solar cell applications, Chemical Physics 586 (2024) 112405. https://doi.org/10.1016/j.chemphys.2024.112405.
[24] J. Ghosh, N.K. Tailor, K. Ghosh, J. Jayarathne, S. Choudhary, C. Crean, P.K. Giri, S. Satapathi, P. Sellin, Cs2AgBiBr6 Double Perovskite Single Crystal/ CsPbBr3 Perovskite Nanocrystals Heterojunction for High-Performance X-Ray Detection, Advanced Optical Materials 13 (2025) 2402497. https://doi.org/10.1002/adom.202402497.
[25] H. Lei, D. Hardy, F. Gao, Lead-Free Double Perovskite Cs2AgBiBr6: Fundamentals, Applications, and Perspectives, Advanced Functional Materials 31 (2021) 2105898. https://doi.org/10.1002/adfm.202105898.
[26] Lead-Free Halide Double Perovskite for High-Performance Photodetectors: Progress and Perspective, (n.d.). https://www.mdpi.com/1996-1944/16/12/4490 (accessed October 20, 2025).
[27] Self-Powered X-ray Detection and Imaging using Cs2AgBiCl6 Lead-Free Double Perovskite Single Crystal | ACS Applied Electronic Materials, (n.d.). https://pubs.acs.org/doi/abs/10.1021/acsaelm.2c00752 (accessed October 20, 2025).

[28] Exploring Lead-Free Hybrid Double Perovskite Crystals of (BA)2CsAgBiBr7 with Large Mobility-Lifetime Product toward X-Ray Detection - Xu - 2019 - Angewandte Chemie International Edition - Wiley Online Library, (n.d.). https://onlinelibrary.wiley.com/doi/abs/10.1002/anie.201909815 (accessed October 20, 2025).
[29] J.A. Steele, W. Pan, C. Martin, M. Keshavarz, E. Debroye, H. Yuan, S. Banerjee, E. Fron, D. Jonckheere, C.W. Kim, Photophysical pathways in highly sensitive Cs2AgBiBr6 double-perovskite single-crystal X-ray detectors, Advanced Materials 30 (2018) 1804450.
[30] Y. Zheng, F. Luo, L. Ruan, J. Tong, L. Yan, C. Sun, X. Zhang, A facile fabrication of lead-free Cs2NaBiI6 double perovskite films for memory device application, Journal of Alloys and Compounds 909 (2022) 164613.
[31] L.J. Sham, Approximations of the Exchange and Correlation Potentials, in: P.M. Marcus, J.F. Janak, A.R. Williams (Eds.), Computational Methods in Band Theory: Proceedings of a Conference Held at the IBM Thomas J. Watson Research Center, Yorktown Heights, New York, May 14–15, 1970, under the Joint Sponsorship of IBM and the American Physical Society, Springer US, Boston, MA, 1971: pp. 458–468. https://doi.org/10.1007/978-1-4684-1890-3_36.
[32] W. Kohn, L.J. Sham, Self-Consistent Equations Including Exchange and Correlation Effects, Phys. Rev. 140 (1965) A1133–A1138. https://doi.org/10.1103/PhysRev.140.A1133.
[33] P. Hohenberg, W. Kohn, Inhomogeneous Electron Gas, Phys. Rev. 136 (1964) B864–B871. https://doi.org/10.1103/PhysRev.136.B864.
[34] M. Petersen, F. Wagner, L. Hufnagel, M. Scheffler, P. Blaha, K. Schwarz, Improving the Efficiency of FP-LAPW Calculations, Computer Physics Communications 126 (2000) 294–309. https://doi.org/10.1016/S0010-4655(99)00495-6.

Chapter I:

Fundamental Physical Properties of Semiconductors

I.1. Introduction:

Semiconductors represent an essential basis of modern science and technology, linking fundamental solid-state physics with practical applications in electronics, optoelectronics, and energy systems. Their importance stems from their characteristic electrical resistivity(ρ), which lies between that of metals and insulators[1]. Typically, semiconductors exhibit resistivity in the range of about $\rho \sim 10^{-5} - 10^{6} \Omega.m$ corresponding to conductivities of approximately $\sigma \sim 10^{-6} - 10^{5} S/m$ [2]. This unique behavior arises from their electronic band structure, characterized by a band gap between the valence and conduction bands, where the energy gap can be tuned through doping, temperature, external electrical field and others; this flexibility makes semiconductors the foundation of modern electronics and optoelectronics. This tunability makes semiconductors indispensable for devices such as transistors, lasers [3], light-emitting diodes (LEDs) [4,5], and solar cells [6,7]. Determining of semiconductor applications requires characterization of their structural, electronic, optical and elastic properties, and others.

The structural properties including crystal symmetry, lattice constants, and bonding nature provide the framework that governs their fundamental behavior. In general, most technologically relevant semiconductors crystallize in zinc-blende (ZB) or wurtzite (WZ) structures, and in some cases, they may also adopt rocksalt (NaCl) or cesium chloride (CsCl) structures. Determining the electronic properties of any material such as the band structure and energy gap is an important tool for defining the performance of electronic devices. Coupled to this, the optical properties including dielectric function, absorption spectra, refractive index and others characterize the interaction of semiconductors with electromagnetic radiation, underpinning their central role in modern photonic and photovoltaic technologies. Equally important are the elastic properties, which describe how semiconductors respond to mechanical stress and strain. Elastic constants and related parameters not only determine mechanical stability but also influence electronic and optical responses via strain engineering.

Before discussing semiconductor materials, it is useful to first examine their main crystal structures and identify the basic characteristics of these crystals. It is also essential to outline their electronic band structures, after which we will explore the fundamental properties of semiconductors in general.

I.2. Structural properties:

When studying semiconductors**,** several structural properties must be determined, because the arrangement of atoms strongly effects their electronic, optical, and mechanical behavior.

I.2.1. General Concepts of Crystal Structures:

Solids are typically organized into crystalline materials and amorphous materials. Crystalline materials include single crystals and polycrystalline materials. We are interested in the crystal structure before we discuss the semiconductor crystal because it directly determines their fundamental physical properties and thus their technological applications [2].

Experimentally, we distinguish whether a material is crystalline or amorphous based on X-ray diffraction (XRD). Crystalline materials have atoms arranged in a long-range, which causes strong constructive interference of X-rays at specific angles. The diffraction condition is illustrated in ***Figure I.1***, which demonstrates that the path difference between X-ray waves, which are secularly reflected from two adjoining (parallel) planes, is $2d.sin\theta$, this constructive interference is described by Bragg diffraction law[1]**:** $2d.sin\theta = n\lambda$. where n (called the order of the corresponding reflection) is an integer, λ is the wavelength of the radiation, d is the periodic spacing between the planes, and θ is the Bragg angle

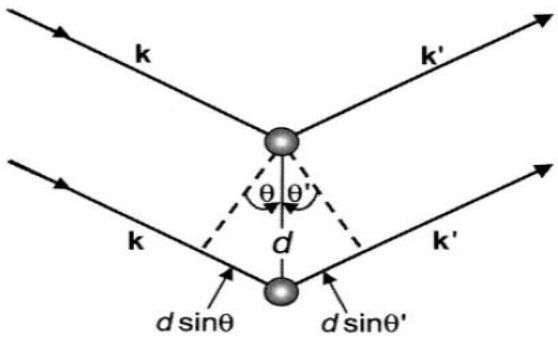


Figure I. 1: **Schematic diagram of the path difference in two-center scattering[1]**

This results in sharp, well-defined diffraction peaks in the XRD pattern, each corresponding to different sets of crystal planes. In contrast, amorphous materials, which do not show sharp peaks.

I.2.1.a. Crystal structure:

A crystalline solid is defined by the periodic arrangement of atoms or ions or group of atoms or molecules in three dimensions. This periodicity can be described in terms of two fundamental concepts: the lattice and the basis.

The lattice is A regular periodic arrangement of points in a three dimensional space such that each point is having an identical surrounding, while the basis is the identical group of atoms that is infinitely repeated at

each lattice point [2,8].The combination of a lattice and its basis generates the full crystal structure as sown in ***Figure I.2***.

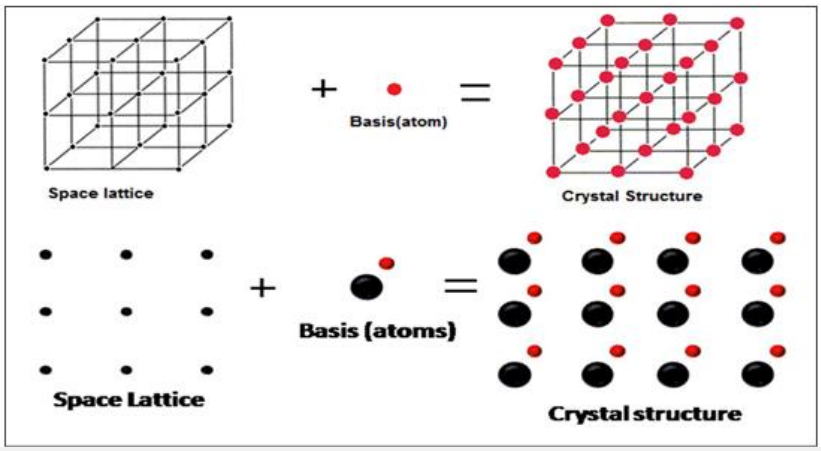


Figure I. 2: ***Combination of basis and lattice forms crystal structure*** **[9]**

To represent this periodic repetition, a unit cell is chosen a finite volume of the crystal that, through translations, reproduces the entire structure. The smallest unit cell that can be repeated to form the lattice is called the primitive cell, but in many cases, larger non-primitive unit cells with orthogonal axes are preferred for convenience. Depending on the relative lengths and angles of the lattice vectors, crystals are classified into one of the seven crystal systems with 14 different ways to arrange the lattice point (14 Bravais lattices) where the cubic system being of particular importance in semiconductors.

The cubic crystal structures represented in ***Figure I.3***, include the simple cubic (SC), where atoms occupy only the corners of the cube; the body centered cubic (BCC), with an additional atom at the cube's center; and the face centered cubic (FCC), where atoms are located at the corners and the centers of each cube face. Many technologically significant semiconductors and III–V compounds, crystallize in derivatives of the FCC lattice, most notably the zinc blende (ZB) and wurtzite (WZ) structures.

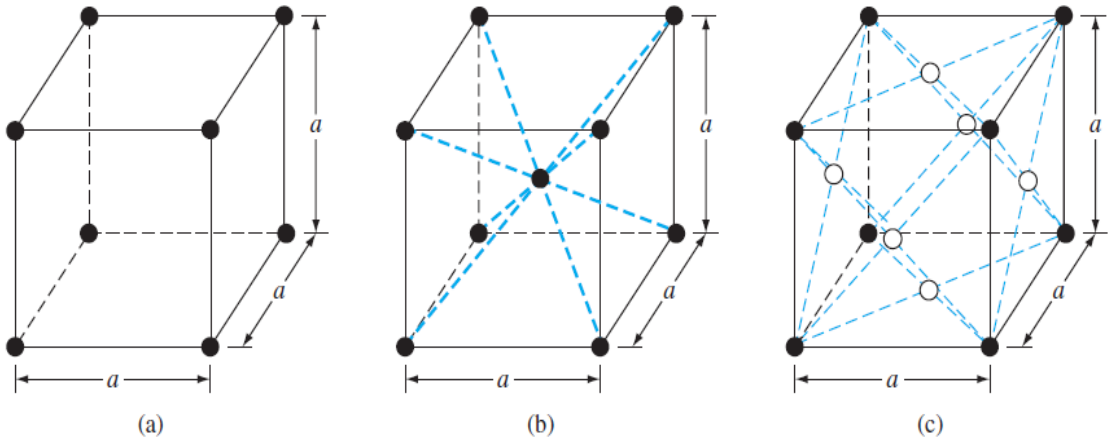


Figure I. 3: ***Crystal structures: (a) simple cubic (SC), (b) body-centered cubic (BCC), and (c) face-centered cubic (FCC)[2].***

I.2.1.b. Bravais Lattices:

A Bravais lattice is a distinct, mathematically defined arrangement of points in space such that each point has an identical environment in the real space [10], and the entire structure can be generated by translations of a set of primitive vectors. This invariance can be described by a translational vector $\vec{R}$ defined as [10]:

$$\vec{R} = n_1\overrightarrow{a_1} + n_2\overrightarrow{a_2} + n_3\overrightarrow{a_3} \qquad (I.\ 1)$$

Where $\overrightarrow{a_1}$, $\overrightarrow{a_2}$, and $\overrightarrow{a_3}$ are the basic vectors describe the distance between the two nearest-neighbor atoms in the x direction,y direction and z direction, respectively while n_1, n_2 and $n_3 \in \mathbb{Z}$

There are exactly 14 distinct Bravais lattices in 3D, grouped into seven crystal systems [11] (cubic, tetragonal, orthorhombic, hexagonal, rhombohedral, monoclinic, and triclinic).

I.2.1.c. Reciprocal Lattice:

To determine the structure of a real space lattice, the most widely used experimental techniques related to particle diffraction, the diffract particles behave as matter waves according to the de Broglie relation ($\lambda = {}^{h}/_{p}$) where λ is the wavelength, h is Planck's constant and p is the momentum magnitude. The propagation of a plane wave is described by its wavevector ($k = {}^{2\pi p}/_{h}$), which is perpendicular to the wave fronts. Combining with the de Broglie relation gives [1]:

$$k = \frac{2\pi}{\lambda} \qquad (I.\ 2)$$

Thus, wave vectors have units of inverse length, which motivates the introduction of a reciprocal lattice defined in momentum space. Therefore, the reciprocal space (k-space as shorthand because the most important variable in reciprocal space is the wavevector k) arises naturally because wave vectors ($\overrightarrow{b_1}$, $\overrightarrow{b_2}$ and $\overrightarrow{b_3}$ are with units of inverse length) interact with real lattice planes and allow present a reciprocal lattice vector $\vec{G}$ *[8]*. Diffraction conditions are expressed compactly in k-space : scattering occurs only if the momentum transfer matches a reciprocal lattice vector. This makes reciprocal space the most convenient framework for analyzing diffraction, Brillouin zones, and band structures *[10–12]*.

The reciprocal lattice is another Bravais lattice, but in wave vector space, (momentum space) as shown in ***Figure I. 4***, integer combinations of the reciprocal primitive vectors generate a reciprocal lattice vector [10]:

$$\vec{G} = n_1\overrightarrow{b_1} + n_2\overrightarrow{b_2} + n_3\overrightarrow{b_3} \qquad (I.\ 3)$$

It is defined such that for every real lattice vector R and every reciprocal lattice vector G:

$$e^{i\vec{G}\vec{R}} = 1 \implies \vec{G}\vec{R} = 2\pi n\,, n \in Z \qquad (I.\ 4)$$

This condition ensures that plane waves $e^{i\vec{G}\vec{R}}$reflect the periodicity of the crystal, as demonstrated by Bloch's theorem (discussed in chapter 3).

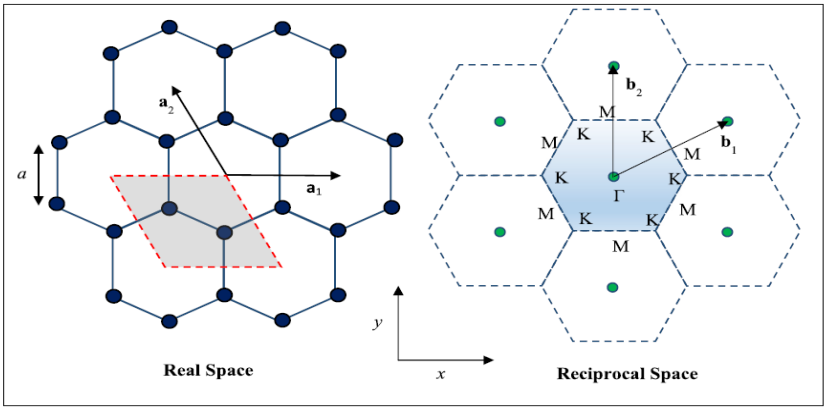


Figure I. 4: ***Real and reciprocal space of graphene showing lattice vectors $\overrightarrow{a_1}$, $\overrightarrow{a_2}$ and reciprocal vectors $\overrightarrow{b_1}$, $\overrightarrow{b_2}$*** **[13]**

I.2.1.d. Wigner Seitz Cell :

The Wigner Seitz (WS) cell is a special type of primitive cell contains exactly one lattice point, accurately reflects the symmetry of the underlying lattice and it's unique for a given lattice [14] (unlike other primitive cells, of which infinitely many can be chosen). The WS cell in the k-space is called the

Brillouin zone, which contains the information about whether a material will be a conductor, semiconductor or an insulator.

I.2.1.e. First Brillouin Zone:

As we will prove in Chapter 3, a wide range of calculations in crystalline solids require integrating periodic functions of the Bloch wave vector, either over the entire Brillouin zone (BZ) or within the irreducible Brillouin zone (IBZ) [15]. Since many fundamental electronic structure codes perform numerical integrals over the first Brillouin zone [16], thus require a detailed understanding of Brillouin zone—together with its high-symmetry points and characteristic lines is essential.

The concept of a Brillouin zone was developed by Léon Brillouin, The different Brillouin zones correspond to primitive cells of a different type that come up in the theory of electronic levels in a periodic potential. The first Brillouin zone is considered as the WS primitive cell in the reciprocal lattice. In other words, the first Brillouin zone is a geometrical construction to the WS primitive cell in the k-space.

The shape of the Brillouin zone (BZ) is uniquely determined by the symmetry of the direct crystal lattice [1], example: simple cubic (cube-shaped BZ), FCC (truncated octahedron), BCC (rhombic dodecahedron) as shown in ***Figure I.5***.

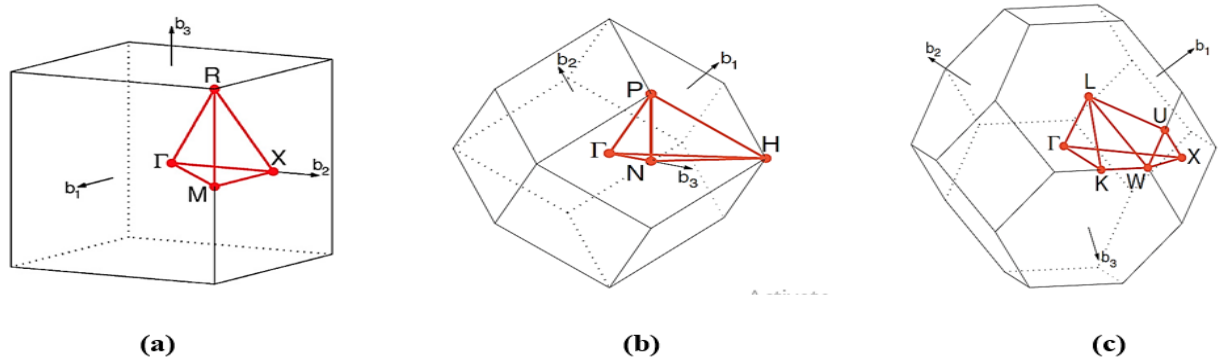


Figure I. 5: ***Brillouin zone (a) for simple cubic (SC), (b) for body-centered cubic (BCC), and (c) for face-centered cubic (FCC)*** *[17]*

I.2.1.f. High Symmetric Points and Lines:

Because the Brillouin zone (BZ) takes the full symmetry of the underlying crystal lattice, it contains characteristic points, lines, and planes of high symmetry such as the center (Γ), edges, and corners. These special k-points correspond to locations in reciprocal space where rotational, mirror, or translational

operations leave the crystal wave functions invariant, thus simplifying the treatment of Bloch states and enabling systematic calculations of the electronic band structure [8,18].

High-symmetry k-points are special high-symmetry point in the Brillouin zone where the valence and conduction bands meet at a single point, and the Fermi level passes directly through this crossing [19]. This points are usually shown in band structure plots such as Γ (zone center), X, L, and M vary depending on the type of lattice (cubic, hexagonal… etc.) as illustrated and explained in the ***Table I. 1***[14,15,17].

Table I. 1: High-Symmetry Points in the Brillouin Zone for Different Crystal Systems

Cubic structure	**Symbols**	
All structures	Γ	Central point in reciprocal space($k_\Gamma = 0,0,0$).
Simple cubic	H	Edge-crossing point at the corner
	N	Face-centered point
	P	Point of contact between three edges.
Body centred cubic	H	Corner point of the Brillouin zone (at the corner of the truncated octahedron).
	N	Midpoint of an edge between two hexagonal faces of the Brillouin zone.
	P	Point located on the body diagonal, inside the Brillouin zone (between Γ and H).
Face centered cubic	K	Midpoint of the edge between two hexagonal faces.
	L	Corner point where four Brillouin zones meet.
	U	Point located on the edge connecting a face and a body diagonal
	W	Edge center connecting X and L points.
	X	Center of a square face of the BZ.

Equally significant are the symmetry lines that connect these points, which reveal how electronic bands evolve across reciprocal space. In cubic systems, the principal directions include Δ (Γ → X) along ⟨100⟩, Σ (Γ → K) lying in mirror planes such as $k_x = k_y$, and Λ (Γ → L) along ⟨111⟩ [8,19]. Together, these symmetry elements form the backbone of modern band-structure studies and are indispensable for both theoretical analysis and practical applications such as interpreting optical transitions, phonon interactions, and transport phenomena in semiconductors.

I.2.2. Basic Crystal Structures:

I.2.2.a. Zinc Blende (ZB) Structure:

Zinc blende structure also called sphalerite or Zinc Sulfide Structure (ZnS) resulting from the combination of two FCC structures displaced from each other by one-quarter of a body diagonal, where the Zn ions are placed on one FCC lattice at the positions (0,0,0) $(0,{}^1/_2,{}^1/_2)$ $({}^1/_2,0,{}^1/_2)$ $({}^1/_2,{}^1/_2,0)$ and S ions on the other FCC lattice at the positions $({}^1/_4,{}^1/_4,{}^1/_4)$ $({}^1/_4,{}^3/_4,{}^3/_4)$ $({}^3/_4,{}^1/_4,{}^3/_4)$ $({}^3/_4,$

$^3/_4, ^1/_4$) [1,8] as presented in ***Figure I. 6***. Some group III–V semiconductor compounds as GaSb, GaP, AlSb, GaAs and InP crystallize in ZB structure [1,20,21].'

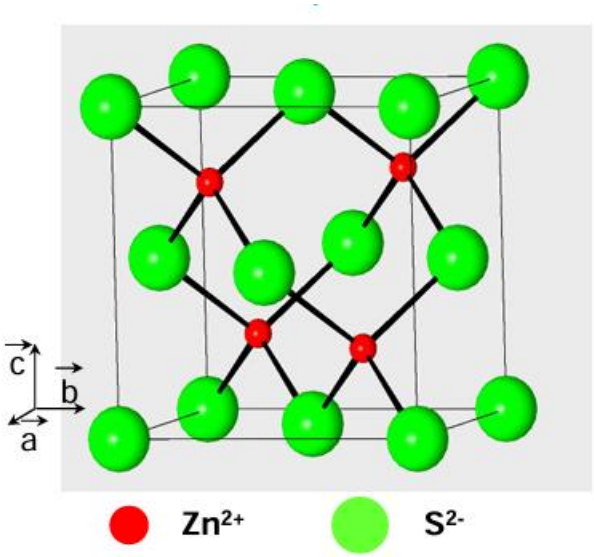


Figure I. 6: ***Zinc blende structure***

I.2.2.b. Wurtzite (WZ) Structure:

The Wurtzite structure resented in ***Figure I.7*** is a hexagonal crystal structure in which atoms are arranged in a hexagonal close-packed (hcp) lattice, with a two-atom basis. Each atom is tetrahedrally coordinated, meaning that every atom is bonded to four nearest neighbors in a tetrahedral geometry [8]. The structure can be described as two interpenetrating hcp sublattices, each occupied by a different type of atom, displaced relative to each other along the threefold c - axis by the fractional amount of $u = {}^3/_8 = 0{,}375$ in the ideal wurtzite structure. The internal parameter u is defined as the ratio of the bond length parallel to the c-axis (the anion–cation bond length, i.e., the nearest-neighbor distance) to the lattice constant c. This structure is typical for various semiconductors such as ZnO, GaN, and AlN.

Both of zinc blende and wurtzite structures exhibit tetrahedral coordination, where each atom is bonded to four nearest neighbors in a tetrahedral geometry; however, the difference between them arises in the arrangement of the second-nearest neighbors, which is determined by the stacking sequence of close-packed planes [2]. In a three-dimensional close-packed arrangement, atoms can occupy three possible positions above a given layer, labeled A, B, and C, and different stacking orders lead to different crystal structures. The zincblende (sphalerite) structure corresponds to the cubic close-packed sequence ABCABC while the wurtzite structure corresponds to the hexagonal close-packed sequence ABABAB [1]

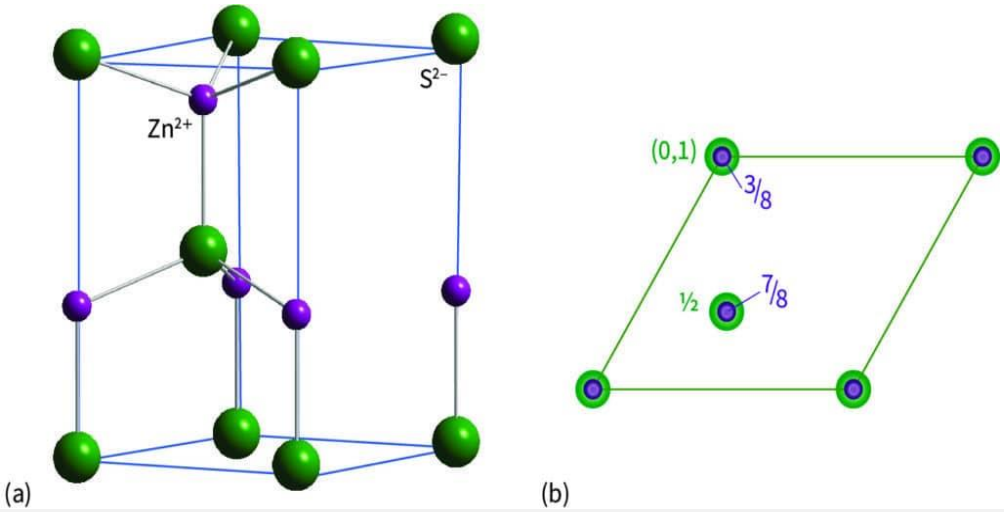


Figure I. 7: ***Wurtzite structure***

I.2.2.c. Sodium chloride (NaCl) structure:

The sodium chloride (NaCl) structure illustrated in ***Figure I.8*** also known as the rock salt structure, it's based on a face-centered cubic lattice, with a basis consisting of one Na^+ ion and one Cl^- ion separated by one-half of the body diagonal of the cube. Each unit cell contains four formula units of NaCl, with ions occupying specific lattice positions; Cl^- anions occupy the positions (0 0 0) (½ ½ 0) (0 ½ ½)(½ 0 ½) while Na^+ cations occupy the complementary positions(½ ½ ½)(½ 0 0) (0 ½ 0)(0 0 ½) [8]. In this arrangement, every atom is surrounded by six nearest neighbors of the opposite type, giving the structure its characteristic six fold coordination.

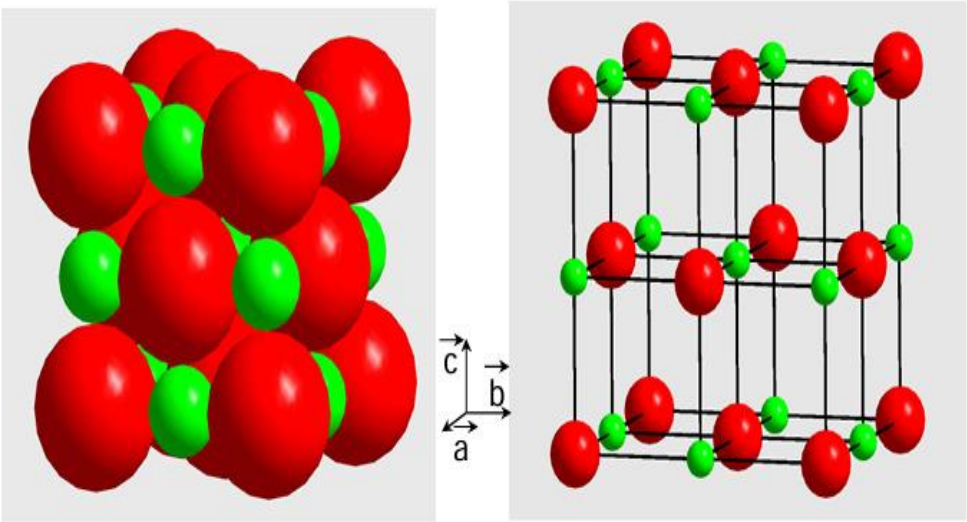


Figure I. 8: ***Sodium chloride structure***

I.2.2.d. Cesium Chloride (Cscl) Structure:

The cesium chloride (CsCl) structure illustrated in ***Figure I.9*** is based on a simple cubic lattice with a two-atom basis. In this arrangement, one Cs^+ ion with red color occupies the corner position (0,0,0) while one Cl^- ion with green color is located at the body center (½,½,½) of the cube [8]. Alternatively, the description can be reversed, with the Cl^- at the corners and Cs^+ at the center. Eight nearest neighbors of the opposite type, resulting in a coordination number of eight, surround each atom. Thus, the CsCl structure differs from the NaCl structure by its higher coordination number and simple cubic lattice, rather than the face-centered cubic lattice of NaCl

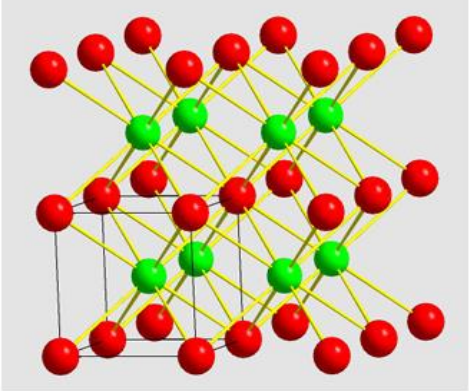


Figure I. 9: ***Cesium chloride crystal structure.***

The following table ***Table I.2***- summarizes the main crystallographic features of these four crystal types [1,2,8]:

Table I. 2: Comparison of Structural Characteristics of ZB, WZ, NaCl, and CsCl.

Properties	**Zinc Blende (ZB)**	**Wurtzite (WZ)**	**Rocksalt (NaCl)**	**Cesium Chloride (CsCl)**
Crystal system	Cubic (face-centered)	Hexagonal (HCP)	Cubic (face-centered)	Cubic (primitive cubic basis)
Space group	F-43m (No.216)	$P6_3mc$ (No. 186)	Fm-3m (No. 225)	Pm-3m (No. 221)
Basis / atomic positions	Atoms A at (0,0,0), B at (¼,¼,¼); two interpenetrating FCC sublattices	Hexagonal close packing with internal parameter u ~ 3/8; atoms at (0,0,0) and (⅓,⅔,⅜)	Two interpenetrating FCC lattices; Na in octahedral voids	Primitive cubic lattice with two-atom basis: one at (0,0,0), the other at (½,½,½)
Coordination number	4 (tetrahedral)	4 (tetrahedral)	6 (octahedral)	8 (cubic)
Stacking / neighbor geometry	ABCABC… cubic close packing	ABAB… hexagonal close packing; tetrahedral coordination	Each Na is in octahedral site in Cl lattice; two FCC sublattices shifted	Cs at body-center of cube formed by Cl at corners

I.2.2.e. *Cubic Double Perovskite Structure :*

Double perovskites are described under the chemical formula $A_2BB'X_6$, where A is a large cation and B/B' are typically transition metals, considering it is originated from the combination of two different perovskites[22].

In the ideal cubic double perovskite structure the crystal symmetry is commonly described by the space group Fm-3m (No. 225), which corresponds to a rock-salt ordering of the B and B′ cations[22,23]. In this structure, the A-site cations occupy the 8c Wyckoff position at $(1/4,1/4,1/4)$, while the B and B′ cations are located at the 4a (0,0,0) and 4b $(1/2,1/2,1/2)$ positions, respectively. The X atoms occupy the 24e Wyckoff site with fractional coordinates $(x,0,0)$, where the internal parameter x determines possible octahedral distortions or tilting. In the ideal undistorted cubic case, x is typically close to 0.25 as shown in ***Figure I. 10***.

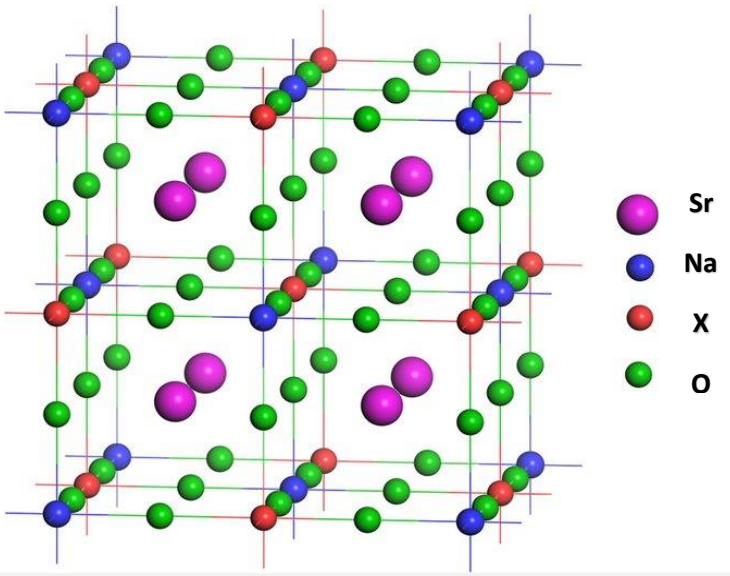


***Figure I. 10**: The crystal structure of the double perovskite unit cell for Sr_2NaXO_6*

I.2.3. Ground State structure and Transition Phase:

The physical properties of semiconductor materials are intrinsically linked to their ground-state crystalline structures, which correspond to the configurations minimizing the total energy of the system. For instance, the equilibrium lattice constant of a crystal is the lattice constant that corresponds to the minimum of the total energy [24]. Once the ground state structure is obtained accurately, any physical property of material can be determined. Different crystal phases often exhibit distinct functionalities, making phase-selective control a powerful means to tailor material behavior. These properties vary from one structure to another, which can impart new functionalities to materials, thereby making them suitable for various applications depending solely on their structure.

Under varying external conditions such as pressure or temperature, materials can undergo phase transitions characterized by rearrangements within the unit cell while retaining chemical composition. The critical pressure at which a transition between two phases occurs can be identified by comparing the enthalpy (H) of each phase as a function of pressure (P) at a fixed temperature. equal to $0K$ using the Mujica relationship [25] given firstly Gibbs free energy(G), then we obtain the enthalpy(H) at $T = 0K$ as a result, the Gibbs free energy becomes equal to the enthalpy described in relationship *(I. 6):*

$$G = U + PV - TS \qquad (I.\ 5)$$

$$G = H = U + PV \qquad (I.\ 6)$$

Where: U is the internal energy, V is the volume and S is the entropy.

I.3. Electronic properties:

I.3.1. Band structure in Solids:

Band theory of solids, also called energy band theory, is a quantum mechanical model that describes the allowed energy states of electrons in solids [26]. The theory is a tool to classified solids as conductors, semiconductors, or insulators; also, it provides a fundamental understanding of semiconductors and their unique physical properties [26].

In an isolated atom, electrons occupy well-defined discrete energy levels following the Pauli's exclusion principle [27] When atoms are packed closely together in a crystal, their electron orbitals overlap with those of neighboring atoms. This overlap causes the discrete atomic energy levels to split and merge, forming continuous ranges of energy called energy bands. These bands, separated by forbidden gap called energy gap [28].

Take, for example, a small silicon crystal composed of N atoms. The single Silicon atom ($_{14}^{A}Si$) has the electronic configuration: $1s^2\ 2s^2\ 2p^6\ 3s^2\ 3p^2$, The inner shells (1s, 2s, 2p) are completely filled and unaffected by neighboring atoms. While the outermost shell has: $3s$ (completely filled) and $3p$ (Partially filled means that out of the six available states, only two are occupied). In crystal system with N atoms, the interaction between the outermost electrons becomes significant [29]. This interaction causes slight modifications in the $3s$ and $3p$ energy levels of each atom. Instead of discrete s and p levels, a large number of closely spaced energy states are formed ($2N$ states formed by $3s$ orbitals and $6N$ states formed by the 3p orbital). Consequently, the s levels broaden into an energy band, and the p levels similarly expand into another band. As a result, the energy gap between the s and p levels of an isolated atom becomes reduced (Thus, the s-band contains $2N$ states and is completely filled, while the p-band consists of $6N$ states, of which only $2N$ are occupied and the rest remain empty). Out of these, $4N$ states are filled while the remaining $4N$ states remain unoccupied [29]. At the actual interatomic spacing in silicon, the $4N$ filled states form the Valence Band (VB)**,** while the remaining $4N$ empty states constitute the Conduction Band (CB)**,** separating these two bands is a forbidden gap represent the energy gap (E_g), with a value of approximately 1.1 eV in silicon at 300 K. The ***Figure I. 11*** illustrates a simplified diagram of the formation of the energy gap:

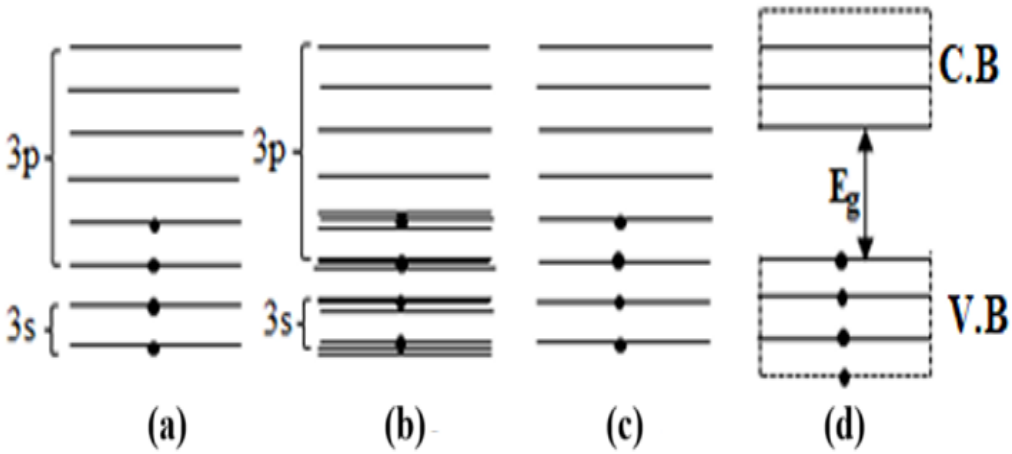


Figure I. 11: ***Schematic Diagram of Energy Gap Formation***

The electronic properties of a solid are mainly determined by the relative positions of the conduction band, valence band, and the forbidden energy gap [28] as shown in ***Figure I. 12:***

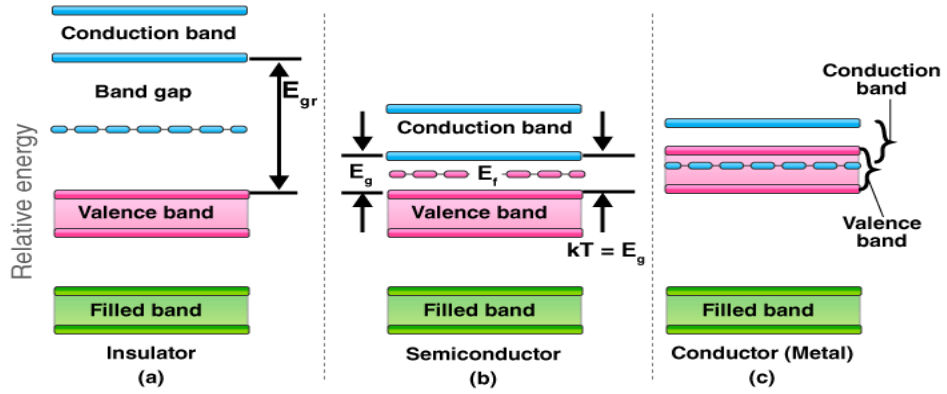


Figure I. 12: ***Energy band schematics for (a) insulator, (b) semiconductor, and (c) conductor*****[30]**

- Insulator: Large band gap $E_g > 3\ eV$ [29]; valence band fully filled and conduction band empty no electrons can jump easily.
- Semiconductor: Small band gap; behaves like an insulator at low temperatures but can conduct at room temperature because thermal energy can excite electrons across the gap [28].
- Conductor: Valence and conduction bands overlap or conduction band is partially filled, allowing easy electron flow ($E_g \cong 0$).

I.3.2. Direct and Indirect Band Gap Semiconductors:

The band gap represents the minimum energy difference between the top of the valence band and the bottom of the conduction band [1]. However, the top of the valence band and the bottom of the conduction band are not generally at the same value of the electron momentum as represent in ***Figure I.13***:

In a direct band gap semiconductor, the minimum of the conduction band and the maximum of the valence band align at the same point in k-space [29] which is usually at the center (Γ-point) of the Brillouin zone for conventional semiconductors. This alignment allows electrons to transition directly between these bands by absorbing or emitting a photon without needing a change in momentum. Optical transitions occur easily as soon as photon energy exceeds the band gap energy. This results in efficient light emission, making direct band gap semiconductors suitable for optoelectronic devices like LEDs and lasers

In an indirect band gap semiconductor, the conduction band minimum and valence band maximum occur at different momentum [29]. Thus, an electron transitioning between these bands must undergo a change in both energy and momentum, to satisfy momentum conservation, the process requires the participation of a phonon (a quantum of lattice vibration) [31]. Because of this additional requirement, optical transitions in indirect-band-gap semiconductors are less probable and less efficient, making these materials unsuitable for light-emitting devices.

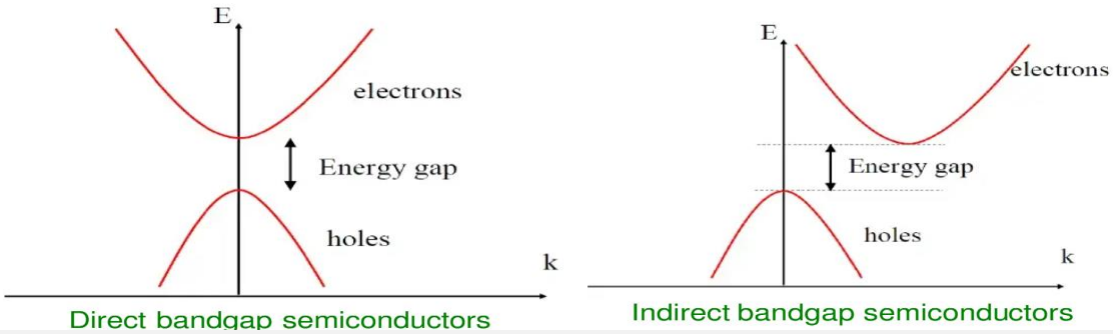


Figure I. 13: ***Direct and Indirect bandgap in semiconductor***

I.4. Optical properties:

A rigorous investigation of the optical properties of a material— including its dielectric function, absorption coefficient, refractive index, energy loss function and other parameters is essential for evaluating its suitability in technological applications to determine their practical applications. These measurements clarify both how the material responds to incident electromagnetic radiation at the macroscopic level also provide valuable insight into its underlying electronic structure.

I.4.1. Dielectric Function:

Dielectric function $\varepsilon(\omega)$ is the profile of the response of a material to an exterior electric field, mathematically it expressed as [32]:

$$\varepsilon(\omega) = \varepsilon_1(\omega) + i\varepsilon_2(\omega) \qquad (I.\ 7)$$

$\varepsilon_1(\omega)$ denote the real part of the dielectric function, which governs the dispersion of electromagnetic waves, whereas the imaginary part $\varepsilon_2(\omega)$ reflects the absorption processes. Both functions are determined from the Kramers–Kronig relations over the first Brillouin zone [32]:

$$\varepsilon_1(\omega) = \frac{2}{\pi} P \int_0^{\infty} \frac{\omega' \varepsilon_2(\omega')}{(\omega'^2 - \omega^2)} d\omega' + 1 \qquad (I.\ 8)$$

$$\varepsilon_2(\omega) = \frac{2\omega}{\pi} P \int_0^{\infty} \frac{1 - \varepsilon_2(\omega')}{(\omega'^2 - \omega^2)} d\omega' \qquad (I.\ 9)$$

Where: P indicate that we take the principal value of the integral.

I.4.2. Refractive Index:

Refractive index $\tilde{n}(\omega)$ describes both the light propagates in a material and its absorption characteristics. It is defined as [32]:

$$\tilde{n}(\omega) = n(\omega) + iK(\omega) \quad (I.\ 10)$$

where $n(\omega)$ is the real part, representing how light propagates through the transparent medium, and $K(\omega)$ is the extinction coefficient, which accounts for attenuation of the wave due to absorption and scattering processes inside the material.

This optical response is directly related to the dielectric function $\varepsilon(\omega)$, since [32]:

$$\tilde{n}(\omega)^2 = \varepsilon(\omega) \quad (I.\ 11)$$

From this relation, the real refractive index and extinction coefficient can be obtained as:

$$n(\omega) = \sqrt{\frac{\varepsilon_1(\omega)}{2} + \frac{\sqrt{\varepsilon_1^2(\omega)+\varepsilon_2^2(\omega)}}{2}} \quad (I.\ 12)$$

$$K(\omega) = \sqrt{\frac{\varepsilon_1(\omega)}{2} - \frac{\sqrt{\varepsilon_1^2(\omega)+\varepsilon_2^2(\omega)}}{2}} \quad (I.\ 13)$$

I.4.3. Absorption Coefficient:

The absorption coefficient $\alpha(\omega)$ quantifies the amount by which light is reduced as it propagates through a material, which governed by the equation [32]:

$$\alpha(\omega) = \sqrt{2\omega}\left[\sqrt{\varepsilon_1^2(\omega) + \varepsilon_2^2(\omega)} - \varepsilon_1(\omega)\right]^{\frac{1}{2}} \quad (I.\ 14)$$

It is directly related to the extinction coefficient $K(\omega)$, reflecting their proportional dependence, and is expressed as [32]:

$$\alpha(\omega) = 2\frac{\omega K(\omega)}{c} \quad (I.\ 15)$$

Where ω is the angular frequency of the incident light and c is the speed of light in vacuum. Because of this relation, $\alpha(\omega)$ and $K(\omega)$exhibit nearly identical variation with frequency.

I.4.4. Normal Incidence Reflectivity:

Reflection takes place at the boundary between two optical media with different refractive indices[32], and it serves as a key factor for analyzing optical transitions in solid-state systems. The reflectivity coefficient $R(\omega)$ can be determined using the following relations [32]:

$$R(\omega) = \left|\frac{\sqrt{\varepsilon(\omega)}-1}{\sqrt{\varepsilon(\omega)}+1}\right|^2 = \left|\frac{(n-1)^2+K^2}{(n+1)^2+K^2}\right|^2 \quad (I.\ 16)$$

I.4.5. Optical Conductivity:

Optical conductivity σ(ω) is a complex, frequency-dependent response function that characterizes how a material conducts electric current in response to an applied light at frequency ω [33] and it's related to dielectric function [34]:

$$\sigma(w) = \frac{-i\omega}{4\pi}\varepsilon(\omega) \quad (I.\ 17)$$

I.5. Elastic Properties:

The elastic properties of material describe how its deform under stress and their ability to return to their original shape once the stress is removed, where atomic or molecular bonds restoring their original condition govern this behavior [35]. The used analogies to understand elastic behavior exhibits a linear relationship between force and displacement over a considerable range of deformation. The principle of this proportionality was formally expressed by Robert Hooke, who established the direct relationship between tensile stress and tensile strain [35,36]. Subsequently, the understanding of elastic deformation in multiple dimensions, maintaining near-linear responses, was advanced through the work of Thomas Young, Siméon-Denis Poisson, Voigt's and other researchers.

In modern tensor notation, and using Voigt's contracted form, Hooke's law for elastic materials is simplified and represented as a linear relationship between the stress vector σ_α and the strain vector ε_β, linked through the stiffness matrix $C_{\alpha\beta}$ (the coefficients are called stiffnesses or elastic constants) as shown [37]:

$$\sigma_\alpha = C_{\alpha\beta}\varepsilon_\beta \quad (I.\ 18)$$

Where the number of independent elastic constants is governed by the symmetry of the crystal system, higher symmetry results in fewer independent stiffness components while the lower-symmetry crystals require a large number of constants [35]. For instance, cubic crystals possess only three independent elastic constants (C_{11}, C_{12} and C_{44}), hexagonal crystals require five independent constants (C_{11}, C_{12} , C_{13} ,C_{33} and C_{44}), whereas the lowest-symmetry triclinic crystals require all twenty-one elastic constants [38].

When the elastic constants are written such that the individual strains are reported in terms of stresses, the coefficients are called compliances, $S_{\alpha\beta}$ such that[39]:

$$\varepsilon_\alpha = S_{\alpha\beta}\sigma_\beta \quad (I.\ 19)$$

The elastic constants C_{ij} offer significant viewpoints regarding structural stability of crystal, mechanical properties, inter atomic bonding and anisotropic characteristics of binding.

I.5.1. Elastic Stability Criteria:

To verify the mechanical stability of a cubic structure, the Born – Huang mechanical stability criteria [40–42] must be satisfied:

$C_{11} - C_{12} > 0, C_{11} + 2C_{12} > 0$ and $C_{44} > 0$ *(I. 20)*

However, the Born–Huang criteria for hexagonal structure are [43]:

$C_{11} > |C_{12}|, (C_{11} + C_{12})C_{33} > 2C_{13}^{2}$ and $C_{44} > 0$ *(I. 21)*

I.5.2. Mechanical Modulus:

The Voigt, Reuss and Hill's model (VRH) are used to describe the mechanical behavior of materials based on the mechanical modulus such as: bulk modulus (B), shear modulus (G), Young's modulus (E), p-wave modulus (M) and the Vicker's hardness H_v based on VRH models which are described and calculated as fellow:

- **Bulk Modulus:** is the measurement of material resistance to uniform compression (change in volume) when pressure is applied [37] and is calculated as [44–46]:

$$B = B_v = B_R = \frac{1}{3}(C_{11} + 2C_{12}) \quad \textit{(I. 22)}$$

- **Shear Modulus:** is the measurement the resistance of a material to shape changes when a shear force is applied. And is a better predictor of hardness than the bulk modulus [47], expressed as [44–46]:

$$G = \frac{1}{2}(G_v + G_R) \quad \textit{(I. 23)}$$

$$G_v = \frac{1}{5}(C_{11} - C_{12} + 3C_{44}) \quad \textit{(I. 24)}$$

$$G_R = \frac{5(C_{11}-C_{12})C_{44}}{4C_{44}+3(C_{11}-C_{12})} \quad \textit{(I. 25)}$$

- **Young's Modulus:** is a measure of the stiffness of an elastic material, representing its resistance to deformation (change in length) under applied stress [47], young's modulus is formulated as [48]**:**

$$E = \frac{9BG}{3B+G} \quad \textit{(I. 26)}$$

- **P-Wave Modulus:** (also called the *longitudinal modulus* or *constrained modulus*) characterize the response of a material under a uniaxial strain, it follows [49]:

$$M = \rho {V_P}^2 \qquad (I.\ 27)$$

Where: V_P is P-wave velocity and ρ is the material density

- **Vicker's Hardness :** represent the resistance of each chemical bond to deformation [48], the material hardness can calculated using the Tian et al formulas:

$$H_v = 0.92 \left(\frac{G}{B}\right)^{1.137} \times G^{0.708} \qquad (I.\ 28)$$

The Voigt model [44] assumes that the strain remains uniform throughout the entire crystal. In contrast, the Reuss model [45] is based on the supposition of uniform stress, leading to static compatibility of the stress fields but resulting in a loss of kinematic compatibility. The Hill model [46] combines both approaches by considering the effects of uniform stress and uniform strain, providing a more balanced estimation of elastic behavior through the averaging of the Voigt and Reuss moduli.

I.5.3. Ductile and Brittle Nature:

A ductile material is one that can undergo significant plastic deformation before fracture. While brittle material exhibits little or no plastic deformation before fracture, usually fracturing with low energy absorption [35]. The ductile or brittle nature of a material is not only observed, but can also be predicted using several criteria:

- **Pugh's Ratio:** defined as the ratio of the bulk modulus (B) to the shear modulus (G). Bulk modulus represents resistance to fracture (volume change), while shear modulus represents resistance to plastic deformation (shearing). A higher ratio means the material favors plastic deformation (ductile), in which[50]:

$$B/G < 1.75 \Rightarrow material\ has\ brittle\ nature$$
$$B/G > 1.75 \Rightarrow material\ has\ \ ductile\ nature$$

- **Cauchy Pressure:** formulated as:

$$C_P = C_{12} - C_{44} \qquad (I.\ 29)$$

Cauchy pressure reveals information about the angular characteristics of atomic bonding in a solid, specifically, it reflects how directional or non-directional the bonding forces are between atoms [51]. Positive values are associated with presence of metallic bonding thus suggests non-directional bonding,

while negative values are linked to presence of covalent bonding which refer to more directional bonding. So [48]:

$$C_P < 0 \Rightarrow material\ has\ brittle\ Nature$$
$$C_P > 0 \Rightarrow material\ has\ \ ductile\ nature$$

- **Poisson's Ratio (v):**is ratio of lateral strain to axial strain, expressed as:

$$\nu = \frac{3B-2G}{2(3B+G)} \qquad (I.\ 30)$$

Poisson's ratio is also linked to the type of chemical bonding in solids [47,48]; ionic bonds correspond to values near 0.25, while covalent bonds show lower values close to 0.10. It is also a parameter to determine the brittle and ductile nature, in which[52]:

$$\nu < 0{,}26 \Rightarrow material\ has\ brittle\ nature$$
$$\nu > 0{,}26 \Rightarrow material\ has\ ductile\ nature$$

I.5.4. Elastic anisotropy:

Elastic anisotropy describes the elastic behaves with the change in the direction of the applied stress or strain. It is determined by several parameters such as:

- **Zener anisotropy factor**$(\boldsymbol{A})$ expressed by [53]:

$$A = 2\frac{C_{44}}{C_{11}-C_{12}} \qquad (I.\ 31)$$

If:
$$A = 1 \Rightarrow material\ \ is\ isotropic$$
$$A \neq 1 \Rightarrow material\ is\ anisotropic$$

- **Universal index**$(\boldsymbol{A^U})$ formulated as[54]:

$$A^U = \frac{B_v}{B_R} + 5\frac{G_V}{G_R} - 6 \qquad (I.\ 32)$$

If:
$$\mathrm{A^U} = 0 \Rightarrow material\ \ is\ isotropic$$
$$\mathrm{A^U} \neq 0 \Rightarrow material\ is\ anisotropic$$

- **Kube's log-Euclidean anisotropy parameter**$(\boldsymbol{A_L})$ expressed as[55]**:**

$$A_L = \sqrt{5\left[ln\left(\frac{{C_{44}}^V}{{C_{44}}^R}\right)\right]^2 + \left[ln\left(\frac{k^V}{k^R}\right)\right]^2} \qquad (I.\ 33)$$

Where the Reuss and Voigt values of C_{44} calculated using the following expressions [55]:

$${C_{44}}^R = \frac{5C_{44}(C_{11}-C_{12})}{12C_{44}+15(C_{11}-C_{12})} \qquad (I.\ 34)$$

$$C_{44}{}^{V} = C_{44}{}^{R} + \frac{15(C_{11} - C_{12} - 2C_{44})^2}{12C_{44} + 15(C_{11} - C_{12})} \quad (I.\ 35)$$

Criteria:

$$A_L = 0 \Rightarrow material\ is\ isotropic$$
$$A_L \neq 0 \Rightarrow material\ is\ anisotropic$$

- **Shear anisotropy Index (A_G):** known also as Chung-Buessem Anisotropy Index [54]:

$$A_G = \frac{G_v - G_R}{G_v + G_R} \quad (I.\ 36)$$

Criteria:

$$A_G = 0 \Rightarrow G\ is\ isotropic$$
$$A_G \neq 0 \Rightarrow G\ is\ anisotropic$$

- **Compression anisotropy(A_B)** expressed by the following equation[56]**:**

$$A_B = \frac{B_v - B_R}{B_v + B_R} \quad (I.\ 37)$$

Criteria:

$$A_B = 0 \Rightarrow B\ is\ isotropic$$
$$A_B \neq 0 \Rightarrow B\ is\ anisotropic$$

I.5.5. Acoustic behavior:

The acoustic behavior of a material refers to the way sound waves propagate through it [8], which may occur in longitudinal or transverse modes. To evaluate this response, researchers often rely on parameters such as: the longitudinal (v_l), transverse (v_t), and average sound velocity (v_a), Debye temperature (θ_D), which reflects lattice vibrations, and the melting temperature (T_{Melt}), which is associated with thermal stability. The parameters calculated using the following equations [48,51,57]:

$$v_l = \left[\frac{3B + 4G}{3\rho}\right]^{1/2} \quad (I.\ 38)$$

$$v_t = \left[\frac{G}{\rho}\right]^{1/2} \quad (I.\ 39)$$

$$v_a = \left[\frac{1}{3}\left(\frac{2}{v_l^2} + \frac{1}{v_t^3}\right)\right]^{-1/3} \quad (I.\ 40)$$

$$\theta_D = \frac{h}{K_B}\left[\frac{3n}{4\pi V_a}\right]^{1/3} \quad (I.\ 41)$$

$$T_{Melt} = [553\ (K) + 5.91C_{11}(GPa)] \pm 300K \quad (I.\ 42)$$

I.6. Thermal properties

Thermal behavior of crystalline solids can be effectively described within the quasi-harmonic approximation. The macroscopic properties as function of pressure and temperature are derived from standard thermodynamic relations. In this model the no equilibrium Gibbs function $G^*(V,P,T)$in the quasi-harmonic Debye model, can be formulated as below [58]:

$$G^*(V,P,T) = E(V) + PV + A_{Vib}(\theta_D(V),T) \quad (I.\ 43)$$

Where $E(V)$ is the total energy per unit cell as a function of volume , the term PV corresponds to the work done under constant hydrostatic pressure P, and $A_{Vib}(\theta_D(V),T)$ is the vibrational Helmhotz free energy depends on temperature T and Debye temperature $\theta_D(V)$ expressed by the equation below [58,59]:

$$A_{Vib}(\theta_D(V),T) = nK_BT\left[\frac{9\theta_D}{8T} + 3ln\left(1 - e^{-(\theta_D/T)}\right) - D(\theta_D/T)\right] \quad (I.\ 44)$$

In this equation: n number of atoms in crystal, K_B denotes Boltzmann's constant and $D(\theta_D/T)$ is the Debye function, representing the integral over phonon modes up to the Debye temperature.

For anisotropic solid, the Debye temperature θ_D can be calculated by incorporating material mechanical properties and geometry through the formula [58]:

$$\theta_D = \frac{\hbar}{K_B}\left[6n\pi^2V^{1/2}\right]^{1/3} f(\upsilon)\sqrt{\frac{B_S}{M}} \quad (I.\ 45)$$

The function $f(\sigma)$is given by the relation:

$$f(\upsilon) = \left\{3\left[2\left(\frac{21+\upsilon}{31-2\upsilon}\right)^{3/2} + \left(\frac{11+\upsilon}{31-\upsilon}\right)^{3/2}\right]^{-1}\right\}^{1/3} \quad (I.\ 46)$$

The heat capacity C_V is obtained using the equation bellow[60]:

$$C_V = 3nK_B\left[4D\left(\theta_D/T\right) - \frac{3\theta/T}{e^{\theta/T}-1}\right] \quad (I.\ 47)$$

I.7. Applications of Advanced Semiconductor Materials: III–V Compounds and Double Perovskites

Advanced semiconductor materials play a central role in modern technology owing to their tunable electronic structures, excellent charge-transport properties, and diverse optical functionalities. Among them, III–V semiconductors and double perovskite compounds have attracted considerable attention for applications in electronics, optoelectronics, photonics, and renewable energy technologies. III–V semiconductors how characterized by direct band gaps, high carrier mobility, high saturation velocity,

excellent optical absorption and emission characteristics, and wide band-gap tunability. These properties make them ideal candidates for light-emitting diodes (LEDs), laser diodes (LDs), photodetectors, optical communication systems, high-electron-mobility transistors (HEMTs), microwave devices, and high-frequency communication technologies[61–65]. In particular, III-nitride materials such as GaN, AlN, InN, and their alloys have revolutionized solid-state lighting and display technologies through highly efficient blue, green, and ultraviolet LEDs and laser diodes. Their large breakdown electric fields, high thermal conductivity, and excellent chemical stability further enable their use in high-power electronics, electric vehicles, aerospace systems, radar technologies, satellite communications, and renewable-energy power converters[64–67].

The possibility of engineering the band gap of III–V alloys over a broad energy range, extending from the infrared to the ultraviolet region, has also enabled the development of infrared detectors, ultraviolet photodetectors, optical sensors, environmental monitoring systems, and high-efficiency multijunction solar cells[62,67,68]. Owing to their direct band gaps and superior carrier transport properties, III–V photovoltaic materials achieve some of the highest solar-energy conversion efficiencies and are widely employed in space and concentrator photovoltaic applications[68].

Alongside III–V semiconductors, double perovskite materials with the general formula $A_2BB'X_6$ have emerged as a promising class of semiconductors due to their structural flexibility, tunable band gaps, long carrier lifetimes, high absorption coefficients, defect tolerance, and improved environmental stability compared with conventional lead-halide perovskites[69–71]. Depending on their chemical composition, double perovskites can exhibit semiconducting, photovoltaic, thermoelectric, magnetic, and photocatalytic properties. Their strong optical absorption and favorable electronic structures make them attractive candidates for solar cells, photodetectors, light-emitting devices, photocatalytic water splitting, CO_2 reduction, and other energy-conversion applications[69–72]. Furthermore, the presence of transition-metal ions can introduce magnetic ordering and spin-dependent electronic behavior, opening opportunities in spintronics and multifunctional electronic devices[70,73]. Their excellent thermoelectric characteristics, including low thermal conductivity and tunable electrical transport properties, also make them promising materials for waste-heat recovery and sustainable energy technologies[72].

Recent advances in material synthesis, computational design, and nanostructure engineering have further expanded the applications of both III–V semiconductors and double perovskites toward flexible electronics, wearable devices, integrated photonic circuits, quantum technologies, biomedical sensors, and Internet-of-Things (IoT) platforms[66,71]. Therefore, the continuous exploration and optimization of these

semiconductor families remain essential for the development of next-generation electronic, optoelectronic, photovoltaic, thermoelectric, and energy-harvesting systems.

References:

[1] B.G. Yacobi, Semiconductor Materials: An Introduction to Basic Principles, 1st ed. 2003, Imprint: Springer, New York, NY, 2003. https://doi.org/10.1007/b105378.
[2] D.A. Neamen, Semiconductor physics and devices: basic principles, 4th ed, McGraw-Hill, New York, NY, 2012.
[3] Y. Ma, X. Guo, X. Wu, L. Dai, L. Tong, Semiconductor nanowire lasers, Advances in Optics and Photonics, Vol. 5, Issue 3, Pp. 216-273 (2013). https://doi.org/10.1364/AOP.5.000216.
[4] S. Nakamura, Nobel Lecture: Background story of the invention of efficient blue InGaN light emitting diodes, Rev. Mod. Phys. 87 (2015) 1139–1151. https://doi.org/10.1103/RevModPhys.87.1139.
[5] E.F. Schubert, Light Emitting Diodes and Solid-State Lighting, (n.d.).
[6] F. Dimroth, High-efficiency solar cells from III-V compound semiconductors, Phys. Status Solidi (c) 3 (2006) 373–379. https://doi.org/10.1002/pssc.200564172.
[7] A.W. Bett, F. Dimroth, G. Stollwerck, O.V. Sulima, III-V compounds for solar cell applications, Applied Physics A: Materials Science & Processing 69 (1999) 119–129. https://doi.org/10.1007/s003390050983.
[8] C. Kittel, Introduction to solid state physics, 8. ed., [repr.], Wiley, Hoboken, NJ, 20.
[9] Unit 3 Crysallography notes With Q-Ans-Problems, (n.d.).
[10] C. Hammond, The basics of crystallography and diffraction, 3rd ed, Oxford university press, Oxford, 2009.
[11] T.Y. Yakich, FUNDAMENTALS OF CRYSTALLOGRAPHY AND MINERALOGY, (n.d.).
[12] T. Tsutaoka, T. Tokunaga, T. Umeda, T. Maehara, Observation of the two-dimensional reciprocal lattice by use of lattice grating sheets and a laser pointer, European Journal of Physics 35 (2014) 055021. https://doi.org/10.1088/0143-0807/35/5/055021.
[13] A. Raj, J. Eapen, Phonon dispersion using the ratio of zero-time correlations among conjugate variables: Computing full phonon dispersion surface of graphene, Computer Physics Communications 238 (2019). https://doi.org/10.1016/j.cpc.2018.12.008.
[14] P.S. Bisht, S.R. Jha, Board of Studies, (n.d.).
[15] D.J. Chadi, M.L. Cohen, Special Points in the Brillouin Zone, Phys. Rev. B 8 (1973) 5747–5753. https://doi.org/10.1103/PhysRevB.8.5747.
[16] W.S. Morgan, J.J. Jorgensen, B.C. Hess, G.L.W. Hart, Efficiency of Generalized Regular k -point grids, Computational Materials Science 153 (2018) 424–430. https://doi.org/10.1016/j.commatsci.2018.06.031.
[17] W. Setyawan, High-throughput electronic band structure calculations: Challenges and tools, (n.d.).
[18] N.W. Ashcroft, N.D. Mermin, Solid state, Physics (New York: Holt, Rinehart and Winston) Appendix C 1 (1976).
[19] M.S. Dresselhaus, G. Dresselhaus, A. Jorio, Group theory: application to the physics of condensed matter, Springer Science & Business Media, 2007.
[20] W. Gouasmia, D. Boudjaadar, F. Oumelaz, O. Nemiri, H. Meradji, S. Ghemid, A. Boumaza, S. Bin Omran, D. Singh, R. Khenata, First-principles assessment of the structural, phase transition, electronic, elastic and thermal properties of the semiconductor alloys AlSb1–xBix (x = 0, 0.25, 0.5, 0.75, 1), Eur. Phys. J. B 98 (2025) 85. https://doi.org/10.1140/epjb/s10051-025-00923-4.
[21] S. Chebouki, O. Nemiri, F. Oumelaz, B. Djamel, A. Boumaza, H. Meradji, S. Ghemid, R. Benredouane, A. Dutta, M. Jeridi, H. Albalawi, From phase transitions to photonics performance: First-principles exploration of InXAl1−XP (x = 0.0 0.25, 0.5, 0.75 and 1) ternary alloys for next-generation optoelectronics, Polyhedron 275 (2025) 117514. https://doi.org/10.1016/j.poly.2025.117514.
[22] A.K. Bowser, Synthesis and Characterization of Novel Double Perovskites, (n.d.).
[23] M. Saeed, I.U. Haq, A.S. Saleemi, S.U. Rehman, B.U. Haq, A.R. Chaudhry, I. Khan, First-principles prediction of the ground-state crystal structure of double-perovskite halides Cs2AgCrX6 (X

= Cl, Br, and I), Journal of Physics and Chemistry of Solids 160 (2022) 110302. https://doi.org/10.1016/j.jpcs.2021.110302.
[24] P.D. Sreedevi, P. Ravindran, R. Vidya, First principles prediction of the ground state crystal structures of antiperovskite compounds A3PN (A= Be, Mg, Ca, Sr, Ba and Zn), Materials Today: Proceedings 8 (2019) 294–300. https://doi.org/10.1016/j.matpr.2019.02.114.
[25] A. Mujica, A. Rubio, A. Muñoz, R.J. Needs, High-pressure phases of group-IV, III–V, and II–VI compounds, Rev. Mod. Phys. 75 (2003) 863–912. https://doi.org/10.1103/RevModPhys.75.863.
[26] P.M. Marcus, J.F. Janak, A.R. Williams, eds., Computational Methods in Band Theory: Proceedings of a Conference held at the IBM Thomas J. Watson Research Center, Yorktown Heights, New York, May 14–15, 1970, under the joint sponsorship of IBM and the American Physical Society, Springer US, Boston, MA, 1971. https://doi.org/10.1007/978-1-4684-1890-3.
[27] Über den Zusammenhang des Abschlusses der Elektronengruppen im Atom mit der Komplexstruktur der Spektren | Zeitschrift für Physik A Hadrons and nuclei, (n.d.). https://link.springer.com/article/10.1007/bf02980631 (accessed August 30, 2025).
[28] S.M. Sze, M.-K. Lee, M.-K. Lee, Semiconductor devices, physics and technology, 3. ed, Wiley, Hoboken, N.J, 2012.
[29] Y. Singh, Semiconductor Devices, I. K. International Pvt Ltd, 2013.
[30] https://byjus.com/jee/semiconductors/, BYJUS (n.d.). https://byjus.com/jee/semiconductors/ (accessed August 30, 2025).
[31] Direct and Indirect Band Gap in Semiconductors | PDF | Band Gap | Chemical Product Engineering, Scribd (n.d.). https://www.scribd.com/document/188863357/Direct-And-Indirect-Band-Gap-In-Semiconductors (accessed August 31, 2025).
[32] M. Fox, Optical properties of solids, 2. ed., reprinted, Oxford Univ. Press, Oxford, 2012.
[33] R.P.S.M. Lobo, 3 - The optical conductivity of high-temperature superconductors, in: X.G. Qiu (Ed.), High-Temperature Superconductors, Woodhead Publishing, 2011: pp. 103–146. https://doi.org/10.1533/9780857091031.1.103.
[34] M. Dressel, G. Grüner, Electrodynamics of solids: optical properties of electrons in matter, Cambridge university press, 2002.
[35] W.D. Callister, Materials Science and Engineering, Wiley, New York, 2019.
[36] R. Hooke, Lectures de Potentia Restitutiva, Or of Spring Explaining the Power of Springing Bodies, John Martyn, 1678.
[37] J.F. Nye, Physical Properties of Crystals: Their Representation by Tensors and Matrices, Clarendon Press, 1985.
[38] K. Lau, A.K. McCurdy, Elastic anisotropy factors for orthorhombic, tetragonal, and hexagonal crystals, Phys. Rev. B 58 (1998) 8980–8984. https://doi.org/10.1103/PhysRevB.58.8980.
[39] L.D. Landau, L.P. Pitaevskii, A.M. Kosevich, E.M. Lifshitz, Theory of Elasticity: Volume 7, Elsevier, 2012.
[40] Dynamical Theory Of Crystal Lattices | Oxford Academic, (n.d.). https://academic.oup.com/book/52786 (accessed October 5, 2025).
[41] J. Wang, S. Yip, S.R. Phillpot, D. Wolf, Crystal instabilities at finite strain, Phys. Rev. Lett. 71 (1993) 4182–4185. https://doi.org/10.1103/PhysRevLett.71.4182.
[42] Z. Zhou, B. Joós, Stability criteria for homogeneously stressed materials and the calculation of elastic constants, Phys. Rev. B 54 (1996) 3841–3850. https://doi.org/10.1103/PhysRevB.54.3841.
[43] F. Mouhat, F.-X. Coudert, Necessary and sufficient elastic stability conditions in various crystal systems, Physical Review B 90 (2014) 224104.
[44] W. Voigt, Theoretische studien über die elasticitätsverhältnisse der krystalle, Königliche Gesellschaft der Wissenschaften zu Göttingen, 1887.

[45] A. Reuß, Berechnung der fließgrenze von mischkristallen auf grund der plastizitätsbedingung für einkristalle., ZAMM-Journal of Applied Mathematics and Mechanics/Zeitschrift Für Angewandte Mathematik Und Mechanik 9 (1929) 49–58.
[46] R. Hill, The elastic behaviour of a crystalline aggregate, Proceedings of the Physical Society. Section A 65 (1952) 349.
[47] A comprehensive DFT based insights into the physical properties of tetragonal superconducting Mo5PB2 - ScienceDirect, (n.d.). https://www.sciencedirect.com/science/article/pii/S2211379721007063 (accessed October 10, 2025).
[48] M.I. Naher, S.H. Naqib, An ab-initio study on structural, elastic, electronic, bonding, thermal, and optical properties of topological Weyl semimetal Ta X (X= P, As), Scientific Reports 11 (2021) 5592.
[49] G. Mavko, T. Mukerji, J. Dvorkin, The rock physics handbook, Cambridge university press, 2020.
[50] XCII. Relations between the elastic moduli and the plastic properties of polycrystalline pure metals: The London, Edinburgh, and Dublin Philosophical Magazine and Journal of Science: Vol 45, No 367, (n.d.). https://www.tandfonline.com/doi/abs/10.1080/14786440808520496 (accessed October 11, 2025).
[51] Theoretical predictions of structure and related properties of intermetallics - D. G. Pettifor, 1992, (n.d.). https://journals.sagepub.com/doi/abs/10.1179/mst.1992.8.4.345 (accessed October 11, 2025).
[52] I.N. Frantsevich, Elastic constants and elastic moduli of metals and insulators, Reference Book (1982).
[53] I.C. Dragomir, T. Ungár, The dislocations contrast factors of cubic crystals in the Zener constant range between zero and unity, Powder Diffraction 17 (2002) 104–111.
[54] S.I. Ranganathan, M. Ostoja-Starzewski, Universal elastic anisotropy index, Physical Review Letters 101 (2008) 055504.
[55] C. Kube, M. Jong, Elastic constants of polycrystals with generally anisotropic crystals, Journal of Applied Physics 120 (2016) 165105. https://doi.org/10.1063/1.4965867.
[56] G.E. Green, D.E. Reades, Boundary conditions, anisotropy and sample shape effects onthe stress-strain behaviour of sand in triaxial compression and plane strain, Geotechnique 25 (1975) 333–356.
[57] A simplified method for calculating the debye temperature from elastic constants, Journal of Physics and Chemistry of Solids 24 (1963) 909–917. https://doi.org/10.1016/0022-3697(63)90067-2.
[58] M.A. Blanco, E. Francisco, V. Luaña, GIBBS: isothermal-isobaric thermodynamics of solids from energy curves using a quasi-harmonic Debye model, Computer Physics Communications 158 (2004) 57–72. https://doi.org/10.1016/j.comphy.2003.12.001.
[59] M. Flórez, J.M. Recio, E. Francisco, M.A. Blanco, A.M. Pendás, First-principles study of the rocksalt–cesium chloride relative phase stability in alkali halides, Phys. Rev. B 66 (2002) 144112. https://doi.org/10.1103/PhysRevB.66.144112.
[60] B.M. Askerov, M. Cankurtaran, Isobaric Specific Heat and Thermal Expansion of Solids in the Debye Approximation, Physica Status Solidi (b) 185 (1994) 341–348. https://doi.org/10.1002/pssb.2221850204.
[61] M.P. Mikhailova, K.D. Moiseev, Y.P. Yakovlev, Discovery of III–V semiconductors: physical properties and application, Semiconductors 53 (2019) 273–290.
[62] I. Vurgaftman, J.R. Meyer, L.R. Ram-Mohan, Band parameters for III–V compound semiconductors and their alloys, Journal of Applied Physics 89 (2001) 5815–5875.
[63] S. Adachi, Properties of semiconductor alloys: group-IV, III-V and II-VI semiconductors, John Wiley & Sons, 2009.
[64] A. Acharya, R.B. Kayastha, Mass and energy balance estimation of Yala glacier (2011–2017), Langtang Valley, Nepal, Water 11 (2018) 6.
[65] U.K. Mishra, P. Parikh, Y.-F. Wu, AlGaN/GaN HEMTs-an overview of device operation and applications, Proceedings of the IEEE 90 (2002) 1022–1031.

[66] X. Gao, Y. Huang, R. Wang, Y. Sun, L. Wang, Advancing flexible optoelectronics with III-nitride semiconductors: from materials to applications, Light: Science & Applications 15 (2026) 141.
[67] I. Akasaki, Nobel Lecture: Fascinated journeys into blue light, Reviews of Modern Physics 87 (2015) 1119–1131.
[68] J.F. Geisz, D.J. Friedman, III–N–V semiconductors for solar photovoltaic applications, Semiconductor Science and Technology 17 (2002) 769–777.
[69] G. Volonakis, M.R. Filip, A.A. Haghighirad, N. Sakai, B. Wenger, H.J. Snaith, F. Giustino, Lead-free halide double perovskites via heterovalent substitution of noble metals, The Journal of Physical Chemistry Letters 7 (2016) 1254–1259.
[70] A.H. Slavney, T. Hu, A.M. Lindenberg, H.I. Karunadasa, A bismuth-halide double perovskite with long carrier recombination lifetime for photovoltaic applications, Journal of the American Chemical Society 138 (2016) 2138–2141.
[71] Z. Xiao, Z. Song, Y. Yan, From lead halide perovskites to lead-free metal halide perovskites and perovskite derivatives, Advanced Materials 31 (2019) 1803792.
[72] N. Louati, F. Oumelaz, O. Nemiri, D. Boudjaadar, A. Boumaza, R. Benredouane, Ş. Uğur, A.K. Kushwaha, G. Uğur, Investigation of structural, optoelectronic, thermoelectric, and elastic properties for Sr2NaXO6 (X= Cl, Br, and I) advanced double perovskite semiconductors: ab initio study, Physica Status Solidi (b) 262 (2025) 2400677.
[73] S. Vasala, M. Karppinen, A2B′ B ″O6 perovskites: a review, Progress in Solid State Chemistry 43 (2015) 1–36.

Chapter II:

Fundamentals of Density Functional Theory (DFT)

Introduction:

Since the discovery of the electron in the late 19 th century and the identification of the components of the nucleus in the early 20 th century, providing quantitative predictions of particular material properties has become one of the significant challenges in theoretical physics [1]. Considering that this properties in condensed matter are fundamentally related to the behavior of electrons with other electrons and surrounding atomic nuclei, which described mathematically by the Schrodinger equation [2]. The solving of Schrodinger equation for multi-particle systems is rigorously challenging pursuit, and often demands a deep understanding of both the mathematical formalism and the underlying physical principles so resorting to some approximations is a necessity. The initial strategy is used on the true, basic Hamiltonian governing the system, which called as '*ab-initio* or *first principles'* approach [2], then it was devloped by the Density Functional Theory (DFT) for many reasons, which is our subject in this chapter.

To provide a clear understanding of density functional theory (DFT), it is essential to trace its historical development, as it highlights how the concepts have evolved over time, which can be mapped out by highlighting several key milestones. In 1926, L. H. Thomas [3] became the first to express energy in terms of density, drawing on the model of a non-interacting electron gas. E. Fermi in 1927 [4] and P. A. Dirac [5] further refined this approach in 1930. However, it wasn't until the mid-1960s that density functional theory (DFT) was formally introduced through two key papers by Hohenberg and Kohn (1964) [6] and Kohn-Sham (1965) [7], which laid the groundwork for the theoretical framework of DFT. Its historical development reflects a continuous effort to refine theoretical concepts and practical applications as the introduction of approximate exchange-correlation functionalism allowed DFT to be used in calculations. We mention, for example, but not limited to the local density approximation (LDA) [8] (1970s), generalized gradient approximation (GGA)[9], and the hybrid functionalism[10–12] beginning from the year 2000.

In this chapter, we will not provide a comprehensive and detailed overview of everything related to DFT. Instead, our aim is to offer a clear and concise introduction to the fundamental equations that are essential for understanding DFT.

II.1. The DFT Foundations

II.1.1. Many-Body Schrodinger Equation Problem

To understand the behavior of quantum particles, determining the ground state energy is crucial with the calculation of the wave function $\Psi(r)$ for every point in the region of interest by solving a Schrodinger equation, as it provides information about the probability distribution of a particle's position. The time independent Schrödinger equation [2] for an N-electron system can be expressed in symbolic form as:

$$\hat{H}\Psi = E\Psi \qquad (II.\ 1)$$

Where $\hat{H}$ is the Hamiltonian operator represents the total energy of a quantum system while their eigenvalues represent the allowed energy E of this system. To clarify further, the Hamiltonian operator for a system containing n electrons in position $r_1, \ldots, r_n$ and N nuclei located at positions $R_1, \ldots, R_N$ is given as follow [13]:

$$\hat{H} = \hat{T}_e + \hat{T}_N + \hat{V}_{e-e} + \hat{V}_{N-N} + \hat{V}_{e-N} \qquad (II.\ 2)$$

Where:

- $\hat{T}_e$: is the kinetic energy of the n electrons of the system, which can be defined as:

$$\hat{T}_e = \sum_{i=1}^{n} \frac{(i\hbar\nabla_i)^2}{2m_e} = \frac{-\hbar^2}{2m_e}\sum_{i=1}^{n}(\nabla_i)^2 \qquad (II.\ 3)$$

- $\hat{T}_N$:is the kinetic energy of the N nuclei of the system, which can be articulated as:

$$\hat{T}_N = \sum_{I=1}^{N} \frac{(i\hbar\nabla_I)^2}{2M_I} = \frac{-\hbar^2}{2M_I}\sum_{I=1}^{N}(\nabla_I)^2 \qquad (II.\ 4)$$

- $\hat{V}_{e-e}$: describe the influence that electrons produce on each other due to electromagnetic forces, designated as'the potential energy of electron-electron interactions', which can be expressed and reduced as:

$$\hat{V}_{e-e} = \frac{1}{2}\frac{e^2}{4\pi\varepsilon_0}\sum_{i\neq j}^{n}\frac{1}{|r_i - r_j|} \qquad (II.\ 5)$$

- $\hat{V}_{N-N}$:is the repulsion among nuclei in an atom can be represented by:

$$\hat{V}_{N-N} = \frac{1}{2}\frac{Z_I Z_J e^2}{4\pi\varepsilon_0}\sum_{I\neq J}^{N}\frac{1}{|R_I - R_J|} \qquad (II.\ 6)$$

- $\hat{V}_{e-N}$:describe the interaction between electrons and nuclei

$$\hat{V}_{e-N} = -\frac{1}{2}\frac{Z_I e^2}{4\pi\varepsilon_0}\sum_{i=1}^{n}\sum_{I=1}^{N}\frac{1}{|R_I - r_i|} \qquad (II.\ 7)$$

In which: $\hbar$ is the reduced Planck's constant, ∇^2 is the Laplace operator defined as: $\nabla^2 = \frac{\partial^2}{\partial x^2} + \frac{\partial^2}{\partial y^2} + \frac{\partial^2}{\partial z^2}$, m_e and M_I is mass of electron and nuclei I,respectively. The elementary charge is typically denotes as e which is related to the charge of a nucleus I with their atomic number Z_I. On the other hand, $\frac{1}{4\pi\varepsilon_0}$ refer to Coulomb's constant.

So can write the Schrödinger:

$$\left[\frac{-\hbar^2}{2m_e}\sum_{i=1}^{n}(\nabla_i)^2 - \frac{\hbar^2}{2M_I}\sum_{I=1}^{N}(\nabla_I)^2 + \frac{1}{2}\frac{e^2}{4\pi\varepsilon_0}\sum_{i\neq j}^{n}\frac{1}{|r_i - r_j|} + \frac{1}{2}\frac{Z_I Z_J e^2}{4\pi\varepsilon_0}\sum_{I\neq J}^{N}\frac{1}{|R_I - R_J|} - \frac{1}{2}\frac{Z_I e^2}{4\pi\varepsilon_0}\sum_{i=1}^{n}\sum_{I=1}^{N}\frac{1}{|R_I - r_i|}\right]\Psi = E\Psi \qquad (II.\ 8)$$

As you seen, each nucleus contributes 3 positional coordinates R_I (x, y, z), so the total contribution from the nuclei would indeed be $3N$, while electrons contribute $3ZN$ positional coordinates r_i and 2 spin states σ_i (up and down) so each electron contributes 4 variables (3 for position and 1 for spin) . Thusly finding an exact solution for many-body Schrodinger equation is certainly very difficult and typically requires sophisticated computational techniques, so various approximations are employed to handle these many-body problems. This is what Paul Dirac expressed in his famous statement in 1929 that the general theory of quantum mechanics is nearly finished; providing a comprehensive understanding of the essential physical laws that underpin much of physics and all of chemistry. He highlighted the need for developing efficient, approximate methods to apply quantum mechanics, allowing for the analysis of complex atomic systems without excessive computation [14]. The first way to tackle this challenge is through the Born-Oppenheimer approximation.

II.1.2. Born Oppenheimer Approximation:

The Born Oppenheimer Approximation is a restricted separation of the electron from the nuclear dynamics due to the considerable mass ratio between the nucleus and its surrounding electrons [15]. The nuclei are significantly heavier than electrons, so they move more slowly compared with the movement of electrons. As a result, we can treat the electrons as if they are moving in a static field created by the fixed nuclei [16]. In this approximation, we can ignore the kinetic energy of the nuclei and consider the repulsive interactions between them as constant in equation $(II.8)$, the obtained Hamiltonian operator depict the behavior of electrons in the fixed field created by of N nuclei and its written as fellow:

$$\hat{H} = \hat{H}_e + \hat{V}_{e-N} \quad (II.\ 9)$$

Where the $\hat{H}_e$ is the electronic Hamiltonian operator, written as:

$$\hat{H}_e = -\frac{\hbar^2}{2m_e}\sum_{i=1}^{n}(\nabla_i)^2 + \frac{1}{2}\frac{e^2}{4\pi\varepsilon_0}\sum_{i\neq j}^{n}\frac{1}{|r_i - r_j|} - \frac{1}{2}\frac{Z_I e^2}{4\pi\varepsilon_0}\sum_{i=1}^{n}\sum_{I=1}^{N}\frac{1}{|R_I - r_i|} \quad (II.\ 10)$$

On the other hand, the XC which detail the electron motion, explicitly related to their coordinates but parametrically linked to the nuclei's coordinates and their electronic energy [16], so it's formulated as:

$$\Psi(R_1, R_2, \dots, R_N;\ r_1\sigma_1, r_2\sigma_2, \dots, r_n\sigma_n) =$$
$$\Psi_N(R_1, R_2, \dots, R_N).\Psi_e(R_1, R_2, \dots, R_N; r_1\sigma_1, r_2\sigma_2, \dots, r_n\sigma_n) \quad (II.\ 11)$$

We can write:

$$\Psi(R_1, R_2, \dots, R_N;\ r_1\sigma_1, r_2\sigma_2, \dots, r_n\sigma_n) = \Psi_N(\{R_N\}).\Psi_e(\{R_N\}; \{r_n\sigma_n\}) \quad (II.\ 12)$$

Therefore, the solution of Schrödinger equation demand to solve the electronic Hamiltonian:

$$\hat{H}_e\Psi_e(\{R_N\}; \{r_n\sigma_n\}) = E_e\{R_N\}.\Psi_e(\{R_N\}; \{r_n\sigma_n\}) \quad (II.\ 13)$$

Where $E_e\{R_N\}$ is the eigenvalues for the electronic Hamiltonian operator, so we can express the total energy of the system as:

$$E_{sys} = E_e\{R_N\} + V_{N-N} \quad (II.\ 14)$$

Solving the Schrödinger equation $(II.1)$ for many-electron systems is significantly more complex despite neglect the motion of nuclei and consider it fixed at their positions, due to the term $\hat{V}_{e-e}$ for the electron-electron interactions, thus requires another approximations. Here is an overview of how this is typically approached, along with some common methods used in practice.

II.1.3. Reduction to Single - Particle Problem

II.1.3.a. Pauli Exclusion Principle

Is a fundamental principle in quantum mechanics that states that no two fermions (particles with half-integer spin, such as electrons, protons, and neutrons) can occupy the same quantum state simultaneously within a quantum system [16]. For electrons, for example, the wave function is related to the spatial coordinate and their spin coordinate, which we will refer (α) or (β). We call a generic (either α or β) spin coordinate (σ_i). We can refer to space-spin coordinates

collectively as $X_i = (r_i \sigma_i)$. Take into account these improvements, the electronic wave function can written as:

$$\Psi_e(R_1, R_2, \dots, R_N; r_1\sigma_1, r_2\sigma_2, \dots, r_n\sigma_n) = \Psi_e(R_1, R_2, \dots, R_N; X_1, X_2, \dots, X_n) \quad (II.\ 15)$$

Thusly, both of the wave function for n electron $(II.12)$ and the electronic Hamiltonian $(II.13)$can written as:

$$\Psi(R_1, R_2, \dots, R_N;\ X_1, X_2, \dots, X_n) = \Psi_N(\{R_N\}).\Psi_e(\{R_N\}; \{X_n\}) \quad (II.\ 16)$$

$$\hat{H}_e \Psi_e(\{R_N\}; \{X_n\}) = E_e\{R_N\}.\Psi_e(\{R_N\}; \{X_n\}) \quad (II.\ 17)$$

Since the Pauli Exclusion Principle states that the wave function of a system with multiple electrons must be antisymmetric with respect to the exchange of any two electrons, the electronic wave function describes as [17]:

$$\Psi_e(R_1, \dots, R_N; X_1, ., X_i, \dots, X_j, \dots, X_n) = -\Psi_e(R_1, \dots, R_N; X_1, \dots., X_j, \dots., X_i, \dots, \dots, X_n) \quad (II.\ 18)$$

II.1.3.b. Hartree Approximation

The Douglas Hartree approximation (1927) [18] is to simplify the n electron wave function by considering each electron is independent and interacts with others in an averaged way, so is treated as if it moves under an effective potential [19], which represents the average interaction between that electron and the other electrons $(n-1)$ and the N nuclei in the system. The treating of each electron individually in the field created by the others is known as the first self-consistent methods. With the help of this simplified model, the Hamiltonian of no interacting electrons in atomic units ($\hbar = m_e = e = {}^{1}/_{4\pi\varepsilon_0} = 1$) is of the form:

$$\hat{H}_e = \sum_i \left(\frac{-1}{2}(\nabla_i)^2 + \hat{V}_{ext} + \hat{V}_{Ha}(r_i) \right) = \sum_i \hat{H}_i \quad (II.\ 19)$$

Where H_i described by the equation bellow :

$$H_i = \frac{-1}{2}(\nabla_i)^2 - \frac{1}{2} Z_I \sum_{I=1}^{N} \frac{1}{|R_I - r_i|} + \frac{1}{2} \sum_{i \neq j} \frac{1}{|r_i - r_j|} \quad (II.\ 20)$$

In the equation *(II. 21)* the first term is the kinetic energy while the second one is the external potential refers to the attractive interaction between the electron (i) and the nucleus in the system. The last term is the Hartree potential arises from the classical Coulomb repulsive interaction between each electron and the average field.

The operators $\hat{H}_i$ have a set of eigenfunctions that are spatial orbitals Φ_i, thusly we can write:

$$H_i\Phi_i = \epsilon_i\Phi \qquad (II.\ 21)$$

So the Schrodinger equation for each electron can written as:

$$\left[\frac{-1}{2}(\nabla_i)^2 - \frac{1}{2}Z_I\sum_{I=1}^{N}\frac{1}{|R_I - r_i|} + \frac{1}{2}\sum_{i\neq j}\frac{e^2}{|r_i - r_j|}\right]\Phi_i(r_i) = \epsilon_i\Phi_i(r_i) \qquad (II.\ 22)$$

As the Hamiltonian consists of a sum of one-electron terms, it can be shown that the total wave function of the system is simply a product of eigenfunctions Φ_i for each electron, which supposition is referred to as the Hartree product [20] defined by the equation:

$$\Psi_e(r_1, r_2, r_3 \dots\dots\dots\dots r_n) = \Phi_1(r_1)\Phi_2(r_2)\Phi_3(r_3)\dots\dots\dots\dots\dots\dots\Phi_n(r_n) \qquad (II.\ 23)$$

The electronic total energy for n electrons can be expressed as the sum of n individual one-electron energies, as outlined below:

$$E_e = \langle\Psi_e|\hat{H}_e|\Psi_e\rangle \qquad (II.\ 24)$$

$$E_e = T_e + E_{ext} + E_{Ha} \qquad (II.\ 25)$$

By detailed it is becomes:

$$E_e = \sum_i\left\langle\Phi_i(r_i)\left|\frac{-1}{2}(\nabla_i)^2\right|\Phi_i(r_i)\right\rangle + \sum_i\langle\Phi_i(r_i)|V_{ext}(r_i)|\Phi_i(r_i)\rangle -$$

$$\frac{1}{2}\sum_{i,j\neq i}\left\langle\Phi_i(r_i)\Phi_j(r_j)\left|\frac{1}{|r_i - r_j|}\right|\Phi_i(r_i)\Phi_j(r_j)\right\rangle \qquad (II.\ 26)$$

$$E_e = \epsilon_1 + \epsilon_2 + \epsilon_3 + \dots\dots\dots\dots\epsilon_n \qquad (II.\ 27)$$

Once the total energy of the electrons calculated, the enables the determination of the system's total energy, as given by equation $(II.14)$.

The Hartree approximation, while simplifying the calculation of a system's electronic structure, overlooks two key principles of quantum mechanics: the antisymmetry of the wave, function and, by extension the Pauli Exclusion Principle. Additionally, it fails to incorporate the exchange and correlation energies that result from the interactions between the system's electrons [19].Consequently, drawbacks of this approach led to the development of a new model designed to address these weaknesses.

II.1.3.c. Hartree-Fock Approximation

The Hartree-Fock method [21] improves upon the Hartree method by adding the missing consideration of exchange interactions, ensuring that the electron wave function respects the

fermionic nature of electrons, it must be antisymmetric under the exchange of any two electrons. The many-electron wave function, which depends on both the spatial and spin coordinates $X_i = (r_i\sigma_i)$ combination of single-particle wave functions called spin orbitals (denoted as ψ_i), should therefore be represented using a Slater determinant [22]. This formalism guarantees the required antisymmetry of the wave function, describes as:

$$\Psi_{HF}(X_1, X_2, X_3, \dots \dots X_N) = \frac{1}{\sqrt{n!}} \begin{vmatrix} \psi_1(X_1) & \psi_2(X_1) & \cdots & \psi_n(X_1) \\ \psi_1(X_2) & \psi_2(X_2) & \cdots & \psi_n(X_2) \\ \vdots & \vdots & \vdots & \vdots \\ \psi_1(X_n) & \psi_2(X_n) & \cdots & \psi_n(X_n) \end{vmatrix} \quad (II.\ 28)$$

Where the factor $\frac{1}{\sqrt{n!}}$ compensates for this over counting by dividing the wave function by the number of possible permutations of the electrons. This ensures that the total probability (integral of the modulus squared of the wave function) is 1, as required for proper normalization in quantum mechanics [19]. The wave function [23] described as:

$$\psi_i(X) = \phi_i(r)\chi_i(\sigma) \quad (II.\ 29)$$

Where: ϕ is the spatial orbital and χ denote the spin wave function. However, r represents the spatial and σ reveals to the spin coordinate of the electron.

Using the Slater determinant, the total energy is:

$$E^{HF}{}_e = T_e + E_{ext} + E_{Ha} + E_x \quad (II.\ 30)$$

Depending on the variational principle [24] the spin orbitals wave functions ψ that minimize the electronic energy will be the optimal set of orbitals, so the energy is described as:

$$E^{HF}{}_e = \underbrace{\sum_i \left\langle \phi_i(r_i) \left| \frac{-1}{2}(\nabla_i)^2 \right| \phi_i(r_i) \right\rangle}_{T_e} + \underbrace{\sum_i \langle \phi_i(r_i) | V_{ext}(r_i) | \phi_i(r_i) \rangle}_{E_{ext}}$$

$$+ \underbrace{\frac{1}{2} \sum_{i,j \neq i} \left\langle \phi_i(r_i)\phi_j(r_j) \left| \frac{1}{|r_i - r_j|} \right| \phi_i(r_i)\phi_j(r_j) \right\rangle}_{E_{Ha}}$$

$$- \underbrace{\frac{1}{4} \sum_{i,j \neq i} \left\langle \phi_i(r_i)\phi_j(r_j) \left| \frac{1}{|r_i - r_j|} \right| \phi_j(r_i)\phi_i(r_j) \right\rangle}_{E_x} \quad (II.\ 31)$$

The total electron-electron interaction energy in a Slater determinant is split into two terms: the direct (Coulomb) interaction and the exchange interaction. The first one named as Hartree

potential E_{Ha} describe the classical electrostatic interaction between pairs of electrons represented in equation$(II.28)$. The second term E_x arises due to the antisymmetry of the electron wave function under particle exchange. So the electronic Schrödinger equation results in an expression for the Hartree - Fock energy [25] is equated as:

$$E^{HF}{}_e = \int \phi_i{}^*(r_i)\left(\frac{-1}{2}\sum_i(\nabla_i)^2 + V_{ext}(r_i)\right)\phi_i(r_i)dr_i \; +$$

$$\frac{1}{2}\sum_{i,j\neq i}\int \frac{\phi_i{}^*(r_1)\phi_i(r_1)\phi_j{}^*(r_2)\phi_j(r_2)}{|r_i - r_j|}\, dr_1 dr_2 \; - \frac{1}{4}\sum_{i,j\neq i}\int \frac{\phi_i{}^*(r_1)\phi_j(r_1)\phi_i(r_2)\phi_j{}^*(r_2)}{|r_i - r_j|}\, dr_1 dr_2 \qquad (II.\,32)$$

This leads to the Hartree-Fock (or SCF) equations:

$$\left(\frac{-1}{2}\left(\hat{\nabla}\right)^2 + \hat{V}_{ext}(r) + \hat{V}_{Ha}(r) + \hat{V}_x(r)\right)\phi_i(r) = \epsilon_i\phi_i(r) \qquad (II.\,33)$$

This equation includes an additional term compared to the Hartree equation the last term, which represents the non-local exchange potential. This term accounts for the exchange interactions between electrons. While it improves upon the limitations of the Hartree approximation, it also makes the calculations significantly more complex. The non-local exchange potential is expressed as follows:

$$V_x(r)\phi_i(r) = -\frac{1}{2}\sum_i^n \left\langle \phi_j(r_i)\left|\frac{1}{|r_i - r_j|}\right|\phi_j(r_j)\right\rangle \phi_i(r) \qquad (II.\,34)$$

In 1933, the Dutch physicist Tom Koopmans gives his theorem known as Koopmans' theorem [26], provides a relationship for estimating the ionization energy (the energy required to remove an electron) of an atom or molecule. According to the theorem, the ionization energy of an atom or molecule can be approximated by the negative of the energy of the molecular orbital (MO) or atomic orbital (AO) from which the electron is removed. Therefore, the orbital energy ϵ_i in the Hartree–Fock equations $(II.34)$ is the negative of the energy required to remove an electron in the state ϕ_i from the solid. Similarly, neglect resonant processes and calculate the (real) energy $E_i{}^{N-1}$ of a $(N-1)$ −particle system with one electron removed from state i. The one-electron energy E^N , is:

$$\epsilon_i = E^N - E_i{}^{N-1} \qquad (II.\,35)$$

In the Hartree-Fock method, since electron correlation is not included, the electron distribution is fixed, and the energy of the orbital from which the electron is removed can serve as an estimate of the ionization energy.

The Hartree-Fock equation plays a critical role in approximating the electronic structure of atoms and molecules, providing orbital energies that can be used in Koopmans' theorem to estimate ionization energies. However, both methods are approximate and neglect important effects such as electron correlation and electron relaxation, which can lead to discrepancies between the predicted and actual ionization energies, especially for systems with significant electron interaction.

II.2. Density Functional Theory

II.2.1. The Thomas-Fermi-Dirac Model

The Thomas-Fermi model is a statistical model used to describe the behavior of electrons suggested in 1927 by Lewellyn Thomas [27] and Enrico Fermi [28], include only the kinetic energy and the coulomb parts in the absence of external potential. The model considered that the electrons surrounding the nucleus at zero temperature are assumed to form a degenerate Fermi gas represent a homogenous gas obey the Pauli Exclusion Principle, which merged by Dirac when introduced the exchange effect (Thomas-Fermi-Dirac model) [29]. So, the model approximate the distribution of electrons in an atom or molecule by treating the electron density $\rho(r)$ in a self-consistent manner, which is spatially uniform, without considering the individual quantum states of each electron.

Thusly that of the electron density $\rho(r)$ can indeed be measured indirectly through various experimental techniques, most commonly through X-ray crystallography, which allow us to visualize electron distributions in molecules or materials. The electron density $\rho(r)$ incorporate details about both the external potential and the electron number n, which obtained by integration the electron density over the spatial variables using the equation:

$$n = \int \rho(r)\, d^3 r \qquad (II.\ 36)$$

Based on electron density the Hartree-Fock energy equation $(I.33)$ will be:

$$E^{HF}{}_e = \underbrace{\int \tau(r) d^3 r}_{T[\rho(r)]} + \underbrace{\frac{1}{2}\int V_{ext}(r)\rho(r) d^3 r}_{E_{ext}[\rho(r)]}$$

$$+ \underbrace{\frac{1}{2}\iint \frac{\rho(r).\rho'(r')}{|\boldsymbol{r}-\boldsymbol{r'}|} d^3 r.\, d^3 r'}_{E_H[\rho(r)]} - \underbrace{\frac{1}{4}\iint \frac{|\rho(r,r')|^2}{|\boldsymbol{r}-\boldsymbol{r'}|} d^3 r.\, d^3 r'}_{E_x[\rho(r,r')]} \qquad (II.\ 37)$$

Where:

- $\tau(r)$ is the kinetic energy density.
- $\rho(r,r') = \sum_i^n \phi_i(r)\phi_i^*(r')$ is the mixed electron density.

So we can obtain the Thomas-Fermi-Dirac total energy $E^{TFD}[\rho]$, which equated by:

$$E^{TFD}[\rho] = C_k \int d^3 r\, \rho(\boldsymbol{r})^{5/3} + \int d^3 r\, V_{\text{ext}}(\boldsymbol{r})\rho(\boldsymbol{r}) + \frac{1}{2}\int d^3 r\, d^3 r'\, \frac{\rho(\boldsymbol{r})\rho(\boldsymbol{r'})}{|\boldsymbol{r}-\boldsymbol{r'}|} - C_x \int d^3 r\, \rho(\boldsymbol{r})^{4/3} \quad \textit{(II. 38)}$$

With: $C_k = \left(\frac{3}{10}\right)(3\pi^2)^{2/3}$ and $C_x = \frac{3}{4}\left(\frac{3}{\pi}\right)^{\frac{1}{3}}$

Demonstration:

Depending on Fermi model, the Fermi energy is the energy of the highest occupied state in the system at $0\ K$. All states with energies less than or equal to E_F be filled, and all states with energies greater than E_F are empty, the Fermi energy is written as:

$$E_F = E_{max} = \frac{{P_F}^2}{2m_e} \quad \textit{(II. 39)}$$

Where: P_F is the Fermi momentum.

Based on Heisenberg Uncertainty Principle [30] the volume of a phase space cell for a single particle is approximately h^3 in three-dimensional space, where h is a constant on Planck. Therefore, the phase space is divided into cells of volume h^3 and each cell can contain only one particle .However, when we are dealing with fermions, we also have to consider spin.

The total number of electrons n in the ground state can be obtained by counting the number of quantum states with momentum less than or equal to P_F. The density of states in momentum space for non-interacting fermions is proportional to the volume of phase space and the available momentum states.

The total number of momentum states with momentum less than or equal to P_F is determined by the volume of a sphere in momentum space with radius P_F, the volume of this momentum space sphere (for a 3D system) is:

$$V = \frac{4}{3}\pi {P_F}^3 \quad \textit{(II. 40)}$$

Now, because each quantum state occupies a phase space cell of volume h^3 , the number of quantum states with momentum less than or equal to P_F is:

$$Number\ of\ states = \frac{n}{2} = \frac{2}{h^3}\frac{4}{3}\pi {P_F}^3 \qquad (II.\ 41)$$

hence (uniform) electron density is:

$$\rho = \frac{n}{V} = \frac{8\pi}{3h^3}{P_F}^3 \qquad (II.\ 42)$$

or, inverting it:

$$P_F = \left(\frac{3h^3\rho}{8\pi}\right)^{1/3} \qquad (II.\ 43)$$

Now, we consider the kinetic energy density $\tau(r)$, the kinetic energy T can be recovered as $\int \tau(r)d^3r$:

$$\tau(r) = \frac{T}{V} = \frac{1}{V}\int \frac{P^2}{2m}dN = \frac{1}{V}\int_0^{P_F}\frac{P^2}{2m}\frac{2.4\pi.V.P^2}{h^3}dP = \frac{8\pi}{2mh^3}\int_0^{P_F}P^4dP = \frac{8\pi}{2mh^3}\frac{{P_F}^5}{5} \qquad (II.\ 44)$$

Substituting $(II.44)$ into $(II.45)$ yields:

$$\tau(r) = \frac{8\pi}{10mh^3}\left(\frac{3h^3\rho}{8\pi}\right)^{5/3} = \left(\frac{3h^2}{10m}\right)\left(\frac{3}{8\pi}\right)^{2/3} \times \rho^{5/3} \qquad (II.\ 45)$$

In atomic units, the equation *(II.45)* becomes:

$$\tau(r) = \underbrace{\left(\frac{3}{10}\right)(3\pi^2)^{2/3}}_{C_k} \times \rho^{5/3} \qquad (II.\ 46)$$

Then the Thomas-Fermi total energy formalism of the electron system in an external potential is:

$$E^{TF}[\rho] = C_k \int d^3\,r\,\rho(\boldsymbol{r})^{5/3} + \int d^3\,r\,V_{\text{ext}}(\boldsymbol{r})\rho(\boldsymbol{r}) + \frac{1}{2}\int d^3\,r\,d^3r'\,\frac{\rho(\boldsymbol{r})\rho(\boldsymbol{r'})}{|\boldsymbol{r}-\boldsymbol{r'}|} \qquad (II.\ 47)$$

The Thomas-Fermi model is based on a classical description of the electrons and does not fully account for quantum mechanical effects; it approximates the electron density in an atom by treating it as a continuous function. On the other hand, the model neglects the effects of electron-electron correlation and the Pauli principle. This requires building more modern approach that builds on the Thomas-Fermi idea but includes a more advanced treatment of electron correlation via exchange-correlation functional. Dirac (1930) suggested a correction term [29] for the Thomas-Fermi energy defined by the equation in atomic units:

$$E^{TFD}[\rho] = E^{TF}[\rho] - \underbrace{\frac{3}{4}\left(\frac{3}{\pi}\right)^{\frac{1}{3}}}_{Cx}\int d^3\,r\,\rho(\boldsymbol{r})^{4/3} \qquad (II.\ 48)$$

The Thomas-Fermi theory, when incorporating Dirac's exchange term, results in an even lower total energy (already too low to begin with). However, despite this, it still does not predict the existence of bound negative ions [31]. In atoms and molecules, the electron density typically varies significantly, rather than being uniform. As a result, the homogeneous electron gas model, which assumes a uniform distribution of electrons, is considered too simplistic and inadequate for describing the complexities of real systems. Early efforts to improve this model, such as the Thomas–Fermi theory, were found to be far from providing accurate quantitative predictions for atomic and molecular systems [32]. The Thomas-Fermi theory introduced a significant shift in the approach to understanding electronic properties by prioritizing electron charge density over the wave function as the fundamental variable. This transition was crucial in the evolution of modern electronic structure theory. By concentrating on electron density—a simpler three-dimensional function in contrast to the complex, high-dimensional wave function—the groundwork for what would evolve into density functional theory (DFT) was laid.

Although the origins of density functional theory (DFT) date back to the early 1930s, it was formally established with the publication of the Hohenberg-Kohn paper in 1964 [33] and the Kohn-Sham paper in 1965 [34]. These theorems establish that the ground-state properties of a many-electron system can be uniquely determined by its electron density. This framework allows energy and other electronic properties to be expressed as functionals of the electron density, facilitating the efficient calculation of complex material properties at a significantly lower computational cost than wave function-based methods.

II.2.2. Hohenberg-Kohn Theorems

The Hohenberg-Kohn (HK) works has seen impressive advancements both in its applications and in its foundational principles, depending on two theorems[33]:

- **The first theorem** ‘the *external potential* $V_{ext}\ (r)$ *is (to within a constant) a unique functional of* $\rho(r)$*; since, in turn* $V_{ext}\ (r)$ *fixes* $\widehat{H}$ *we see that the full many particle ground state is a unique functional of* $\rho(r)$‘.

The theorem implies that for non-degenerate ground states, no two distinct external potentials can produce the same electron density. This establishes a unique functional relationship between the density and the potential, allowing one to be determined from the other [1,35]. This means that there cannot be two distinct external potentials, ${V_{ext}}^{a}\ (r)$ and ${V_{ext}}^{b}\ (r)$ that produce

the same ground state electron density. Consequently, if we have access to the electron density $\rho(r)$, we can derive the external potential $V_{ext}\ (r)$, as well as all properties of the system, including its Hamiltonian H and wave function [35].

Demonstration:

The proof of the first theorem of HK follows a proof by contradiction, the initial step is to considering a system of multiple electrons, which are confined in a large spatial region, and they experience both an external potential $V_{ext}\ (r)$ and mutual Coulomb repulsion V_{e-e} . The Hamiltonian that governs the behavior of this system takes the form of:

$$\widehat{H} = \hat{T} + \hat{V}_{ext}\ (r) + \hat{V}_{e-e} \qquad (II.\ 49)$$

Where:

$$T = \frac{1}{2}\int \nabla\psi^*(r)\nabla\psi(r)\ dr \qquad (II.\ 50)$$

$$V_{ext} = \int v(r)\psi^*(r)\psi(r)\ dr \qquad (II.\ 51)$$

$$V_{e-e} = \frac{1}{2}\int \frac{1}{|r-r'|}\psi^*(r)\psi^*(r')\psi(r')\psi(r)\ drdr' \qquad (II.\ 52)$$

The second step is to consider two external potentials, ${V_{ext}}^a\ (r)$ and ${V_{ext}}^b\ (r)$ which differ by an amount that is not constant, despite the differences, both of them must produce the same electron density $\rho_o(r)$, linked to the non-degenerate ground states probability of n particles. So there are two normalized ground-state wave functions $\psi_{0,a}$ and $\psi_{0,b}$ corresponding for the two Hamiltonians, $\widehat{H}_a$ and $\widehat{H}_b$, respectively, which differ primarily in their external potentials (${V_{ext}}^a\ (r)$ and ${V_{ext}}^b\ (r)$). Since the Hamiltonians differ, the eigenfunctions representing the ground-state energies $E_{0,a}$and $E_{0,b}$ will also differ. These Hamiltonians are:

$$\widehat{H}_a = \hat{T} + {\hat{V}_{ext}}^a\ (r) + \hat{U} \qquad (II.\ 53)$$

$$\widehat{H}_b = \hat{T} + {\hat{V}_{ext}}^b\ (r) + \hat{U} \qquad (II.\ 54)$$

Using the minimal feature of the ground state, we can equate:

$$E_{0,a} < \langle\psi_{0,b}|\widehat{H}_a|\psi_{0,b}\rangle \qquad (II.\ 55)$$

$$\langle\psi_{0,b}|\widehat{H}_a + \widehat{H}_b - \widehat{H}_b|\psi_{0,b}\rangle = \langle\psi_{0,b}|\widehat{H}_a - \widehat{H}_b|\psi_{0,b}\rangle + \langle\psi_{0,b}|\widehat{H}_b|\psi_{0,b}\rangle \qquad (II.\ 56)$$

Thusly:

$$E_{0,a} < \left\langle \psi_{0,b} \left| \hat{V}_{ext}{}^{a}(r) - \hat{V}_{ext}{}^{b}(r) \right| \psi_{0,b} \right\rangle + E_{0,b} \quad (II.\ 57)$$

$$E_{0,a} < \int \left|\psi_{0,b}\right|^2 (v_{ext}{}^{a}(r) - v_{ext}{}^{b}(r))dr + E_{0,b} \quad (II.\ 58)$$

$$E_{0,a} < \int \rho_o(r)\,(v_{ext}{}^{a}(r) - v_{ext}{}^{b}(r))dr + E_{0,b} \quad (II.\ 59)$$

In the same manner, we identify:

$$E_{0,b} < \int \rho_o(r)\,(v_{ext}{}^{b}(r) - v_{ext}{}^{a}(r))dr + E_{0,a} \quad (II.\ 60)$$

The sum of $(II.59)$ and $(II.60)$ leads to a contradiction:

$$E_{0,a} + E_{0,b} < E_{0,b} + E_{0,a} \quad (II.\ 61)$$

As the result in the equation $(II.61)$ is false, it follows that our initial assumption is false. Hence, v_{ext} can be uniquely expressed as a functional of the ground-state density $\rho_o(r)$, and the many-electron ground state is uniquely defined as a functional of $\rho_o(r)$.

- **The second theorem (Variational principle):** '*For a given external potential, the true density $\rho_o(r)$ minimizes the total energy functional $E_v[\rho_{tr}]$', so:*

$$E_0 = E_v(\rho_o) = \min_{\rho} \mathrm{E}\,[\rho] \leq E_v[\rho_{tr}(r)] \quad (II.\ 62)$$

Hohenberg and Kohn showed that for any initial guess for density function $\rho_{tr}(r)$ that meets the following two conditions [36]: firstly, the total density integrates to the total number of particles n, i.e., $\int \rho_{tr}(r)dr = n$, secondly, the density is always non-negative, i.e., $\rho_{tr}(r) > 0$ for all points in space, thusly the relationship $(II.61)$ is achieved. The term $E_v(\rho_o)$ of the equation $(II.62)$ is given by its expression:

$$E_0 = E_v(\rho_o) = \int v(r).\rho_o(r)\,dr + \bar{T}[\rho_o(r)] + \bar{V}_{e-e}[\rho_o(r)] \quad (II.\ 63)$$

$$E_0 = E_v(\rho_o) = \int v(r).\rho_o(r)\,dr + F_{HK}[\rho_o(r)] \quad (II.\ 64)$$

Where:

The term F_{HK} is Hohenberg-Kohn functional:

$$F_{HK} = E_0 = \langle \psi[\rho_o(r)]\,|H\,|\psi[\rho_o(r)]\,\rangle = \bar{T}[\rho_o(r)] + \bar{V}_{e-e}[\rho_o(r)] \quad (II.\ 65)$$

Demonstration:

Suppose that $\rho_{tr}(r)$ satisfies the two conditions above, according to the Hohenberg–Kohn theorem, this density $\rho_{tr}(r)$ uniquely determines the external potential $v_{tr}(r)$. Furthermore, this external potential $v_{tr}(r)$ uniquely determines the wave function ψ_{tr}corresponding to the density $\rho_{tr}(r)$ with Hamiltonian operator $\widehat{H}$, based on the equation (*II.70*), we can write:

$$\langle\psi_{tr}|\widehat{H}|\psi_{tr}\rangle = \int \rho_{tr}(r)v_{tr}(r)\,d\boldsymbol{r} + F_{\mathrm{HK}}[\rho_{tr}(r)] = E[\rho_{tr}(r)] \geq E[\rho_o(r)] \qquad (II.\ 66)$$

This demonstrates that no approximated electron density can yield a ground-state energy lower than that of the true ground-state density. In other words, the true ground-state electron density always provides the lowest possible energy, and any trial density will result in an energy that is equal to or higher than the true ground-state energy which introduced by the equation:

$$E_0 = min\{\int v(r)\rho_o(r)\ dr + F_{\mathrm{HK}}[\rho_o(r)]\} \qquad (II.\ 67)$$

The determination of the ground-state energy depends on defining the function $F_{HK}[\rho_o(r)]$, yet the interactions between electrons complicate the solution process, that is why HK were suggest to separate it from the classical Coulomb energy, easy to determined, and get [33]:

$$F[n] = \frac{1}{2}\int \frac{\rho_o(r)\rho_o(r')}{|r-r'|}\,dr\,dr' + G[\rho_o(r)] \qquad (II.\ 68)$$

Where $G[\rho_o(r)]$ is the universal functional. The exact expression for this universal functional is unknown and is one of the central challenges of DFT. Therefore, $G[\rho_o(r)]$ can be thought of as the part of the energy functional that is exact but still not determined

II.2.3. Kohn-Sham Equations

The Kohn-Sham workers [34] provides a practical way to approximate the ground-state properties of a system of an interacting inhomogeneous electron gas in a static potential $v(r)$, based on the equation $(II.67)$ and $(II.68)$ we derive the energy expressions, which reach their minimum for the correct density function:

$$E_0 = \int v(r)\rho(r)\ dr + \frac{1}{2}\int \frac{\rho(r)\rho(r')}{|r-r'|}\,dr\,dr' + G[\rho(r)] \qquad (II.\ 69)$$

Kohn and Sham propose an approximation for the universal functional $G[\rho(r)]$ in density functional theory (DFT), leading to a computational approach similar to Hartree's method by considering the systems in which paired electrons are described by the same spatial one-electron

orbitals. Their formulation, shown in the equation($II.\ 70$), incorporates both the kinetic energy $T_S[\rho(r)]$ of non-interacting electrons in homogenous gas and an effective potential that captures electron exchange and correlation effects $E_{XC}[\rho(r)]$, which is defined by equation ($II.71$).

$$G[\rho(r)] = T_S[\rho(r)] + E_{XC}[\rho(r)] \qquad (II.\ 70)$$

$$E_{XC}[\rho(r)] = \int \rho(r)\epsilon_{XC}\left(\rho(r)\right)dr \qquad (II.\ 71)$$

For the non-interacting auxiliary system, the auxiliary Hamiltonian can be expressed as:

$$\widehat{H}_s = \sum_{i=1}^{N}\left(-\frac{1}{2}\nabla_i^2\right) + \sum_{i=1}^{N} v_{KS}(r_i) \qquad (II.\ 72)$$

Therefore, the electronic energy of an n electron system can be written in atomic units as:

$$E[\rho(r)] = -\frac{1}{2}\sum_{i=1}^{n}\int \psi_i^{*}(r_1).\nabla_1^{2}.\psi_i(r_1)dr_1 + \frac{Z_I}{M_I}\sum_{I=1}^{N}\frac{\rho(r_1)}{|r_1 - R_1|}dr_1 + \frac{1}{2}\int\frac{\rho(r_1)\rho(r_2)}{|r_1 - r_2|}\,dr_1\,dr_2 + E_{XC}[\rho(r_1)] \qquad (II.\ 73)$$

The first term corresponds to the kinetic energy of the electrons. The second term represent the attractive interaction between the electrons and the nuclei, summing over all N nuclei, indexed by I, with atomic number Z_I. The third term describes the Coulomb interaction between the charge distributions of the electrons, which are derived from all Kohn-Sham orbitals, evaluated at positions r_1 and r_2. The last term represents the exchange-correlation energy, which incorporates the effects of electron-electron interactions, including both exchange and correlation contributions [34].

Among all the terms, $E_{XC}[\rho(r_1)]$ is the one for which we currently lack an exact method of calculation due to absence of its analytical formalism, so, we are compelled to use approximate expressions to model it. The initial three terms are easy to evaluate from $\rho(r)$ and provide the dominant contributions to the ground-state energy, we need to find the ground-state electron density [37].

We can find E_0 from $\rho_0(r)$ if we can find the KS orbitals $\psi_i(r)$:

$$\rho_0(r) = \sum_{i=1}^{n}|\psi_i(r)|^2 \qquad (II.\ 74)$$

The Kohn–Sham orbitals are derived by solving the Kohn–Sham equations ($II.72$), which result from applying the variational principle [24] to the electronic energy $E[\rho(r)]$. The one-electron orbitals $\psi_i(r_1)$ satisfy the following KS equations:

$$\left(-\frac{1}{2}\nabla^2 + v_{KS}\right)\psi_i(r_1) = \varepsilon_i\psi_i(r_1) \quad \textit{(II. 75)}$$

Where:

- The eigenvalues ε_i is the energy of non-interacting single-particle equation leading to:

$$E = \sum_{i=1}^{N} \varepsilon_i \quad \textit{(II. 76)}$$

- The KS potential v_{KS} represents the effective potential that non-interacting electrons experience in a fictitious system designed to simulate the behavior of interacting electrons, in which is the combination of potentials:

$$v_{KS} = v_{eff} = v_{ext}(r) + v_H(r) + v_{xc}(r) \quad \textit{(II. 77)}$$

The term $v_{xc}(r)$ is the exchange–correlation potential, in which is a functional derivative of the exchange–correlation energy:

$$v_{xc}(r) = \frac{\delta E_{XC}[\rho(r)]}{\delta\rho} \quad \textit{(II. 78)}$$

$$\left[-\frac{1}{2}\nabla_1{}^2 dr_1 + \frac{Z_I}{M_I}\sum_{I=1}^{N}\frac{1}{|r_1 - R_I|} + \frac{1}{2}\int\frac{\rho(r_2)}{|r_1 - r_2|}\, dr_2 + v_{xc}[\rho(r_1)]\right]\psi_i(r_1) = \epsilon_1\psi_i(r_1) \quad \textit{(II. 79)}$$

If the exchange-correlation energy $E_{XC}[\rho(r)]$ is known, the exchange-correlation potential v_{xc} can be derived according to the relation in equation $(II.81)$. The significance of the Kohn-Sham (KS) orbitals lies in their ability to compute the electron density $\rho(r)$ using equation $\rho_0(r) = \sum_{i=1}^{n}|\psi_i(r)|^2$. In this framework, the KS equations are solved iteratively in a self-consistent manner. The process begins with an initial guess for the electron density $\rho(r)$, which is often based on a superposition of atomic densities [37,38]. Throughout the iterations, an approximate form of the functional $E_{XC}[\rho(r)]$ is kept constant to calculate $v_{xc}(r)$ as a function of $\rho(r$..Once an initial set of KS orbitals is obtained by solving the KS equations, this set is used to compute an improved electron density. This iterative cycle continues until both the electron density and the exchange correlation energy converge within a specified tolerance. Ultimately, the total electronic energy is determined by minimizing the corresponding energy functional represented by the equation $(II.77)$[26,37–39]. Without forgetting the spin variable, the spin-orbital function $\psi_i(X) = \varphi_i(r)\chi_i(\sigma)$ as given in the equation $(II.29)$ lead to the total density is composed of the sum of both spin densities.

$$\rho(r) = \rho(r,\uparrow) + \rho\,(r,\downarrow) \quad \textit{(II. 80)}$$

Within this approach, the Kohn Sham equations are written as:

$$\left(-\frac{1}{2}\nabla^2 + \hat{V}_{ext}(r) + \hat{V}_H(r) + \hat{V}_{\mathrm{xc},\sigma}(\boldsymbol{r})\right)\psi_{i\sigma}(\boldsymbol{r}) = \varepsilon_{i\sigma}\psi_{i\sigma}(\boldsymbol{r}) \qquad (II.\ 81)$$

With the spin-dependent exchange-correlation potential and the spin density are given as follow:

$$v_{\mathrm{xc},\sigma}(r) = \frac{\delta E_{\mathrm{xc}}[\sigma_\uparrow,\sigma_\downarrow]}{\delta n_\sigma(r)} \qquad (II.\ 82)$$

$$\rho_\sigma(r) = \sum_{i=1}^{N_\sigma}|\psi_{i\sigma}(r)|^2 \qquad (II.\ 83)$$

This methodology effectively transforms the complex problem of interacting electrons into a more manageable one involving non-interacting particles as shown in ***Figure II. 1*** [40], thereby simplifying calculations while retaining essential physical properties of the system

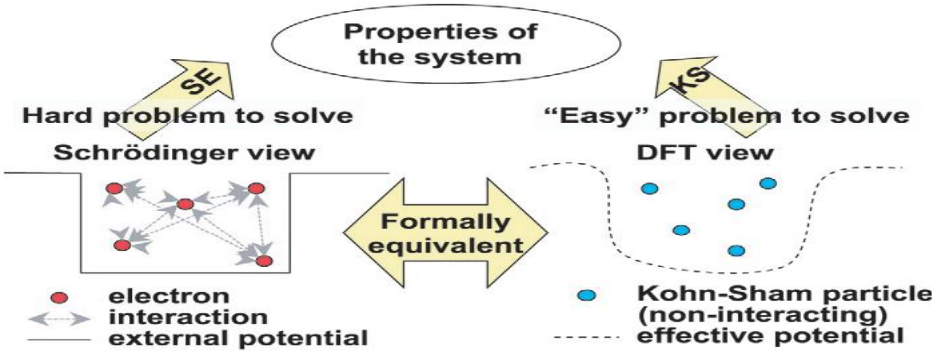


Figure II. 1: ***Visual depiction of the Kohn–Sham method***

II.2.4. Exchange Correlation Functionals

Exchange-correlation (XC) functional is a fundamental component of density functional theory (DFT); these functional provide a way to approximate the exchange and correlation energies that arise from electron-electron interactions as given in the Kohn-Sham equation. The quality of the approximations for $E_{\mathrm{xc}}[\sigma_\uparrow,\sigma_\downarrow]$ significantly affects the overall performance of DFT. Several major classes of approximations have been developed over the years, an ideal approximate density functional $E_{\mathrm{xc}}[\sigma_\uparrow,\sigma_\downarrow]$ should possess several key characteristics: First: it should have a non-empirical foundation, based on well-established principles of quantum mechanics, which are fundamentally sufficient. Second: it should be universal, meaning that a single functional should be applicable to a wide variety of systems—such as atoms, molecules, and solids—regardless of their bonding nature (e.g., covalent, ionic, metallic, hydrogen bonds, or van der Waals interactions). Third: it should be simple, as simplicity is essential for gaining an intuitive understanding and for ensuring computational feasibility; and fourth it must be sufficiently

accurate to be useful in realistic calculations for a broad range of physical systems [41]. We will prioritize the important approximations, particularly the ones that are integral to our work:

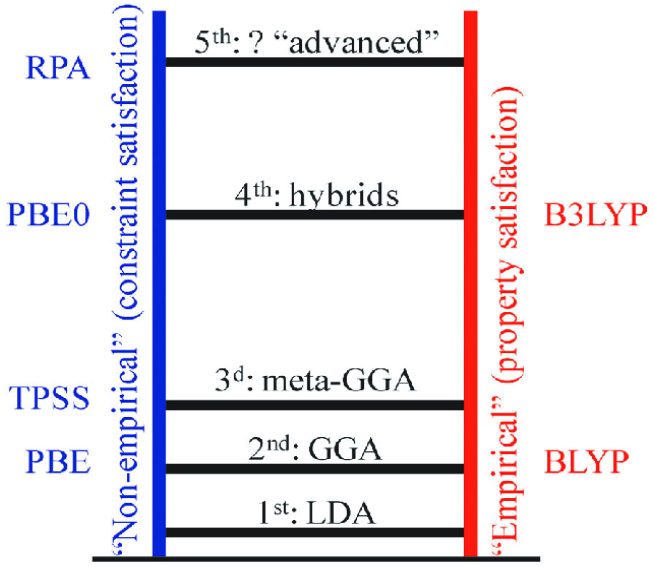


Figure II.2: ***Jacob's Ladder of Exchange–Correlation Functionals in DFT.***

II.2.4.a. Local Density Approximation (LDA)

The Local Density Approximation **(LDA)** is indeed the simplest and one of the most commonly used functionals for describing the exchange-correlation potential in Density Functional Theory (DFT), the concept of using this model was first introduced in the original 1965 paper by Kohn and Sham [34] grounded in the uniform homogeneous electron gas of the Thomas-Fermi model [27,28]. The term 'Local' means that, for each spatial point r in the system, the exchange-correlation energy depends only on the electron density $\rho(r)$ at that point, not on how the density varies at other points in space, which is valid when the density changes slowly from one point to another [36]. Therefore, LDA treats the electron density locally, assuming that it behaves similarly to a uniform electron gas with the same density at each point. The approximation relies on the assumption that the electron density at a specific point in space is locally homogeneous, and hence the exchange-correlation energy can be described by a functional of the local density , as indicated in the equation [1,36]:

$$E_{xc}^{LDA}[\rho(r)] = \int \frac{dE_{xc}^{HEG}}{V} = \int \rho(r)\varepsilon_{xc}^{hom}[\rho(r)]dr \qquad (II.\ 84)$$

The function $\varepsilon_{xc}^{hom}[\rho(r)]$ refers to the exchange-correlation energy per electron in a uniform electron gas with electron density $\rho(r)$, which is the sum of the exchange and correlation contributions:

$$\varepsilon_{xc}^{hom}[\rho(r)] = \varepsilon_{x}^{hom}[\rho(r)] + \varepsilon_{c}^{hom}[\rho(r)] \quad (II.\ 85)$$

The term $\varepsilon_{x}^{hom}[\rho(r)]$ refer to the exchange part, while the $\varepsilon_{c}^{hom}[\rho(r)]$ refer to correlation part.

On the other hand, based on the equations $(II.84)$ and $(II.85)$ the exchange-correlation energy can written as the sum of exchange energy $E_{x}^{LDA}[\rho(r)]$ and correlation energy$E_{c}^{LDA}[\rho(r)]$:

$$E_{xc}^{LDA}[\rho(r)] = E_{x}^{LDA}[\rho(r)] + E_{c}^{LDA}[\rho(r)] \quad (II.\ 86)$$

The exchange energy $E_{x}^{LDA}[\rho(r)]$ was initially formulated by Bloch and Dirac in the late 1920 [29], and was later adapted by Slater [22] in his approximation to the Hartree-Fock exchange based on by the formulation [1,35]:

$$E_{x}^{LDA}[\rho(r)] = \int \rho(r)\varepsilon_{x}^{hom}[\rho(r)]dr = -\frac{3}{4}\left(\frac{3}{\pi}\right)^{\frac{1}{3}}\int \rho^{\frac{4}{3}}(r)dr \quad (II.\ 87)$$

Where:

$$\varepsilon_{x}^{hom}[\rho(r)] = -\frac{3}{4}\left(\frac{3}{\pi}\right)^{\frac{1}{3}}\rho^{\frac{1}{3}} \quad (II.\ 88)$$

The exchange potential $v_{x}^{LDA}[\rho(r)]$ in the Local Density Approximation (LDA) can be derived by taking the functional derivative of the exchange energy $E_{x}^{LDA}[\rho(r)]$ in equation (*II.87*), we get:

$$v_{x}^{LDA}[\rho(r)] = -\left(\frac{3}{\pi}\right)^{\frac{1}{3}}\rho^{\frac{1}{3}} \quad (II.\ 89)$$

In contrast to the exchange energy that can be expressed analytically in the Local Density Approximation (LDA) (equation $(II.87)$), the correlation energy does not have a simple and an exact analytical form. Instead, it is typically determined numerically for the homogeneous electron gas using advanced computational techniques such as Quantum Monte Carlo (QMC) [42,43] simulations. To make the correlation energy usable in practical DFT calculations, several parameterizations have been developed based on the QMC data. These parameterizations use mathematical forms, such as Hedin and Lundqvist (1971) [44], Padé approximations by Vosko, Wilk, and Nussair (1980) [45] ,Perdew-Zunger (1981) [46] and Perdew-Wang (1992) [47] .

In the preceding pragraphes we mentioned that the approximated wave functions are usually based on spatial coordinate and the spin coordinates, this brings us to the spin-polarized systems. Where the Local Density Approximation (LDA) is extended to the Local Spin Density

Approximation (LSDA) [35] to take into account the spin polarization of the electron density. In LSDA, the exchange-correlation functional is treated as a function of both the local electron density and the local spin density, which allows writing the exchange-correlation energy as follow:

$$E_{xc}^{LSDA}[\rho(r,\uparrow) + \rho(r,\downarrow)] = \int \rho(r)\varepsilon_{xc}^{hom}[\rho(r,\uparrow) + \rho(r,\downarrow)]dr \qquad (II.\ 90)$$

The term $\varepsilon_{xc}^{hom}[\rho(r,\uparrow) + \rho(r,\downarrow)]$ represents the exchange-correlation energy per particle for a spin-polarized, homogeneous electron gas, where $\rho(r,\uparrow)$ and $\rho(r,\downarrow)$ denote the densities of spin-up and spin-down electrons, respectively.

Despite the LDA broad use, it has several key drawbacks that can reduce its accuracy and predictive effectiveness across various applications. One significant deficiency of LDA is the substantial upshift in orbital energies it produces[48,49]. It also often fails to accurately describe the electronic structure of materials this underestimation can result in incorrect predictions regarding electronic properties [48] which is caused by its incapacity to capture the non-local effects of the exchange-correlation potential, and because of this also, it is unable to describe van der Waals interactions [50]. To address these deficiencies, various improvements and alternatives to LDA have been developed.

II.2.4.b. Generalized Gradient Approximations (GGA)

The ground state properties of many-electron systems can be determined using the exchange-correlation energy, initially approximated through the Local Density Approximation (LDA) from which the Local Spin Density Approximation (LSDA) was derived. Over time, LDA has been improved, first through the Density-Gradient Expansion (GEA), and further advanced to the generalized gradient approximation (GGA), which encompasses various forms.

II.2.4.b.1. Gradient-Expansion Approximation (GEA)

The GEA was initially developed by Kohn and Sham [34] based on the local density approximation (LDA), which involves introducing a weak and slowly varying external potential. This approach incorporates the density gradients of the form $|\nabla\rho(r)|, |\nabla\rho(r)|^2, |\nabla\rho(r)|^3, \ldots$, providing a more detailed representation of electron interactions in non-uniform systems. The general form of the gradient expansion for the exchange-correlation energy $E_x^{GEA}[\rho(r)]$ can be viewed as an infinite summation, their first terms are:

$$E_x^{\mathrm{GEA}}[\rho(r)] = E_x^{\mathrm{LDA}}[\rho(r)] + C_x^{(2)} \int_{R^3} \frac{|\nabla\rho(r)|^2}{\rho(r)^{4/3}} dr + C_{x,1}^{(4)} \int_{R^3} \frac{|\nabla^2\rho(r)|^2}{\rho(r)^2} dr +$$

$$C_{x,2}^{(4)} \int_{R^3} \frac{|\nabla\rho(r)|^2 \nabla^2\rho(r)}{\rho(r)^3} dr + \cdots \qquad (II.\ 91)$$

The information provided pertains to the coefficients in the context of the expansion of the exchange energy functional in terms of the electron density (r) , its gradient $|\nabla\rho(r)|$and its Laplacian $|\nabla\rho(r)|^2$,...,. These coefficients are crucial for understanding the corrections to the exchange energy in LDA. The Second-Order Coulombic Correction $C_x^{(2)}$ is estimated by W. Kohn and L. J. Sham [51] using the screened Yukawa interaction. His estimate was approximately $C_x^{(2)} \approx -0.001667$, However, later research found the correct value to be $C_x^{(2)} \approx -0.002382$[52] . The two fourth-order correction coefficients $C_{x,1}^{(4)}$ and $C_{x,2}^{(4)}$ have been approximated by P.S. Svendsen and U. von Barth as: $C_{x,1}^{(4)} \approx -0.000036$ and $C_{x,2}^{(4)} \approx 0.00009$. The coefficients $C_x^{(2)}$ and $C_{x,1}^{(4)}$ are also calculated by E. Visko [53,54] and confirmed later by other analytical calculations[52].

The gradient expansion approximation typically converges very slowly, especially when higher-order gradient terms are included. This is because the expansion is valid only when the density varies smoothly (i.e., when the gradients of the electron density are small). In regions where the electron density changes rapidly (e.g., near atomic cores or in the presence of steep density variations)[55–57], the higher-order terms become less accurate, thus make GEA provides less accurate results than LDA for real electronic systems, despite being theoretically more advanced. GEA can violate the physical requirement that the exchange-correlation hole must be negative, resulting in unphysical descriptions of electron interactions [58], It can also contravene the sum rule for the exchange-correlation hole, which is crucial for maintaining charge neutrality and accurate electron correlation descriptions [59]. The second-order gradient expansion (GEA2) does not always align with exact conditions or constraints for exchange-correlation energy functionals. This mismatch makes it less effective than generalized gradient approximations (GGAs), which are designed to better satisfy these constraints while maintaining computational efficiency[58].

II.2.4.b.2. Generalized Gradient Approximations (GGA)

The analysis of the GEA failure has lead some authors [60,61] to introduce a generalized gradient approximation, which based on both of LDA/LSDA and GEA approximations by including the gradient of the electron density, $\nabla\rho(r)$, as an additional factor in the functional. By

introducing this gradient correction, GGA functionals become semi-local, as it involve the values of ρ at (r) and in an infinitesimal neighborhood of (r), as a result, the exchange-correlation energy in GGAs is expressed as a function of both the electron density $\rho(r)$ and its gradient $\nabla\rho(r)$ as:

$$E_{xc}^{\mathrm{GGA}}[\rho(r),\nabla\rho(r)] = \int \rho(r)\varepsilon_{XC}^{GGA}[\rho(r),\nabla\rho(r)]dr \qquad (II.\ 92)$$

The energy functional within the GGA for systems with spin polarization takes into consideration the spin-up and spin-down electron densities can be expressed as follows[36]:

$$E_{xc}^{GGA}[\rho\uparrow,\rho\downarrow] = \int \rho(r)\varepsilon_{xc}^{GGA}[\rho\uparrow,\rho\downarrow,\nabla\rho\uparrow,\nabla\rho\downarrow]dr \qquad (II.\ 93)$$

Unlike LDA, which has a straightforward functional form, GGA lacks a universal expression. Instead, it is often represented with an enhancement factor $F(s)$, which modifies the LDA energy. This factor depends on the reduced gradient s, defined as:The general form of the GGA exchange-correlation functional can be expressed as[55]:

$$s = \frac{|\nabla\rho(r)|}{2k_F\rho(r)} = \frac{|\nabla\rho(r)|}{2(3\pi^2)^{\frac{1}{3}}\rho(r)^{4/3}} \qquad (II.\ 94)$$

Where $k_F = (3\pi^2 n)^{1/3}$ is the Fermi wave vector. The GGA energy can be expressed as[62]:

$$E_{xc}^{GGA}[\rho,s] = \int \rho(r)\varepsilon_{xc}^{LDA}[\rho(r)]F^{GGA}(s)dr \qquad (II.95)$$

The improvement factor $F(s)$ is often determined empirically or fitted to experimental data and physical constraints, since no simple functional form can describe the exchange-correlation energy in all situations accurately.

The goal of the enhancement factor is to correct the LDA approximation by incorporating the effects of density gradients and the non-locality of electron interactions, which is critical in more accurate simulations of materials and molecules in GGA-based density functional theory. Different GGA functionals use different forms of $F(s)$ (e.g., PBE, BLYP, PW91) leading to variations in their performance for different materials and molecules [61 - 62]. Below is a brief discussion of the enhancement factor in some popular GGA functionals.

a) PBE-GGA Exchange-Correlation Functional:

The Perdew Burke Ernzerhof (PBE) [63] exchange-correlation functional is a simplified version of the PW91 functional, designed to improve usability and computational efficiency while maintaining reasonable accuracy. Unlike PW91, which aimed to satisfy numerous exact conditions, PBE focuses on energetically significant conditions, making it less complex by using

fundamental constants for parameterization. This makes PBE simpler and more practical for a broad range of systems, leading to its widespread popularity in density functional theory (DFT) applications. The GGA-PBE energy can be expressed as:

$$E_{xc}^{PBE}[\rho(r)] = \int \rho(r)\ \varepsilon_{xc}^{PBE}\big(\rho(r), \nabla\rho(r)\big)\, dr \qquad (II.\ 96)$$

As we said previously, the exchange-correlation energy per electron Includes both of exchange part ε_x^{PBE} and correlation part ε_C^{PBE} introduced as [64]:

$$\varepsilon_x^{PBE} = \varepsilon_x^{LDA}\, F_x^{PBE}(s) \qquad (II.\ 97)$$

$$\varepsilon_c^{PBE} = \varepsilon_c^{LDA} + H(t) \qquad (II.\ 98)$$

The exchange part is written as an enhancement factor $F_x^{PBE}(s)$ multiplied on to the LSDA functional, where the dimension less gradient variable s is defined in equation [64]:

$$F_x^{PBE}(s) = 1 + \kappa - \frac{\kappa}{1+\frac{\mu}{\kappa}s^2} \qquad (II.\ 95)$$

For $s \cong 0$, $F_x^{PBE}(s)$ simplifies to the LDA form, ensuring consistency with the homogeneous electron gas limit [64]. For large s, $F_x^{PBE}(s)$ approaches a constant value determined by the parameter κ, ensuring compliance with the Lieb-Oxford bound on exchange-correlation energy [64], thus exhibit limitations when applied to solids, particularly due to the sharp cutoff in the exchange enhancement factor $F_x^{PBE}(s)$. Leading to an overestimated exchange energy for solids. This overestimation overlooks the electron's spread in space density characteristic of these materials. The sharp cutoff results in inaccuracies in predicting lattice constants and total energies, which are critical for modeling solid-state systems[65–67]. This is because the PBE functional is less effective at capturing the diffuse nature of electron density gradients in solids. Therefore, several modifications of PBE have been proposed [68] to address these .

The correlation part is similarly written as an enhancement factor $H(t)$ added to the LSDA functional, where the t variable is related to the s variable by means of yet another spin-polarization function[63,64]:

$$H(t) = c\phi^3 Ln\left[1 + dt^2\left(\frac{1+At^2}{1+At^2+A^2t^4}\right)\right] \qquad (II.\ 99)$$

$$A = d\left[exp\left(-\frac{\varepsilon_c^{LDA}}{c\phi^3}\right) - 1\right]^{-1} \qquad (II.\ 96)$$

$$\phi(\xi) = \frac{1}{2}\left[(1+\xi)^{2/3} + (1-\xi)^{2/3}\right] \qquad (II.\ 97)$$

$$t = \left[2(3\pi^2)^{1/3}\phi(\xi)\right]^{-1} s \qquad (II.\ 98)$$

The κ, μ, c and d are empirical parameters, where $\kappa = 0.804$ selected based on the Lieb-Oxford bound, ensuring that the enhancement factor remains physically meaningful across all density gradients and $\mu = 0.21951$ Chosen to maintain good linear response properties of LDA for a uniform electron gas under weak perturbations[68,69]. $\xi = {(\rho_\uparrow - \rho_\downarrow)}/{\rho}$ is the relative spin polarization, while $\phi(\xi)$ is a spin-scaling factor and t is a dimensionless density gradient [63].

b) WC-GGA Exchange-Correlation Functional:

The Wu-Cohen (WC-GGA) [70] exchange-correlation functional is a generalized gradient approximation (GGA) developed by Z. Wu and R. E. Cohen in 2006 was designed to address some of the limitations of PBE-GGA, particularly in describing lattice constants, crystal structures, and metal surface by modifies the exchange-correlation functional to include additional terms or parameters that improve its performance. This involves adjusting the enhancement factors presented in the equation (*II. 108*), which becomes:

$$F_s^{WC}(x) = 1 + \kappa - \frac{\kappa}{1+\frac{x}{\kappa}} \qquad (II.\ 99)$$

where $\kappa = 0.804$, is designed to smooth out the decay of the exchange functional in the limit of slowly varying density. It has been suggested the following ensatz for x :

$$x^{WC} = \left(\frac{10}{81}\right)s^2 + \left[\mu - \frac{10}{81}\right]s^2\, exp(-s^2) + ln(1 + cs^4) \qquad (II.\ 100)$$

With $\mu = 0.21951$ and $c = 0.0079325$ is set to recover the fourth order parameters in Equation (5) for small s[70].

WC-GGA typically provides lattice constants that are closer to experimental measurements compared to PBE or LDA[71]. When it comes to transition-metal surfaces, WC-GGA performs better than both PBE and LDA in predicting surface formation energies, making it especially suitable for metallic systems. While WC-GGA excels for solids and surfaces, it tends to be less accurate than PBE when it comes to predicting the energetics of covalent and noncovalent bonds in molecular systems [70,71]. For systems dominated by weak interactions, such as interlayer distances in graphite, WC-GGA is less reliable than LDA, which tends to overbind and is better at capturing these interactions [70,72].

c) PBEsol Exchange-Correlation Functional:

The PBEsol (PBE for solids) [73] exchange-correlation functional is a variant of the Perdew-Burke-Ernzerhof (PBE) functional, specifically optimized for solids and densely packed systems, It is designed to better describe lattice constants**,** bulk moduli**,** and surface energies for solid-state materials by correcting some of the shortcomings of the standard PBE functional when applied to solids. The PBEsol form for the exchange energy is simply:

$$E_x^{PBEsol}[\rho(r)] = \int d^3\, r\, \epsilon_x^{\text{unif}}\big(\rho(r)\big) F_x^{PBEsol}(s) \qquad (II.101)$$

The fundamental difference between PBE and PBEsol lies in the restoration of the gradient expansion (GE) in PBEsol, $\mu_{GE} \approx 0.1234$ is used. This adjustment is crucial for correctly accounting for the exchange energy in solids, treating them as systems with slowly varying electron densities. In contrast, PBE uses $\mu = 2\mu_{GE} \approx 0.21951$, which is more suitable for describing the exchange energy of free neutral atoms [74]. The parameter μ is related to the enhancement factor $F_x^{PBEsol}(s)$ of the given GGA, which, when recovering the uniform gas limit, takes the form of the corresponding expression [73]:

$$F_x^{PBEsol}(s) = 1 + \mu s^2 + \cdots \qquad \text{,as (s} \rightarrow 0 \text{)} \qquad (II.102)$$

On the other hand, the correlation energy component of PBEsol is represented by the following formula [73]:

$$E_c^{PBEsol}[\rho(r)] = \int d^3\, r\, \rho(r)\big[\epsilon_c^{\text{unif}}\big(n(r)\big) + \beta t^2(r) + \cdots\big] \qquad (II.103)$$

With $\beta = {}^{3\mu_{GE}}/_{\pi^2}$, should have $\beta = 0.0375$ according the value of μ_{GE}, by using $\beta = 0.046$ in the final PBEsol framework [74], t is a dimensionless density gradient $t = \frac{|\nabla\rho(r)|}{2k_{\text{TF}}\rho(r)}$, $k_{\text{TF}} = \sqrt{\frac{4k_F}{\pi}}$ is called the Thomas-Fermi screening wavevector, k_F is introduced in previous paragraphs.

d) EV-GGA Exchange-Correlation Functional:

The Engel-Vosko Generalized Gradient Approximation (EV-GGA) [75] exchange functional is a specialized exchange-only functional within the GGA framework of density functional theory (DFT). Most GGAs (like PBE) are constructed to improve total energies, but often fail to produce realistic potentials, which are crucial for band structure, ionization potentials,

electron densities in molecules and solids[75]. Therefore, the EV-GGA designed to optimize the potential for band structure calculations, particularly improving the accuracy of electronic band gaps. The energy for EV − GGA functional can be expressed as [75]:

$$E_{xc}^{EV-GGA}[\rho] = \int \rho(r)\ \epsilon_{xc}^{EV-GGA}\big(\rho(r), \nabla\rho(r)\big)\, dr \quad (II.104)$$

The EV-GGA exchange functional is formulated as:

$$E_{x}^{EV-GGA}[\rho] = \int \varepsilon_{x}^{LDA}[\rho] F^{EV-GGA}(x_\sigma) dr \quad (II.105)$$

Where the enhancement factor, central to EV-GGA, is defined as:

$$F^{EV-GGA}(x_\sigma) = \frac{1+a_1 x_\sigma + a_2 {x_\sigma}^2 + a_3 {x_\sigma}^3}{1+b_1 x_\sigma + b_2 {x_\sigma}^2 + b_3 {x_\sigma}^3} \quad (II.106)$$

Where: x_σ is the dimensionless density gradient symbolized as t in the previous paragraph, a_1, a_2, a_3, b_1, b_2 *and* b_3 are constants, which are equal to: $a_1 = 1.647127$, $a_2 = 0.980118$, $a_3 = 0.017399$, $b_1 = 1.523671$, $b_2 = 0.367229$, $b_3 = 0.011282$.

The Engel-Vosko Generalized Gradient Approximation (EV-GGA) is primarily designed to improve the exchange energy functional in density functional theory (DFT). It focuses on achieving better potential profiles, particularly for Kohn-Sham orbital energies, which are essential for electronic structure calculations. However, EV-GGA lacks a correlation functional, making it necessary to pair it with other generalized gradient approximation (GGA) correlation functional. This combination offers several advantages: Error cancellation between exchange and correlation components [76], improved band gap predictions in molecular and solid-state systems [75], better potential profiles leading to more accurate Kohn-Sham orbital energies which is particularly useful for electronic structure calculations and optical property predictions [77].

II.2.4.b.3. The Improved Modified Becke-Johnson (K-Mbj) Potential

Accurately predicting electronic band gaps remains a major challenge in density functional theory (DFT). The Becke-Johnson (BJ) exchange potential [78] offered a simple yet effective alternative to more complex orbital-dependent methods. However, its performance for solid-state systems especially semiconductors and insulators was limited. To address these shortcomings, Tran and Blaha introduced a modified version, known as the mBJ potential [79], which

significantly improved the results. This approach was further refined by Koller, Tran, and Blaha, leading to the development of the k-mBJ potential [80], which offers even better accuracy.

a) The Becke-Johnson (BJ) Potential:

Becke and Johnson (2006) proposed an optimized effective potential-like exchange potential, formulated solely in terms of on electron density and kinetic energy density to replicate the exact exchange potential in atoms and correct the energy gap values produced by LDA and GGA calculations. It avoids the computational complexity of two-electron integrals required in Hartree-Fock calculations. The BJ potential is formulated as [78]:

$$v_x^{BJ}(r) = v_x^{BR} + \frac{1}{\pi}\sqrt{\frac{5}{12}}\sqrt{\frac{2\tau(r)}{\rho(r)}} \qquad (II.\ 107)$$

Here,$\rho(r)$ denotes the electron density, τ(r) represents the kinetic energy density, and v_x^{BR} refers to the Becke-Roussel exchange potential, which is defined as [78]:

$$v_x^{BR} = -\left(\frac{8\pi\rho_\sigma}{x^3 e^{-x}}\right)^{1/3}\left(1 - e^{-x(r)} - \frac{1}{2}x(r)e^{-x(r)}\right) \qquad (II.\ 108)$$

b) Modified BJ (TB-mBJ) Potential:

Tran and Blaha (2009) introduced the modified BJ (TB-mBJ) potential[79] to enhance applicability in solid-state systems:

$$v_x^{TB-mBJ}(r) = cv_x^{BR} + (3c-2)\frac{1}{\pi}\sqrt{\frac{5}{12}}\sqrt{\frac{2\tau(r)}{\rho(r)}} \qquad (II.\ 109)$$

Here, v_x^{BR} is the Becke-Roussel potential, originally developed to model the Coulomb potential from the exchange hole. The parameter c is crucial and defined empirically as:

$$c = \alpha + \beta\sqrt{\frac{1}{V_{cell}}\int\frac{|\nabla\rho(r)|}{\rho(r)}dr} \qquad (II.\ 110)$$

In the equation (I. 130): $\alpha = -0.012$ (dimensionless) and $\beta = 1.023$ (Bohr)$^{1/2}$ as determined by Tran and Blah[79].

The TB-mBJ potential enhances band gap predictions but still falls short in accurately capturing the gaps for certain wide-gap insulators[80]. Its empirical basis restricts its applicability across different materials, with performance inconsistencies being particularly pronounced in transition-metal oxides[81].

c) Improved TB-mBJ by Koller et al. (KTB-mBJ):

Koller, Tran, and Blaha (2012) identified limitations in the TB-mBJ approach, especially for complex oxides and rare-gas solids. They reparametrized the coefficient c using a broader test set of materials, resulting in the improved TB-mBJ (KTB-mBJ)[80]:

$$c = \alpha + \beta\left(\frac{1}{V_{cell}}\int\frac{|\nabla\rho(r)|}{\rho(r)}dr\right)^{e} \quad (II.111)$$

Different parameter sets were optimized for varying material classes summarized in the ***Table II. 1*** [80]:

***Table II. 1**: KTB-mBJ potential parameters for different material classes*

Coefficient	α	$\beta(bohr^{1/2})$	e
P-original (TB-mBJ)	-0.012	1.023	0.5
P-present((balanced for all materials))	0.488	0.500	1.0
P-semiconductor (optimized for small/medium-gap semiconductors))	0.267	0.656	1.0

The proposed approach demonstrates several key improvements over existing methods. Notably, it achieves a more balanced performance across different classes of materials, including semiconductors, insulators, and transition-metal oxides [80,82]. This is accompanied by a statistically significant reduction in both mean absolute error and relative error in band gap predictions, all while maintaining a low computational cost [83]. However, certain limitations remain. In particular, the method tends to overestimate band gaps for specific ionic compounds such as NaF and LiF when operating in a semiconductor-optimized mode. Additionally, its performance is sensitive to the choice of the fitting data-set, indicating the absence of a universally applicable correction formula. Furthermore, the approach does not yield accurate results for strongly correlated systems unless supplemented with additional corrections [83].

II.2.4.b.4. Hybrid Functional

A hybrid exchange-correlation (XC) functional in Kohn–Sham density functional theory (KS-DFT) is a functional that mixes a fraction of exact exchange energy from Hartree–Fock (HF) theory into standard DFT functionals to enhance accuracy[84]. These functionals often outperform pure semi local ones (LDA, GGA, meta-GGA) particularly in systems where nonlocal exchange effects and the elimination of self-interaction errors are critical [84]. Hybrid density functionals,

first introduced by Axel D. Becke in 1993 [85], are theoretically justified by the adiabatic connection formalism in den approximations (GGAs). Becke proposed the following general form for a hybrid exchange-correlatsity functional theory (DFT). In this framework, a fraction of the exact exchange energy E_x^{HF}, derived from Hartree-Fock theory, is mixed with the exchange and correlation components from generalized gradiention functional[85]:

$$E_{xc}^{Hybrid} = E_{xc}^{LSDA} + a(E_x^{HF} - E_x^{LSDA}) + b\Delta E_x^{GGA} + c\Delta E_c^{GGA} \quad (II.\ 112)$$

Where:

- E_{xc}^{LSDA}: exchange-correlation energy from the local spin-density approximation,
- E_x^{HF}: exact Hartree-Fock exchange energy,
- ΔE_x^{GGA}: gradient correction to exchange (e.g., Becke 1988),
- ΔE_c^{GGA}: gradient correction to correlation (e.g., Perdew-Wang 1991),
- a, b, c: semi-empirical mixing parameters determined by fitting to experimental data. In Becke's 1993 formulation (Three parameters), these coefficients were optimized as: $a = 0.20$, $b = 0.72$ and $c = 0.81$

The typical hybrid functional has the form given in the equation *(II. 116)*, where a is the mixing coefficient (commonly 0.2–0.25):

$$E_{xc}^{Hybrid} = aE_x^{\text{exact}} + (1-a)E_x^{\text{GGA}} + E_c^{\text{GGA}} \quad (II.\ 113)$$

Among the most widely used hybrid functionals are B3LYP, PBE0, and HSE06, their key important informations represented in the ***Table II. 1:***

Table II. 1: Key Features for tha main Hybrid Functionals

Functional	Exchange	Correlation	Mixing Ratio a	Empirical Parameters
B3LYP[85]	HF + Becke88	LYP	0.20	3 fitted parameters
PBE0[86]	HF + PBE	PBE	0.25	No (parameter-free, derived from theory)
HSE06[87]	Screened HF + PBE	PBE	0.25 (short-range)	Semi-empirical

B3LYP (Becke, 3-parameter, Lee–Yang–Parr) is particularly popular in quantum chemistry due to its balance between accuracy and computational cost [85]. PBE0 (also known as PBE1PBE) integrates the Perdew–Burke–Ernzerhof (PBE) exchange-correlation with a fixed percentage of HF exchange, offering reliable performance for a broad range of systems [86]. HSE06 (Heyd–Scuseria–Ernzerhof) introduces a range-separation parameter to screen the

exchange interaction, making it suitable for solid-state systems where long-range interactions are significant [87].

Hybrid functionals systematically offer higher predictive accuracy for total energies, electron densities and ionization potentials (IPs) [100 - 101]. By incorporating exact Hartree-Fock exchange (E_x^{HF}): , hybrids significantly reduce self-interaction error, which is common in pure DFT functionals[90]. The better Treatment of the Kohn-Sham Derivative Discontinuity allows hybrid functionals to: partially correct the underestimated band gaps in semiconductors and better handle charge-transfer excitations[85,91].

II.3. Solving the Kohn–Sham equations

Solving the Kohn–Sham equations, as outlined in equation *(II. 79)*, is fundamental to density functional theory (DFT), allowing the determination of ground-state properties of many-electron systems. This is accomplished by representing the interacting system as non-interacting electrons moving within an effective potential. The core difficulty lies in the mutual dependence between the effective potential V_{eff} (from equation (*II.81*)) and the electron density $\rho(r)$, which requires a self-consistent field (SCF) approach (as shown in ***Figure II.3***) [92]. The process involves an iterative procedure that updates the wave functions and corresponding density until consistency between V_{eff} and $\rho(r)$ is achieved. Here's a step-by-step summary of how this self-consistent solution is obtained[93]:

- Initialization**:** Begin with atomic positions R_i and initial guess for the electron density $\rho^{ini}(r)$, typically constructed as a superposition of atomic charge densities.
- Construct the KS Hamiltonian using:

$$\widehat{H}_{KS}\phi_i = \varepsilon_i\phi_i \qquad (II.114)$$

With $\widehat{H}(r) = \left(-\frac{1}{2}\nabla^2 + \hat{V}_{eff}(\mathrm{r})\right)$ is Kohn-Sham Hamiltonian matrix

Using the initial guess electron density, compute the effective potential V_{eff} by evaluating three components: the external potential due to nuclear attraction, the Hartree potential V_H, which is obtained by solving Poisson's equation given in equation *(II.117)*, and the exchange-correlation potential V_{xc}, approximated using appropriate functionals such as LDA or GGA.

$$\nabla^2 V_H(r) = \frac{e}{\varepsilon_0}\rho(r) \qquad (II.115)$$

- Compute matrix elements of the Hamiltonian and overlap integrals:

$$H_{ij} = \int dr \phi_i(r) \left[-\frac{1}{2}\nabla^2 + V_{ext}(r) + V_H(r) + V_{xc}(r) \right] \phi_j(r) \quad (II.116)$$

$$S_{ij} = \int dr \phi_i^*(r)\, \phi_j(r) \quad (II.117)$$

- Solve the Kohn-Sham equations for each k-point in the Brillouin zone. This involves diagonalizing the Hamiltonian matrix to obtain eigenvalues ε_i and eigenvectors C_i

$$(H - \varepsilon S)C = 0 \quad (II.118)$$

- Compute Total Energy and New Density: Use the eigenvalues $\varepsilon_i^{(i)}$ and eigenfunctions $\phi_i^{(i)}$ to calculate the total energy of the system and a new electron density:

$$\phi_i(r) = \sum_j C_{ij}\, \phi_j(r) \quad (II.119)$$

$$\rho^{i+1}(r) = \sum_i^{occ} \left| \phi_i^i(r) \right|^2 \quad (II.120)$$

- Repeat Iterations in each iteration of the self-consistent cycle, the trial electron density is updated using a mixing scheme:

$$\rho^{new}(r) = (1 - \alpha)\rho^i + \alpha \rho^{i+1} \quad (II.121)$$

where: ρ^i is the density from the previous iteration, ρ^{i+1} is the newly computed density and α is the mixing parameter (typically $0 < \alpha < 1$).

This process is repeated until convergence is achieved, i.e., both of the following conditions are satisfied:

$$E^{i+1} - E^i < \epsilon \quad (II.122)$$

$$\rho^{i+1} - \rho^i < \eta \quad (II.123)$$

Where: ϵ is the energy convergence threshold, η is the density convergence threshold.

If the convergence criteria are not satisfied, the charge density is updated, and the procedure is repeated from Step 2. Once convergence is achieved, the final Kohn-Sham eigenvaluesε_i, orbitals ϕ_i, and electron density $\rho(r)$ are used to calculate the physical observables."

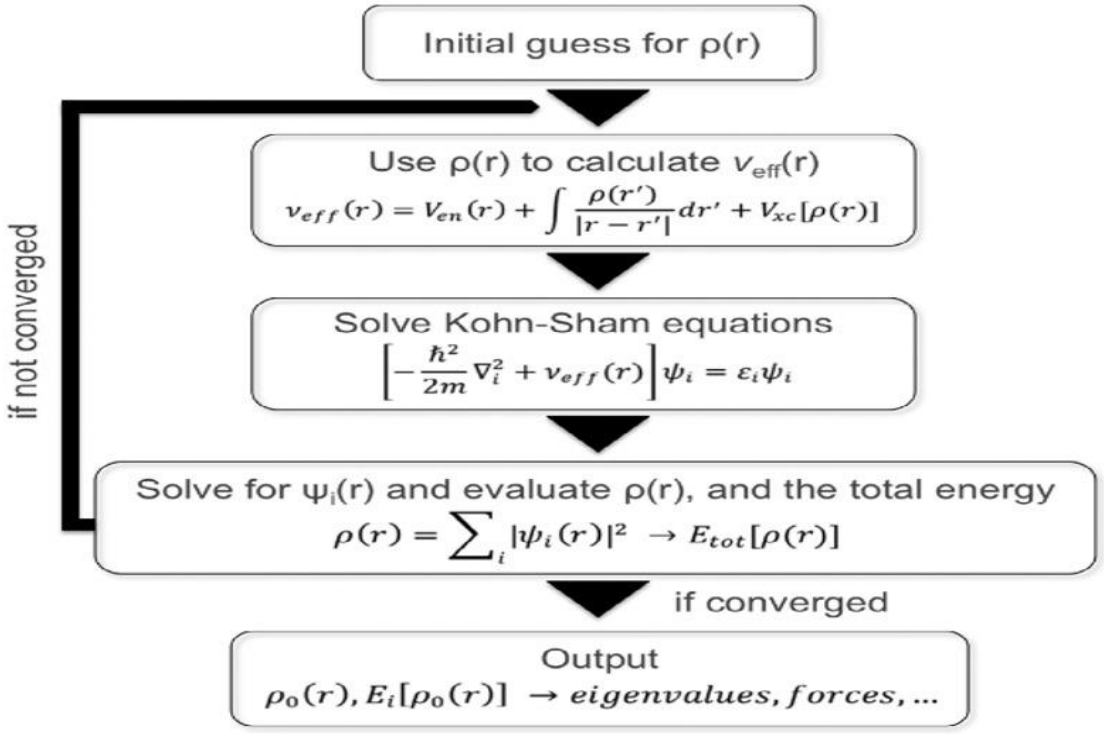


Figure II.3: ***Self-Consistent Kohn–Sham Density Functional Theory (DFT) Workflow***

References:

[1] F. Giustino, Materials modelling using density functional theory: properties and predictions, 1st ed, Oxford University Press, Oxford, 2014.
[2] E. Engel, Density Functional Theory: An Advanced Course, Springer Berlin / Heidelberg, Berlin, Heidelberg, 2011.
[3] L.H. Thomas, The calculation of atomic fields, Math. Proc. Camb. Philos. Soc. 23 (1927) 542–548. https://doi.org/10.1017/S0305004100011683.
[4] E. Fermi, Statistical method to determine some properties of atoms, (n.d.).
[5] P.A.M. Dirac, Note on Exchange Phenomena in the Thomas Atom, Math. Proc. Camb. Philos. Soc. 26 (1930) 376–385. https://doi.org/10.1017/S0305004100016108.
[6] P. Hohenberg, W. Kohn, Inhomogeneous Electron Gas, Phys. Rev. 136 (1964) B864–B871. https://doi.org/10.1103/PhysRev.136.B864.
[7] W. Kohn, L.J. Sham, Self-Consistent Equations Including Exchange and Correlation Effects, Phys. Rev. 140 (1965) A1133–A1138. https://doi.org/10.1103/PhysRev.140.A1133.
[8] R.O. Jones, O. Gunnarsson, The density functional formalism, its applications and prospects, Rev. Mod. Phys. 61 (1989) 689–746. https://doi.org/10.1103/RevModPhys.61.689.
[9] J.P. Perdew, K. Burke, M. Ernzerhof, Generalized Gradient Approximation Made Simple, Phys. Rev. Lett. 77 (1996) 3865–3868. https://doi.org/10.1103/PhysRevLett.77.3865.
[10] J. Tao, J.P. Perdew, V.N. Staroverov, G.E. Scuseria, Climbing the Density Functional Ladder: Non-Empirical Meta-Generalized Gradient Approximation Designed for Molecules and Solids, (2003). http://arxiv.org/abs/cond-mat/0306203 (accessed October 28, 2024).
[11] J. Heyd, G.E. Scuseria, M. Ernzerhof, Hybrid functionals based on a screened Coulomb potential, J. Chem. Phys. 118 (2003) 8207–8215. https://doi.org/10.1063/1.1564060.
[12] C. Adamo, V. Barone, Toward reliable density functional methods without adjustable parameters: The PBE0 model, J. Chem. Phys. 110 (1999) 6158–6170. https://doi.org/10.1063/1.478522.
[13] N. Manini, T. Coleman, Thomas-Fermi model for diatomic molecules, (n.d.).
[14] A. Zangwill, A half century of density functional theory, Phys. Today 68 (2015) 34–39. https://doi.org/10.1063/PT.3.2846.
[15] M. Born, R. Oppenheimer, Zur Quantentheorie der Molekeln, Ann. Phys. 389 (1927) 457–484. https://doi.org/10.1002/andp.19273892002.
[16] Szabo, Attila, and Neil S. Ostlund. Modern quantum chemistry: introduction to advanced electronic structure theory. Courier Corporation, 2012.
[17] I.G. Kaplan, The Pauli Exclusion Principle and the Problems of Its Experimental Verification, Symmetry 12 (2020) 320. https://doi.org/10.3390/sym12020320.
[18] D.R. Hartree, The Wave Mechanics of an Atom with a Non-Coulomb Central Field. Part I. Theory and Methods, Math. Proc. Camb. Philos. Soc. 24 (1928) 89–110. https://doi.org/10.1017/S0305004100011919.
[19] Lee, June Gunn. Computational materials science: an introduction. CRC press, 2016.
[20] Seminario - Ramon - O metodo de Hartree-Fock.pdf, (n.d.). https://www.ifsc.usp.br/~strontium/Teaching/Material2014-1%20SFI5774%20Mecanicaquantica/Seminario%20-%20Ramon%20-%20O%20metodo%20de%20Hartree-Fock.pdf (accessed November 15, 2024).
[21] V. Fock, N�herungsmethode zur L�sung des quantenmechanischen Mehrk�rperproblems, Z. F�r Phys. 61 (1930) 126–148. https://doi.org/10.1007/BF01340294.

[22] J.C. Slater, The Theory of Complex Spectra, Phys. Rev. 34 (1929) 1293–1322. https://doi.org/10.1103/PhysRev.34.1293.
[23] M.K. Harbola, A. Banerjee, Many-Electron Problem in Terms of the Density: From Thomas–Fermi to Modern Density-Functional Theory, J. Theor. Comput. Chem. 02 (2003) 301–322. https://doi.org/10.1142/S021963360300046X.
[24] V.I. Arnold, Variational principles, in: V.I. Arnold (Ed.), Math. Methods Class. Mech., Springer, New York, NY, 1978: pp. 55–74. https://doi.org/10.1007/978-1-4757-1693-1_3.
[25] N.M. Harrison, An Introduction to Density Functional Theory, (n.d.).
[26] J.C. Phillips, Generalized Koopmans' Theorem, Phys. Rev. 123 (1961) 420–424. https://doi.org/10.1103/PhysRev.123.420.
[27] L.H. Thomas, The calculation of atomic fields, Math. Proc. Camb. Philos. Soc. 23 (1927) 542–548. https://doi.org/10.1017/S0305004100011683.
[28] E. Fermi, Eine statistische Methode zur Bestimmung einiger Eigenschaften des Atoms und ihre Anwendung auf die Theorie des periodischen Systems der Elemente, Z. F�r Phys. 48 (1928) 73–79. https://doi.org/10.1007/BF01351576.
[29] P.A.M. Dirac, Note on Exchange Phenomena in the Thomas Atom, Math. Proc. Camb. Philos. Soc. 26 (1930) 376–385. https://doi.org/10.1017/S0305004100016108.
[30] Quantum Mechanic Dr. Fadhela Muhammad, (n.d.).
[31] C.F.V. Weizs�cker, Zur Theorie der Kernmassen, Z. F�r Phys. 96 (1935) 431–458. https://doi.org/10.1007/BF01337700.
[32] D. Feil, The molecular electron density distribution. Meeting place of X-ray diffraction and quantum chemistry intermediate between theory and experiment, J. Mol. Struct. THEOCHEM 255 (1992) 221–239. https://doi.org/10.1016/0166-1280(92)85012-A.
[33] P. Hohenberg, W. Kohn, Inhomogeneous Electron Gas, Phys. Rev. 136 (1964) B864–B871. https://doi.org/10.1103/PhysRev.136.B864.
[34] W. Kohn, L.J. Sham, Self-Consistent Equations Including Exchange and Correlation Effects, Phys. Rev. 140 (1965) A1133–A1138. https://doi.org/10.1103/PhysRev.140.A1133.
[35] W. Koch, M.C. Holthausen, A Chemist's Guide to Density Functional Theory, 1st ed., Wiley, 2001. https://doi.org/10.1002/3527600043.
[36] I.N. Levine, Quantum chemistry, Seventh edition, Pearson, Boston Columbus Indianapolis New York San Francisco Upper Saddle River Amsterdam Cape Town Dubai London, 2014.
[37] P.W. Atkins, R. Friedman, Molecular quantum mechanics, 4th ed, Oxford University Press, New York, 2005.
[38] R. Cuevas-Saavedra, V.N. Staroverov, Exact expressions for the Kohn–Sham exchange-correlation potential in terms of wave-function-based quantities, Mol. Phys. 114 (2016) 1050–1058. https://doi.org/10.1080/00268976.2015.1131861.
[39] I. Hargittai, Walter Kohn Centennial—Nobel laureate for density functional theory, Struct. Chem. 34 (2023) 2375–2377. https://doi.org/10.1007/s11224-023-02147-7.
[40] F. Brockherde, L. Vogt, L. Li, M.E. Tuckerman, K. Burke, K.-R. Müller, Bypassing the Kohn-Sham equations with machine learning, Nat. Commun. 8 (2017) 872. https://doi.org/10.1038/s41467-017-00839-3.
[41] C. Fiolhais, F. Nogueira, M.A.L. Marques, eds., A Primer in Density Functional Theory, Springer Berlin Heidelberg, Berlin, Heidelberg, 2003. https://doi.org/10.1007/3-540-37072-2.

[42] M. Morales, R. Clay, C. Pierleoni, D. Ceperley, First Principles Methods: A Perspective from Quantum Monte Carlo, Entropy 16 (2013) 287–321. https://doi.org/10.3390/e16010287.
[43] B. Stojanovicˇ, LOCAL DENSITY APPROXIMATION OF SPHERICALLY SYMMETRIC ATOMIC GROUND STATES, (2020).
[44] L. Hedin, B.I. Lundqvist, Explicit local exchange-correlation potentials, J. Phys. C Solid State Phys. 4 (1971) 2064–2083. https://doi.org/10.1088/0022-3719/4/14/022.
[45] Vosko, S.H., Wilk, L. and Nusair, M. (1980) Accurate Spin-Dependent Electron Liquid Correlation Energies for Local Spin Density Calculations A Critical Analysis. Canadian Journal of Physics, 58, 1200-1211. - References - Scientific Research Publishing, (n.d.). https://www.scirp.org/reference/referencespapers?referenceid=2770335 (accessed January 17, 2025).
[46] J.P. Perdew, A. Zunger, Self-interaction correction to density-functional approximations for many-electron systems, Phys. Rev. B 23 (1981) 5048–5079. https://doi.org/10.1103/PhysRevB.23.5048.
[47] J.P. Perdew, Y. Wang, Accurate and simple analytic representation of the electron-gas correlation energy, Phys. Rev. B 45 (1992) 13244–13249. https://doi.org/10.1103/PhysRevB.45.13244.
[48] J. Toulouse, Review of approximations for the exchange-correlation energy in density-functional theory, (2022). https://doi.org/10.48550/arXiv.2103.02645.
[49] O.V. Gritsenko, Ł.M. Mentel, E.J. Baerends, On the errors of local density (LDA) and generalized gradient (GGA) approximations to the Kohn-Sham potential and orbital energies, J. Chem. Phys. 144 (2016) 204114. https://doi.org/10.1063/1.4950877.
[50] A. Van De Walle, G. Ceder, Correcting overbinding in local-density-approximation calculations, Phys. Rev. B 59 (1999) 14992–15001. https://doi.org/10.1103/PhysRevB.59.14992.
[51] L.J. Sham, Approximations of the Exchange and Correlation Potentials, in: P.M. Marcus, J.F. Janak, A.R. Williams (Eds.), Comput. Methods Band Theory Proc. Conf. Held IBM Thomas J Watson Res. Cent. Yorktown Heights N. Y. May 14–15 1970 Jt. Spons. IBM Am. Phys. Soc., Springer US, Boston, MA, 1971: pp. 458–468. https://doi.org/10.1007/978-1-4684-1890-3_36.
[52] P.S. Svendsen, U. Von Barth, Gradient expansion of the exchange energy from second-order density response theory, Phys. Rev. B 54 (1996) 17402–17413. https://doi.org/10.1103/PhysRevB.54.17402.
[53] E. Engel, S.H. Vosko, Wave-vector dependence of the exchange contribution to the electron-gas response functions: An analytic derivation, Phys. Rev. B 42 (1990) 4940–4953. https://doi.org/10.1103/PhysRevB.42.4940.
[54] E. Engel, S.H. Vosko, Erratum: Wave-vector dependence of the exchange contribution to the electron-gas response functions: An analytic derivation, Phys. Rev. B 44 (1991) 1446–1446. https://doi.org/10.1103/PhysRevB.44.1446.
[55] C. Filippi, X. Gonze, C.J. Umrigar, Generalized gradient approximations to density functional theory: comparison with exact results, in: Theor. Comput. Chem., Elsevier, 1996: pp. 295–326. https://doi.org/10.1016/S1380-7323(96)80090-2.
[56] A.-R.E. Mohammed, V. Sahni, Density-functional-theory gradient expansion approximation for the screened-Coulomb exchange energy, Phys. Rev. B 29 (1984) 3687–3690. https://doi.org/10.1103/PhysRevB.29.3687.

[57] The Convergence Problem Of Gradient Expansion In The Relaxation Time Approximation, (n.d.). https://arxiv.org/html/2405.10846v2 (accessed January 20, 2025).
[58] J.P. Perdew, K. Burke, Comparison shopping for a gradient-corrected density functional, Int. J. Quantum Chem. 57 (1996) 309–319. https://doi.org/10.1002/(SICI)1097-461X(1996)57:3%253C309::AID-QUA4%253E3.0.CO;2-1.
[59] K.J. Daas, D.P. Kooi, A.J.A.F. Grooteman, M. Seidl, P. Gori-Giorgi, Gradient Expansions for the Large-Coupling Strength Limit of the Møller–Plesset Adiabatic Connection, J. Chem. Theory Comput. 18 (2022) 1584–1594. https://doi.org/10.1021/acs.jctc.1c01206.
[60] D.C. Langreth, M.J. Mehl, Beyond the local-density approximation in calculations of ground-state electronic properties, Phys. Rev. B 28 (1983) 1809–1834. https://doi.org/10.1103/PhysRevB.28.1809.
[61] J.P. Perdew, J.A. Chevary, S.H. Vosko, K.A. Jackson, M.R. Pederson, D.J. Singh, C. Fiolhais, Atoms, molecules, solids, and surfaces: Applications of the generalized gradient approximation for exchange and correlation, Phys. Rev. B 46 (1992) 6671–6687. https://doi.org/10.1103/PhysRevB.46.6671.
[62] Computational Materials Science | An Introduction, Second Edition | Ju, (n.d.). https://www.taylorfrancis.com/books/mono/10.1201/9781315368429/computational-materials-science-june-gunn-lee (accessed January 26, 2025).
[63] J.P. Perdew, K. Burke, M. Ernzerhof, Generalized Gradient Approximation Made Simple, Phys. Rev. Lett. 77 (1996) 3865–3868. https://doi.org/10.1103/PhysRevLett.77.3865.
[64] F. Jensen, Introduction to computational chemistry, John wiley & sons, 2017.
[65] G. Santra, J.M.L. Martin, What Types of Chemical Problems Benefit from Density-Corrected DFT? A Probe Using an Extensive and Chemically Diverse Test Suite, J. Chem. Theory Comput. 17 (2021) 1368–1379. https://doi.org/10.1021/acs.jctc.0c01055.
[66] R. Liu, D. Zheng, X. Liang, X. Ren, M. Chen, W. Li, Implementation of the meta-GGA exchange-correlation functional in numerical atomic orbital basis: With systematic testing on SCAN, rSCAN, and r2SCAN functionals, J. Chem. Phys. 159 (2023) 074109. https://doi.org/10.1063/5.0160726.
[67] L. Li, K. Trepte, K.A. Jackson, J.K. Johnson, Application of Self-Interaction Corrected Density Functional Theory to Early, Middle, and Late Transition States, J. Phys. Chem. A 124 (2020) 8223–8234. https://doi.org/10.1021/acs.jpca.0c06485.
[68] G.K.H. Madsen, Functional form of the generalized gradient approximation for exchange: The PBE$α$ functional, Phys. Rev. B 75 (2007) 195108. https://doi.org/10.1103/PhysRevB.75.195108.
[69] J. Garhammer, F. Hofmann, R. Armiento, S. Kümmel, On the challenge to improve the density response with unusual gradient approximations, Eur. Phys. J. B 91 (2018) 159. https://doi.org/10.1140/epjb/e2018-90119-4.
[70] Z. Wu, R.E. Cohen, A More Accurate Generalized Gradient Approximation for Solids, (2006). https://doi.org/10.1103/PhysRevB.73.235116.
[71] F. Tran, R. Laskowski, P. Blaha, K. Schwarz, Performance on molecules, surfaces, and solids of the Wu-Cohen GGA exchange-correlation energy functional, Phys. Rev. B 75 (2007) 115131. https://doi.org/10.1103/PhysRevB.75.115131.
[72] P. Haas, F. Tran, P. Blaha, K. Schwarz, Construction of an optimal GGA functional for molecules and solids, Phys. Rev. B 83 (2011) 205117. https://doi.org/10.1103/PhysRevB.83.205117.

[73] J.P. Perdew, A. Ruzsinszky, G.I. Csonka, O.A. Vydrov, G.E. Scuseria, L.A. Constantin, X. Zhou, K. Burke, Restoring the Density-Gradient Expansion for Exchange in Solids and Surfaces, Phys. Rev. Lett. 100 (2008) 136406. https://doi.org/10.1103/PhysRevLett.100.136406.
[74] L. Vega, F. Viñes, Generalized gradient approximation adjusted to transition metals properties: Key roles of exchange and local spin density, J. Comput. Chem. 41 (2020) 2598–2603. https://doi.org/10.1002/jcc.26415.
[75] E. Engel, S.H. Vosko, Exact exchange-only potentials and the virial relation as microscopic criteria for generalized gradient approximations, Phys. Rev. B 47 (1993) 13164–13174. https://doi.org/10.1103/PhysRevB.47.13164.
[76] R. Peverati, D.G. Truhlar, Exchange–Correlation Functional with Good Accuracy for Both Structural and Energetic Properties while Depending Only on the Density and Its Gradient, J. Chem. Theory Comput. 8 (2012) 2310–2319. https://doi.org/10.1021/ct3002656.
[77] E. Engel, J.A. Chevary, L.D. Macdonald, S.H. Vosko, Asymptotic properties of the exchange energy density and the exchange potential of finite systems: relevance for generalized gradient approximations, Z. Für Phys. At. Mol. Clust. 23 (1992) 7–14. https://doi.org/10.1007/BF01436696.
[78] A.D. Becke, E.R. Johnson, A simple effective potential for exchange, (n.d.).
[79] F. Tran, P. Blaha, Accurate Band Gaps of Semiconductors and Insulators with a Semilocal Exchange-Correlation Potential, (2009).
[80] D. Koller, F. Tran, P. Blaha, Improving the modified Becke-Johnson exchange potential, (2012).
[81] D. Koller, F. Tran, P. Blaha, Merits and limits of the modified Becke-Johnson exchange potential, Phys. Rev. B 83 (2011) 195134. https://doi.org/10.1103/PhysRevB.83.195134.
[82] M.S. Halati, O.Y. Khyzhun, A. Khireddine, M. Piasecki, I. Radkowska, K.H. Cherif, Z. Lounis, Y. Caudano, A. Bedjaoui, A. Alghamdi, P. Paramasivam, C. Prakash, S.S.M. Ghoneim, Structural, elastic, electronic, optical and anisotropy properties of newly quaternary Tl2HgGeSe4 via DFPT predictions associated to XPES and RS experiments, Sci. Rep. 14 (2024) 16293. https://doi.org/10.1038/s41598-024-67231-2.
[83] R.A. Jishi, O.B. Ta, A.A. Sharif, Modeling of Lead Halide Perovskites for Photovoltaic Applications, (2014). https://doi.org/10.48550/arXiv.1405.1706.
[84] A.V. Arbuznikov, Hybrid exchange correlation functionals and potentials: Concept elaboration, J. Struct. Chem. 48 (2007) S1–S31. https://doi.org/10.1007/s10947-007-0147-0.
[85] A.D. Becke, Density-functional thermochemistry. III. The role of exact exchange, J. Chem. Phys. 98 (1993) 5648–5652. https://doi.org/10.1063/1.464913.
[86] C. Adamo, V. Barone, Toward reliable density functional methods without adjustable parameters: The PBE0 model, J. Chem. Phys. 110 (1999) 6158–6170. https://doi.org/10.1063/1.478522.
[87] J. Heyd, G.E. Scuseria, M. Ernzerhof, Hybrid functionals based on a screened Coulomb potential, J. Chem. Phys. 118 (2003) 8207–8215. https://doi.org/10.1063/1.1564060.
[88] N. Mardirossian, M. Head-Gordon, Thirty years of density functional theory in computational chemistry: an overview and extensive assessment of 200 density functionals, Mol. Phys. 115 (2017) 2315–2372. https://doi.org/10.1080/00268976.2017.1333644.
[89] J.P. Perdew, Jacob's ladder of density functional approximations for the exchange-correlation energy, in: AIP Conf. Proc., AIP, Antwerp (Belgium), 2001: pp. 1–20. https://doi.org/10.1063/1.1390175.

[90] T. Stein, H. Eisenberg, L. Kronik, R. Baer, Fundamental gaps of finite systems from the eigenvalues of a generalized Kohn-Sham method, (n.d.).
[91] A. Dreuw, M. Head-Gordon, Failure of Time-Dependent Density Functional Theory for Long-Range Charge-Transfer Excited States: The Zincbacteriochlorin−Bacteriochlorin and Bacteriochlorophyll−Spheroidene Complexes, J. Am. Chem. Soc. 126 (2004) 4007–4016. https://doi.org/10.1021/ja039556n.
[92] Martin, Richard M. Electronic structure: basic theory and practical methods. Cambridge university press, 2020.
[93] F. Bechstedt, Kohn-Sham Scheme, in: Many-Body Approach Electron. Excit., Springer Berlin Heidelberg, Berlin, Heidelberg, 2015: pp. 89–104. https://doi.org/10.1007/978-3-662-44593-8_6.

Chapter III:

Full Potential Linearized Augmented Plane Wave method

III.1. Introduction

In the previous chapter, we simplified the complex many-body problem of interacting electrons and nuclei using the Born–Oppenheimer approximation and Density Functional Theory (DFT). This led to a system of non-interacting particles moving in an effective potential created by fixed nuclei, as described by the Kohn–Sham equations. To apply the Kohn–Sham formalism to extended systems—such as solids or crystalline liquids—a practical numerical scheme becomes essential. These systems contain an infinite number of non-interacting electrons in the static potential field generated by an infinite array of nuclei or ions. This introduces two major challenges: first, the necessity to compute a wave function for each electron in an infinite system; and second, the extended nature of these wave functions, which span the entire crystal lattice. Consequently, the Schrödinger equation must be reformulated as an algebraic equation for the expansion coefficients, requiring a complete basis set for accurate representation.

As a result, analytic solutions become impossible, and the problem must be reformulated using a computer-friendly basis set—most commonly is Full Potential Linearized Augmented Plane Wave (FP-LAPW) method .

The Full-Potential Linearized Augmented Plane Wave (FP-LAPW) method has its origins in the Augmented Plane Wave (APW) method introduced by J.C. Slater in 1937 [1]. This early formulation marked one of the first efforts to solve the Schrödinger equation in periodic potentials using a combined plane-wave and atomic-like basis. In the 1970s, the method was extended by O.K. Andersen through the introduction of the Linearized Augmented Plane Wave (LAPW) approach, which involved a linearization procedure applied to the radial basis functions [2]. In the 1980s and 1990s, further developments were made by E. Wimmer, H. Krakauer, M. Weinert, and D.J. Singh, who formulated (FP-LAPW) method which demonstrate their power and accuracy primarily through a series of calculations involving surface and electronic structures[3,4]. Later, additional refinements led to the development of the LAPW with local orbitals (LAPW+lo), designed to enrich the basis set with localized functions[5]. A parallel development followed with the Augmented Plane Wave plus local orbitals (APW+lo) method, introduced in the early 2000s, offering another route to improve basis completeness[6].

This chapter provides an overview of the evolution of these computational methods in electronic structure calculations—from the original APW method to the modern FP-LAPW approach. It outlines the

theoretical foundations, strengths, and limitations of each method and introduces the WIEN2k software for FP-LAPW-based calculations. Additionally, it covers the use of plane-wave basis sets in periodic systems, the application of Bloch's theorem, and the development of methods to simplify the treatment of core electron interactions.

III.2. Plane-Waves

Plane waves are a natural choice for representing electronic wave functions in periodic systems for many reasons:

III.2.1. Translational Symmetry in Crystals

Crystals are defined by a repeating, periodic arrangement of unit cell, each unit cell may contain one or multiple atoms or molecules. This periodicity can be described by a lattice of points that remains invariant under translations, known as Bravais lattices. The position vector $\vec{R}$ of any lattice point must satisfy the condition[7]:

$$\vec{R} = n_1\vec{a}_1 + n_2\vec{a}_2 + n_3\vec{a}_3 \qquad (III.\ 1)$$

Where n_1, n_2 and $n_3 \in \mathbb{Z}$ (i.e., integers), and $\vec{a}_1$, $\vec{a}_2$ and $\vec{a}_3$ are the primitive lattice vectors that span the 3D unit cell of volume:

$$\Omega = \vec{a}_1(\vec{a}_2 \times \vec{a}_3) \qquad (III.\ 2)$$

This periodicity leads to many important physical consequences. One of them is that the effective potential V_{eff}^{KS} in the Kohn-Sham equations unchanged under translations by a Bravais lattice vector, thus can reduce the computational cost for solving the Kohn–Sham equations[7]:

$$V_{eff}^{KS}(r) = V_{eff}^{KS}(r + R) \qquad (III.\ 3)$$

The periodic nature of $V_{eff}^{KS}(r)$ also implies that the potential may be expressed as a Fourier series[8]:

$$V_{eff}^{KS}(r) = \sum_G V_{eff}(G)e^{iGr} \qquad (III.\ 4)$$

Where the G are a set of vectors, $e^{iGT} = 1\ ; i.e.\ G.R = 2\pi p$ with p is an integer number and the $V_{eff}(G)$ are Fourier coefficients introduced as[8]:

$$V_{eff}(G) = \frac{1}{\Omega}\int V_{eff}(r)e^{-iGr}d^3r \qquad (III.\ 5)$$

This invariance for effective potential V_{eff}^{KS} in the Kohn-Sham equations is fundamental to the derivation of Bloch's theorem and the resulting band structure of solids.

III.2.2. Bloch's Theorem:

Bloch's theorem is a cornerstone of condensed matter physics, providing a fundamental description of electron wavefunctions in crystalline solids. It states that the solutions to the Schrödinger equation for electrons moving in a periodic potential must be expressed as plane waves modulated by functions with the periodicity of the crystal lattice, meaning the wavefunction changes by only a phase factor upon lattice translation[9]. The eigenfunctions $\psi_{n,k}(r)$ of the single-electron Hamiltonian can be chosen to have the form[9]:

$$\psi_{n,k}(r) = e^{ikr}u_{n,k}(r) \qquad \textit{(III. 6)}$$

Therefore, the result *(III.6)* expresses the Bloch theorem: the eigenfunctions of the wave equation for a periodic potential are the product of a plane wave e^{ikr} times a function $u_{n,k}(r)$ with the periodicity of the crystal lattice.

Here, k is the crystal wavevector, usually restricted to the first Brillouin zone and n is the band index. Each value of k corresponds to multiple allowed energy levels due to the periodic potential of the crystal, these levels are organized into bands and each one is labeled by a discrete index n ($n = 1$: lowest (first) energy band, $n = 2$: second band, possibly overlapping with or separated by a gap from the first, $n = 3,4,5,\ldots$: higher energy bands, which may be unoccupied at zero temperature)[9].

The $u_k(r)$ is a non-degenerate function with the same periodicity as the lattice[10]:

$$u_{n,k}(r + R) = u_{n,k}(r) \qquad \textit{(III. 7)}$$

Where the periodic part $u_{n,k}(r)$ can itself be expanded in terms of plane waves:

$$u_{n,k}(r) = \sum_G C_G^{n,k}(G)e^{iGr} \qquad \textit{(III. 8)}$$

Here, $C_G^{n,k}(G)$ are the expansion coefficients. Thus, the total Bloch wavefunction becomes[10]:

$$\psi_{n,K}(r) = \sum_G C_G^{n,k}(G)e^{iKr} \qquad \textit{(III. 9)}$$

Where $K = k + G$ is the total wavevector, where k lies within the first Brillouin zone and G are reciprocal lattice vectors. This defines the plane-wave basis used to expand the electronic states. Since an infinite number of reciprocal lattice vectors G exist, an infinite number of plane waves would be required in principle[4].

However, in practical computations, including an infinite number of plane waves is not feasible due to limitations in memory and computational power. To address this, a restriction is imposed: 'Only plane

waves with kinetic energy below a certain threshold are retained'[10]. This is enforced by introducing a cut-off energy E_{cut}:

$$E_{cut} = \frac{\hbar^2}{2m} K_{max}^2 \qquad (III.\ 10)$$

Only wave vectors K that satisfy: $|K|^2 \leq K_{max}^2$ are included in the basis. Geometrically, this corresponds to all reciprocal lattice vectors that lie within a sphere of radius K_{max} centered at the origin of reciprocal space[9,10].

The cut-off energy E_{cut} plays a crucial role in determining the accuracy and computational cost of plane-wave-based simulations. A higher E_{cut}t allows more plane waves to be included in the basis set, leading to a more accurate representation of the $\psi_{n,K}(r)$. However, the improved accuracy is achieved at the expense of increased computational cost. [11]. In practical simulations, convergence tests are performed by gradually increasing E_{cut}until key quantities such as total energy or atomic forces stabilize within acceptable limits[12]. The optimal cut-off energy can vary significantly depending on the material system. For instance, materials with rapidly varying potentials—such as those containing transition metals generally require higher E_{cut} values to achieve convergence[12].

III.2.3. Sampling the Brillouin-zone and K-points:

The first Brillouin Zone (BZ) is a uniquely defined primitive cell in the reciprocal space of a crystal lattice; this dual space arises from the Fourier transform of the real lattice, simplifying the problem to constructing a mesh of allowed wave vectors that reflect the periodicity of the crystal lattice. The BZ can be thought of as the Wigner-Seitz cell in reciprocal space and contains all the unique information about wave vectors needed for analyzing periodic systems, as a results electronic properties—such as total energy, charge density, and band structure—are expressed as integrals over the BZ[13]. To reduce computational effort without sacrificing accuracy, the first BZ is further reduced to the irreducible Brillouin zone (IBZ) by applying symmetry operations[14]. Since these operations preserve all necessary physical information, only k-points within the IBZ are needed; as shown in ***Figure III.1***, the IBZ for the full zone can then be obtained by applying the symmetry operations (rotations, inversions, etc.)[14]:

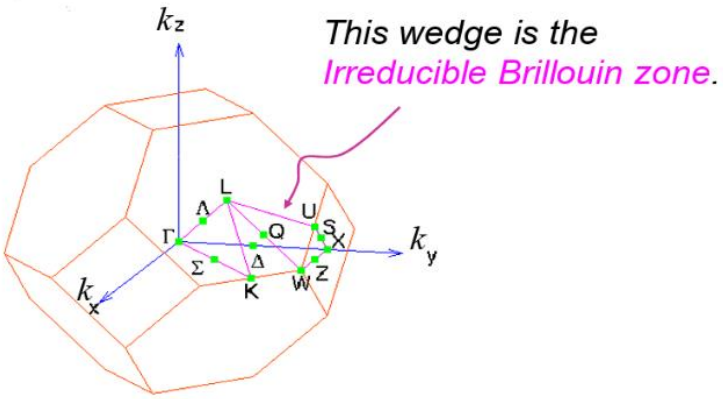


Figure III. 1: ***Smallest wedge of the 1st BZ such that any wave-vector k in the 1st BZ can be obtained from a wave-vector k in the IBZ***

Although the Schrödinger equation must, in principle, be solved at all k-points in the BZ, practical considerations make this infeasible. Fortunately, two key physical insights allow for dramatic simplification: (1) due to symmetry operations such as rotations and inversions, many k-points in the BZ are symmetry equivalent and yield redundant information, and (2) electronic wavefunctions vary smoothly with k, so states at nearby k-points are very similar. These properties enable the reduction of the full BZ to the irreducible Brillouin zone (IBZ), the smallest portion of the BZ that, when symmetry operations are applied, generates the entire zone. For example, a 10×10×10 Monkhorst–Pack mesh in the full BZ of a face-centered cubic (FCC) crystal—comprising 1000 points—can be reduced to merely 35 symmetry-inequivalent k-points in the IBZ [15,16]. Integration over the BZ is then approximated by a weighted summation over these discrete k-points in the IBZ.

In computational materials science, reciprocal-space methods are advantageous not only because they respect the periodicity of solids but also because they enable system size reduction. A large periodic system is typically modeled by a finite supercell in real space, which is then transformed into reciprocal space for band-structure calculations. There, the electronic states are mapped using discrete k-points, allowing all quantum-mechanical quantities to be evaluated via summation or extrapolation across this reduced set. Modern electronic structure codes (e.g., VASP, Quantum ESPRESSO, WIEN2K,…) include built-in algorithms for automatic k-point generation, typically based on the Monkhorst–Pack or similar schemes, requiring only the user-specified grid density or spacing [16,17]. However, care must be taken in systems with broken symmetry (e.g., defects, surfaces, or disordered phases), where a full-zone sampling may be necessary to capture all relevant phenomena.

III.3. Augmented Plane Wave (APW) approaches

III.3.1. The Muffin-Tin (MT) Approximation

To solve the Kohn-Sham equations, a variation approach is adopted, where the wave function is constrained to satisfy Bloch's theorem , is expanded into a set of plane waves—that is, represented as a Fourier series (as given in Equation *III.9*). The plane wave basis set has some important advantages: plane

waves are orthogonal and diagonal in momentum space, thus facilitating their application in numerical methods. However, as Slater first recognized in 1937[1], the singular nature of the crystal potential near the nucleus leads to wavefunctions that vary rapidly in those regions, unlike between atoms. Representing these sharp variations using planewaves alone requires an extremely high cutoff energy (large K_{max}), which in turn makes the Hamiltonian matrix very large and computationally expensive to handle — especially for all-electron calculations. To reduce and manage this complexity in electronic structure calculations, the muffin-tin (MT) approximation is a widely adopted simplification. This approximation partitions space into two main regions: muffin-tin spheres and the interstitial region, as illustrated in ***Figure III.2***[1,18]:

- Muffin-tin spheres (*S*), which are centered on each atomic nucleus and have a defined radius R_{mt}.
- The interstitial region (*I*), which occupies the space between these spheres.

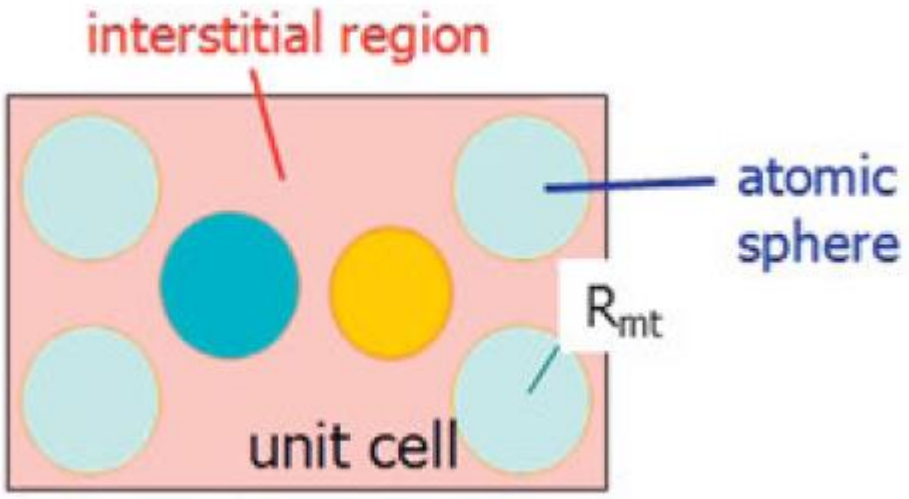


Figure III. 2: Schematic representation of unit cell Volume partitioned into muffin-tin and interstitial regions.

The muffin-tin spheres, denoted as (S), are non-overlapping, spherically symmetric regions centered on each atomic site, with a radius R_{MT}. Inside these spheres, the potential is assumed to be radially symmetric, which allows the use of a basis set formed by products of radial functions and spherical harmonics. The interstitial region (I) lies between the spheres and is characterized by a smoother, nearly constant potential. In this region, electronic wavefunctions are efficiently expanded in plane waves.

This piecewise treatment of space leads to the potential being defined as[1]:

$$V(r) = \begin{cases} V(r) & (r \in S) \\ Constant & (r \in I) \end{cases} \qquad (III.\ 11)$$

Such a decomposition forms the basis of the Augmented Plane Wave (APW) method.

III.3.2. APW Method:

The APW method solves the Kohn–Sham equations of density functional theory (DFT) by expanding the electronic wavefunctions in a hybrid basis[3]:

- Inside MT spheres: Basis functions are constructed from the exact solutions to the radial Schrödinger equation at a chosen energy. These atomic spheres with radii *R*MT must not overlap, but should be chosen for computational efficiency as large as possible with the additional constraint that R_{MT} for *d*-elements should be chosen to be about 10%–20% bigger than for *sp*-elements[19]. On the other hand, f-elements should get even larger spheres because for identical sphere sizes the number of plane-waves (PWs) to reach convergence is largest for the localized 4f (5f) electrons, medium for 3*d* (4*d*, 5*d*)-electrons, and much smaller for *sp*-states[19]. In WIEN2k, these sphere radii can be set automatically in an optimal way using the setrmt utility.
- In the interstitial: Plane waves with the vectors *K* defined in the reciprocal space are used due to the nearly constant potential, because they naturally align with Bloch's theorem. According to this theorem, the wavefunction can be written as a product of a plane wave and a periodic function.

So, The total electronic wavefunction $\psi(r)$is described differently in two regions of space[3] :

$$\psi(r,E) = \begin{cases} \sum_{lm} A_{lm}^{\vec{K}}\, u_l(r,E) Y_m^l(\theta,\varphi) & r \in S \\ \Omega^{-1/2} \sum_G C_G e^{i(\vec{K})\vec{r}} & r \in I \end{cases} \qquad (III.\ 12)$$

Where: $A_{lm}^{\vec{K}}$are expansion coefficients undetermined yet as the enrgy E, in which L abbreviates the quantum numbers l and m, $Y_m^l(\theta,\varphi)$ are the spherical harmonics basis functions, C_G represent expansion coefficients for the plane waves and $u_l(r,E)$ is the solution of the radial Schrodinger equation to the energy parameter E_l in the spherical potential, which given as[3]:

$$\left\{-\frac{d^2}{d\vec{r}^2} + \frac{l(l+1)}{\vec{r}^2} + V(\vec{r}) - E_l\right\} r u_l(r,E) = 0 \qquad (III.\ 13)$$

In this equation, $V(\vec{r})$ denotes the spherical part of Muffin potential inside the sphere, often referred to as the muffin tin potential. Meanwhile, E_l represent the linearization energy. The radial functions defined by the equation (*III.13*) are orthogonal with respect to each nuclear eigenstate inside the sphere. However, it is important to note that this orthogonality no longer holds at the boundary of the sphere, as demonstrated by the corresponding Schrödinger equation[4]:

$$(E_2 - E_1)\vec{r} u_1 u_2 = u_2 \frac{d^2 \vec{r} u_1}{d\vec{r}^2} - u_1 \frac{d^2 \vec{r} u_2}{d\vec{r}^2} \qquad (III.\ 14)$$

In which: u_1 and u_2 reveal to radial components solutions at varied energies E_1 and E_2.

The continuity and differentiability of the wavefunction across the boundary separating the MT spheres and the interstitial region are vital for the APW method validity, this continuity ensured by the potential as shown in ***Figure III.3***. This requirement is essential for a well-defined kinetic energy operator in the variational formulation of the Schrödinger equation. Slater justified the particular choice of basis functions—plane waves in the interstitial and radial solutions within the spheres—by observing that plane waves naturally solve the Schrödinger equation in regions of constant potential, while the radial functions are solutions in a spherically symmetric potential, valid only when the energy parameter E_l coincides with the eigenvalue. This muffin-tin approximation is particularly effective in calculating electronic structure of transition metals and their compounds, where it proves particularly accurate for close-packed crystal structures such as FCC and ideal HCP. However, its reliability decreases when applied to more open or less symmetric systems like BCC or structures with lower atomic coordination.

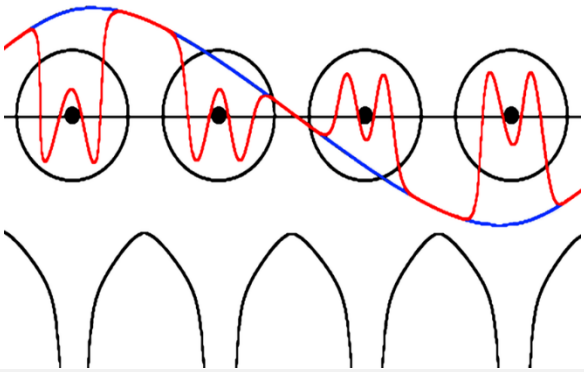


***Figure III. 3*: Muffin-tin and interstitial regions with APWs (red) matched to plane waves (blue) at sphere boundaries.[20]**

To guarantee that the wavefunction remains continuous at the muffin-tin boundary, the plane waves in the interstitial region are expanded into spherical harmonics and Bessel functions within the atomic spheres. This expansion yields the coefficients A_{lm}, which are entirely determined by the plane wave coefficients C_G, the spherical Bessel functions J_ℓ, , and the spherical harmonics Y_{lm}^*The resulting expression for these coefficients, evaluated at the sphere boundary R_{mt}, is given by[4]:

$$A_{lm} = \frac{4\pi i^{\ell}}{\frac{1}{\Omega^2} u_\ell(R_{mt})} \sum_G C_G J_\ell \left(\left|\vec{K} + \vec{G}\right| R_{mt}\right) Y_{lm}^* \left(\widehat{\vec{K} + \vec{G}}\right) \qquad (III.\ 15)$$

Here, $u_\ell(R_{mt})$is the radial solution of the Schrödinger equation evaluated at the muffin-tin radius. This expression guarantees a smooth and continuous matching of the plane-wave basis in the interstitial region

with the spherical (radial × angular) solutions inside the muffin-tin spheres, a key requirement for physical validity of the wavefunction. However, since this expansion formally involves an infinite number of angular momentum channels l, it must be matched with the spherical harmonics (which also have an angular resolution governed by l_{max}). A reasonable choice of l_{max} is determined by equating the spatial resolution of the angular basis functions and the plane waves: for spherical harmonics, the maximum number of angular nodes along a great circle is $2l_{max}$, giving a node density of $l_{max}/\pi R_{MT}$; for plane wave. The shortest wavelength corresponds to a node density of k_{max}/π. Matching these gives the condition $l_{max} = R_{MT}k_{max}$, ensuring that both basis sets offer comparable spatial resolution[21]. Choosing l_{max} beyond this value leads to numerical instabilities and overfitting behavior at the sphere boundary, analogous to fitting high-order polynomials to sparse data. Furthermore, this relationship implies that the muffin-tin radii for different atoms should not differ significantly, as a common l_{max} must be suitable for all atoms in the system.

The original Augmented Plane Wave (APW) method has significant computational challenges that make it impractical for many electronic structure calculations. The key issues are:

- The APW basis functions inside the atomic spheres are solutions of the Schrödinger equation at a fixed energy parameter u_ℓ. This means the basis functions have no variational freedom to adjust as the band energy changes, requiring u_ℓ to be set equal to the band energy itself. Consequently, the energy bands cannot be obtained from a single diagonalization; instead, the secular determinant must be solved repeatedly as a function of energy. This iterative process is computationally expensive, especially for general k-points where symmetry cannot reduce the secular matrix size, and for systems with many bands[2,4,6].
- The "asymptote problem" arises because the radial function $u_\ell(R_{mt})$ appears in the denominator of the matching conditions at the sphere boundary. If $u_\ell(R_{mt})$ vanishes (near an asymptote), the plane waves and radial functions can decouple, causing strong variations in the secular determinant and numerical instability[4,21].
- The energy-dependent basis set is optimized for states near the eigenvalues used to generate the radial solutions, which reduces accuracy for higher-energy (unoccupied) states[2].

To address this problem, several modifications to the APW method have been introduced, the most famous being developed by Koelling[22] and Andersen[2].

III.4. Linearized Augmented Plane Wave (LAPW)

In 1975, Ole K. Andersen developed Linearized Augmented Plane Wave (LAPW)[2] by linearizing the APW method's energy-dependent radial functions. This innovation was introduced to overcome the problem of finding the exact energy u_ℓ necessary to construct the basis functions and solve the secular equation *(II.13)*. This is accomplished by introducing the energy derivative of the radial function, defined as:

$$\dot{u}_\ell = \frac{du_\ell}{dE_\ell}\Big|_{E=E_\ell} \qquad (III.\ 16)$$

which satisfies the inhomogeneous differential equation[2]:

$$\left\{-\frac{d^2}{d\vec{r}^2} + \frac{l(l+1)}{\vec{r}^2} + V(\vec{r}) - E_l\right\} r\dot{u}_l(r) = ru_l(r) \qquad (III.\ 17)$$

Instead of the APW wavefunction representation given in equation (II.12), which involves a single energy-dependent radial function u_ℓ, the LAPW method employs a linear combination of u_ℓ and its energy derivative $\dot{u}_\ell$, both evaluated at a fixed linearization energy E_ℓ. The LAPW wavefunctions are then given by[4]:

$$\psi(r) = \begin{cases} \Omega^{-1/2} \sum_G C_G e^{i(\vec{k}+\vec{G})\vec{r}} & r \in I \\ \sum_{\ell m} \left[A_{lm}^{\vec{K}} u_l(r) + B_{lm}^{\vec{K}} \dot{u}_l(r)\right] Y_m^l(\theta, \varphi) & r \in S \end{cases} \qquad (III.\ 18)$$

The $B_{lm}^{\vec{K}}$ coefficients linked to the energy variations, much like $A_{lm}^{\vec{K}}$ are determined by matching conditions for the value and slope of the wavefunction at the boundary between the interstitial region and the MT sphere. The resulting improvement over the APW method is particularly significant when the fixed linearization energy E_l differs slightly from the true band energy E. In such cases, the linearized form can be expressed as a Taylor expansion[4]:

$$u_l(\epsilon, r) = u_l(E_l, r) + (\epsilon - E_l)\dot{u}_l(\epsilon, r) + O((\epsilon - E_l)^2) \qquad (III.\ 19)$$

Here, the second-order term $O((\epsilon - E_l)^2)$ denotes the squared error in energy. While the LAPW framework ensures continuity of the wavefunction at the muffin-tin (MT) sphere boundary—something the original APW method struggled with—this comes with a trade-off in computational accuracy. Specifically, the LAPW method introduces an error of order $(\epsilon - E_l)^2$ in the wavefunctions and of order $(\epsilon - E_l)^4$in the computed band energies[2]. Despite these inherent approximations, the LAPW basis remains highly effective for representing all valence bands within a relatively broad energy range using a single linearization energy E_l. When this is not sufficient, dividing the energy window into two distinct regions often yields a simpler and more practical solution than the original APW approach. Therefore, the

LAPW method while offering significant improvements over the original APW method also has several notable drawbacks that affect its applicability, computational efficiency and cost. These drawbacks include:

- Higher computational cost due to derivative matching: LAPW basis functions must satisfy both value and derivative continuity at MT sphere boundaries. This necessitates a more stringent matching condition between the interstitial plane waves and the solutions inside the MT spheres[18]. Consequently, a higher plane wave cutoff is required to maintain accuracy, significantly increasing the size of the basis set and computational demand compared to the original APW method.
- The LAPW method aims to deliver accurate band energy calculations near the linearization energies E_l [4]. While selecting E_l near the band center works for many materials, it fails for systems with localized 4f orbitals or transition metals, where a single E_l cannot capture all relevant states[23–26]. These materials often contain semi-core states, which lie between core and valence levels and are difficult to treat with a standard LAPW basis. Additionally, accurately modeling high angular momentum states in heavy elements requires significantly increasing the plane-wave cutoff and muffin-tin radii, leading to higher computational costs [27].
- Sensitivity to Muffin-Tin sphere radii: The choice of MT sphere radii critically affects convergence behavior. While larger spheres are often chemically intuitive, they may lead to poor numerical convergence or even sphere overlap, which must be avoided[4]. In practice, optimal performance sometimes requires smaller-than-expected spheres for large atoms, necessitating non-intuitive and system-specific tuning to achieve convergence and computational efficiency.

To address these limitations several possible strategies have been proposed: The reduction of the size of the muffn-tin radius, so-called two-window calculations, and the use of local orbitals.

III.5. Semi-Core States Problem:

Based on whether or not electrons in an atom participate in chemical bonding with other atoms, they generally classified into two categories. Core electrons are tightly bound to their nuclei and remain entirely localized within the Muffin-Tin (MT) spheres; their wave functions—and hence their electron densities—are strictly confined inside these spheres, with negligible amplitude in the interstitial regions. Because of this confinement, they do not interact significantly with neighboring atoms and are not involved in chemical bonding; these are referred to as core state. In contrast, valence electrons are more

weakly bound and extend beyond the MT spheres into the interstitial regions, this allows them to interact with neighboring atoms and participate in the formation of chemical bonds.

However, for many elements, this clear-cut division is not always strictly applicable, e.g., in 3*d* transition metals, the 3*s* and 3*p* states which are normally considered core, can leak slightly outside the atomic sphere, so they're obligate to treated as valence in calculations[19]. To clarify their unique behavior and avoid confusion with the conventional classification, we refer to them as semi-core states. These states often share the same angular quantum number l as the valence states but differ in their principal quantum number n, making their classification and treatment more nuanced[23,24]. At the same time, describing them as valence states using a single linearization energy E_l as given in LAPW method becomes problematic The description of valence states becomes poor, if E_l is chosen near the semicore level ; conversely, selecting E_l close to the valence energy fails to represent semicore states accurately. This mismatch can lead to numerical artifacts such as unphysical "ghost bands"[28]. Several approaches have been developed to address this issue:

- **Two-window (energy panel) method**: is explained in the uploaded paper by Singh and Krakauer[24], where distinct linearization energies for the semicore and valence states are adopted to treat each within an independent energy window. One energy window is chosen for semicore states with an appropriate E_l close to the semicore level, while for valence states is used another separate window with energy E_l closer to the Fermi level. Each window uses a tailored basis optimized for the energy range it targets. However, strict orthogonality between states from different windows is not secured[24,28], and this requires additional computational effort as the calculations for each window must be handled separately[24].

- **Super-linearized LAPW (SLAPW) approch**: was introduced to treat both semicore and valence states within a single basis set, avoiding the drawback of two-window method, SLAPW employs multiple radial functions and matches the wavefunction and its first three radial derivatives at the sphere boundary[24]. This approach, known as the SLAPW-4 method, involves four radial functions, four expansion coefficients, and four matching conditions[28]. A simplified variant, called SLAPW-3, reduces this requirement by using only three matching conditions[28].

- **LAPW+LO (Local Orbitals) approch**: A more efficient and widely adopted solution, proposed by Singh[23] (1991), extends the basis set by introducing specifically constructed local orbitals (LOs). The following sections provide a detailed analysis of this approach.

III.5.1. LAPW with Local Orbital (LAPW+LO):

LOs add flexibility to the basis set by allowing the treatment of two states with the same angular momentum quantum number l but different principal quantum numbers n (e.g., 3s and 4s) with a linearization energy value E_{1l} suitable for the highest of the two valence states (4s in previous example)[19]. This is important when valence electrons occupy higher-n states while the lower-n states are not fully contained within the atomic sphere of the LAPW method. The LO functions are localized entirely within the atomic sphere (hence "local") and vanish in the interstitial region, so they do not introduce additional plane waves. Inside the sphere, the LO is expressed as a linear combination of radial functions at two different energies $E_{1,l}$ and $E_{2,l}$, plus their energy derivatives, multiplied by spherical harmonics $Y_m^l(\theta,\varphi)$[23]:

$$\psi^{LO}(r) = \begin{cases} 0 & r \in I \\ \sum_{lm}[A_{lm}u_l(r,E_{1l}) + B_{lm}\dot{u}_l(r,E_{1l}) + C_{lm}u_l(r,E_{2l})]\,Y_m^l(\theta,\varphi) & r \in S \end{cases} \qquad (III.\ 20)$$

The coefficients A_{lm}, B_{lm}, and C_{lm} are determined by normalization and the requirement that the LO and its derivative vanish at the sphere boundary[23]:

$$\psi^{LO}(R_{MT}) = 0,\ \frac{d}{dr}\psi^{LO}(r)|_{R_{MT}} = 0 \qquad (III.\ 21)$$

III.5.2. APW with Local Orbital (APW+lo):

One of the primary limitations of the original Augmented Plane Wave (APW) method lies in the energy dependence of the entire basis set, which complicates the solution of the eigenvalue problem. Although the LAPW+LO method successfully eliminates this energy dependence by linearizing around a fixed energy E_l and introducing additional local orbitals, it does so at the cost of a significantly larger basis set, resulting in increased computational demand.

To address the limitations of both the APW and LAPW+LO methods, Sjöstedt, Nordström, and Singh proposed the APW+lo method[6] where the linearization of the energy-dependent radial wave function was facilitated by an extra local orbital (lo, different from an LO) that corrects the linearization error. This leads to a hybrid basis set that effectively assure higher precision with fewer basis functions than LAPW, making the method computationally more efficient.

A key advantage of the APW+lo method lies in its superior plane wave (PW) convergence compared to the standard LAPW approach. Studies [4,29]have shown that it can reduce the number of required plane waves by nearly 50%, resulting in significantly improved computational efficiency. Although this method necessitates the inclusion of additional local orbital (lo) basis functions, it requires only a slightly higher plane wave cutoff than the original APW method, striking an effective balance between accuracy and performance. In the APW+lo scheme, the basis consists of two components**:**

- **Augmented Plane Waves (APW) with a set of fixed energies E_l:** These are constructed using radial functions $u_l(r, E_l)$for a fixed energy E_l, providing a solid foundation for linearizing the eigenvalue problem[19]:

$$\psi(r) = \begin{cases} \Omega^{-1/2} \sum_G C_G e^{i(\vec{K})\vec{r}} & r \in I \\ \sum_{lm} \left[A_{lm}^{\vec{K}} u_l(r, E_l) \right] Y_m^l(\theta, \varphi) & r \in S \end{cases} \quad \textit{(III. 22)}$$

- **Local orbitals:** the APWs do not permit variations in the radial functions for eigenvalues that differ from the chosen linearization energy E_l, making them a less effective basis[4]. To address this limitation, the energy dependence is managed through a local orbital (lo), which is confined to the Muffin-Tin (MT) sphere and vanishes outside it[19]:

$$\psi^{lo}(r) = \begin{cases} 0 & r \in I \\ \sum_{lm} \left[A_{lm}^{lo} u_l(r, E_{1l}) + B_{lm}^{lo} \dot{u}_l(r, E_{1l}) \right] Y_m^l(\hat{r}) & r \in S \end{cases} \quad \textit{(III. 23)}$$

Semi-core states cannot be described accurately by APW+lo due to uses only one linearization energy per angular momentum channel[19]**,** which may not be sufficient when both semi-core and valence states of the same angular momentum l. For these states, the basis set has to be improved, and this can be done by adding another type of local orbitals (LO) — resulting in the APW+lo+LO approach. The definition of a local orbital (LO) for APW+lo is[21]:

$$\psi^{LO}(r) = \begin{cases} 0 & r \in I \\ \sum_{lm} [A_{lm}^{LO} u_l(r, E_{1l}) + C_{lm}^{LO} u_l(r, E_{2l})] \, Y_m^l(\hat{r}) & r \in S \end{cases} \quad \textit{(III. 24)}$$

Unlike the local orbitals used in LAPW, the APW+lo local orbitals do not include the energy derivative of u_l. Instead, the two coefficients A_{lm}^{LO} and C_{lm}^{LO} are chosen such that the orbital is normalized and vanishes at the muffin-tin sphere boundary — though its slope at the boundary is not required to be zero.

III.6. The Full Potential Linearized Augmented Plane Wave (FP-LAPW) method:

The full-potential linearized augmented-plane-wave (FLAPW) method is regarded as one of the most pricese implementations for solving the Kohn-Sham equations of density functional theory (DFT). It is often considered as a reference for validation other computational methods. In this method, there are no shape approximation to the potential and charge density— neither in the interstitial region nor inside the muffin-tin spheres[3], thereby it treats all electrons, so it capturing the full electronic environment of a material[30]. The FLAPW method treats all electrons explicitly[3,30]: core electrons are handled fully relativistically, while valence electrons are typically treated semi-relativistically, neglecting spin-orbit coupling unless explicitly included.

The term "full-potential" originates from the method's precise representation of the potential:

- Inside each atomic (MT) sphere, the potential and charge density are expanded in lattice harmonics,
- In the interstitial region, they are expressed as a Fourier series.

The mathematical expression of the potential and charge density in this context can be summarized by:

$$V(r) = \begin{cases} \sum_{lm} V_{lm}(r) Y_{lm}(\theta,\phi) & r \in S \\ \sum_{k} V_k e^{i(\vec{K})\vec{r}} & r \in I \end{cases} \quad (III.\ 25)$$

$$\rho(r) = \begin{cases} \sum_{lm} \rho_{lm}(r) Y_{lm}(\theta,\phi) & r \in S \\ \sum_{k} \rho_k e^{i(\vec{K})\vec{r}} & r \in I \end{cases} \quad (III.\ 26)$$

This formulation ensures the continuity and differentiability of the potential across the boundaries between MT spheres and the interstitial space, significantly enhancing the accuracy of total energy and electronic structure calculations.

III.7. WIEN2k Code:

III.7.1. WIEN2K Computational Code:

WIEN2k is a powerful and widely used computational tool for accurate electronic structure calculations in solids, with a long history of development and optimization. The first public release under the name WIEN originates from its development location, Vienna and it was published by P. Blaha, K. Schwarz, P. Sorantin, and S. B. Trickey in (1990)[31], this version, written in FORTRAN, enabled full-potential calculations and became known for its precision in treating complex crystal structures. The WIEN package improved UNIX-compatible versions in 1993, 1995 and 1997 (as WIEN93, WIEN95 and

WIEN97, respectively)[32] which introduced spin-polarized calculations, scalar relativistic effects, and a more user-friendly interface[33]. The major transformation came in 2001 with the release of WIEN2k, marking a new era for the code with enhanced functionality and user experience, where the APW+lo method is implemented[34,35].

Many properties can be calculated using WIEN2k, making it a highly flexible and accurate tool for first-principles studies of materials. It offers in-depth insights into the electronic structure, including calculations of band structures, density of states (DOS), charge densities and others. For structural investigations, WIEN2k enables total energy evaluations, structural parameters, bulk modulus B, determination of elastic constants, and equations of state.It is equally capable of predicting optical properties, including the dielectric function $\varepsilon(\omega)$, absorption coefficient α and the parts of complex refractive index $\tilde{n}(\omega)$. The code also handles magnetic properties. Through interfaces with external packages like BoltzTraP, WIEN2k can also address transport and thermoelectric properties, such as such as the Seebeck coefficient factor PF and figure of merit ZT . To determine these properties, several software packages must be installed such as[32]: Fortran 90 compiler (gfortran is also suitable), csh or tcsh, FFTW3, ghostscript (with JPEG support) for graphical output, gnuplot (with PNG support) are required and others.

III.7.2. Core Components of the WIEN2k Code:

The main or "core" programs of WIEN2k, executed at least once per calculation, are divided into two main groups[33]:

- Initialization programs
- Self-consistency cycle programs(SCF)

The initialization phase precedes several important steps that prepare the system for a self-consistent field (SCF) calculation. These steps presented in ***Figure III.4*** are summarized as follows:

a) Naming conventions: Choosing a consistent and descriptive name for the calculation ‘case’ (Under UNIX, filenames typically follow the **case.type** pattern), which is used as a prefix for all related files. Suppose you choose "GaSb-ZB" as the case name—then files like GaSb-ZB.struct, GaSb-ZB.vol, GaSb-ZB.in2, among others, will be created accordingly.

b) Starting the w2web server: To run the w2web interface, you want to execute WIEN2K with the command **w2web [-p xxxx]** where **xxxx** is a free port number not currently in use. An interface

will appear asking you to username and password, which is required to connect to this server as shown in ***Figure III.4***.



Figure III. 4: starting the w2web server

c) Creating a new session (or select an old one**):** In the w2web graphical interface of WIEN2k, every user operates within a session, which allow quick switching between various calculations. To create a new session: select "Create New Session", then enter a name for your session (GaSb) and click "Create" (If you have previously worked in WIEN2k choose your session name from the dropdown list).

After creating/choosing a session, you need to create new directory or select current directory (For example, you might name your directory **GaSb-ZB** for calculate the structural properties of Gallium Antimonide in the Zincblende structure, The stages are displayed in the ***Figure III.5*****.**

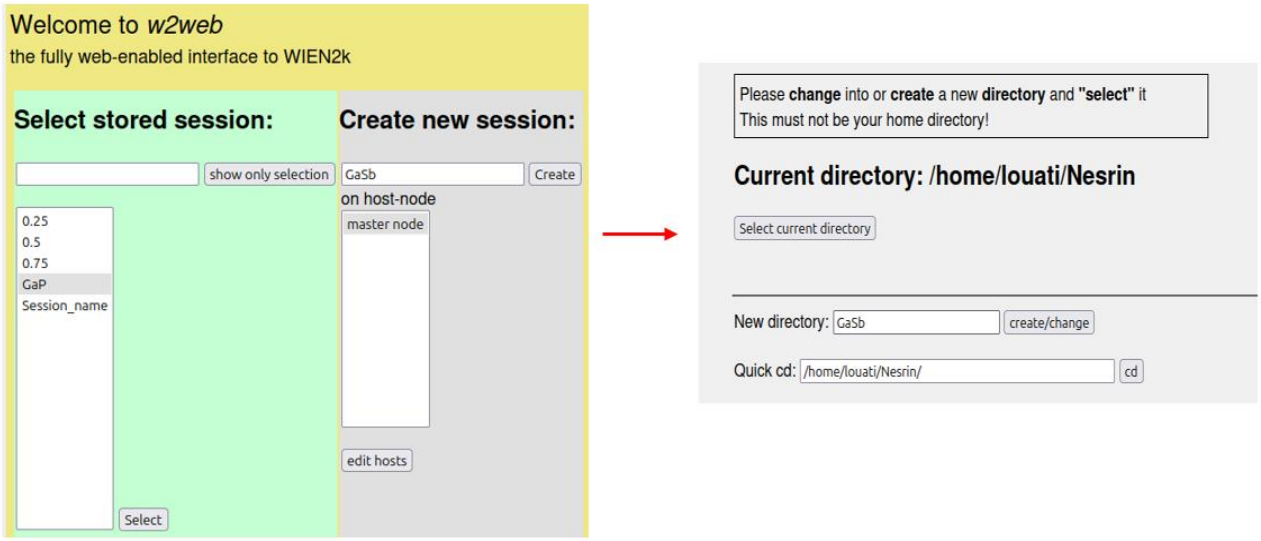


Figure III. 5: The creation of a new session and directory

d) Creating the master input file (struct file): The file **case.struct** is often referred to as the master input file in WIEN2k because of its central and essential role in every calculation. For example, to calculate the properties of GaSb in the ZB structure, we must create the file **GaSb-ZB.struct** by following these steps:

- In the w2web interface, navigate to Execution → StructGen, then enter the number of independent atoms in the initial structure→ Generate template .
- For a new case, w2web will open an empty structure template where you can input the required structural data including: crystal symmetry, Lattice parameters a, b, and c (given in Bohr units or Angstroms) as well as the lattice angles α, β, and γ, the *the atoms in the unit cell* and their positions.
- Click "Save Structure" (the atomic charge number will be updated automatically) and "set and continue editing. When you are done, exit StructGen with "save file and clean up". This will generate the file GaSb-ZB.struct.

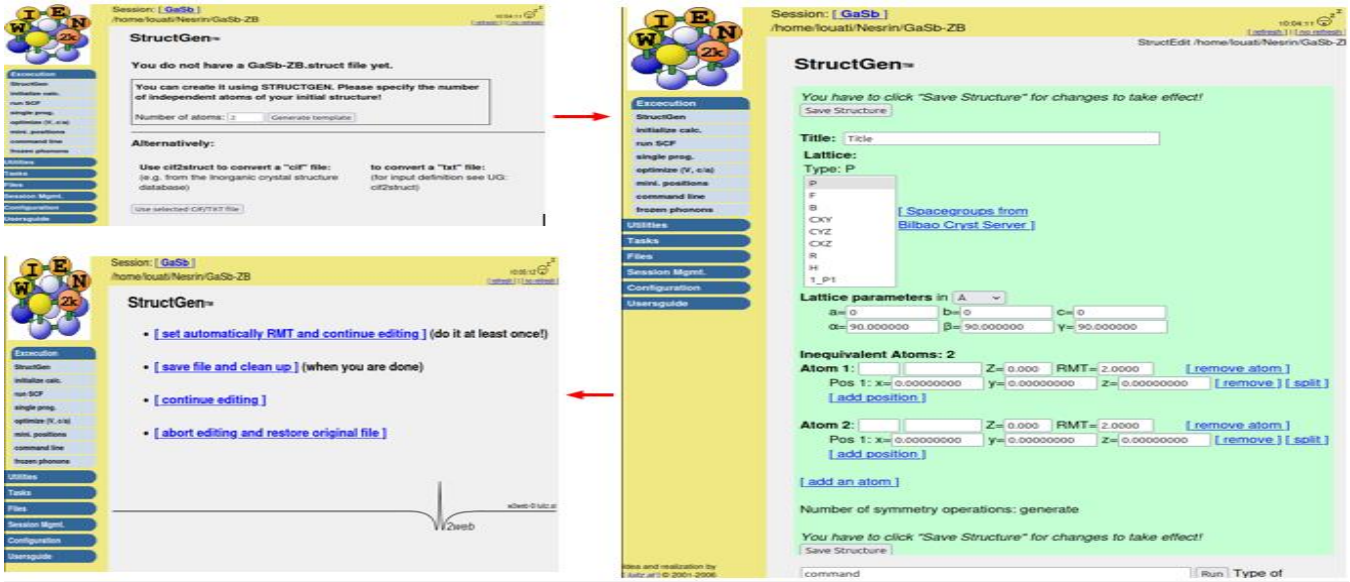


Figure III. 6: ***Creating the master input file (struct file)***

III.7.2.a. Initialization of the calculation:

After the basic input file has been created, the initialization of the calculation is carried out using a graphical interface, as shown in *Figure III.7*.

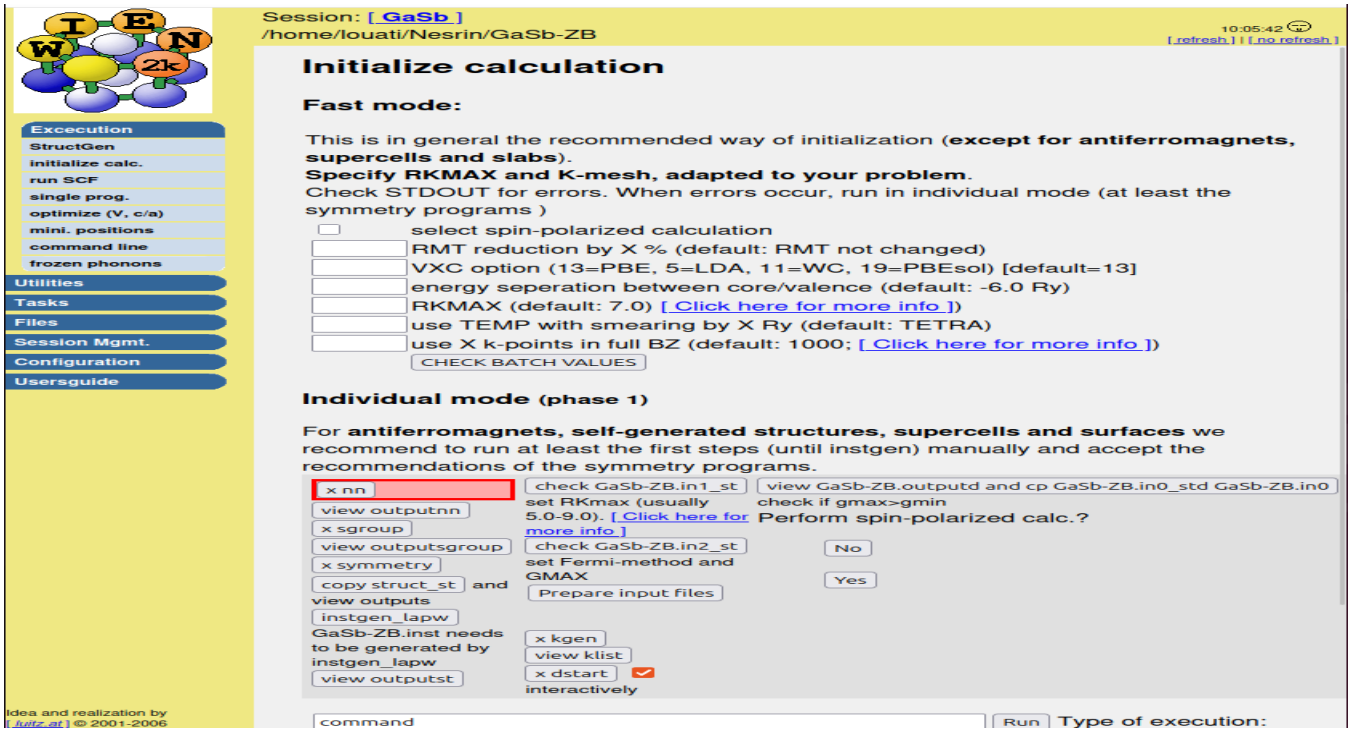


Figure III. 7: ***Initialization with w2web***

This interface recommended using the "Fast mode or the "Individual mode" requires you to perform each initialization step manually and in order. Initializing the calculation will run several steps automatically, where x is the script to start WIEN2k programs thus allowing you to gain a deeper understanding of how the setup works[32,33,35]:

- **x nn**: refer to nearest neighbor distances, by analyzes the atomic geometry from case.struct file it computing the nearest neighbors up to a certain cutoff distance and next-nearest neighbor distances, allowing the program to suggest suitable R_{MT} without overlapping atomic spheres, also determines bond angles, and verifies the correct definition of equivalent atoms. It can also generate a corrected structure file under the name '**case.struct nn'** if equivalences are inconsistent
- **view outputnn:** checks for overlapping atomic spheres, coordination numbers, nearest neighbor distances, and angles and it Allows verification of information recorded in a case.struct file.
- **x sgroup:** determines the space-group as well as all point-groups of non-equivalent sites for the given structure, it will check and determine the smallest possible (primitive) cell and create the corresponding structure file if necessary under the name **'case.struct sgroup'**.

- **x symmetry:** determines space-group symmetry operations, atomic site point groups.
- **x lstart:** stands for Local(-spin) START, the program that generates the initial atomic data for LAPW calculations using LDA or LSDA. Its primary purpose is to generate atomic charge densities that serve as input for **dstart**, which constructs the initial electronic density for an SCF calculation. In addition to the atomic densities, **lstart** creates all necessary SCF input files—**case.in0**, **case.in1**, **case.in2**, **case.inc**, and **case.inm**—based on the calculated atomic eigenvalues. You must choose the exchange-correlation potential and set the energy separating core and valence states.
- **x kgen:** creates the k-point mesh in the irreducible wedge of the Brillouin zone (IBZ) on a special grid suitable for the modified tetrahedron method. The user can define the mesh in one of two ways: by total number of k-points in the full Brillouin zone, or by specifying the number of divisions along each reciprocal lattice vector (three integers). This second option is selected when the kgen number is set to zero, in which case the program explicitly constructs the k-point grid.
- **x dstart**: constructs the initial crystalline charge density **case.clmsum** by Superposing atomic charge densities (**case.rsp**) previously generated with **lstart** and creates the starting density for the SCF cycle. The program retrieves information on the LM components of the lattice-harmonic representation, as well as the number of Fourier coefficients for the interstitial charge density, from the files **case.in1** and **case.in2**.

III.7.2.b. Self-Consistency Cycle (SCF) Calculation:

After initializing the case, click "Run SCF" under "Run Programs" to initiate the self-consistent field calculation using the **run_lapw** command. It involves the following key steps[35]:

- **lapw0 (generates potential):** Calculates the total potential V_{tot} by summing the Coulomb potential V_C and the exchange–correlation potential V_{XC}, using the total electron (or spin-resolved) density as input. The resulting potential is split into two components: the spherical ($l = 0$) part, stored in **case.vsp**, and the non-spherical part, stored in **case.vns**. For spin-polarized calculations, the separate spin densities (**case.clmup** and **case.clmdn**) produce two sets of potential files:
  - Spin-up: case.vspup (spherical) and case.vnsup (non-spherical)
  - Spin-down: case.vspdn (spherical) and case.vnsdn (non-spherical)
- **lapw1 (generates eigenvalues and eigenvectors):** constructs the Hamiltonian and overlap matrices and diagonalizes them to obtain eigenvalues and eigenvectors, which are stored in

case.vector. It supports both the standard LAPW basis and the APW+lo method, allowing mixed basis sets for efficiency. Additional local orbitals (LOs) can be added for semicore states, high-energy states, or improved accuracy in nuclear magnetic resonance parameters (NMR) and spectroscopy calculations; proper separation of E -parameters is required to avoid ghost bands, optional higher-derivative LOs (HDLOs) improve linearization for d- and f-states.

- **lapw2 (generates valence charge density expansions):** reads **case.energy** and **case.vector** to compute the Fermi energy (set to the valence band maximum for semiconductors) and expand the electronic charge density for each occupied state and *k*-point. From these expansions, it integrates to obtain partial charges inside the atomic spheres.
- **Lcore (generates core states):** it computes the core states for the current spherical part of the potential (**case.vsp**), yields core eigenvalues, the file **case.clmcor** with the corresponding core densities, and the core contribution to the atomic forces.
- **MIXER (adding and mixing of charge densities):** combines the core, semicore, and valence electron densities from the previous steps to produce the total output density. It ensures proper normalization (adding a constant in the interstitial if needed) and stabilizes the SCF cycle by mixing the new output density with the old input density instead of replacing it directly.

The **case.scf** file in WIEN2k records a detailed summary of each iteration of the self-consistent field (SCF) cycle. Important variables in this file are prefixed with LABEL:, making it easier to monitor convergence and extract data using tools like the Utils → Analyse function in the w2web interface. This file accumulates essential data throughout the SCF cycle to provide a coherent history of the iterative process and summary of previous iterations.

Once convergence is achieved, it is critical to back up all relevant input and output files. This can be done via the Utils → Save option in w2web or using the save_lapw command at the command line. The save_lapw command creates a backup by saving the current state of all calculation files in a unique directory, which is very useful for managing multiple calculation stages or parameter optimizations.

In essence, these tools extend the functionality of the main SCF calculation by enabling post-processing analyses and the derivation of various physical properties.

We can summarize the main programs of WIEN2k, including the initialization and self-consistency cycle (SCF) programs, in ***Figure III.8***.

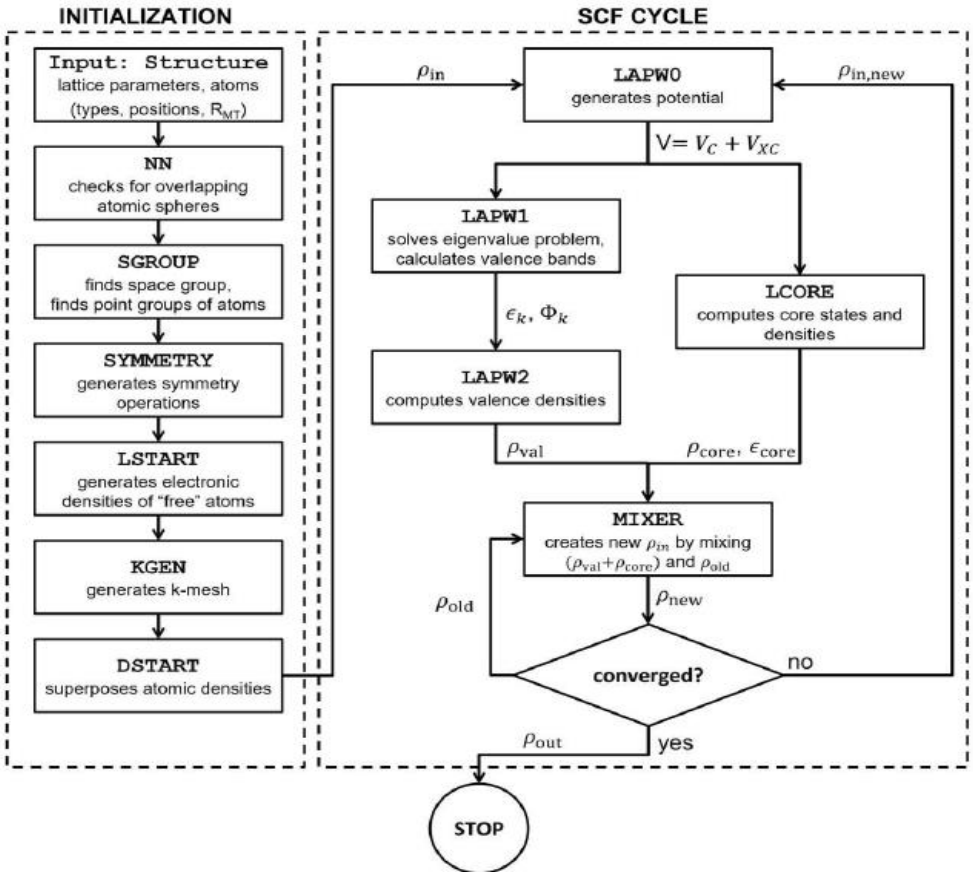


Figure III. 8:Flowchart illustrating workflow of a WIEN2k calculation, covering the initialization phase and the SCF cycle[32].

III.7.3. Calculating properties:

After the SCF cycle has produced a converged electronic density, a third set of programs can be employed to examine the results in more detail or to compute additional material properties. Typical examples include: **TETRA** (Density of States Integration) for computing the total and partial densities of states, **SPAGHETTI** (Band Structure Plotting) for generating the electronic band structures along specified k-point paths, **OPTIC** (Optical Matrix Elements) for determining the optical properties and others. This can be done via Tasks option in w2web:

III.7.3.a. Volume Optimization:

The auxiliary program **optimize** (or **x optimize**) creates, from an existing case.struct file — or from **case_initial.struct** (which is automatically generated during the first run) — a set of structure files with varying volumes, c/a ratios, or other adjusted parameters, depending on the user's input:

[1] VARY VOLUME with CONSTANT RATIO A:B:C
[2] VARY C/A RATIO with CONSTANT VOLUME (tetr and hex lattices)
[3] VARY C/A RATIO with CONSTANT VOLUME and B/A (orthorh lattice)
[4] VARY B/A RATIO with CONSTANT VOLUME and C/A (orthorh lattice)
[5] VARY A and C (2D-case) (tetragonal or hexagonal lattice)
[6] VARY A, B and C (3D-case) (orthorhombic lattice)
[7] VARY A, B, C and Gamma (4D-case) (monoclinic lattice)
[8] VARY C/A RATIO and VOLUME (2D-case) (tetr and hex lattices)

Next, specify how many cases you want to generate and the percentage change for each (e.g., 5 cases with ±2%). For volume variation, typical values might be −4%, −2%, 0%, +2%, and +4%, allowing you to explore how total energy changes with volume. Once the parameters are set, run the **optimize.job** script. After completion, click **Plot** to visualize the energy curve.

If the volume is varied while maintaining a constant A:B:C ratio, the calculation yields the total energy as a function of lattice volume, through which it can be derived several important as: equilibrium volume (V_0), Minimum total energy (E_0) Bulk modulus (B_0) and it first derivative (B_0') , equation of state parameters and the details are also stored in **case.outputeos** file.

III.7.3.b. Band structure:

Following the completion of a self-consistent calculation for the specified atomic structure, one can investigate the electronic structure, The energy eigenvalues as a function of the **k**-vector obtained at the end of the KS calculation define the band structure. From the Tasks menu, select Band structure then follow the buttons step by step as shown in ***Figure III.9***. Band structure calculations require a specialized k-point mesh along high-symmetry directions in the Brillouin zone,, this mesh can be generated from WIEN2k default templates[36], generated graphically using **XCrySDen**[37], or manually specified. The process begins by creating the file **case.klist_band** and executing **x lapw1 -band**, which reads the specified band-structure k-mesh instead of the default mesh. For band-character plotting—where the

radius of plotted circles reflects the contribution of specific orbital characters—partial charges must be obtained using **x lapw2 -qtl –band**. This process, followed by inserting the correct Fermi energy (which can be found in the saved scf-file) in the case.insp file along with the energy range for accurate plots.

Visualization of the band structure was carried out using the **x spaghetti** module, which generates output files such as **case.spaghetti.ps** for PostScript viewers (e.g., Ghostscript, gv) and **case.bands.agr** for xmgrace[32]. These outputs permit detailed customization of plot parameters, including axis ranges, labels, and plotting styles. Alternatively, the results can be rendered and analyzed using plotting programs such as gnuplot.

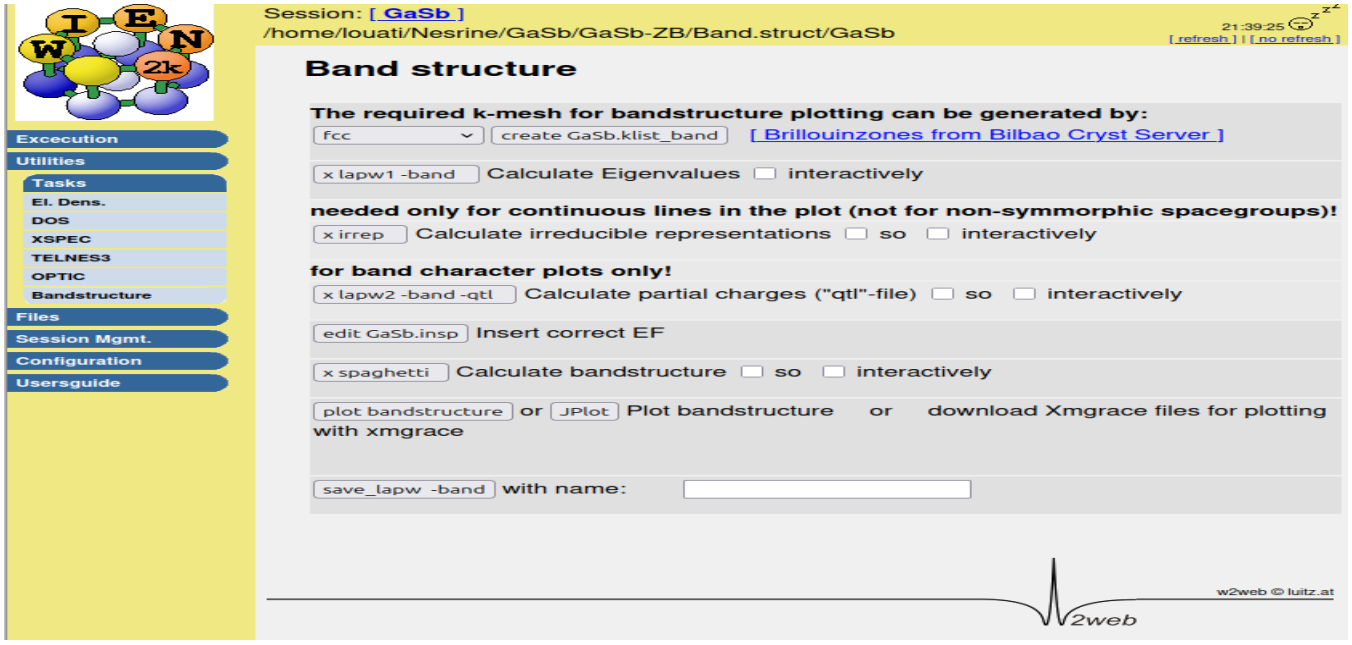


Figure III. 9:w2web window for Calculating the band structure

III.7.3.c. Density of States (DOS):

From the KS eigenvalues calculated on a sufficiently fine **k**-grid in the irreducible BZ, one can obtain the density of states (DOS). By using the partial charges, one can decompose the total DOS into partial DOS (PDOS), to calculate them go to Tasks, pick DOS, and click the buttons presented in *Figure III.10* in order.

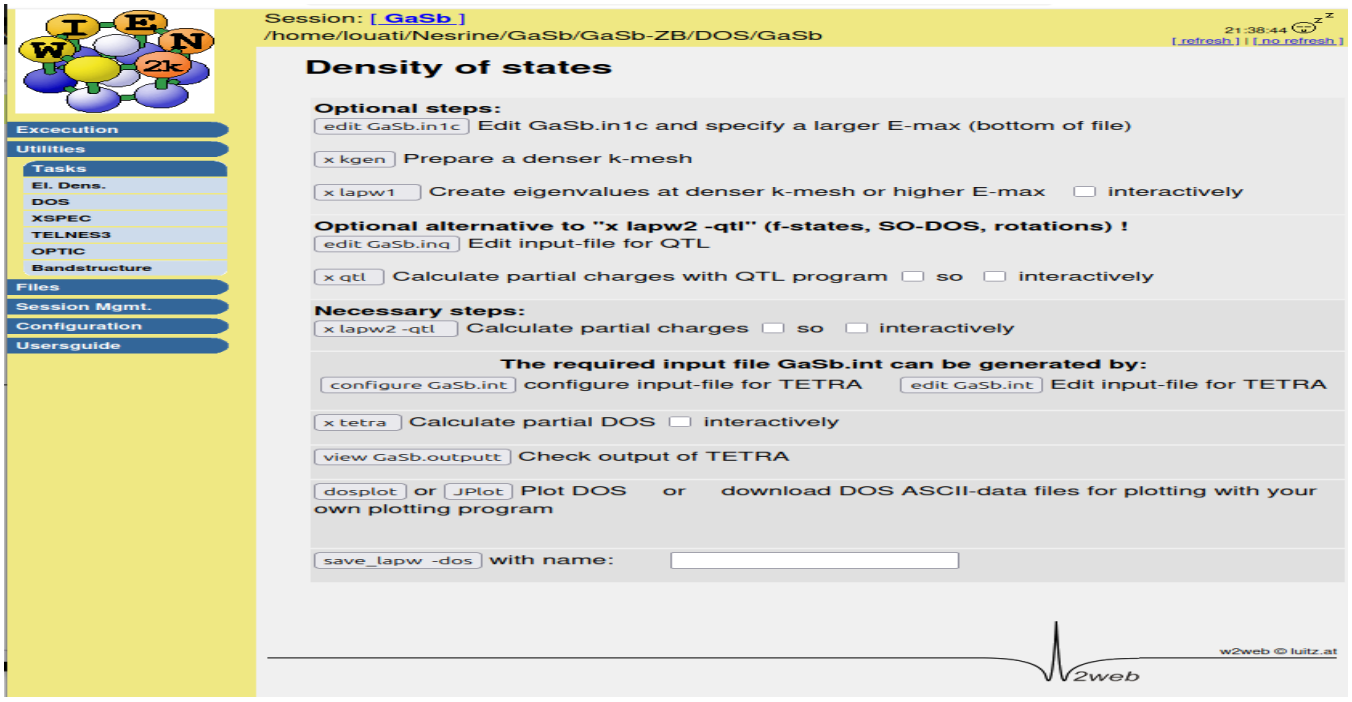


Figure III. 10:w2web window for calculating the density of state

- Optionally, specify an extended energy range to include unoccupied electronic states or choose a denser k-point mesh (k-mesh) for improved resolution.
- Compute partial charges using the command:**x lapw2 –qtl** This step calculates site- and orbital-resolved charge distribution from the previously generated **case.vector** file, which must be produced using a valid tetrahedral k-mesh.
- Create or configure the **case.int** file, this file defines total and partial DOS components to be calculated by specifying the calculation parameters and orbital projections. It can be generated automatically with the configure **case.int** utility or edited manually from the template.
- Calculate the DOS by running: **x tetra**, this command performs integration over the Brillouin zone using the tetrahedron method.
- Visualize the DOS results using WIEN2k plotting tools: **dosplot** for standard plotting and **dosplot2** for interactive plotting and customization, which requires gnuplot.
-

III.7.3.d. Optical properties:

Optical spectra, such as the frequency-dependent dielectric function, conductivity, reflectivity, absorption, or the loss function, are derived by evaluating momentum matrix elements between occupied and unoccupied electronic states[19]. The process employs the independent-particle approximation and requires a dense sampling of the Brillouin zone with finely resolved eigenvalues and eigenvectors. WIEN2k's optic module calculates the dipole transition matrix elements, which are then integrated over the Brillouin zone by the joint program to yield the imaginary part of the dielectric tensor. The real part is subsequently obtained via Kramers-Kronig relations[38], which is computed using the step-by-step procedure outlined below as shown in ***Figure III. 11***:

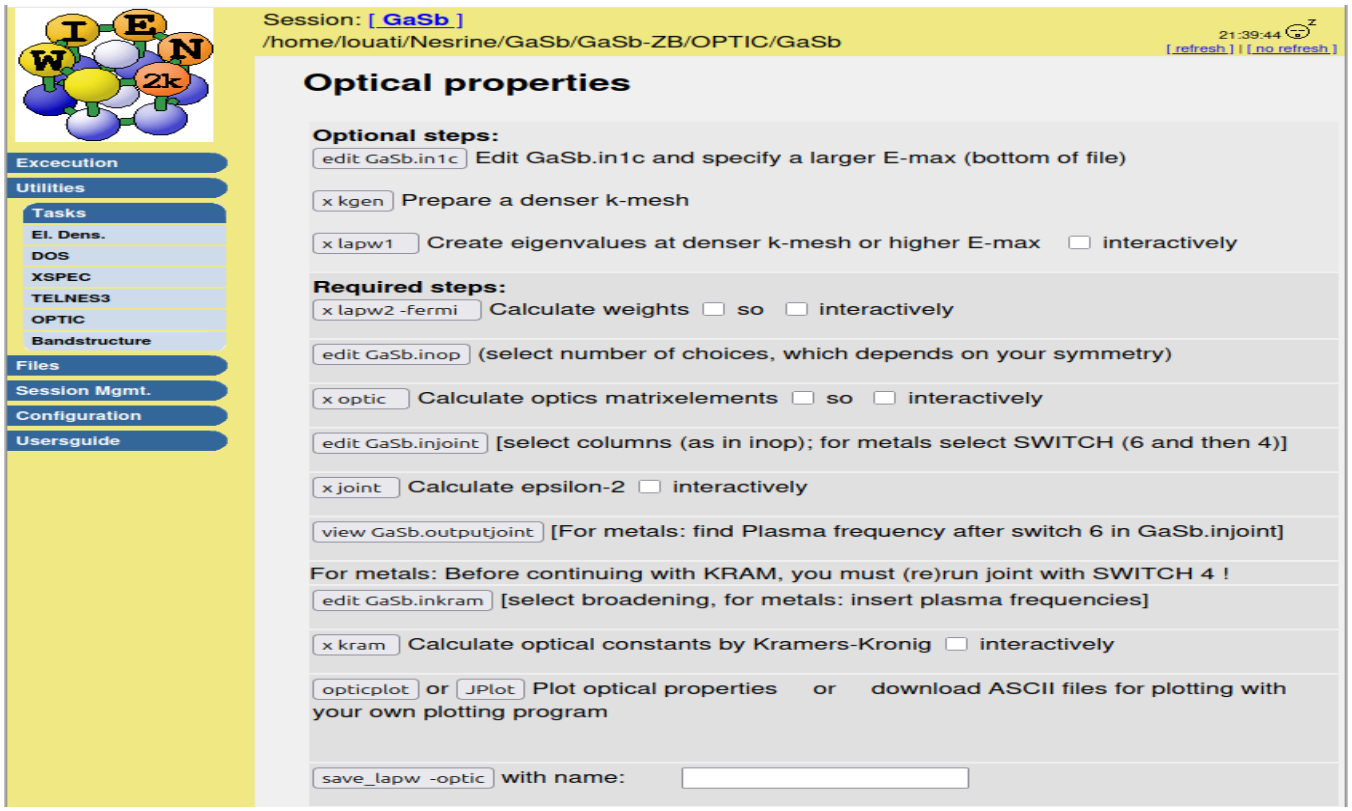


***Figure III. 11**: w2web window for calculating the optical properties*

1. Generate a Dense k-Point Mesh: Use the kgen utility to create a fine and dense k-point mesh for accurate Brillouin zone sampling, essential for optical calculations.
2. Perform Self-Consistent Field (SCF) Calculations: Run the standard SCF cycle including lapw1 and lapw2 modules to obtain converged eigenvalues and eigenvectors:

- Run lapw1 to calculate eigenvalues and eigenvectors,
- Then run lapw2 with the FERMI option.

3. Generate the Vector File: The vector file (case.vector) required by the optic module is generated by lapw1.
4. Calculate Momentum Matrix Elements: Execute the optic program to calculate the symmetrized squared momentum matrix elements corresponding to dipole transitions between occupied and unoccupied states at each k-point. The output files include:
    - case.symmat containing the matrix elements,
    - case.mat_diag for diagonal elements in orthogonal lattices.
5. Perform Brillouin Zone Integration: Use the joint program to integrate the calculated matrix elements over the Brillouin zone and compute the imaginary part of the frequency-dependent dielectric tensor.
6. Obtain Real Part of Dielectric Tensor: Run the kram program to perform a Kramers-Kronig transformation, yielding the real part of the dielectric function.
7. Include Additional Physical Effects
8. Perform Advanced Calculations (Optional)
    - To compute XMCD spectra, prepare a k-mesh covering the entire Brillouin zone,
    - Modify input files to output core wavefunctions and run spin-polarized, spin-orbit-coupled calculations as per WIEN2k guidelines,
    - Run optic with spin-orbit and spin-polarized flags to compute XMCD-relevant matrix elements,
    - Integrate results with joint.

References:

[1] J.C. Slater, Wave functions in a periodic potential, Physical Review 51 (1937) 846.
[2] O.K. Andersen, Linear methods in band theory, Physical Review B 12 (1975) 3060.
[3] E. Wimmer, H. Krakauer, M. Weinert, A.J. Freeman, Full-potential self-consistent linearized-augmented-plane-wave method for calculating the electronic structure of molecules and surfaces: O 2 molecule, Phys. Rev. B 24 (1981) 864–875. https://doi.org/10.1103/PhysRevB.24.864.
[4] D.J. Singh, Planewaves, Pseudopotentials and the LAPW Method, Springer US, Boston, MA, 1994. https://doi.org/10.1007/978-1-4757-2312-0.
[5] Planewaves, Pseudopotentials and the LAPW Method, Springer US, 2006. https://doi.org/10.1007/978-0-387-29684-5.
[6] E. Sjöstedt, L. Nordström, D.J. Singh, An alternative way of linearizing the augmented plane-wave method, Solid State Communications 114 (2000) 15–20. https://doi.org/10.1016/S0038-1098(99)00577-3.
[7] P. Kratzer, J. Neugebauer, The Basics of Electronic Structure Theory for Periodic Systems, Front. Chem. 7 (2019) 106. https://doi.org/10.3389/fchem.2019.00106.
[8] J. Grotendorst, S. Blügel, John von Neumann-Institut für Computing, eds., Computational nanoscience: do it yourself! winter school, 14 - 22 February 2006, Forschungszentrum Jülich, Germany ; lecture notes, NIC-Secretariat, Research Centre Jülich, Jülich, 2006.
[9] C. Kittel, Introduction to Solid State Physics, (n.d.).
[10] S. Cottenier, Density Functional Theory and the family of (L) APW-methods: a step-by-step introduction, Instituut Voor Kern-En Stralingsfysica, KU Leuven, Belgium 4 (2002) 41.
[11] B.S. Kulkarni, S. Krishnamurty, S. Pal, Influence of plane wave cut-off on structural and electronic properties in Sn-BEA and Ti-BEA zeolite water molecule interaction, Chemical Physics Letters 484 (2010) 374–379. https://doi.org/10.1016/j.cplett.2009.11.041.
[12] T. Wang, H. Chen, A. Zhou, Y. Zhou, D. Massatt, Convergence of the Planewave Approximations for Quantum Incommensurate Systems, Multiscale Model. Simul. 23 (2025) 545–576. https://doi.org/10.1137/23M1553650.
[13] J. Sólyom, A modern szilárdtestfizika alapjai, ELTE Eötvös Kiadó, Budapest, 2002.
[14] P. Wisesa, K.A. McGill, T. Mueller, Efficient generation of generalized Monkhorst-Pack grids through the use of informatics, Physical Review B 93 (2016) 155109.
[15] K. Lejaeghere, G. Bihlmayer, T. Björkman, P. Blaha, S. Blügel, V. Blum, D. Caliste, I.E. Castelli, S.J. Clark, A. Dal Corso, S. De Gironcoli, T. Deutsch, J.K. Dewhurst, I. Di Marco, C. Draxl, M. Dułak, O. Eriksson, J.A. Flores-Livas, K.F. Garrity, L. Genovese, P. Giannozzi, M. Giantomassi, S. Goedecker, X. Gonze, O. Grånäs, E.K.U. Gross, A. Gulans, F. Gygi, D.R. Hamann, P.J. Hasnip, N.A.W. Holzwarth, D. Iuşan, D.B. Jochym, F. Jollet, D. Jones, G. Kresse, K. Koepernik, E. Küçükbenli, Y.O. Kvashnin, I.L.M. Locht, S. Lubeck, M. Marsman, N. Marzari, U. Nitzsche, L. Nordström, T. Ozaki, L. Paulatto, C.J. Pickard, W. Poelmans, M.I.J. Probert, K. Refson, M. Richter, G.-M. Rignanese, S. Saha, M. Scheffler, M. Schlipf, K. Schwarz, S. Sharma, F. Tavazza, P. Thunström, A. Tkatchenko, M. Torrent, D. Vanderbilt, M.J. Van Setten, V. Van Speybroeck, J.M. Wills, J.R. Yates, G.-X. Zhang, S. Cottenier, Reproducibility in density functional theory calculations of solids, Science 351 (2016) aad3000. https://doi.org/10.1126/science.aad3000.
[16] M.C. Payne, M.P. Teter, D.C. Allan, T.A. Arias, J.D. Joannopoulos, Iterative minimization techniques for *ab initio* total-energy calculations: molecular dynamics and conjugate gradients, Rev. Mod. Phys. 64 (1992) 1045–1097. https://doi.org/10.1103/RevModPhys.64.1045.
[17] J. Hafner, *Ab-initio* simulations of materials using VASP: Density-functional theory and beyond, J Comput Chem 29 (2008) 2044–2078. https://doi.org/10.1002/jcc.21057.

[18] K. Schwarz, Computation of Materials Properties at the Atomic Scale, in: M.R. Pahlavani (Ed.), Selected Topics in Applications of Quantum Mechanics, InTech, 2015. https://doi.org/10.5772/59108.
[19] P. Blaha, K. Schwarz, F. Tran, R. Laskowski, G.K.H. Madsen, L.D. Marks, WIEN2k: An APW+lo program for calculating the properties of solids, The Journal of Chemical Physics 152 (2020) 074101. https://doi.org/10.1063/1.5143061.
[20] J. Grotendorst, S. Blügel, John von Neumann-Institut für Computing, eds., Computational nanoscience: do it yourself! winter school, 14 - 22 February 2006, Forschungszentrum Jülich, Germany ; lecture notes, NIC-Secretariat, Research Centre Jülich, Jülich, 2006.
[21] S. Cottenier, Density Functional Theory and the Family of (L)APW-methods: a step-by-step introduction, (n.d.).
[22] D.D. Koelling, G.O. Arbman, Use of energy derivative of the radial solution in an augmented plane wave method: application to copper, J. Phys. F: Met. Phys. 5 (1975) 2041–2054. https://doi.org/10.1088/0305-4608/5/11/016.
[23] D. Singh, Ground-state properties of lanthanum: Treatment of extended-core states, Physical Review B 43 (1991) 6388.
[24] D. Singh, H. Krakauer, *H* -point phonon in molybdenum: Superlinearized augmented-plane-wave calculations, Phys. Rev. B 43 (1991) 1441–1445. https://doi.org/10.1103/PhysRevB.43.1441.
[25] D.J. Singh, K. Schwarz, P. Blaha, Electric-field gradients in YBa 2 Cu 3 O 7 : Discrepancy between experimental and local-density-approximation charge distributions, Phys. Rev. B 46 (1992) 5849–5852. https://doi.org/10.1103/PhysRevB.46.5849.
[26] S. Goedecker, K. Maschke, Alternative approach to separable first-principles pseudopotentials, Phys. Rev. B 42 (1990) 8858–8863. https://doi.org/10.1103/PhysRevB.42.8858.
[27] C. Ambrosch-Draxl, Augmented planewave methods, Physica Scripta 2004 (2004) 48.
[28] A.V. Nikolaev, D. Lamoen, B. Partoens, Extension of the basis set of linearized augmented plane wave (LAPW) method by using supplemented tight binding basis functions, The Journal of Chemical Physics 145 (2016) 014101. https://doi.org/10.1063/1.4954962.
[29] G.K.H. Madsen, P. Blaha, K. Schwarz, E. Sjöstedt, L. Nordström, Efficient linearization of the augmented plane-wave method, Phys. Rev. B 64 (2001) 195134. https://doi.org/10.1103/PhysRevB.64.195134.
[30] M. Weinert, E. Wimmer, A.J. Freeman, Total-energy all-electron density functional method for bulk solids and surfaces, Phys. Rev. B 26 (1982) 4571–4578. https://doi.org/10.1103/physrevb.26.4571.
[31] P. Blaha, K. Schwarz, P. Sorantin, S.B. Trickey, Full-potential, linearized augmented plane wave programs for crystalline systems, Computer Physics Communications 59 (1990) 399–415. https://doi.org/10.1016/0010-4655(90)90187-6.
[32] D.K. Schwarz, An Augmented Plane Wave + Local Orbitals Program for Calculating Crystal Properties, (n.d.).
[33] T. Ruh, Optimizing the Density Functional Theory Code WIEN2k, (n.d.).
[34] K. Schwarz, P. Blaha, Solid state calculations using WIEN2k, Computational Materials Science 28 (2003) 259–273. https://doi.org/10.1016/S0927-0256(03)00112-5.
[35] K. Schwarz, P. Blaha, G.K.H. Madsen, Electronic structure calculations of solids using the WIEN2k package for material sciences, Computer Physics Communications 147 (2002) 71–76. https://doi.org/10.1016/S0010-4655(02)00206-0.

[42] Carnegie Mellon University. WIEN2k Quick Start Guide. Euler Cluster Documentation. Accessed August14,2025. https://euler.phys.cmu.edu/cluster/WIEN2k/3Quick_Start.html#SECTION04211000000000000000

[37] A. Kokalj, Computer graphics and graphical user interfaces as tools in simulations of matter at the atomic scale, Computational Materials Science 28 (2003) 155–168. https://doi.org/10.1016/S0927-0256(03)00104-6.

[38] V. Lucarini, K.-E. Peiponen, J.J. Saarinen, E.M. Vartiainen, eds., Kramers-Kronig Relations and Sum Rules in Linear Optics, in: Kramers-Kronig Relations in Optical Materials Research, Springer, Berlin, Heidelberg, 2005: pp. 27–48. https://doi.org/10.1007/3-540-27316-6_4.

Chapter IV:

Results and discussions

IV.1. Introduction

Motivated by the remarkable properties of both gallium nitride alloys and double perovskites, we conduct a detailed study to examine the structural, phase transition, electronic, optical, elastic and mechanical behavior, in addition thermal properties in zinc blende structure characteristics for $YN_{1-x}Sb_x$ III - V (Y=B, Al and Ga) ternary alloys at different composition x = 0, 0.25, 0.5, 0.75 and 1. Furthermore, we investigate the structural, electronic, optical, elastic, mechanical, and thermal characteristics of Sr_2NaXCl_6 (X = Cl, Br and I) double perovskites oxide.

IV.2. Methodology

In our work all calculation are performed thought the Wien2k [1] code package based on Density Functional Theory (DFT) [2,3]. It realized by Full Potential Linearized Augmented Plane Wave (FP - LAPW) method [4–6], for solving the many body system of interacting electrons which represented by the Kohn – Sham equations [7] in order to obtain the total energy and therefore determine the properties of systems. For III - V ternary alloys, the adopted exchange - correlation (XC) potentials for structural, elastic and thermal properties is WC-GGA scheme[8], while for double perovskite materials the PBEsol [9] is adopted. Electronic properties calculated thought the modified Becke – Johnson scheme [10] developed by Tran and Blaha then modified by Becke and Johnson (TB - mBJ) [11] and improved mBJ by D. Koller and al (KTB - mBJ) [12]. However, we adopt KTB - mBJ potential schemes for Density of states (DOS) and optical properties. Elastic properties are computed using the IRelast package in conjunction with WIEN2k code, while the transition phase and thermal properties have studied by using GIBBS2 package [13] based on the quasi-harmonic Debye model [14].

In the FP - LAPW method, the muffin-tin radius (R_{MT}) refers to the radius of non-overlapping spheres around each atom within which the potential and wave functions are expanded in spherical harmonics. The R_{MT} values for III-V ternary alloys and double perovskite compounds are listed in ***Table IV.1*** and ***Table IV.2***, respectively, were optimized to maximize the sphere size without overlapping neighboring spheres, and to avoid charge leakage from the atomic core regions. Inside these spheres, spherical harmonics expansion is often carried out up to a maximum angular momentum quantum number $l_{max} = 10$. The plane wave basis expansion in the interstitial region is controlled by the cutoff parameter $R_{MT}.K_{max}$ which is conventionally set to 8 for III-V ternary alloys and 7 for double perovskites in which this parameter influences the size of the secular matrix and the convergence and accuracy of the calculations. The Fourier

expansion of the charge density uses a cutoff parameter G_{max}=12 a.u.$^{-1}$ effectively representing the reciprocal space resolution. Convergence is assured by tightening the total energy change criterion of 10 $^{-5}$ Ry.

The sampling of Brillouin zone is with:

- (14×14×14) generated K - mesh for binary compounds.
- (7×7×7) generated K - mesh for ternary compounds.
- (14×14×14) generated K - mesh for double perovskites materials.

Table IV. 1:Adopted values of the muffin-tin radius (R_{MT}) for YN1-xSbx (Y = B, Al and Ga) alloy at x=0.0, 0.25, 0.50, 0.75 and 1.0 s in ZB structure

Alloys			0.0	0.25	0.50	0.75	1.0
$BN_{1-x}Sb_x$	R_{MT} (a.u)	B	1.30	1.39	1.54	1.63	1.70
		N	1.43	1.72	1.90	2.02	
		Sb		1.89	2.08	2.21	2.30
$AlN_{1-x}Sb_x$	R_{MT} (a.u)	Al	1.73	1.71	1.97	2.08	2.17
		N	1.64	1.8	2.07	2.20	
		Sb		1.98	2.28	2.42	2.50
$GaN_{1-x}Sb_x$	R_{MT} (a.u)	Ga	4.42	1.90	2.07	2.19	2.28
		N	1.6	1.80	1.97	2.08	
		Sb		1.00	2.18	2.30	2.40

Table IV. 2: Adopted values of the muffin-tin radius (R_{MT}) for Sr_2NaXO_6 (X=Cl, Br and I) double perovskites

Alloys	Sr	Na	X			O
			Cl	Br	I	
Sr_2NaClO_6	2.40	1.73	1.67			1.67
Sr_2NaBrO_6	2.34	1.75		1.77		1.60
Sr_2NaIO_6	2.49	1.79			1.85	1.59

IV.3. Properties of $YN_{1-x}Sb_x$ (Y = B, Al and Ga) Alloys (x = 0, 0.25, 0.50, 0.75 and 1)

IV.3.1. Structural properties

The initial step of our calculations is analyzing the most stable structure for the binary compounds BN, BSb, AlN, AlSb, GaN and GaSb, along with their ternary alloys in $YN_{1-x}Sb_x$ (Y = B, Al and Ga) system, in which x = 0.25, 0.50 and 0.75. To achieve this, we carried out the total energy calculations as a function of volume for various candidate structures, including zinc blende (ZB), sodium chloride (NaCl), cesium chloride (CsCl), and wurtzite (WZ). The results obtained from these calculations, represented in ***Figure IV.1, Figure IV.2*** and ***Figure IV.3*** for $BN_{1-x}Sb_x$,

$AlN_{1-x}Sb_x$ and $GaN_{1-x}Sb_x$, respectively, identify the structure with the lowest energy curves, indicating the most stable structure.

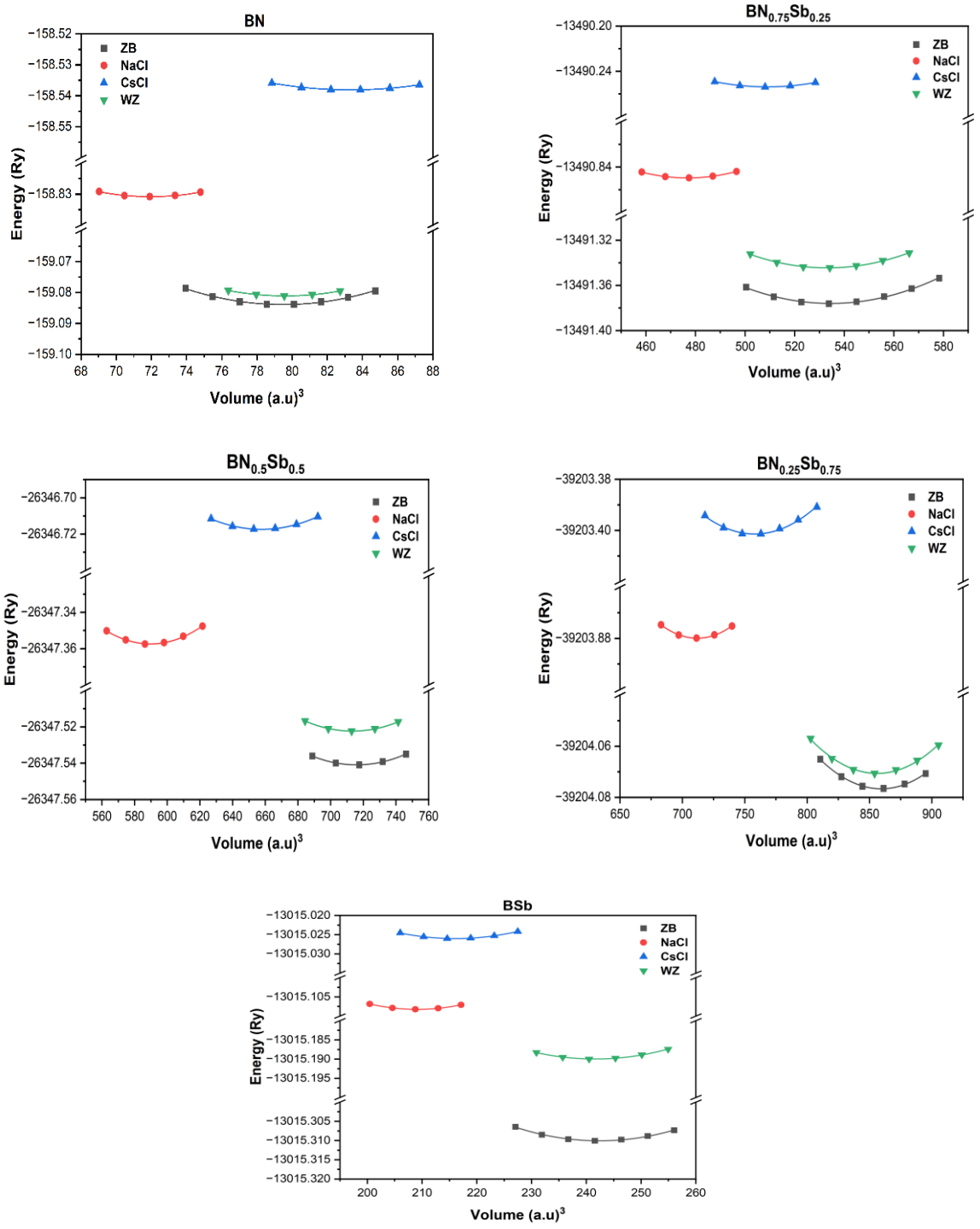


Figure IV. 1: ***The total energy volume curves for $BN_{1-x}Sb_x$ x=0, 0.25, 0.50, 0.75 and 1) alloys***

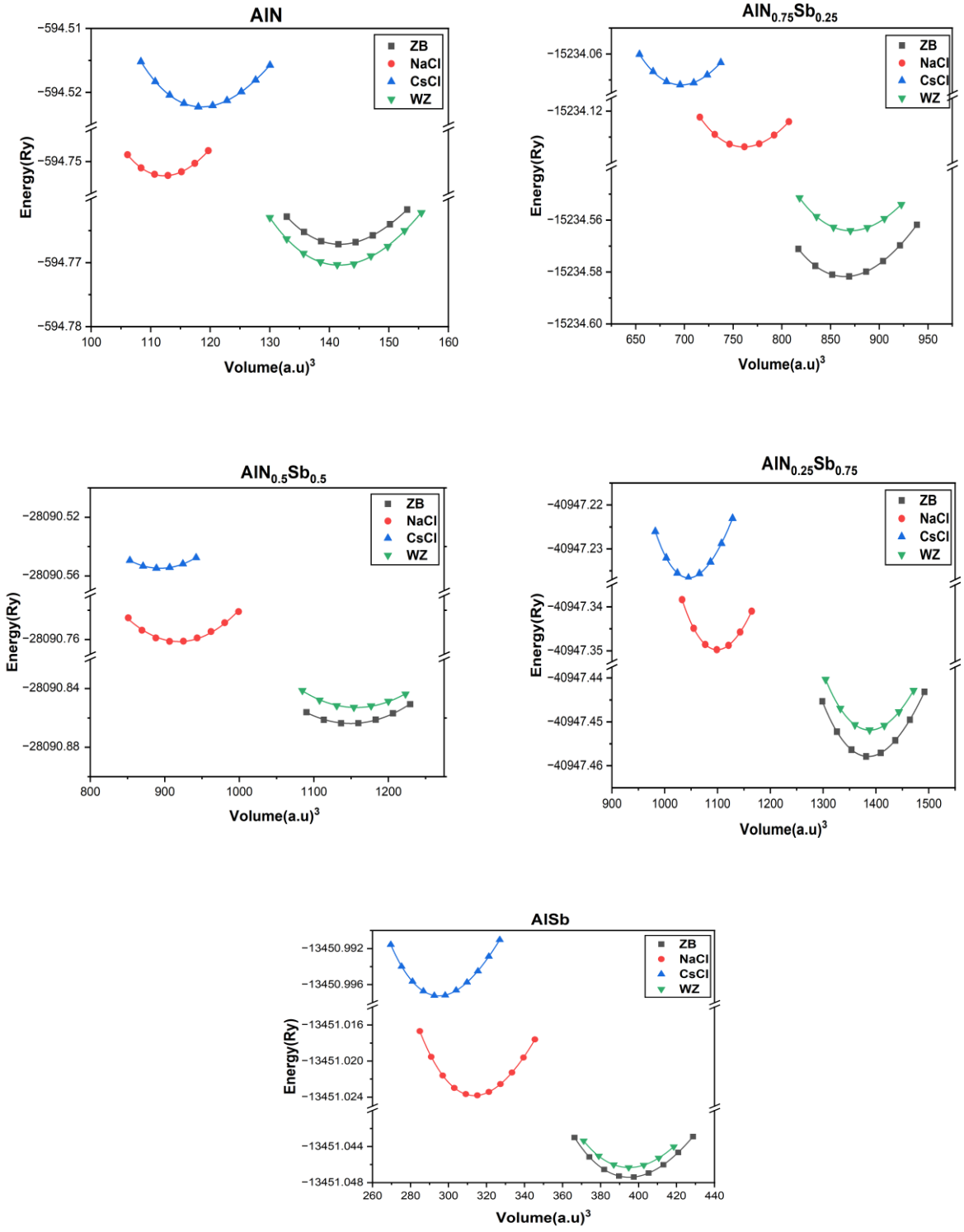


Figure IV. 2: The total energy volume curves for $AlN_{1-x}Sb_x$(x=0, 0.25, 0.50, 0.75 and 1). alloys

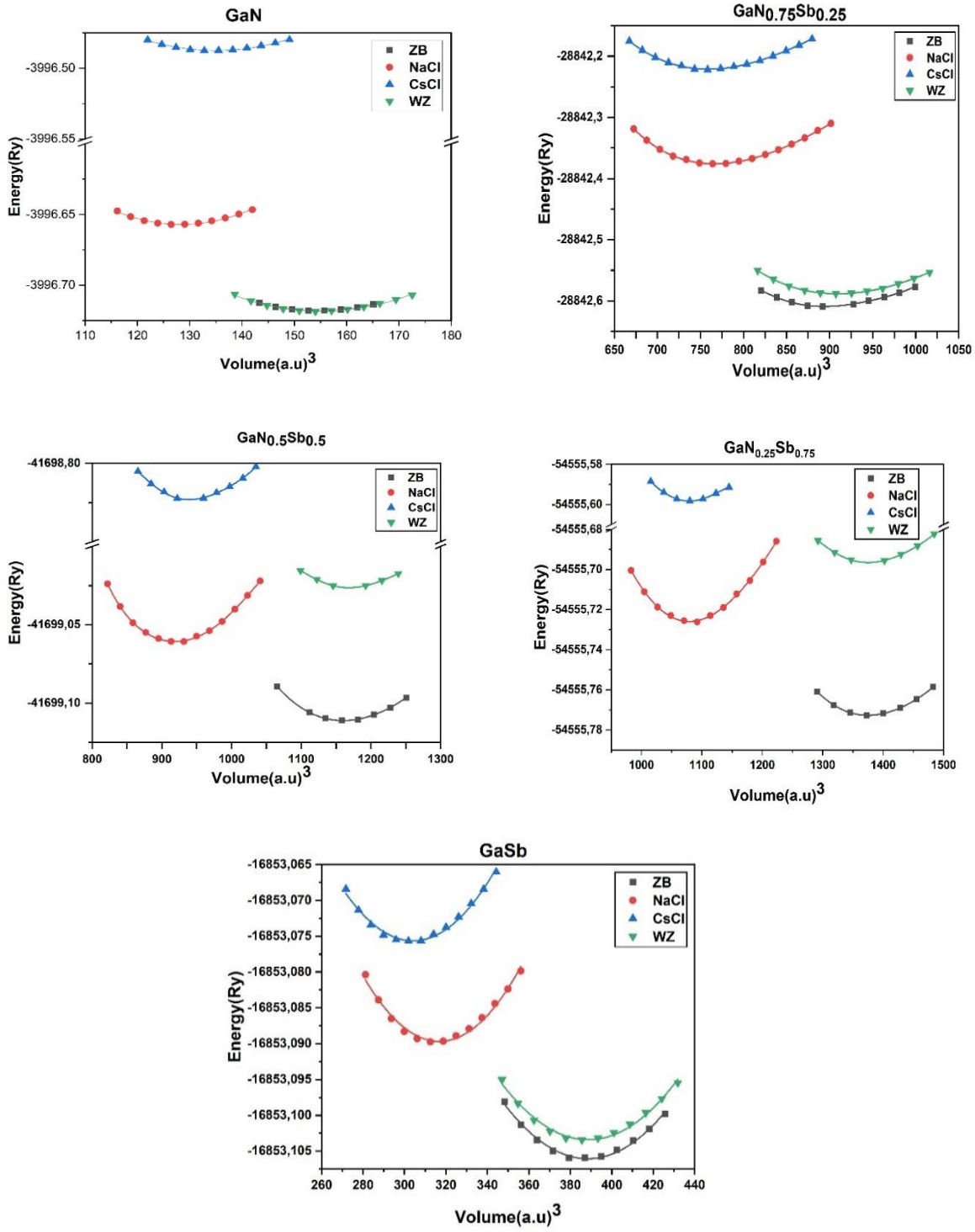


Figure IV. 3: ***The energy versus volume curve of $GaN_{1-x}Sb_x$ ternary alloys with $x = \{0, 0.25, 0.50, 0.75 \text{ and } 1\}$.***

As shown in ***Figure IV.1, Figure IV.2*** and ***Figure IV.3,*** $BN_{1-x}Sb_x$ (x = 0, 0.25, 0.50, 0.75 and 1) alloys, $AlN_{1-x}Sb_x$ (x = 0.25, 0.50, 0.75 and 1) alloys and $GaN_{1-x}Sb_x$ (x= 0.25, 0.50, 0.75 and 1) ternary alloys exhibited the lowest total energy per unit cell in the zinc blende structure. Indicating it is the most stable phase at P =0 GPa. With reduced stability in the wurtzite (WZ) then sodium chloride (NaCl) structures, and the lowest stability in the cesium chloride (CsCl) phase. While Both of AlN (x = 0 in $AlN_{1-x}Sb_x$ system) and GaN (x = 0 in $GaN_{1-x}Sb_x$ system) found stable in the wurtzit structure which is only marginally more stable than the zinc blende phase, with a minimal energy difference of only 0.001 eV. This finding is not surprising, as both the zinc blende and wurtzite phases exhibit tetrahedral local bonding, differing primarily in their second-nearest-neighbor interactions [15,16].

For BN compound, the two most commonly studied structures are hexagonal and cubic notably; experimental phase diagrams based on thermodynamic and in situ x-ray diffraction measurements strongly suggest that ZB structure is more stable than WZ structure under normal conditions [17,18]. For BSb, the LDA ab initio findings performed by S. Daoud [19] and M. Benchehima and al [20] demonstrate that the ZB structure is energetically favored and more stable than the NaCl structure. For AlN our results are agree with those given by A. Siegel and al [21] obtained using the VASP package, also the results given by K. Karch and al [22] investigated using the plane-wave pseudo-potential approach within the Local Density Approximation (LDA). In the case of AlSb, obtained results are in accordance with those given by P. Rodriguez-Hernandez and al [23] based on the First Principles Self-Consistent Local Density calculations with non-local pseudo-potentials. The studies by A. Bendahah and al [24] using first principles calculations within Density Functional Theory (DFT), have shown that GaN and Sc-doped GaN favor the wurtzite phase as the thermodynamically stable structure under ambient conditions. This stability is attributed to the wurtzite phase lower formation energy and strong bond geometry. The stability analysis of these phases, coupled with the investigation of other properties, reveals only marginal differences, prompting us to extend our analysis to the zinc blende phase for a more comprehensive comparison. In contrast, GaSb exhibits the lowest energy in the zinc blende structure, consistent with findings reported in previous studies [25,26].

Based on the Murnaghan's equation of state [27], we have identified the ground state structural parameters for $YN_{1-x}Sb_x$ (Y=B, Al and Ga) ternary Alloys in the ZB phase as the lattice

constant (a_0), the bulk modulus (B_0) are listed in ***Table IV. 3*** and compare them with experimental and theoretical values from the literature.

Table IV. 3: *Lattice constant and bulk modulus of $YN_{1-x}Sb_x$ (Y=B, Al and Ga) (x=0, 0.25, 0.50, 0.75 and 1) ternary alloys in the ZB phase*

Alloys	x	Lattice constant a_0 $(°A)$			Bulk modulus $B_0(GPa)$		
$BN_{1-x}Sb_x$		Our work	Exp.	Other calc.	Our work	Exp.	Other calc.
	0	3.6085	3.615[28]	3.623[29] 3.574[30] 3.6081[31] 3.63[32]	386.2550	369[28]	385.54[31] 371.24[32]
	0.25	4.2903			196.4595		
	0.50	4.7326			139.5945		
	0.75	5.0272			114.1735		
	1	5.2331	5.21 [33]	5.2291[31] 5.139 [19] 5.1911[34] 5.2306[35]	105.6360		106.37[31] 107.7[19] 110.96[34] 106.8[35]
$AlN_{1-x}Sb_x$	0	4.379		4.38 [36] 4.37[37] 4.32[38] 4.35[39] 4.34[40]	202.1044		202.82[36] 203.80[37] 203[38] 211.78[39] 197.27[40]
	0.25	5.0415			107.1430		
	0.50	5.5391			74.4107		
	0.75	5.8990			60.2860		
	1	6.1636	6.1361[41,42]	6.166[43] 6.236[44] 6.22 [45] 6.086 [23]	53.8300	57.3[46]	54.41[43] 58.70 [44] 51.27 [45] 58[23]
$GaN_{1-x}Sb_x$	0	4.50	4.50 [41,47]	4.554 [48] 4.48[49] 4.51[50]	191.44	205 [51]	175[48] 206.30[49] 201[38]
	0.25	5.10			100.32		
	0.50	5.56			70.03		
	0.75	5.89			57.97		
	1	6.12	6.10 [51]	6.10[26] 6.20[52]	52.74	56.3 [53]	51.8[26] 46.03[52]

As an overview, the ***Table IV. 3*** demonstrates that our results are in good agreement with experimental data and previously reported theoretical calculations, confirming the accuracy of our findings. To clarify further, the experimental values of lattice constant, bulk modulus for boron nitride differs from the calculated ones by only $0.0068°A$, $17GPa$ and $0.299GPa$ respectively. While for boron antimony, the lattice parameter differ by $0.0231°A$. The published results of

lattice constant and bulk modulus obtained by D. Bouragba and al [31] using (GGA-PBEsol) approach shown strong alignment with obtained results corresponding to a relative deviation of about 0.01% and 0.18% , respectively for BN and about 0.07% and 0.69% respectively for BSb. The AlN and AlSb binary compounds are in good harmony with results given by R. Moussa [36] and H. Salehi [43] obtained using the same approximation. For AlN, we remark unviability experimental data, however the experimental lattice parameter obtained using x-ray diffraction [41,42] for AlSB is in good accordance with our obtained value, however, B_0 obtained from angular resolved XRD and given in ref [46] are larger than our obtained results. The theoretical results using the Local Density Approximation [23,37,40] or Perdew – Burke - Ernzerhof (PBE) - GGA approximation [44,45] shown a good agreement with our calculated lattice parameter, however, a small deviation in bulk modulus compared with our results. The computed lattice constant and bulk modulus values for the GaN and GaSb compounds are also exhibit strong agreement with experimental [41,47,51,53] and theoretical data reported [26,48,54] although no such data are available for the ternary alloys. For the ternary compounds $YN_{1-x}Sb_x$ (Y = B, Al and Ga) systems no references are available in the literature, so the present work can be considered an important reference for the future experimental investigations.

In order to place our findings for $BN_{1-x}Sb_x$ in context, we compare our results with those reported for the related $BSb_{1-x}N_x$ alloys studied by D. Bouragba and al [31] and F. El Haj Hassan [55]. Since both alloy formulations describe the same binary end-members (BN and BSb) but with inverted composition notation, of lattice constant and bulk modulus for $BN_{1-x}Sb_x$ (x = 0.25, 0.50 and 0.75) and $BSb_{1-x}N_x$ (x = 0.25, 0.50 and 0.75) alloys are presented in ***Table IV.4.***

Table IV. 4: *Lattice constant a_0 $(°A)$ and bulk modulus $B_0(GPa)$ for $BN_{1-x}Sb_x$ (x = 0.25, 0.50 and 0.75) and $BSb_{1-x}N_x$ (x = 0.25, 0.50 and 0.75) alloys*

	$BN_{1-x}Sb_x$ (x = 0.25, 0.50 and 0.75)			$BSb_{1-x}N_x$ (x = 0.25, 0.50 and 0.75)		
	$BN_{0.75}Sb_{0.25}$	$BN_{0.5}Sb_{0.5}$	$BN_{0.5}Sb_{0.5}$	$BSb_{0.25}N_{0.75}$	$BSb_{0.5}N_{0.5}$	$BSb_{0.75}N_{0.25}$
a_0 $(°A)$	4.2903	4.7326	5.0272	4.2919[31]	4.725[31]	5.0163[31]
				4.320[55]	4.770[55]	5.066[55]
$B_0(GPa)$	196.4595	139.5945	114.1735	180.0904[31]	134.2951[31]	116.5398[31]
				188[55]	133[55]	108[55]

The comparison demonstrates that both lattice constant and bulk modulus values for $BN_{0.75}Sb_{0.25}$, $BN_{0.5}Sb_{0.5}$ and $BN_{0.5}Sb_{0.5}$ shown a good alignment with $BSb_{0.25}N_{0.75}$, $BSb_{0.5}N_{0.5}$ and $BSb_{0.75}N_{0.25}$, respectively. On the other hand, both of $BN1_{-x}Sb_x$ and $BN_{1-x}Sb_x$ follow the same

physical tendency: lattice expansion accompanied by a reduction in mechanical rigidity with increasing substitution of larger atoms. This consistent behavior provides confidence in the accuracy of the present $BSb_{1-x}N_x$ calculations.

Table IV. 3, shown clearly inverse relationship between lattice parameter and bulk modulus as Sb concentration increase, in which lattice parameter increase while bulk modulus decrease. According to Vegard's law [56], the variation of lattice parameter and bulk modulus as a function of Sb concentration can be written as:

$$y_{a_0}(x) = x.a_0(BSb) + (1-x)a_0(BN) - x(1-x)b_1 \quad \textit{(IV. 1)}$$

$$y_{B_0} = x.B_0(BSb) + (1-x)B_0(BN) - x(1-x)b_2 \quad \textit{(IV. 2)}$$

For more details, we have plot the lattice parameter and bulk modulus for $YN_{1-x}Sb_x$ (Y = B, Al and Ga) alloys. We have plot the lattice parameter and bulk modulus for $YN_{1-x}Sb_x$ *(x=0, 0.25, 0.50, 0.75 and 1)* alloys as function of Sb concentration as shown in ***Figure IV.4***

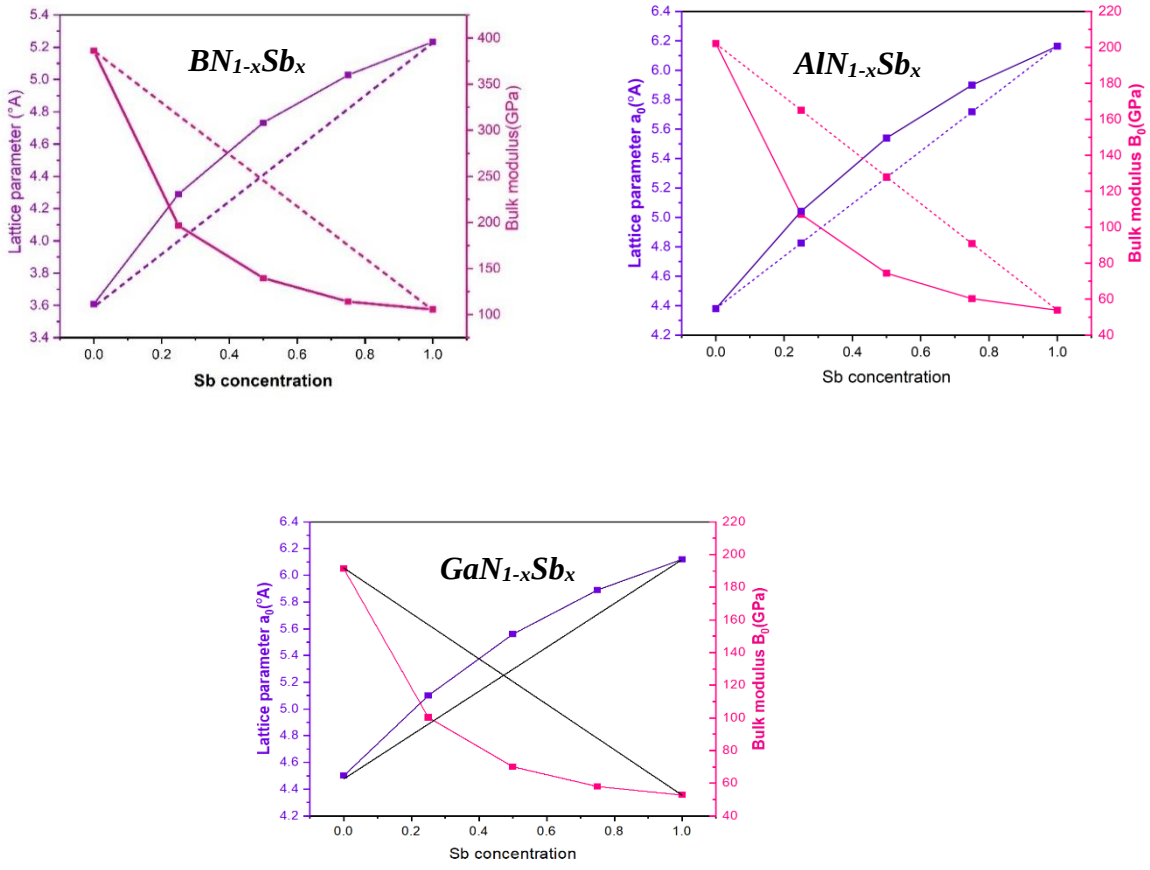


Figure IV. 4: ***Lattice parameter and bulk modulus variation with Sb concentration in $YN_{1-x}Sb_x$ (Y = B, Al and Ga) ternary alloys in zinc blende phase.***

Figure IV. 4 demonstrate the inverse proportion relation between lattice parameter and bulk modulus $\left(a_0 \ \alpha \ \frac{1}{B_0}\right)$, in which the lattice parameter increase nonlinearly and the bulk modulus decrease nonlinearly with the Sb concentration. The substituted of N with Sb does not introduce significant lattice distortion or bowing, in contrast with bulk modulus. the bowing parameter value of $-1{,}2565$ °A , $-1{,}0684$ °A and $-0{,}99429$ °A in an upward direction for lattice parameter and equal 450,24GPa, 223,5638GPa and 217.1542GPa in downward direction for bulk modulus for $YN_{1-x}Sb_x$ (Y = B, Al and Ga) systems respectively. This deviation from linear composition dependence is due to the highly mismatched of lattice constant and bulk modulus of our two binary compounds (YN and YSb) in which (Y = B, Al and Ga), respectively. The reported lattice constant bowing parameters for the $BSb_{1-x}N_x$ alloys (-1.285 °A [55] and -1.2287 °A [31]) are very close to our calculated bowing parameter of -1.2565 °A for the $BN_{1-x}Sb_x$ alloy. Similarly, the reported bulk-modulus bowing parameters ($428\ GPa$ [55] $439.147\ GPa$ [31]) are in good agreement of our calculated value of $450{,}24\ GPa$.

IV.3.2. Structural transition phase

To determine the critical pressure corresponding to the phase transition $YN_{1-x}Sb_x$ (Y = B, Al and Ga) alloys, we have calculated for each structure (ZB, NaCl, CsCl, and WZ) .Then we have plot the enthalpy versus pressure as shown in ***Figure IV.5***, ***Figure IV.6*** and ***Figure IV.7*** for $BN_{1-x}Sb_x$, $AlN_{1-x}Sb_x$ and $GaN_{1-x}Sb_x$ systems.

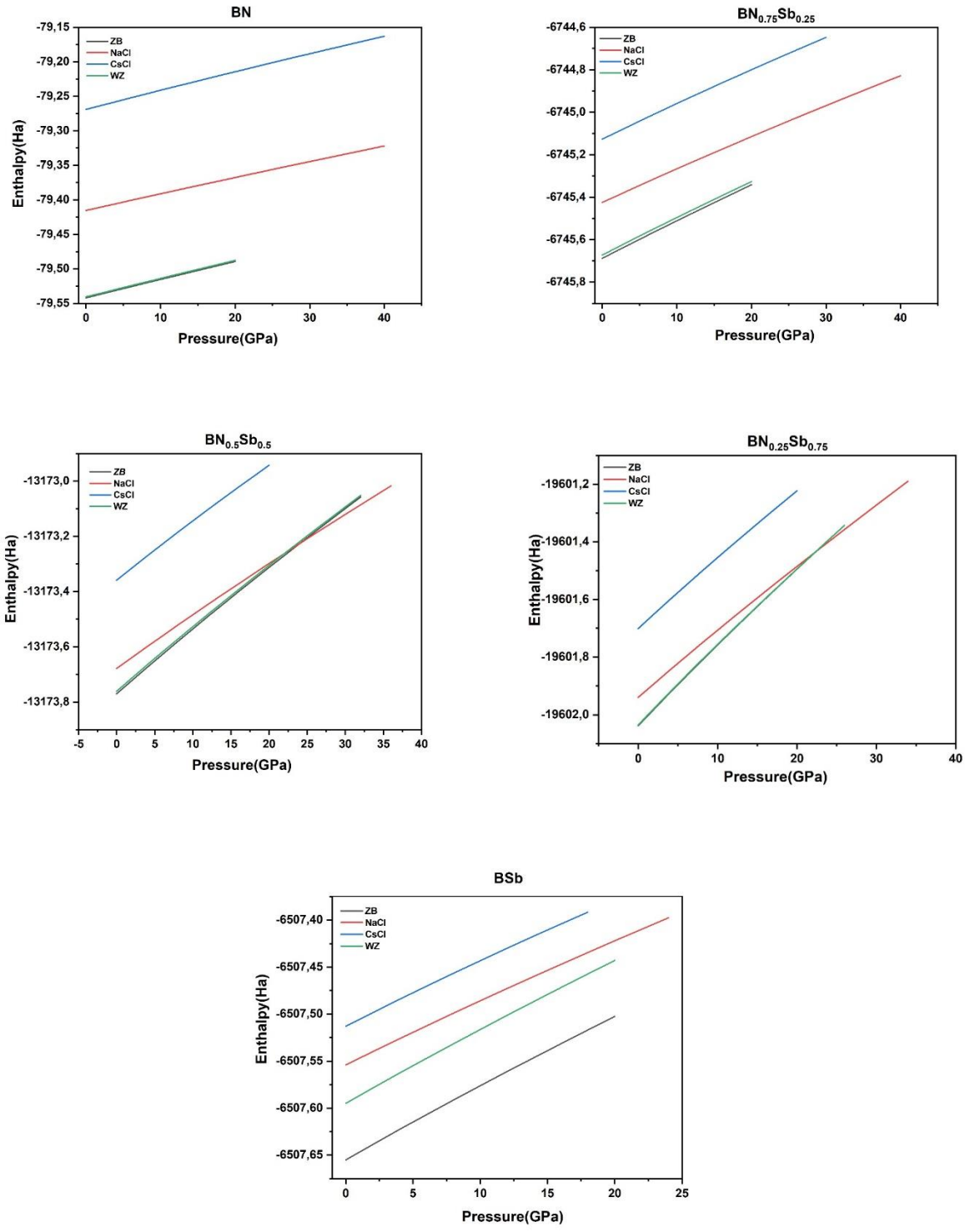


Figure IV. 5: ***Enthalpy (Ha) variation versus pressure (GPa) for ZB, NaCl, CsCl, WZ phases for $BN_{1-x}Sb_x$ (x=0, 0.25, 0.50, 0.75 and 1) alloys***

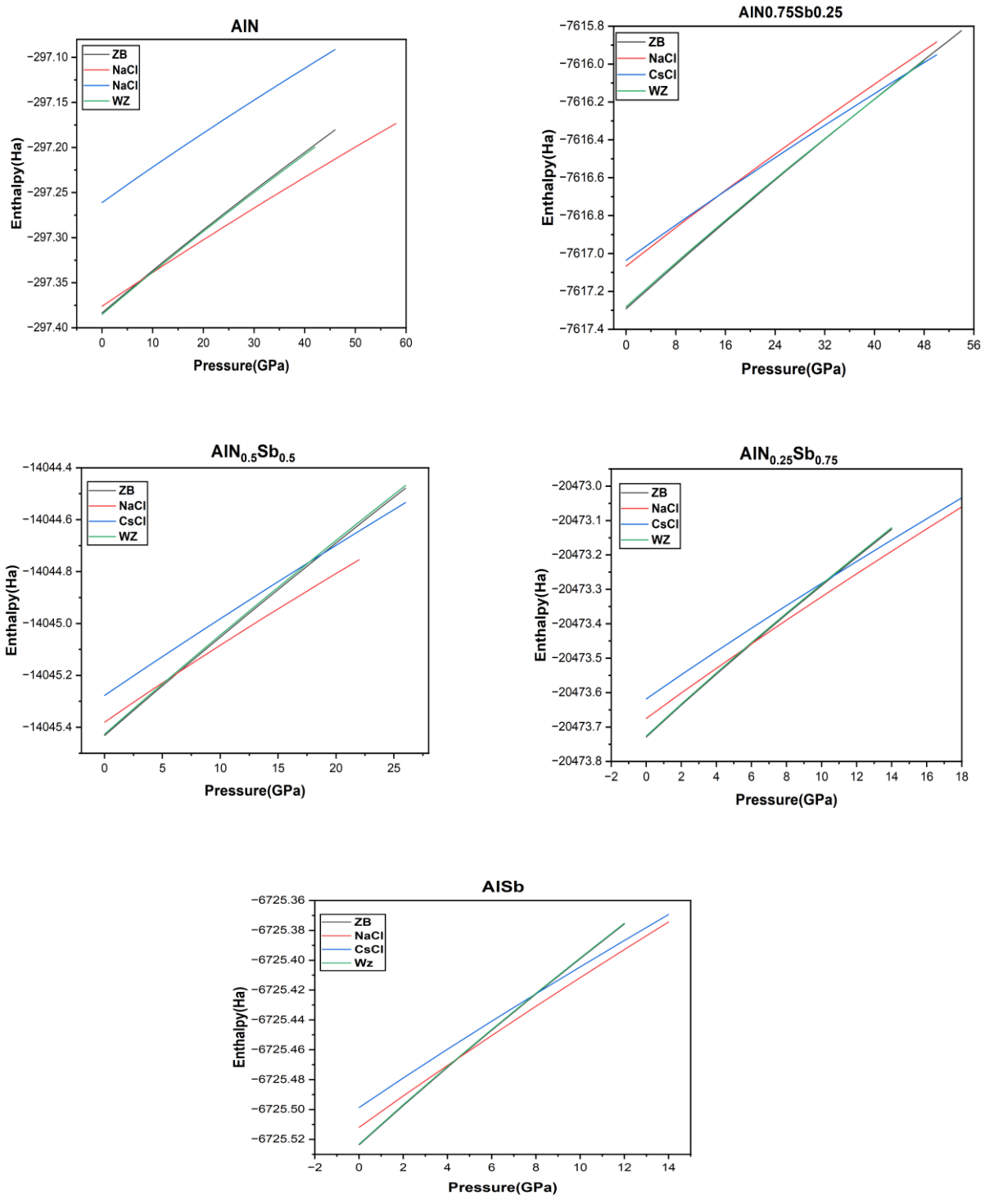


Figure IV. 6: ***Enthalpy (Ha) variation versus pressure (GPa) for ZB, NaCl, CsCl, WZ phases for $AlN_{1-x}Sb_x$ (x=0, 0.25, 0.50, 0.75 and 1) alloys***

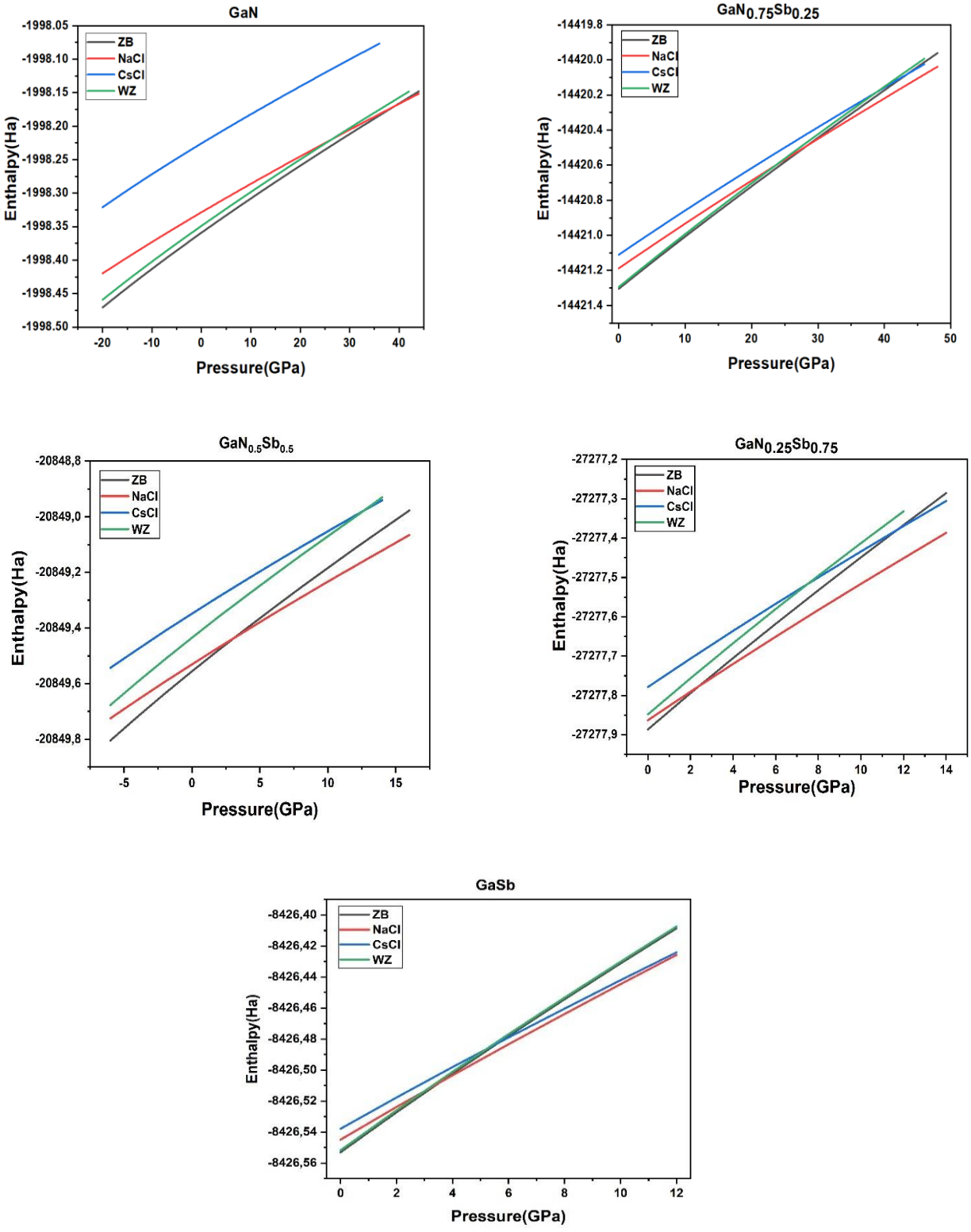


Figure IV. 7: Enthalpy (Ha) variation versus pressure (GPa) for ZB, NaCl, CsCl, WZ phases for $GaN_{1-x}Sb_x$ (x=0, 0.25, 0.50, 0.75 and 1) alloys

The pressure at which two curves intersect identifies the critical transition pressure between the studied phases. The obtained results for $AlN_{1-x}Sb_x$ and $GaN_{1-x}Sb_x$ are presented in **Table IV. 5.**

Table IV. 5: Critical pressure for NaCl, CsCl, ZB, and WZ phases for $AlN_{1-x}Sb_x$ and $GaN_{1-x}Sb_x$ alloys

$AlN_{1-x}Sb_x$	x	Transition phase	Critical pressure		
			Our work	Exp.	Other calc.
	0.0	$NaCl \rightarrow ZB$ $NaCl \rightarrow WZ$	7.55 9.53	0 – 14[57], 22.9 [58]	8[40], 7.1[59] 13.5[40], 15[60],16.6[61,62], 13.3[63]
	0.25	$NaCl \rightarrow CsCL$ $ZB \rightarrow WZ$ $CsCl \rightarrow ZB$ $CsCl \rightarrow WZ$	14.67 37.30 45.2 46.00		
	0.5	$NaCl \rightarrow WZ$ $NaCl \rightarrow ZB$ $CsCl \rightarrow WZ$ $CsCl \rightarrow ZB$	5.51 6.33 17.68 18.90		
	0.75	$NaCl \rightarrow WZ$ $NaCl \rightarrow ZB$ $CsCl \rightarrow WZ$ $CsCl \rightarrow ZB$	5.62 5.97 10.22 10.65		
	1.0	$NaCl \rightarrow ZB$ $NaCl \rightarrow WZ$ $CsCl \rightarrow WZ$ $CsCl \rightarrow ZB$	4.51 4.35 7.92 8.02	8.3±0.3[64], 6.6[65]	5.3[66], 5.6[67], 8[68], 4.59[69] 7.81[69] 8.24[69]
$GaN_{1-x}Sb_x$	0	$WZ \rightarrow NaCl$ $ZB \rightarrow NaCl$	26.43 39.18	37[70]	38.10[48] 38.15[48], 38.21[71]
	0.25	$ZB \rightarrow NaCl$ $WZ \rightarrow CsCl$ $WZ \rightarrow CsCl$ $ZB \rightarrow CsCl$	28.20 23.66 38.81 43.5		
	0.5	$ZB \rightarrow NaCl$ $WZ \rightarrow CsCl$	3.16 12.69		
	0.75	$ZB \rightarrow NaCl$ $WZ \rightarrow CsCl$ $ZB \rightarrow CsCl$	2.41 7.52 11.73		
	1	$WZ \rightarrow NaCl$ $ZB \rightarrow NaCl$ $WZ \rightarrow CsCl$ $ZB \rightarrow CsCl$	2.96 3.51 5.17 5.66	7.6[72]	5.41[26], 4[73]

For $BN_{1-x}Sb_x$ system, no transition phase is observed for both binary compounds (BN and BSb) and for $BN_{0.75}Sb_{0.25}$ alloy. However, for $BN_{0.75}Sb_{0.25}$ a transition $WZ \rightarrow NaCl$ at 22.09 GPa followed by a $ZB \rightarrow NaCl$ transition at 23.70 GPa. A similar behavior is observed for the $BN_{0.25}Sb_{0.75}$ alloy, which also transforms into the $NaCl$ phase at critical pressure around 21.92 GPa. The works of C. He and al [74] also of W. J. Yu and al [75] demonstrate that transition phase from $WZ \rightarrow ZB$ is kinetically forbidden, although both phases are sp^3-bonded, but have incompatible stacking (ABCABC… in ZB structure and ABAB… in wurtzite structure. Converting from ABC to AB stacking requires a collective shear of all atomic layers and the breaking/reforming of the entire tetrahedral bond network. This produces an extremely large activation barrier and no low-energy crystallographic pathway so such this transformations have very high-energy barriers. On the other hand, the study by A. Zaoui and al [76] using the WEIN97 code with FP - LAPW method reports a structural phase transition from ZB structure to the NaCl phase at an extremely high pressure of approximately 550 GPa for BN and about 216 GPa for BSb. While for BN, a reported pressure of 1110 GPa given by RM. Wentzcovitch and al [77]. For BSb a different critical pressure values of 59 GPa and 68GPa given by E. Deligoz and al [78] and by El Haj Hassan and al [79], respectively. This result highlights the very high-pressure stability range of the ZB structure before transforming to the more densely packed NaCl structure, also reflect the strong covalent bonding and structural stiffness present. For AlN the value of transition pressure from the ZB structure into the NaCl structure is in good agreement with that reported by S. Louhibi-Fasla and al [40] and by M.B. Kanoun and al [59] using the Local Density Approximation (LDA) approximation. We also report transition pressure from WZ to NaCl at 9.53 GPa, this value obey the experimental value data given in reference [57], however, a large deviation from the experimented values given in reference [58], on the other hand, it's smaller the other calculations [40,60–63]. For AlSb, our results are in well agreement with those given by L. Salmi [69]. We predict a transition pressure value from ZB structure to NaCl structure, this value is in accordance with the values given by P. Capper and al [66] and by S. B. Zhang [67], but it's smaller than the experimental values [64,65] and the investigated one given by D. Varshneya [68]. The calculated transition pressures for gallium nitride, from wurtzite and zinc blende to NaCl, are 26.43GPa and 39.18GPa, respectively. These values indicate that the transition from the wurtzite to NaCl phase occurs at a lower pressure than the experimental data reported by H. Xia and al.[70] and theoretical predictions [48]. Nevertheless, the remaining results are in good agreement with earlier studies

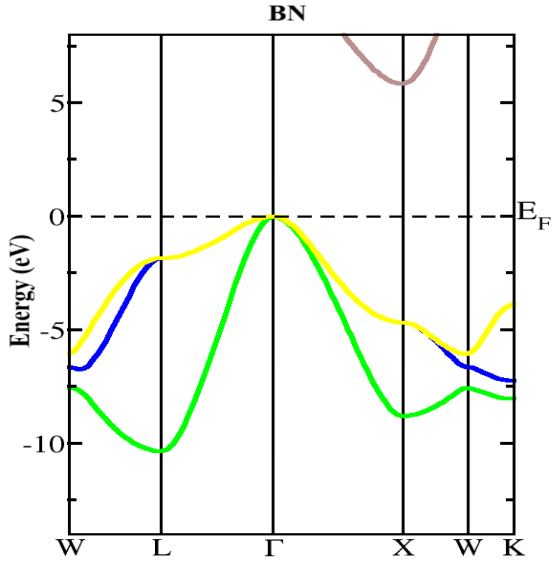
[48,71] . For GaSb, our computed transition pressures are slightly lower than those reported experimentally and theoretically [26,72,73]. It is important to note that phase transition data for the studied ternary alloys are currently unavailable. We can noted also, that we must applied high pressure to move from the less stable phase to the stable one, this agree with our structural results. No previous data are available for ternary compounds, preventing any comparison with earlier studies.

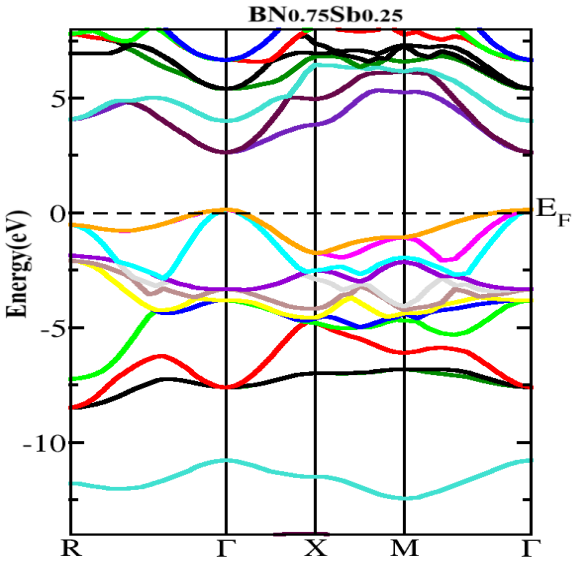
IV.3.3. Electronic properties

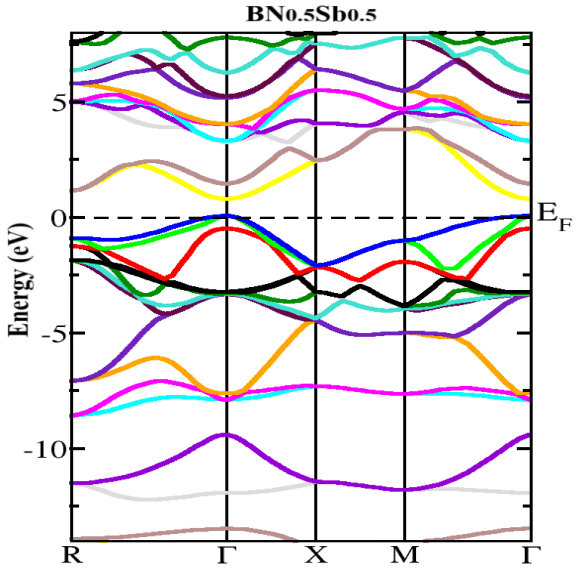
The electronic band structures of ZB binary and ternary compounds for $YN_{1-x}Sb_x$ (Y = B, Al and Ga) system at different composition $x = 0, 0.25, 0.5, 0.75\ and\ 1$ using WC – GGA, TB - mBJ and KTB - mBJ as exchange – correlation potential are investigated in our study. Calculated band gaps (Eg) for all the compounds have been listed in ***Table IV. 6***, accompanied by other available data from theory and experiments, and we suffice with mentioning only the band structures obtained using KTB - mBJ scheme in ***Figure IV. 8***, ***Figure IV. 9*** and ***Figure IV. 10***.

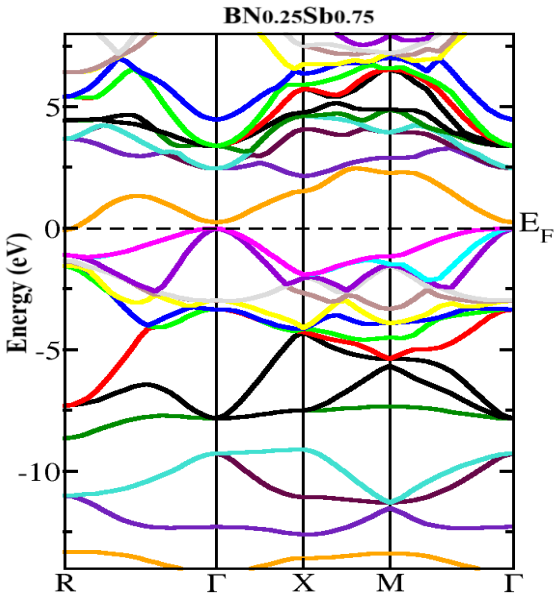
Table IV. 6: *Energy band gaps (eV) of $YN_{1-x}Sb_x$ (Y = B, Al and Ga) alloys in the ZB phase*

Alloy	x	WC-GGA	TB-mBJ	KTB-mBJ	Type of band gap	Exp.	Other calc.
$BN_{1-x}Sb_x$	0.0	4.34	5.81	5.85	$\Gamma \rightarrow \chi$	6[80], 6.49[81]	4.45[32], 4.450[55], 5.424[55], 4.45[76],
	0.25	1.52	2.46	2.50	$\Gamma \rightarrow \Gamma$		
	0.50	0	0.71	0.72	$\Gamma \rightarrow \Gamma$		
	0.75	0	0.2	0.25	$\Gamma \rightarrow \Gamma$		
	1.0	0.66	1.08	1.08	$\Gamma \rightarrow \chi$		0.663[34], 1.109[34], 0.653[55], 1.230[55], 0.98[78], 1.274[82]
$AlN_{1-x}Sb_x$	0.0	3.21	4.86	4.86	$\Gamma \rightarrow \chi$	5.3[83]	4.838[36], 3.306[36] 3.25[37], 3.23[39]
	0.25	1.41	1.68	2.33	$\Gamma \rightarrow \Gamma$		
	0.50	0.55	0.84	1.24	$\Gamma \rightarrow \Gamma$		
	0.75	0.06	0.76	0.73	$\Gamma \rightarrow \Gamma$		
	1.0	1.14	1.81	1.77	$\Gamma \rightarrow \chi$	1.6[42] 1.615[84]	1.796[85], 1.746[86]
$GaN_{1-x}Sb_x$	0.0	1.66	2.97	2.98	$\Gamma \rightarrow \Gamma$	3.299[47], 3.30[87]	3.1[88], 1.6[89,90], 1.9[91], 1.89[92]
	0.25	0.28	1.40	1.40	$\Gamma \rightarrow \Gamma$		
	0.50	0.05	0.54	0.33	$\Gamma \rightarrow \Gamma$		
	0.75	0	0.24	0.25	$\Gamma \rightarrow \Gamma$		
	1.0	0	0.90	0.85	$\Gamma \rightarrow \Gamma$	0.8[12]	0[93], 0.396[93], 0.876[26]


BN
Energy (eV)
5
0
-5
-10
E_F
W
L
Γ
X
W
K


BN0.75Sb0.25
Energy(eV)
5
0
-5
-10
E_F
R
Γ
X
M
Γ


BN0.5Sb0.5
Energy (eV)
5
0
-5
-10
E_F
R
Γ
X
M
Γ


BN0.25Sb0.75
Energy (eV)
5
0
-5
-10
E_F
R
Γ
X
M
Γ

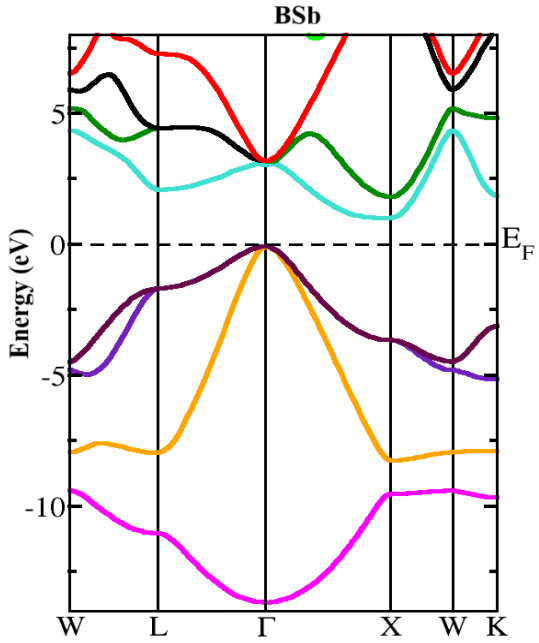
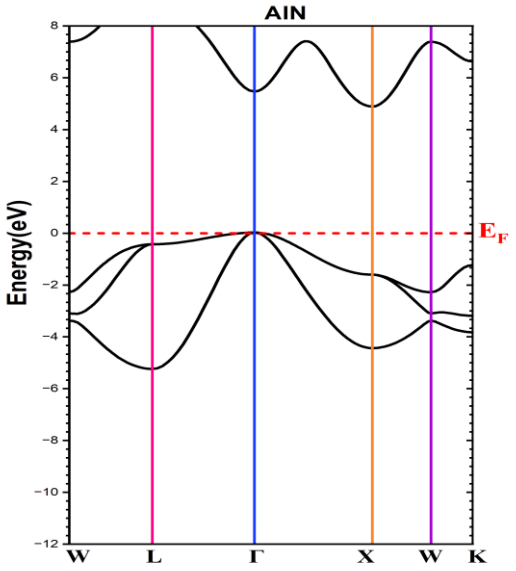
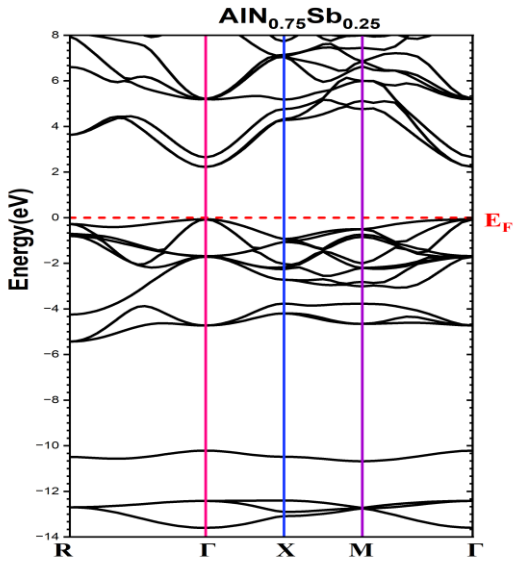
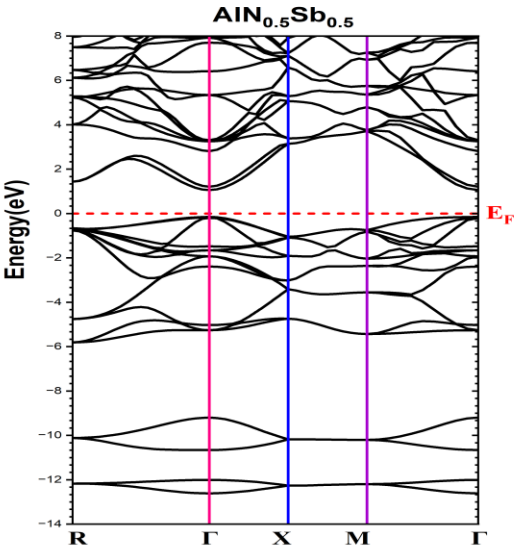
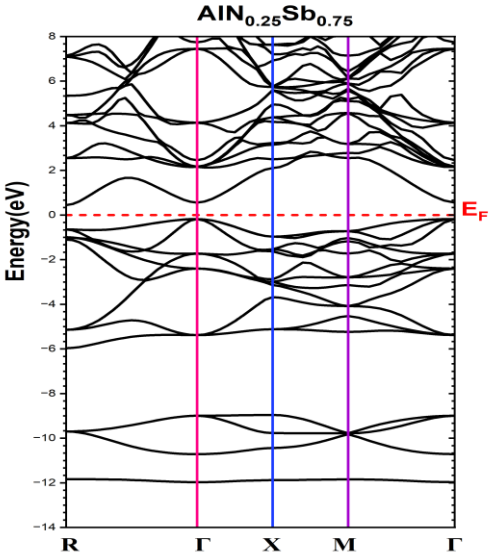


Figure IV.8: ***Energy band structure diagram of $BN_{1-x}Sb_x$ (x = 0, 0.25, 0.50, 0.75 and 1) alloys using KTB potential scheme***


AlN
Energy(eV)
E_F
W
L
Γ
X
W
K


AlN0.75Sb0.25
Energy(eV)
E_F
R
Γ
X
M
Γ


AlN0.5Sb0.5
Energy(eV)
E_F
R
Γ
X
M
Γ


AlN0.25Sb0.75
Energy(eV)
E_F
R
Γ
X
M
Γ

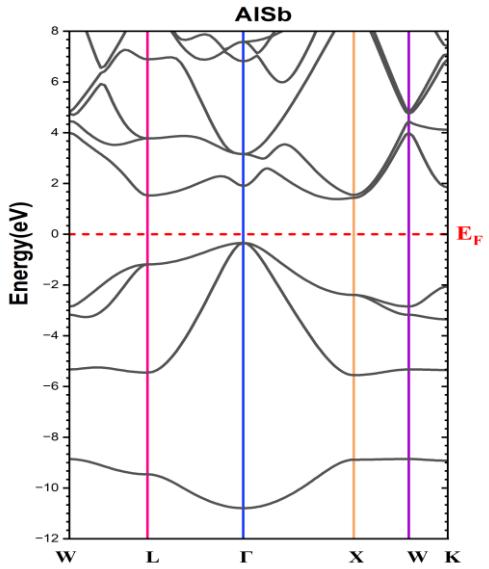
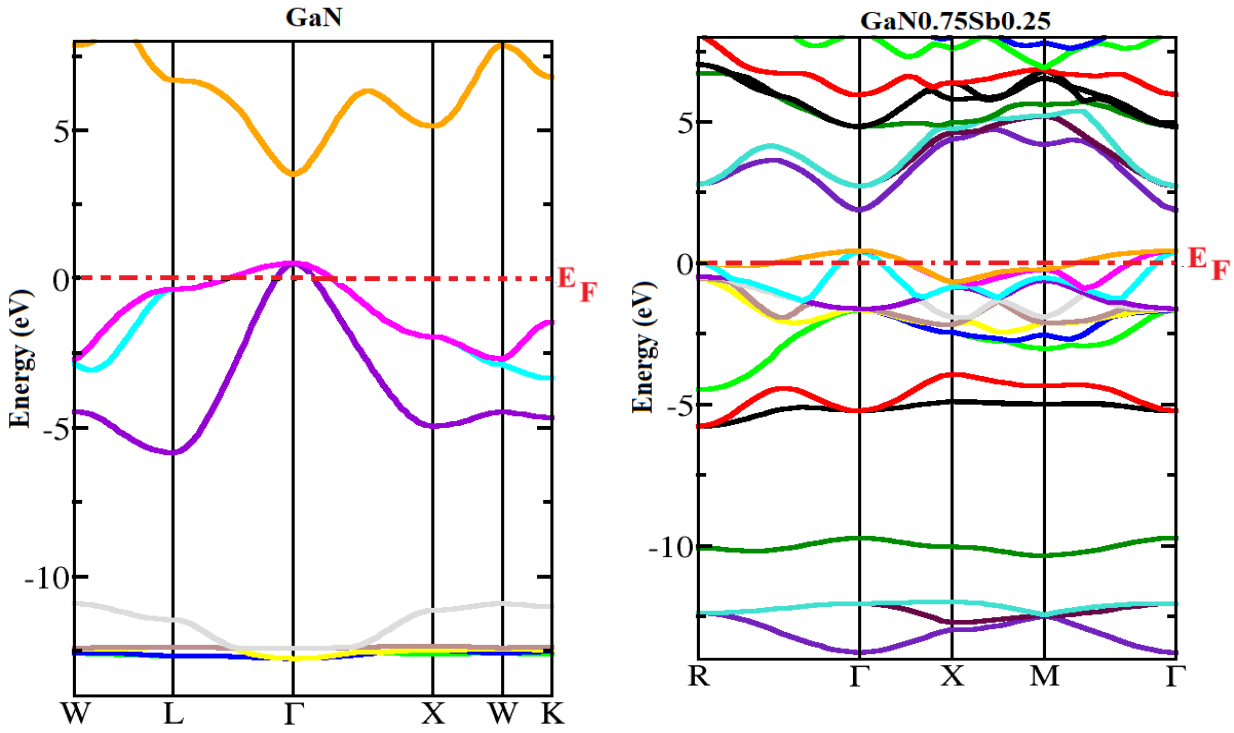


Figure IV. 9: Energy band structure diagram of $AlN_{1-x}Sb_x$ (x = 0, 0.25, 0.50, 0.75 and 1) alloys using KTB potential scheme



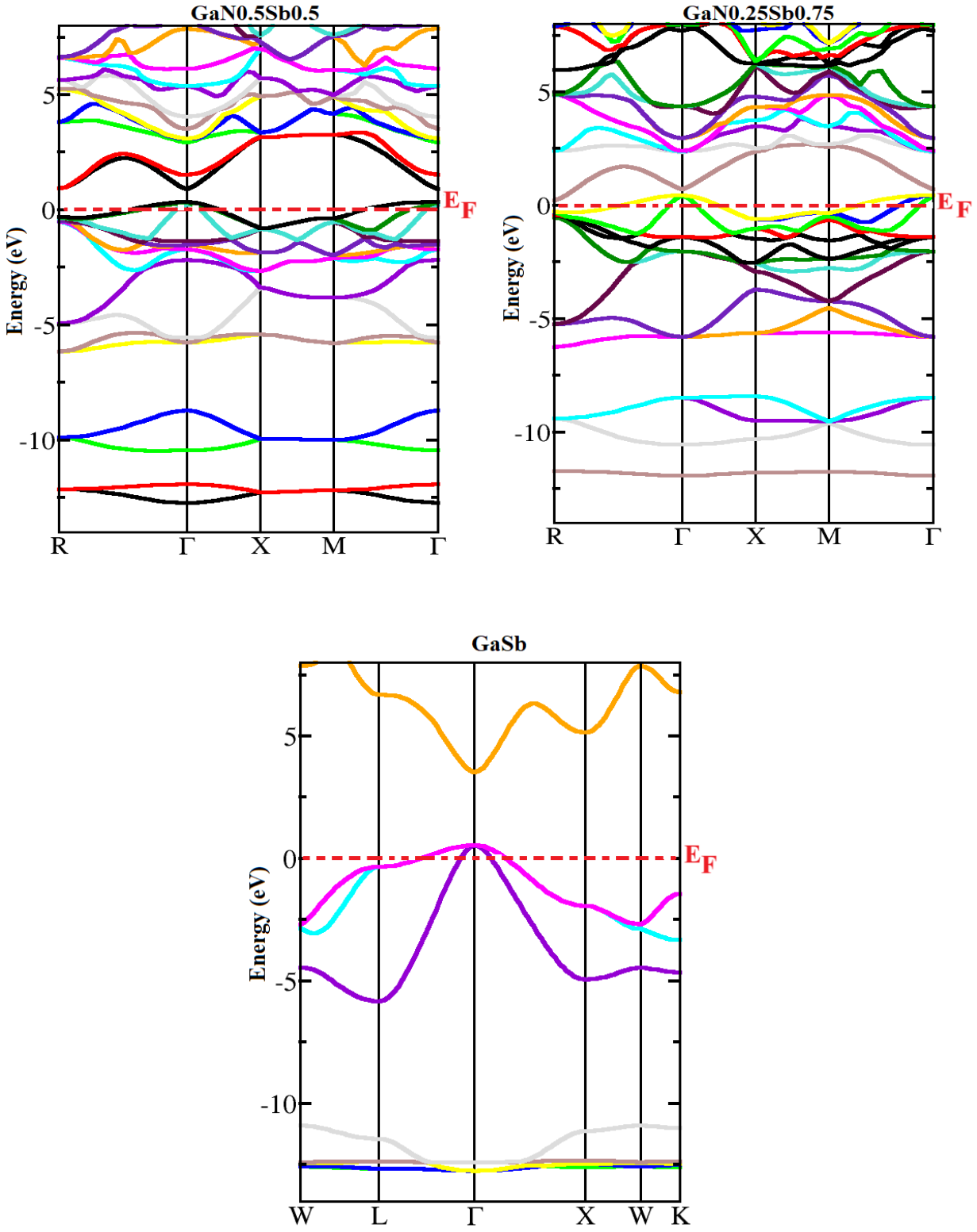


Figure IV. 10: ***Energy band structure diagram of $GaN_{1-x}Sb_x$ (x = 0, 0.25, 0.50, 0.75 and 1) alloys using KTB potential scheme***

As an overview of the results recorded in the ***Table IV. 6***, they shown a consistency between the calculated values of binary compounds and both experimental and theoretical studies, while no available data for ternary alloys. A clear decrement in the fundamental band gap with increment in antimony concentration, the binary BN have a wide band gab while the binary GaSb have the lowest one from the studied binary compounds. Doping with Sb introduces localized states near the band edges that hybridize with host valence and conduction bands, effectively shifting them closer together and reducing the gap [94], also Sb's larger atomic radius (compared with B, N, Al) and lower electronegativity cause lattice strain and favor formation of weaker, more covalent bonds, increasing disorder and tail states in the gap [95].

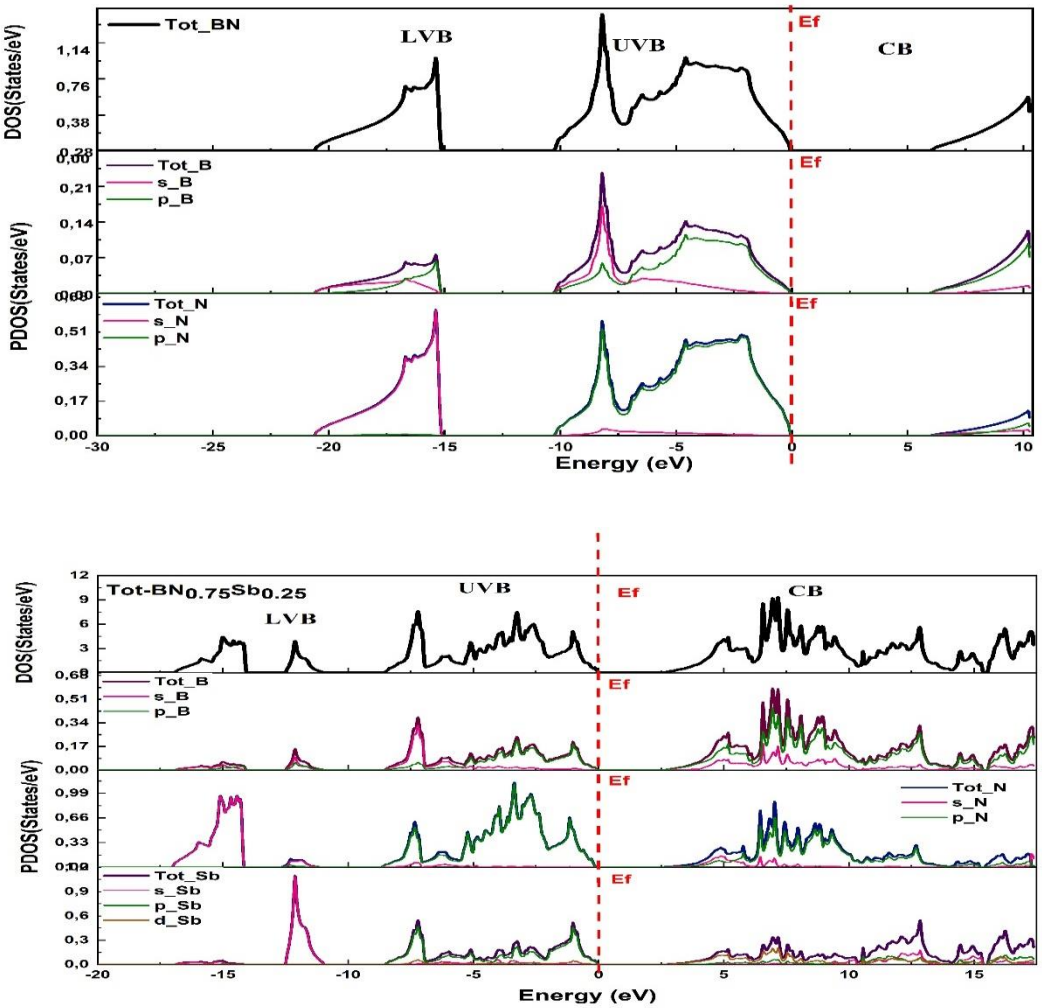
On the other hand, the energy gab value obtained using WC - GGA approximation are inferior to those obtained by using both of TB - mBJ and KTB - mBJ approximations and experimental results due to its simplified treatment of exchange - correlation. On the other hand, a clear consistency is found between the TB-mBJ and KTB-mBJ results for all materials under investigation. The observed enhancement of the band gap is primarily associated with the improved description of the exchange–correlation potential Vxc within the TB-mBJ and KTB-mBJ frameworks. Unlike semi local functionals such as WC-GGA, which systematically underestimate band gaps due to the absence of the derivative discontinuity and self-interaction errors [96,97], the TB-mBJ and KTB-mBJ potentials introduce a modified Becke–Johnson exchange term that effectively incorporates a screened fraction of Hartree – Fock like exchange [11,12]. This semi-local formulation enhances the treatment of the exchange potential without the computational expense of hybrid functional [11,12]. Consequently, TB-mBJ and KTB-mBJ yield band gaps in closer agreement with experimental and higher-level theoretical results, underscoring their suitability for accurate electronic calculations.

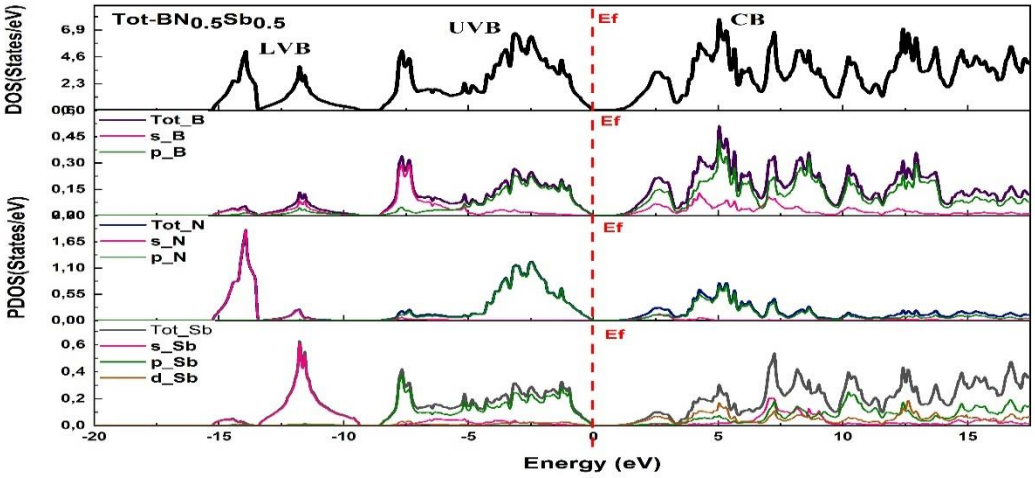
The extract energy gab value using both TB-mBJ and KTB-mBJ for BN are in good agreement with experimental value obtained by V.A. Fomichev and al[80], however it vary form second value (6.49eV [81]) by 11% and 10%, respectively. On the other hand the values obtained using EV-GGA for binary compounds by F. El Haj Hassan [55] are in good agreement with those obtained using TB-mBJ or KTB-mBJ. For AlN the obtained values underestimated by TB-mBJ and KTB-mBJ is more closely to experimental value [83]. On the other hand, the obtained values

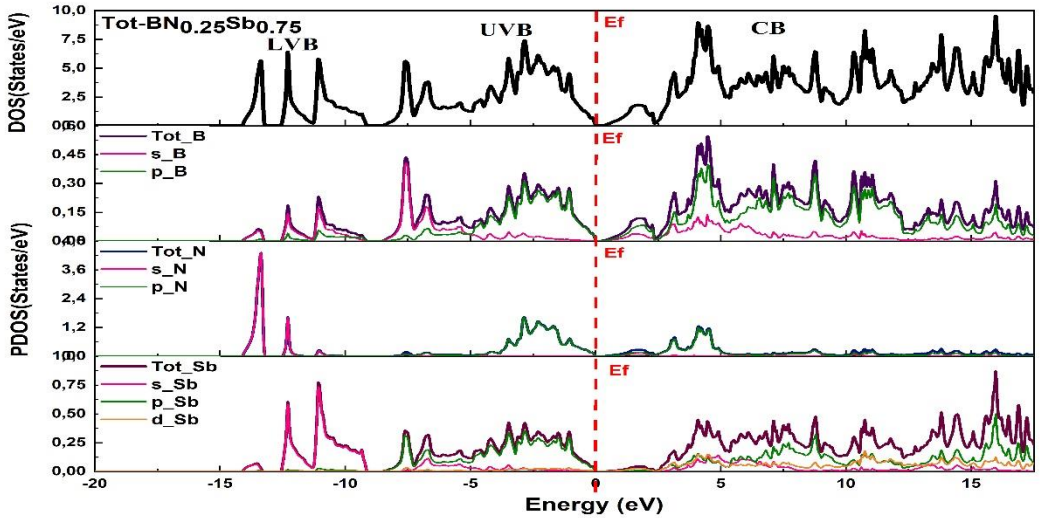
based on TB-mBJ is in perfect aligned with those disclosed by R. Moussa and al[36] using the same approximation. For AlSb, KTB-mBJ gives good results compared with experimental values [66,84], furthermore, our results are in accordance with those given by F. Annane [85] and K. Nakano [86]. The values obtained using both the TB-mBJ and KTB-mBJ approaches are lower than the corresponding experimental value for GaN [47,87], whereas they show good consistency in the case of GaSb [12]. On the other hand, a high degree of accordance is observed between the obtained results and the theoretical ones. Unfortunately, no data refer to ternary alloys in system for comparison.

Based on ***Figure IV. 8***, ***Figure IV. 9*** and ***Figure IV. 10***, the $YN_{1-x}Sb_x$ (x = 0, 0.25, 0.50, 0.75 and 1) systems exhibit semiconducting behavior, in which the higher of the valence band is situated at the high-symmetry Γ point. However, the position of the conduction band minimum varies: it lies at the X point for BN BSb, AlN and AlSb and at the Γ point for GaN, GaSb binary compounds. This indicates an indirect Γ – X band gap for binary compounds BN BSb, AlN and AlSb, which makes them vital to numerous applications as photo-detectors, transistors and integrated circuits, solar cells, thermoelectric devices and other applications. The direct band gap for GaN, GaSb and $YN_{1-x}Sb_x$ (Y = B, Al and Ga for x = 0.25, 0.50 and 0.75) ternary alloys making them an important compounds in modern technology and communication systems for application of electroluminescent diodes (LEDs), laser diodes (LDs). The semiconducting behavior for the $BN_{1-x}Sb_x$ (x=0, 0.25, 0.50, 0.75 and 1) systems agree with the study of D. Bouragba and al [31] for $BSb_{1-x}N_x$ alloys at nitrogen concentrations x ($0 \leq x \leq 1$) using TB-mBJ potential.

Analysis of the density of states (DOS) provides insight into the sources of electronic states by revealing the contributions of atomic orbitals in forming electronic states in the band structures on either side of the Fermi level (0 eV) . Adopting KTB - mBJ approximation, we suffice with presenting partial density of states (PDOS) and total density of states (TDOS) for each of the compounds under the $BN_{1-x}Sb_x$ and $AlN_{1-x}Sb_x$ systems, the results presented in ***Figure IV. 11*** and ***Figure IV. 12***


Tot_BN
LVB
UVB
CB
Ef
DOS(States/eV)
Tot_B
s_B
p_B
Tot_N
s_N
p_N
PDOS(States/eV)
Energy (eV)
Tot-BN0.75Sb0.25
Tot_Sb
s_Sb
p_Sb
d_Sb


Tot-BN0.5Sb0.5
LVB
UVB
Ef
CB
DOS(States/eV)
Tot_B
s_B
p_B
Tot_N
s_N
p_N
Tot_Sb
s_Sb
p_Sb
d_Sb
PDOS(States/eV)
Energy (eV)


Tot-BN0.25Sb0.75
LVB
UVB
Ef
CB
DOS(States/eV)
Tot_B
s_B
p_B
Tot_N
s_N
p_N
Tot_Sb
s_Sb
p_Sb
d_Sb
PDOS(States/eV)
Energy (eV)

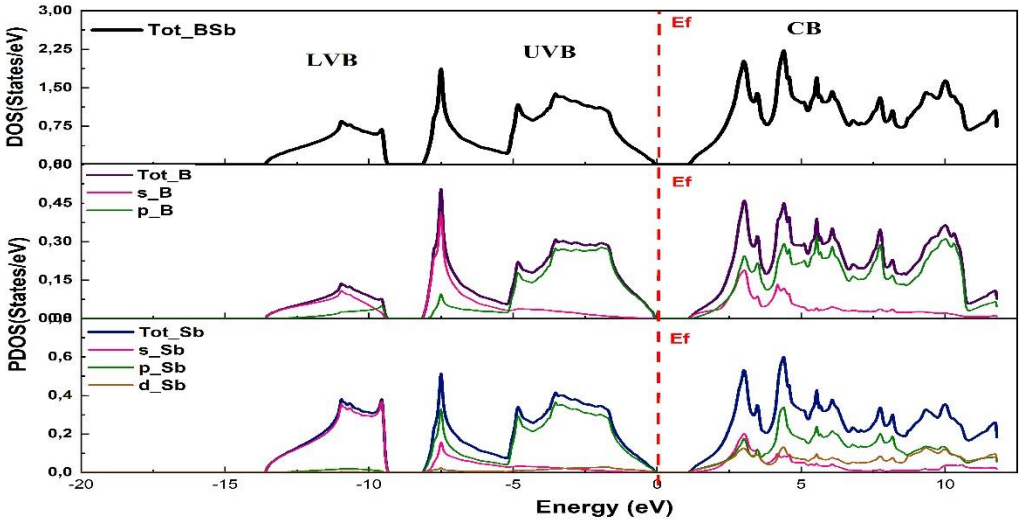
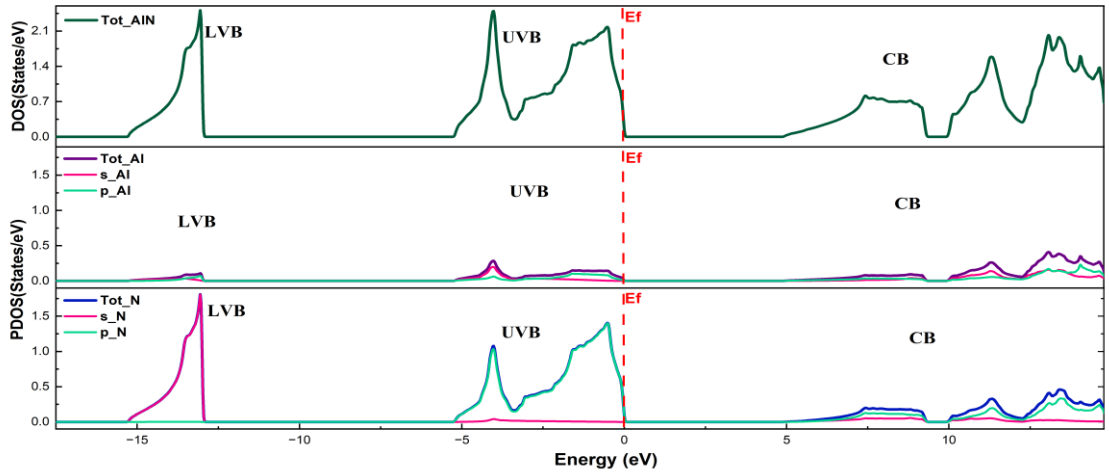
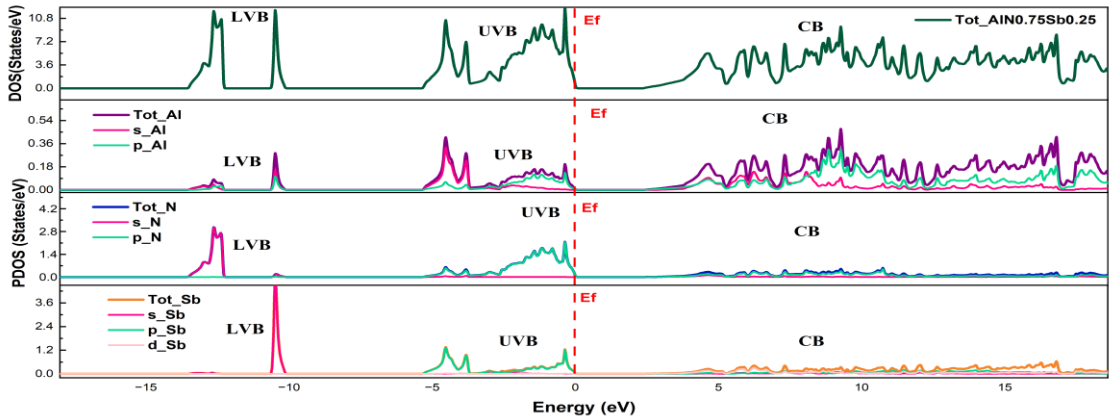
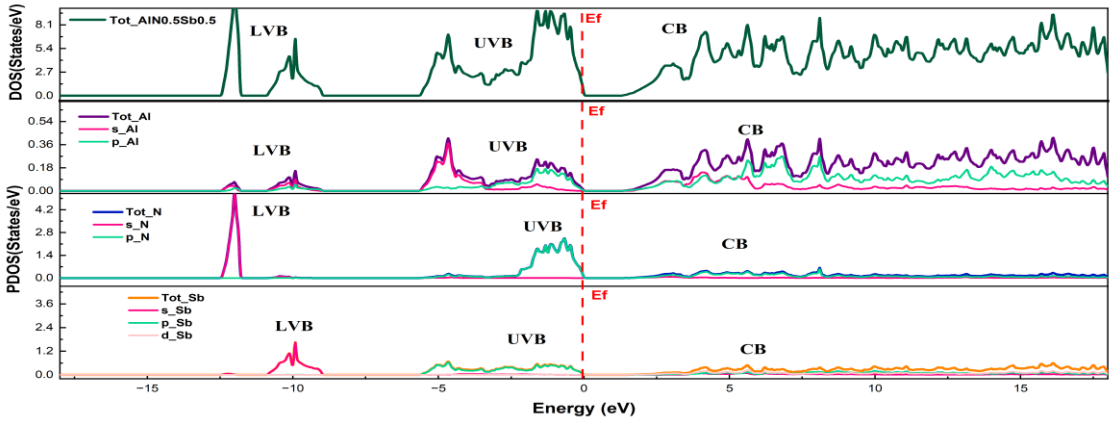
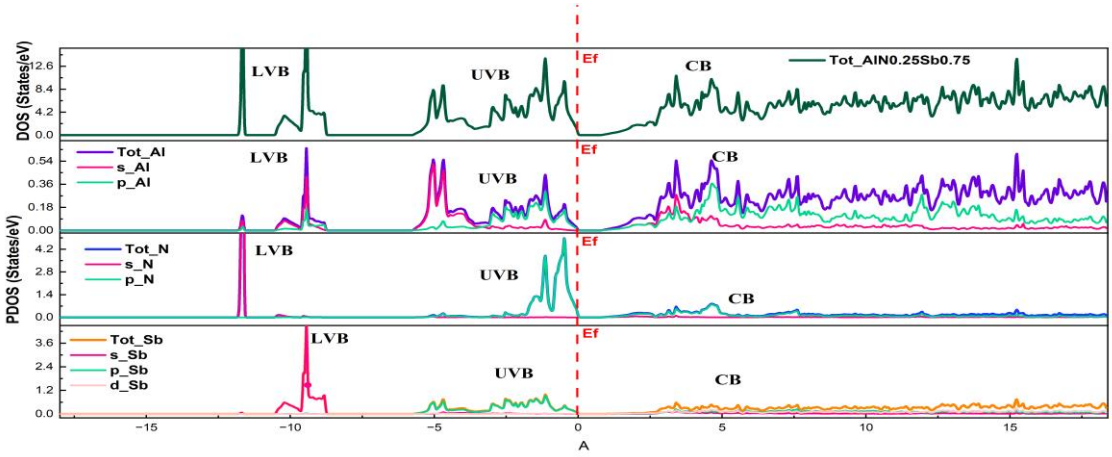


***Figure IV. 11*: Total and partial density of states for $BN_{1-x}Sb_x$ (x=0, 0.25, 0.50, 0.75 and 1) system using KTB-mBJ approximation.**




DOS(States/eV)
PDOS (States/eV)
Tot_AlN0.75Sb0.25
Tot_Al
s_Al
p_Al
Tot_N
s_N
p_N
Tot_Sb
s_Sb
p_Sb
d_Sb
LVB
UVB
Ef
CB
Energy (eV)


DOS(States/eV)
PDOS(States/eV)
Tot_AlN0.5Sb0.5
Tot_Al
s_Al
p_Al
Tot_N
s_N
p_N
Tot_Sb
s_Sb
p_Sb
d_Sb
LVB
UVB
Ef
CB
Energy (eV)


DOS (States/eV)
PDOS (States/eV)
Tot_AlN0.25Sb0.75
Tot_Al
s_Al
p_Al
Tot_N
s_N
p_N
Tot_Sb
s_Sb
p_Sb
d_Sb
LVB
UVB
Ef
CB
A

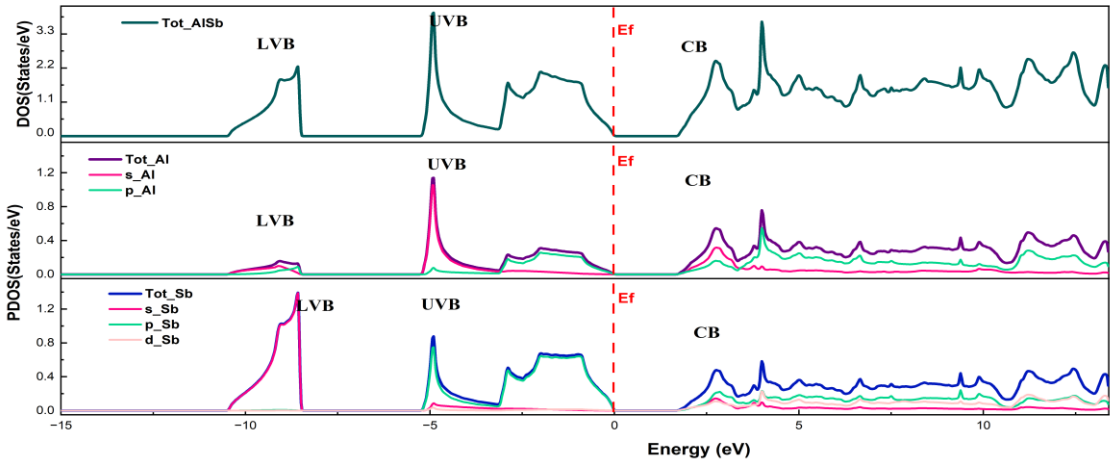


***Figure IV. 12*: Total and partial density of states for $AlN_{1-x}Sb_x$ (x=0, 0.25, 0.50, 0.75 and 1) system using KTB-mBJ approximation.**

The electronic states can be classified into three distinct regions; the lower valence band (LVB), upper valence band (UVB) and conduction band (CB), each region of theme situated at different energy range according to Sb concentration in both of $BN_{-x}Sb_x$ and $AlN_{-x}Sb_x$ systems. Furthermore, the difference between the final value of the UVB and the first value of CB region confirms the obtained energy gap values using the same approximation. For BN, the LVB is made by contribution of s-N state with minor contributions from s, p - B states, while the UVB is dominated by p-N state accompanied by small contribution of s, p-B states. The last region is mostly formed by p-B contribution. This analysis is in good accordance with previous reports by M. Benchehima and al using TB-mBJ approximation [34]. For ternary alloys, the LVB is governed by contribution of s-N and s-P states, in contrast, both of the UVB and CB predominant from p state of boron, nitrogen, and antimony atoms, in addition to s-B state in the first peak of UVB with different quantities. In which, with increasing Sb concentration, the contribution of Sb states to the electronic structure increases, whereas the contribution from N states decreases. In BSb, Finally, the LVB is dominated by the s-Sb orbitals, the UVB is made by a noticeable p-Sb contribution over the B-p states and the conduction band states are dominated by B states. The present analysis is consistent with the findings reported by V. Tiwari and al [35]. For AlN, the LVBs dominated by the N-s states, the UVBs located in the range of -5.3 eV and zero, it dominated by the N-p states. However major contribution in CBs comes from Al atoms and it is located between 4.8eV and 15eV, this results agree with those given by A. Kafi and al [100] using GGA-PBEsol potential

scheme. For AlSb, Sb-s has the major contribution in LVBs; however, both of Al-s and Sb-p dominate the UVBs, which located between -5.25 eV and zero. Whereas the CBs originated from Al-p and Sb-p and with small contribution of Al-s, Sb-s and Sb-d, it placed in the range of 1.7 eV and 13.5 eV, this results are in good accordance with those given by S. Nabi and al [44] using GGA-PBEsol potential scheme. For ternary alloys $AlN_{0.75}Sb_{0.25}$, $AlN_{0.5}Sb_{0.5}$ and $AlN_{0.25}Sb_{0.75}$, the LVBs lead to the contribution of s orbital of AL, N and Sb however, the UVBs lead to contribution N-p and both of Al-s and Al-p.

IV.3.4. Optical properties

Optical properties such as the dielectric function, absorption coefficient, reflectivity and refractive index of a material can affect the characteristics of light passing through it, in which is crucial for determining their technological application. So, we have calculated the real and imaginary components of complex dielectric function $\varepsilon(\omega)$, refractive index $n(\omega)$, extinction coefficient $k(\omega)$ and optical absorption coefficient $\alpha(\omega)$ for *YN1-xSbx (Y=B, Al and Ga) alloys at x=0.0, 0.25, 0.50, 0.75 and 1.0* in zinc blende stable phase. The results are presented in ***Figure IV. 12, Figure IV. 13*** and ***Figure IV. 14***. *YN1-xSbx (Y=B, Al and Ga)* systems are optically.

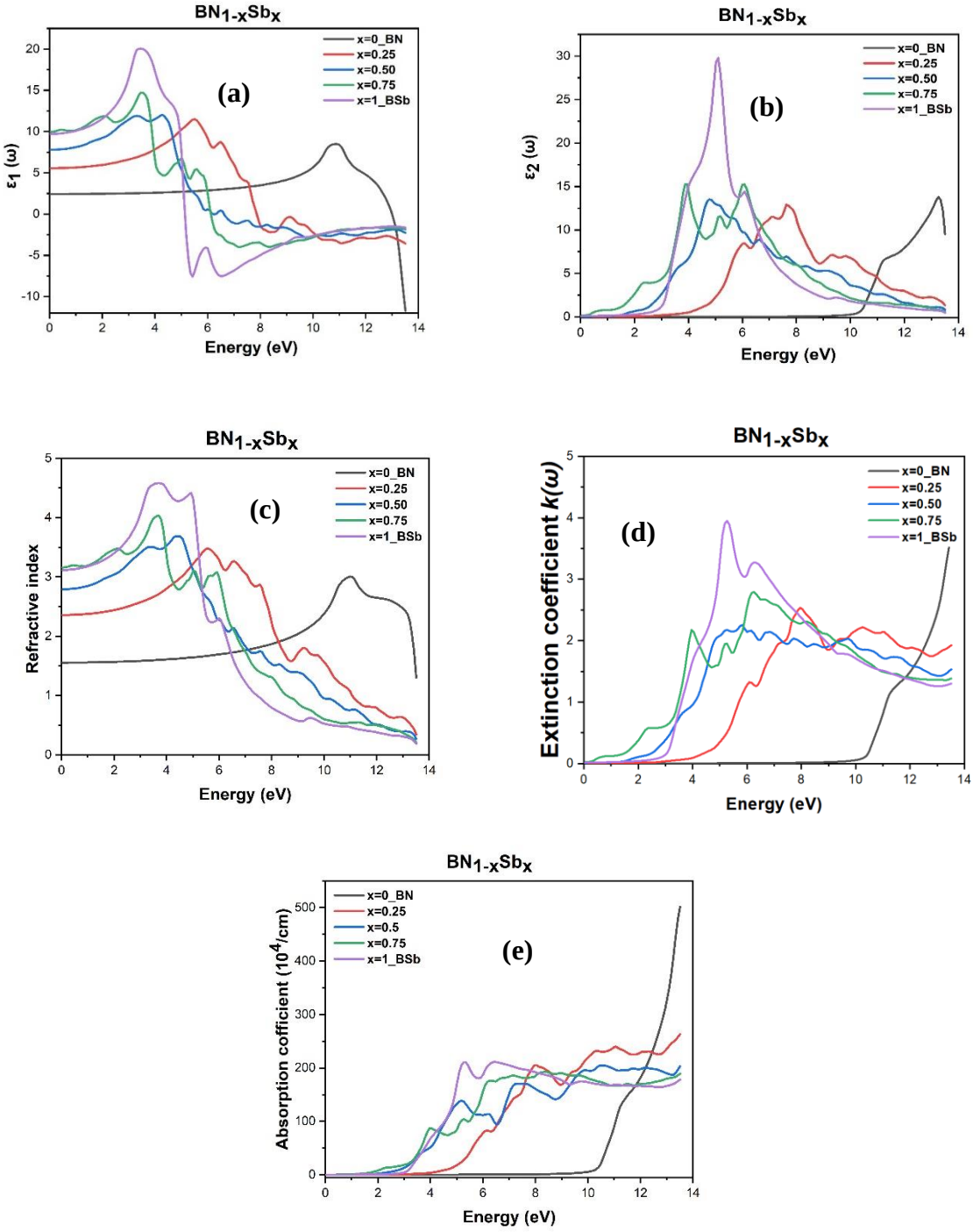


***Figure IV. 13**: Variation of the dielectric function, refractive index, and absorption versus energy of $BN_{1-x}Sb_x$ ($x = 0.0, 0.25, 0.5, 0.75$ and 1.0) alloys*

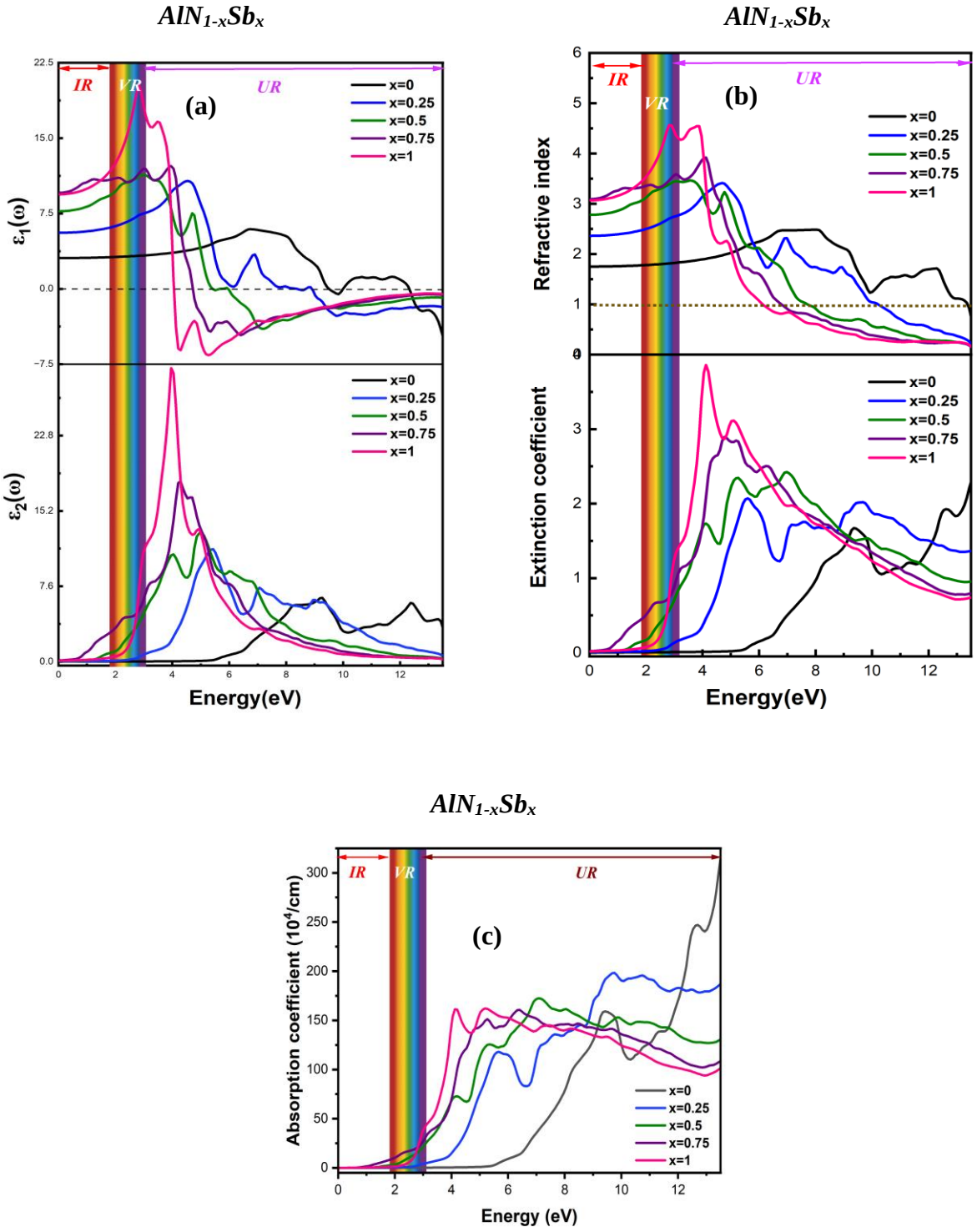


***Figure IV. 14*: Variation of the dielectric function, refractive index, and absorption versus energy of $AlN_{1-x}Sb_x$ ($x = 0.0, 0.25, 0.5, 0.75$ *and* 1.0) alloys**

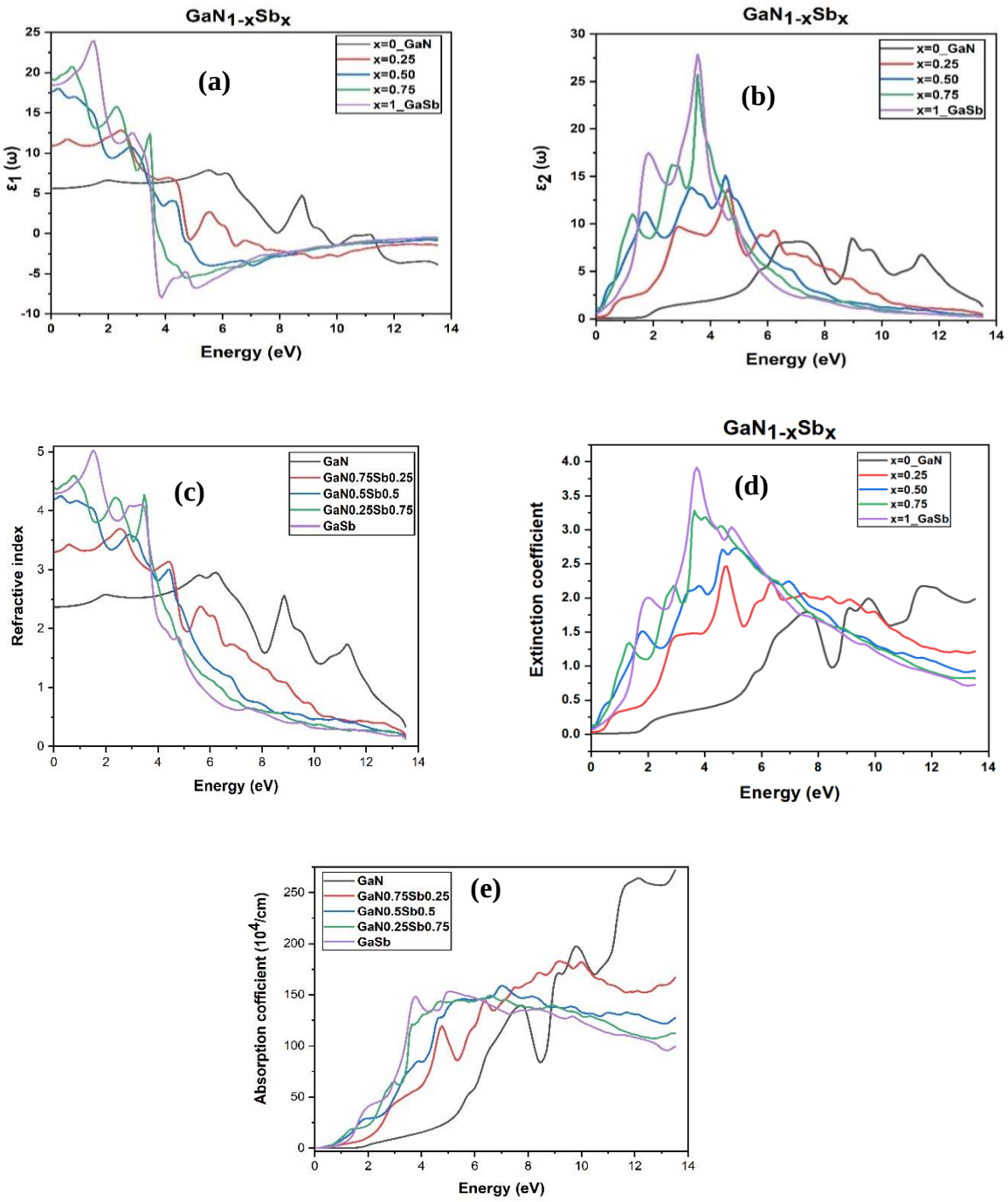


Figure IV. 15: ***Variation of the dielectric function, refractive index, and absorption versus energy of $GaN_{1-x}Sb_x$ $(x = 0.0, 0.25, 0.5, 0.75$ and $1.0)$ alloys***

- **Dielectric Function $\varepsilon(\omega)$:**

The $\varepsilon_1(\omega)$ curves (***Figure IV.13* (a)**) for $BN_{1-x}Sb_x$ start with an almost negligible increase especially for Sb concentration of x = 0, 0.25 and 0.5. Then followed with clear increase until reached to the highest peak at energy of 10.89eV (8.62), 5.51 eV (11.52), 4.28 eV (12.34), 3.46 eV (14.80) and 3.45 eV (20.15) for BN, $BN_{0.75}Sb_{0.25}$, $BN_{0.5}Sb_{0.5}$, $BN_{0.25}Sb_{0.75}$ and BSb, respectively. This indicates a strong dispersion effect, reaching its maximum in the ultraviolet range, where the maximum value increase as Sb concentration increase . A decreasing trend is observed after the highest peak, then it crosses zero and becomes negative from energy of 12.98 eV, 7.91eV, 6.69 eV, 6.16 eV and 5.12 eV for Sb concentration $x = 0, 0.25, 0.5, 0.75$ and 1 in $BN_{1-x}Sb_x$ system, respectively. A prominent peak at energy of 10.87 eV and 3.50 eV for BN and BSb is observed in $\varepsilon_1(\omega)$ curves using TB - mBJ approximation scheme according to the results of D. Bouragba and al [31], while the works of M. Benchehima and al [34] found that this peak is at energy of 3.38 for BSb. On the other hand, $\varepsilon_1(\omega)$ curves becomes negative at 5.102 eV for BSb, these results show good agreement with our findings. Each specimen in $\varepsilon_2(\omega)$ curves (***Figure IV. 13* (b)**) shown almost constant near zero then starts increasing at the critical points slowly while the BSb curve shown a sharp increase, attains the highest peak, this followed by a smooth decrease toward an almost zero value. The highest peak of $\varepsilon_2(\omega)$ curves indicated a high absorption of electromagnetic waves located at energy of 12.26eV (13.87), 7.63eV (12.94), 4.77eV (13.66), 3.87eV (15.42) and 5.10eV (29.66). Based on the results obtained by Bouragba and al [31], the maximum peak occurs at energy of 13.21 eV and 5.10 eV for BN and BSb, respectively in agreement with our work.

Based on ***Figure IV. 14* (a)**, the $\varepsilon_1(\omega) = f(Energy)$ for each of compounds from $AlN_{1-x}Sb_x$ system, the curves start increase until reaches the maximum value in the range of 2.81eV to 6.84 eV, the maximum peaks equal to 5.87, 10.74, 11.26, 12.29 and 20.25 for AlN, $AlN_{0.75}Sb_{0.25}$, $AlN_{0.5}Sb_{0.5}$, $AlN_{0.25}Sb_{0.75}$ and AlSb, respectively, which indicate high intensity of dispersion. Clearly, the dispersion increase as the Sb antimony increase, the highest amount of scattering located at the visible region (VR) for $AlN_{0.25}Sb_{0.75}$ and AlSb and at the ultra-violet region (UR) for AlN, $AlN_{0.75}Sb_{0.25}$ and $AlN_{0.5}Sb_{0.5}$. After the highest peak the dispersion start decrease and still shown negative indicated anomalous dispersion due to the metallic behavior; the metallic behavior for $AlN_{1-x}Sb_x$ (x = 0.25, 0.5, 0.75 and 1.0) alloys is acquired starting from around of 8.88 eV, 5.98 eV, 4.7 eV and 3.95 eV, respectively. However, AlN compound acquire a metallic

behaviour in small ranges. This values applies to absence of dispersion 'Static dielectric function ' $\varepsilon_1(\omega) = 0$ on the other hand it correspond to the maximum absorption in the $\varepsilon_2(\omega) = f(Energy)$ curves, which found exactly at values 9.26 eV (6.24), 5.42 eV (11.24), 5.04 eV (12.93), 4.28 eV (18.21) and 3.95 eV (29.68), respectively.

The maximum absorption for $AlN_{1-x}Sb_x$ system falls in UV range, making the compounds appropriate for UV applications as UV photo-detectors and photo-diodes, solar blind detectors and UV light emitting diodes (LEDs). Moreover, the obtained maximum values refer to ε_2 are obtained at 10.11 eV (9.12) [101] and at 9.978 eV [100] for AlN, and it is equal to 3.862 eV (32.815) [44] for AlSb, this results are in good accordance with our obtained results. The $\varepsilon_2(\omega) = f(Energy)$ curves started at 5.43 eV, 2.57 eV, 1.46 eV, 0.80 eV and 2.08 eV corresponding to the Antimony 'Sb' compositions 0.0, 0.25, 0.5, 0.75, and 1.0, respectively, due to electronic transitions from VBs to the CBs. This point known as the first critical point E_0 and represent the fundamental absorption edge and it directly related to the obtained energy gap Eg, the intensity of this absorption edge depends on the type of energy gap (direct or indirect). As a results AlN and AlSb alloys acquired indirect absorption edge, however ternary alloys acquired direct absorption edge.

From ***Figure IV. 15* (a),** we observe notable changes in the GaN spectra with increasing antimony (Sb) content. As the Sb concentration increases, the dispersion of electromagnetic radiation also increases, resulting in a rise in the real part of the dielectric function, $\epsilon_1(\omega)$, which peaks at different energies for each concentration. The peaks are observed at values of 7.88 (5.51 eV), 12.75 (2.40 eV), 18.07 (0.28 eV), 20.68 (0.77 eV), and 24 (1.52 eV) for concentrations equal to 0, 0.25, 0.50, 0.75, and 1.0, respectively. Additionally, the real part of the dielectric function shows negative values. These values of the real part of the dielectric function, indicate metallic behavior, highly reflective behavior, where electromagnetic waves are unable to propagate and are predominantly reflected. The point at which $\varepsilon_1(\omega)$ crosses zero typically marks the onset of strong absorption. These negative regions, corresponding to forbidden bands for wave propagation, highlight the material's potential as an effective electromagnetic shielding layer. The analysis of the imaginary part of the dielectric function $\varepsilon_2(\omega)$ in ***Figure IV. 15* (b)** reveals a similar trend, albeit with different values in the range of 0 to 13.5 eV. At 0 eV, the spectra for $\varepsilon_2(\omega)$begin 0.042, 0.181, 0.731, 1.163, 0.555 for GaN, $GaN_{0.75}Sb_{0.25}$, $GaN_{0.5}Sb_{0.5}$, $GaN_{0.25}Sb_{0.75}$ and GaSb respectively. Subsequently, all the curves rise sharply to a first peak, after which they decrease with increasing energy. The absorption curves then rise sharply again, reaching their highest peaks

at energies of 8.93 eV, 4.61 eV, 4.53 eV, 3.55 eV, and 3.54 eV. These correspond to absorption values of 8.57, 13.47, 15.08, 25.63, and 27.72 for Sb compositions ranging from 0 to 1. From these results, the wavelengths at which the maximum absorption occurs are 138.84 nm, 268.95 nm, 273.70 nm, 349.25 nm, and 350.24 nm for Sb concentrations of 0, 0.25, 0.50, 0.75, and 1.0, respectively. These wavelengths lie within the visible and ultraviolet regions of the electromagnetic spectrum.

- **refractive index $n(\omega)$ and extinction coefficient $k(\omega)$:**

Figure IV.13 (c) represent the variation of the refractive index $n(\omega)$ as function of photon energy $BN_{1-x}Sb_x$ systems, in which it represent one clear peak at energy of 10.97 eV, 5.59 eV, 4.36eV, 3.72eV and 3.71eV for $BN_{1-x}Sb_x$ with x varying in increments of 0.25. After reaching the highest peak, the $n(\omega)$ curves decrease as the phonon energy increase.

Figure IV.13 (d) represent the variation of the extinction coefficient $k(\omega)$ as function of photon energy. The $k(\omega)$ curves change similar to $\varepsilon_2(\omega)$ curves. The highest peak located at energy of 7.95 eV, 5.10 eV, 6.24 eV and 5.26 eV for $BN_{0.75}Sb_{0.25}$, $BN_{0.5}Sb_{0.5}$, $BN_{0.25}Sb_{0.75}$ and BSb, respectively while no peak is observed for boron nitride.

Both of refractive index and extinction coefficient versus photonic energy for $AlN_{1-x}Sb_x$ (x = 0.0, 0.25, 0.5, 0.75 and 1.0) alloys represented in ***Figure IV.14 (b)***. Clearly, the refractive index started from zero eV and increase until amount of 1.79, 2.36, 2.78, 3.09 and 3.06, the intense peaks situated in the range of 3.7 eV and 8.2 eV from the incident photon energy, an improvement in refractive index peak values with increasing Sb-composition. For extinction coefficient $K(\omega)$, it directly related to absorption and scattering, as a results its variation is proportional to imaginary part of dielectric function.

Remarkably, the refractive index ***Figure IV.15 (c)*** exhibits a trend similar to that of $\varepsilon_1(\omega)$. The refractive index increases with increasing energy until the principal peaks located at 6.24 eV, 2.57 eV, 2.89 eV, 0.77 eV and 1.51eV which have the magnitudes of 2.96, 3.69 , 3.59, 4.60 and 5.02 for the concentrations 0, 0.25, 0.5, 0.75 and 1, respectively.

Figure IV.15 (d) illustrates the variation of K(ω) as a function of photon energy. The obtained curves follow a trend similar to that of imaginary part of the dielectric function $\varepsilon_2(\omega)$,

confirming the direct link between electronic transitions and optical absorption. However, it is clear that the extinction coefficient increases then decreases, followed by an increase sharply until the reach the summit at 4.77 eV (2.46), 3.71 eV (3.91) for $GaN_{0.25}Sb_{0.75}$and GaSb, respectively. However, for GaN and $GaN_{0.5}Sb_{0.5}$ and $Ga_{0.25}Sb_{0.75}$ the third peak is the highest one, located at 11.71 eV (2.17), 4.61 eV (2.72) and 3.63 eV (3.25), respectively.

Furthermore, the $n(\omega) = f(Energy)$ and $K(\omega) = f(Energy)$curves The energy decreased with increasing excitation, settling at minimum values, with minor peaks appearing to the right of the principal peaks

The systematic shift of the refractive index toward lower energies reflects an enhanced optical response at low photon energies, indicating that Sb incorporation significantly alters the electronic structure and light matter interactions. Beyond the peak, the refractive index curves gradually decline, with a minor secondary rise before decreasing up to 10 eV, highlighting the complex dispersive behavior and the influence of Sb concentration on optical dispersion across the studied energy range.

- **Absorption coefficient $\alpha(\omega)$:**

The first look shows identical variation of absorption coefficient and extinction coefficient, this predicted due to proportional relation between them.

Figure IV.13 (e) represent the variation of Absorption coefficient $\alpha(\omega)$ as function of photon energy. The curves of $BN_{1-x}Sb_x$ system shown equal zero in the first range indicate that no absorption occurs in infrared (IR). Then the $\alpha(\omega)$ curves increase slowly until reached the highest peak at energies mark the UV range of 11.06eV ($242.50\times 10^4/cm$), 10.48 eV ($206.54\times 10^4/cm$), 8.36 eV ($194.29\times 10^4/cm$) and 5.34 eV ($210.93\times 10^4/cm$) for $BN_{0.75}Sb_{0.25}$, $BN_{0.5}Sb_{0.5}$, $BN_{0.25}Sb_{0.75}$ and BSb, respectively while no peak is observed for boron nitride. Which start increase sharply from 10.3 eV.

The absorption spectrums of $AlN_{1-x}Sb_x$ system presented in ***Figure IV.14 (c)*** shown an absorption edge in the ulta violet range for AlN, in the infrared range for $AlN_{0.25}Sb_{0.75\ and}$ in the visible range for $AlN_{0.75}Sb_{0.25,}$ $AlN_{0.5}Sb_{0.5\ and}$ AlSb, with values equal to 5.17 eV, 2.79 eV, 1.83 eV, 1.10 eV and 2.09 eV from AlN to AlSb. However the highest peak is located in ultra violet

range in amount of 247.49×10^4 /cm (12.73 eV), 197.35×10^4 /cm (9.75 eV), 172.88×10^4 /cm (7.06 eV), 160.37×10^4 /cm (6.40 eV) and 162.14×10^4.

Figure IV.14 (e) illustrates the absorption coefficient of $GaN1-xSbx$ alloys as function of energy. The absorption process starts at the fundamental absorption edge, representing the minimum photon energy needed to excite electrons from the valence band (VB) to the conduction band (CB). Photons with energy below this threshold cannot induce interband electronic transitions, so the absorption remains very low. This weak absorption in the sub band gap region indicates that the investigated alloys are largely transparent to low energy photons. At the absorption edge, however, the curves exhibit a pronounced and sharp rise, signifying the onset of efficient electronic transitions across the band-gap.This sharp increase highlights the direct involvement of inter band transitions in the optical response of the studied alloys. The absorption spectrums start at the bandgap energies of 1.7, 0.62, 0.28, 0.44, and 0.52 eV for GaN to GaSb, respectively. In addition, it shows different peaks, the highest one at energy of 12.12 eV (264.45×10^4 /cm), 9.18 eV (183.04×10^4 /cm), 7.06 eV(185.84×10^4 /cm), 6.57 eV (148×10^4 /cm) and 5.10 eV (145.4×10^4 /cm) for x = 0, 0.25, 0.5, 0.75 and 1, respectively. These distinct peaks indicate strong absorption in the ultraviolet (UV) region of the spectrum, suggesting potential applications in UV photo detectors and photo catalysis.

- **Static values and critical points:**

Magnitudes of the $\varepsilon_1(\omega)$ and $n(\omega)$ near zero incident frequency are known as the respective static dielectric function, static refractive index and static reflectivity. The calculated values of zero-frequency limits $\varepsilon_1(0)$, $n(0)$ and accompanied with the critical points energies (eV) in $\varepsilon_2(\omega)$ curves and compared with available theoretical and experimental values for $BN_{1-x}Sb_x$ systems are presented in ***Table IV.7***:

Table IV. 7: *Values of zero-frequency limits $\varepsilon_1(0)$, $n(0)$ and The critical points energies (eV) in $\varepsilon_2(\omega)$ of $YN_{1-x}Sb_x$ (Y=B, Al and Ga) alloys in the ZB phase using the KTB-mBJ scheme*

Alloy	x		$\varepsilon_1(0)$	$n(0)$	E_0	E_1
$BN_{1-x}Sb_x$	0.0	Our work.	2.35	1.53	10.34	11.25
		Exp. Other calc.	4.5[102] 3.93[31], 3.46[32]	2.17[102] 1.87[31], 1.86[32]	5.81[31]	11.38[31]

	0.25	Our work	5.52	3.34	3.38	6.08
	0.5	Our work	7.81	2.79	0.92	3.71
	0.75	Our work	10.10	3.17	0.048	2.40
	1	Our work	9.77	3.12	1.06	4.07
		Exp.				
		Other calc.	9.63[31], 10[20] 10.91[35]	3.163[20] 3.30[35]	1.10[31] 1.09[20]	4.10[31] 4.10[20]
$AlN_{1-x}Sb_x$	0.0	Our work.	3.06799	1.75	5.43	8.29
		Exp.	4.68[100]	2.16[100]	6.29[103]	8.02[103]
		Other calc.	4.29[101]		5.53[104] 4.69[103]	8.48[104] 8.54[103]
	0.25	Our work	5.58384	2.36	2.57	3.87
	0.5	Our work	7.72738	2.77	1.46	3.09
	0.75	Our work	9.56141	3.09	0.80	2.28
	1	Our work	9.40394	3.06	2.08	2.94
		Exp.			2.27[105]	2.81[105]
		Other calc.	9.42[106], 9.9[107]	3.06[106], 3.19[108], 3.23[109]	1.76[106] 2.68[110] 2.27[107]	3.11[106] 3.37[110] 2.83[107]
$GaN_{1-x}Sb_x$	0.0	Our work.	5.60	2.36	7.14	8.93
		Exp.	4.6[12]		7.51[111]	10.72[111]
		Other calc.	3.90[112], 5[113]	1.97[112], 2.41[114], 2.10[114], 2.34[115]	8.61[116]	10.86[116]
	0.25	Our work	10.91	3.30	2.29	4.61
	0.5	Our work	17.62	4.19	1.67	3.30
	0.75	Our work	19.24	19.24	1.26	2.65
	1	Our work	18.43	4.29	1.83	3.55
		Exp.				
		Other calc.	14.42[117], 19.13[118]	3.79[117], 4.38[118]		

For binary compounds, the obtained values for static dielectric function, static refractive index static and critical points energies are in high accordance with other theoretical amounts, however no data to compare for ternary alloys. A clear deviation from experimental values [102] of BN compound is noted. For GaN, the reported data of Y. Yin and al [116] about $GaN_{1-x}Bi_x$ alloys using CASTEP software package, showed a critical points in the imaginary part of the dielectric function at about 8.61eV and 10.86eV, respectively during the energy range going up to 20 eV. This values are closely related to the experimental values [12] of 7.51eV and 10.72eV . The studied materials exhibit strong absorption in the visible and UV ranges. This makes them promising for optoelectronic applications, including solar cells, photo detectors, and photo catalysis.

IV.3.5. Elastic properties

The elastic properties of solid material offer valuable insights about the forces and bonding nature prevailing in solids; on the other hand, it provides information about its mechanical behavior. DFT calculations used to study the elastic and mechanical properties for $YN_{1-x}Sb_x$ (Y=B, Al and Ga) in the zinc-blend structure (C_{11},C_{12} and C_{44}) due to symmetry of cubic structure. The obtained elastic constants for each compound are presented in ***Table IV. 8,*** accompanied by Cauchy pressure C' and Kleinman parameter ξ.

Table IV. 8: The estimated elastic constants C_{ij} (GPa), Cauchy pressure C' (GPa) and Kleinman parameter ξ of $YN_{1-x}Sb_x$ (Y=B, Al and Ga) systems

Alloys	x		C_{11}	C_{12}	C_{44}	C'	ξ
$BN_{1-x}Sb_x$	0.0	Our work	792.01	182.41	426.96	-242.55	0.38
		Exp.	820[119]	190[119]	480[119]		0.1[38]
		Other calc.	990[120] 837[38]	441[120] 182[38]	394[120] 493[38]		
	0.25	Our work	354.95	114.98	190.81	-75.83	0.46
	0.5	Our work	236.13	93.71	153.63	-59.92	0.53
	0.75	Our work	202.55	72.69	106.77	-34.08	0.50
	1	Our work	190.57	61.04	112.40	-51.36	0.46
		Exp.					
		Other calc.	193.53[78] 205 [121] 192[79]	68.42[78] 62.5[121] 58.5[79]	104.12[78] 112.1[121] 105[79]		
$AlN_{1-x}Sb_x$	0.0	Our work	286.14	157.42	210.34	-52.914	0.66
		Exp.					0.6[38]
		Other calc.	288.50[100] 313.24[92]	159.45[100] 156.47 [92]	223.22 [100]	-50[92]	0.67[92]

			304[38] 286.085 [36] 296.3[121]	152[38] 159.42[36] 156.6 [121]	202[92] 199[38] 221.03[36] 200.4 [121]	-47.7[121]	0.55[122]
	0.25	Our work	149.90	85.80	113.46	-27.66	0.68
	0.5	Our work	101.65	60.39	79.95	-19.56	0.70
	0.75	Our work	85.14	44.98	62.12	17.14	0.64
	1	Our work	81.91	42.27	47.67	-5.4	0.63
		Exp.	87.69 [123]	43.41[123]	40.76[123]		
		Other calc.	83.29[68] 81.610[43] 85.5[121]	43.41[68] 35.548[43] 41.4[121]	40.76[68] 53.929[43] 39.9 [121]	22.1[121]	0.6035[68] 0.601[121]
GaN1-xSbx	0.0	Our work	266.1306	144.8017	180.7574	-35.94	0.76
		Exp.					0.5[38]
		Other calc.	296[38] 293[122] 285[124]	154[38] 159[122] 161[124]	206[38] 155[122] 149[124]		0.61[122] 0.67[124]
	0.25	Our work	153,5593	85,0763	125,2801	-40.20	0.66
	0.5	Our work	97.0139	55.8214	79.8213	-23.99	0.51
	0.75	Our work	82,4997	43,6373	64,3889	-20.75	0.64
	1	Our work	82,9524	39,5017	90,6384	-51.13	0.60
		Exp.	84.4[51]	40.3[51]	43.2[51]		
		Other calc.	90.8[125] 92.7 [121]	39.1[125] 38.7[121]	41.9[125] 46.2[121]		

Based on ***Table IV. 8***, all of mentioned compounds in $YN_{1-x}Sb_x$ (Y=B, Al and Ga) systems obey the stability standards for cubic structure [126,127]:

$C_{11} - C_{12} > 0$, $C_{11} + 2C_{12} > 0$ and $C_{44} > 0$

Our results for binary compounds (BN, BSb, AlN, AlSb, GaN and GaSb) are in high accordance with other theoretical results and experimental data, with some minor differences due to the type of approximation used, computational method and implementation, structural optimization details and others. However, no previous data refer to ternary alloys. Cauchy pressure C'provides details to the atomic bonding in compounds, which directly effected ductility/brittleness of compounds. The calculated Cauchy pressure values for compounds in $YN_{1-x}Sb_x$ (Y=B, Al and Ga) systems are negative demonstrates brittle behavior consequently covalent bonds (indicates the directional bonding) are dominated in compound and the materiel is

nonmetallic [128]. For comprehensive analysis to atomic bondings, we resort to the Kleinman parameter ξ, which named also 'internal strain parameter' and described the relative tendency of bond bending against bond stretching. Most calculated values for $YN_{1-x}Sb_x$ (Y=B, Al and Ga) ternary alloys. The obtained values Kleinman parameter ξ of the most compounds in the said system are in the range of $1 > \xi \geq 0.5$, thus demonstrate dominate of bond bending and a large resistance to the bond stretching, while in BN, $BN_{0.75}Sb_{0.25}$ and BSb the bond stretching dominates under stress as $0 < \xi < 0.5$.

BN exhibits the highest elastic stiffness in $YN_{1-x}Sb_x$ (Y=B, Al and Ga) systems, which is associated with strong covalent bonds and a compact lattice, resulting in large elastic constants and high resistance to deformation. Replacing nitrogen with the heavier antimony atom leads to a pronounced softening of the elastic response, in which elastic constants drops to a third compared to values of BN. Although BSb is mechanically softer than BN, it still shows a distinct elastic response due to the nature of B – Sb bonding and the heavier atomic mass of Sb. This also applies to AlN and GaN, in which AlN and GaN are elastically stiffer than AlSb and GaSb, consistent with the stronger metal – nitrogen bonds compared to metal – antimony bonds. Between the antimonides, AlSb generally exhibits higher elastic constants than GaSb, reflecting relatively stronger Al – Sb bonding. In contrast, BN and BSb display Kleinman parameter values near to zero, indicating that bond stretching is the dominant deformation mechanism under external stress. This behavior highlights a fundamental difference in elastic constants compared to the group IIIV compounds, where angular forces play a more significant role.

Overall, the elastic constants decreases with increasing atomic mass and bond length, following the general trend: BN > AlN > GaN > BSb > AlSb > GaSb

This comparative analysis demonstrates that variations in elastic behavior across these materials are governed primarily by bonding nature and atomic size effects.

The mechanical properties of $YN_{1-x}Sb_x$ (Y=B, Al and Ga) systems have been determined thought the elastic constants, therefore the bulk modulus(B), shear modulus (G), Young modulus (E), Poisson's ratio (v), and Pugh ratio(B/G) are computed the framework of the 'Voigt Reuss-Hill (VRH)' approximation [129–131], the micro-Hardness H_v described using 'Vicker's micro-hardness model'[132]. The results present in ***Table IV. 9:***

Table IV. 9: The Estimated mechanical parameters (B, G, E, ν, H_v and B/G) elastic anisotropy parameters (A, A_G, A_B and A^U) for $YN_{1-x}Sb_x$ (Y=B, Al and Ga) systems in ZB phase

Alloys	x	B	A_B	G	A_G	E	ν	B/G	H_v	A	A^U
$BN_{1-x}Sb_x$	0.0	385.61	0	350.56	0.07	807.16	0.15	1.09	52.83	1.08	0.85
	0.25	194.97	0	158.42	0.02	373.97	0.18	1.23	26.24	1.59	0.26
	0.50	141.18	0	112.46	0.06	267.28	0.18	1.25	20.21	2.15	0.74
	0.75	115.95	0	87.46	0.02	209,61	0.19	1.32	15.90	1.64	0.30
	1.0	104.21	0	89.90	0.03	209.43	0.16	1.15	18.96	1.73	0.39
$AlN_{1-x}Sb_x$	0.0	200.33	0	131.11	0.15	322.90	0.23	1.52	17.93	3.26	1.88
	0.25	107.17	0	68.58	0.17	169.58	0.23	1.56	11.05	3.54	2.18
	0.50	74.14	0	46.70	0.20	115.79	0.23	1.58	8.26	3.87	2.56
	0.75	58.36	0	39.55	0.14	96.79	0.22	1.47	7.98	3.09	1.70
	1.0	55.48	0	33.52	0.04	83.71	0.24	1.65	6.23	2.40	0.98
$GaN_{1-x}Sb_x$	0.0	185.24	0	116.79	0.13	289.54	0.23	1.58	15.84	2.97	1.57
	0.25	107.90	0	74.78	0.18	182.25	0.21	1.44	12.86	3.65	2.31
	0.50	69.55	0	46.63	0.20	114.34	0.22	1.49	8.86	3.82	2.55
	0.75	56.59	0	39.99	0.16	96.96	0.21	1.41	8.44	3.31	1.93
	1.0	53.98	0	51.51	0.22	117.24	0.13	1.04	14.21	2.89	2.89

Based on ***Table IV. 9:***

- ✓ The bulk modulus values by the Voigt - Reuss-Hill (VRH) method (***Table IV. 9***) are in good agreement with those given by Murnaghan equation of state (***Table IV. 3***).
- ✓ Clearly, in every system bulk modulus, shear modulus, Young modulus and Vicker's Hardness decrease due to addition of Sb, thusly the resistance to volume change, shape change and hardness of $YN_{1-x}Sb_x$ (Y = B, Al and Ga) decrease from YN to YSb. On the other hand this parameter decrease following this trend BN > AlN > GaN > BSb > AlSb > GaSb. This support the result obtained based on ***Table IV. 8.***
- ✓ The obtained Poisson's ratio (ν) values are less than 0.26, revealing the brittle nature of the materials. This behavior is also confirmed by the Pugh ratio(B/G), whose values are below the critical limit of 1.75. This result is further support the Cauchy pressure values.
- ✓ For ideal isotropic materiel the Zener anisotropy factor is equal one, however any deviates from one indicate anisotropic materiel. For $BN_{1-x}Sb_x$ and $AlN_{0.25}Sb_{0.75}$, we record $A < 1$ indicate anisotropic nature with maximum rigidity along the $< 100 >$ while for the rest compounds, we record $A > 1$ indicate anisotropic nature and upper toughness along cube diagonal in each alloy.

- ✓ The anisotropic nature for studied system can be confirmed using the universal index (A^U), our obtained values distinct from one indicate anisotropic nature for our system and validates the previous results.
- ✓ Compression anisotropy $A_B = 0$ is independent of the three directional of loading while shear anisotropy (A_G) is higher than zero implies anisotropy in shear modulus.

The isotropic behavior for Bulk modulus and the anisotropic nature for both of Shear and Young modulus can be clearly illustrated based on can be clearly illustrated based on ***Figure IV. 16, Figure IV. 17*** and ***Figure IV. 18*** for $BN_{1-x}Sb_x$, ***Figure IV. 19, Figure IV. 20*** and ***Figure IV. 21*** for $AlN_{1-x}Sb_x$ and ***Figure IV. 22, Figure IV. 23***, ***Figure IV. 24*** for $GaN_{1-x}Sb_x$.

The figures represent the 3D-directional dependence of the Bulk modulus (B in GPa), Shear modulus (G in GPa) and Young modulus (E in GPa) accompanied with its projections in different planes. Where the spherical shape indicate isotropic nature, however non-spherical shape indicates anisotropic nature. Concerning Bulk modulus, ***Figure IV. 16, Figure IV. 19*** and ***Figure IV. 22*** represent a spherical shape for AlN1-xSbx system, however, a clear deviation from spherical shape recorded for Shear modulus (***Figure IV. 17, Figure IV. 20*** and ***Figure IV. 23***) and Young modulus (***Figure IV. 18, Figure IV. 21*** and ***Figure IV. 24***) in all Sb concentration.

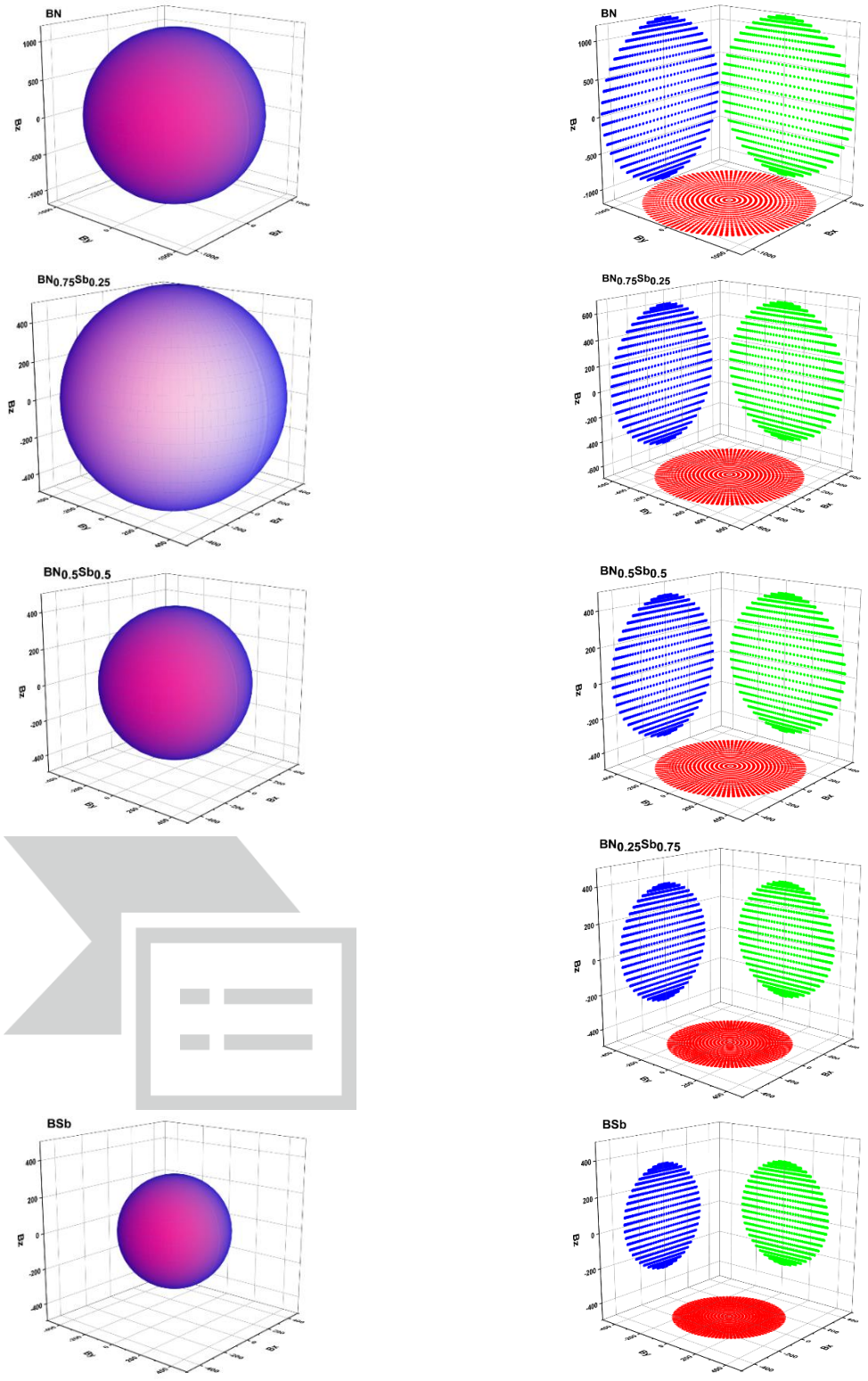


Figure IV. 16: 3D-directional dependence of the Bulk modulus (B in GPa) accompanied with its projections in different planes for $BN_{1-x}Sb_x$

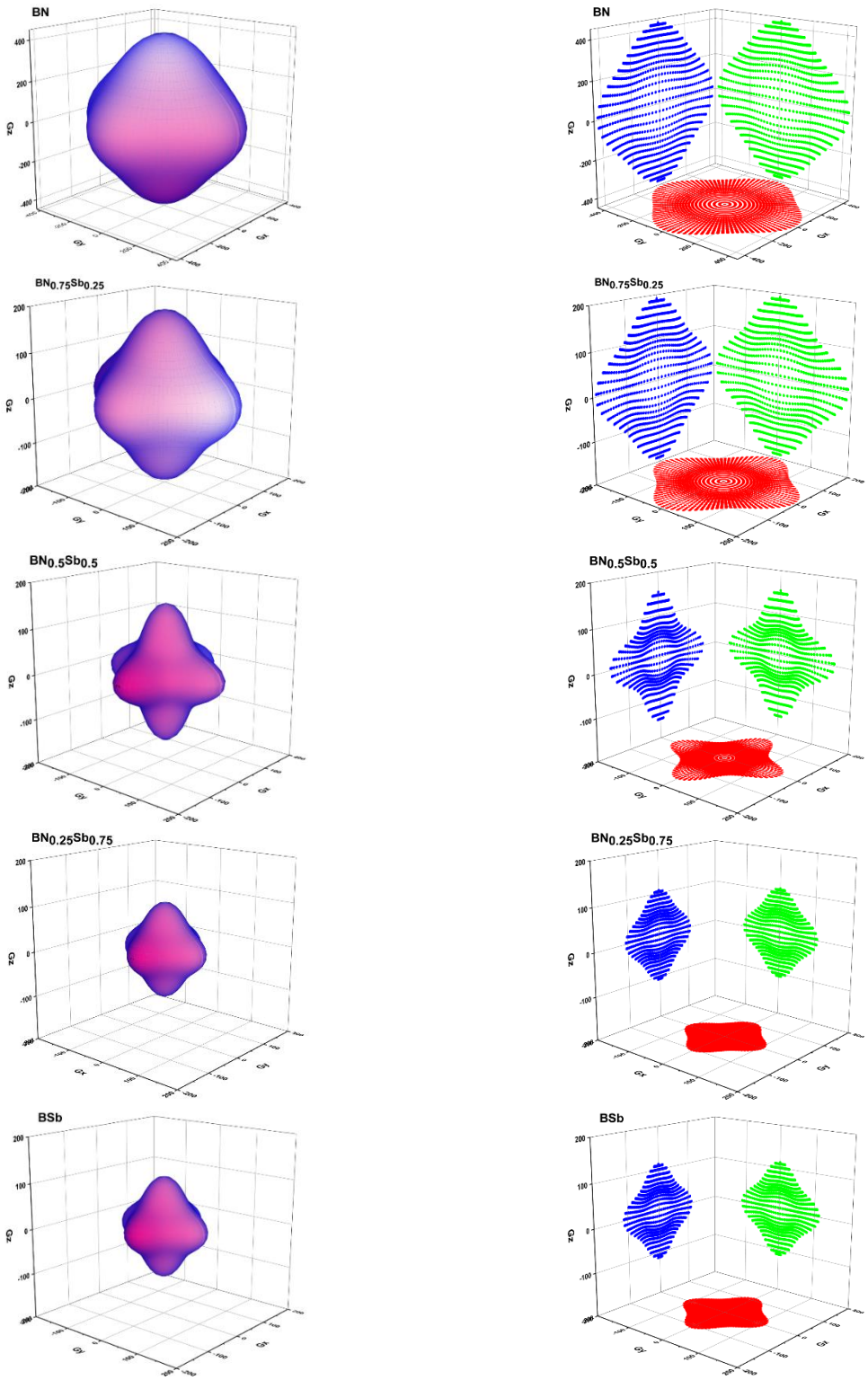


Figure IV. 17: 3D-directional dependence of the Shear modulus (B in GPa) accompanied with its projections in different planes for $BN_{1-x}Sb_x$

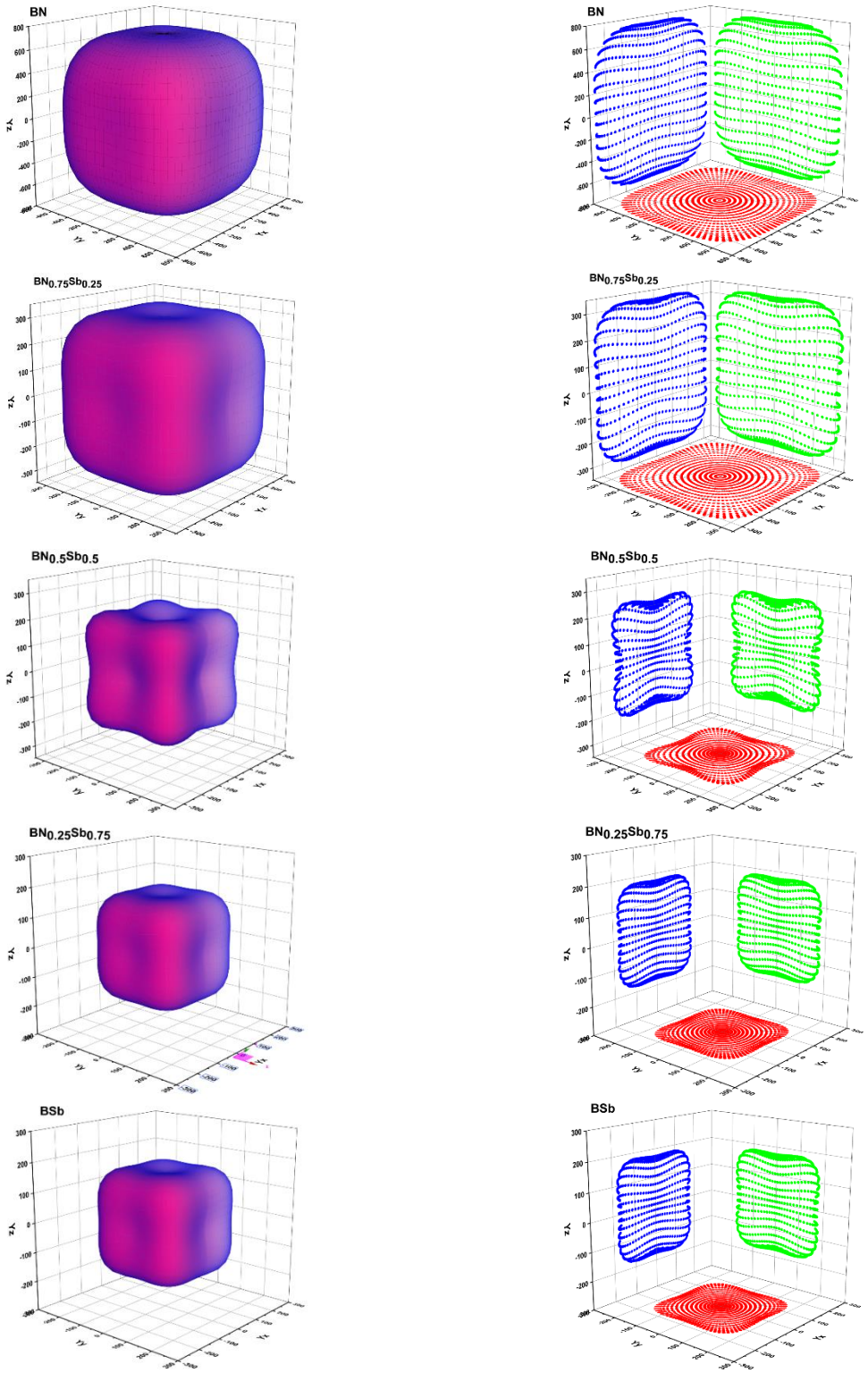


Figure IV. 18: 3D-directional dependence of the Young modulus (B in GPa) accompanied with its projections in different planes for $BN_{1-x}Sb_x$

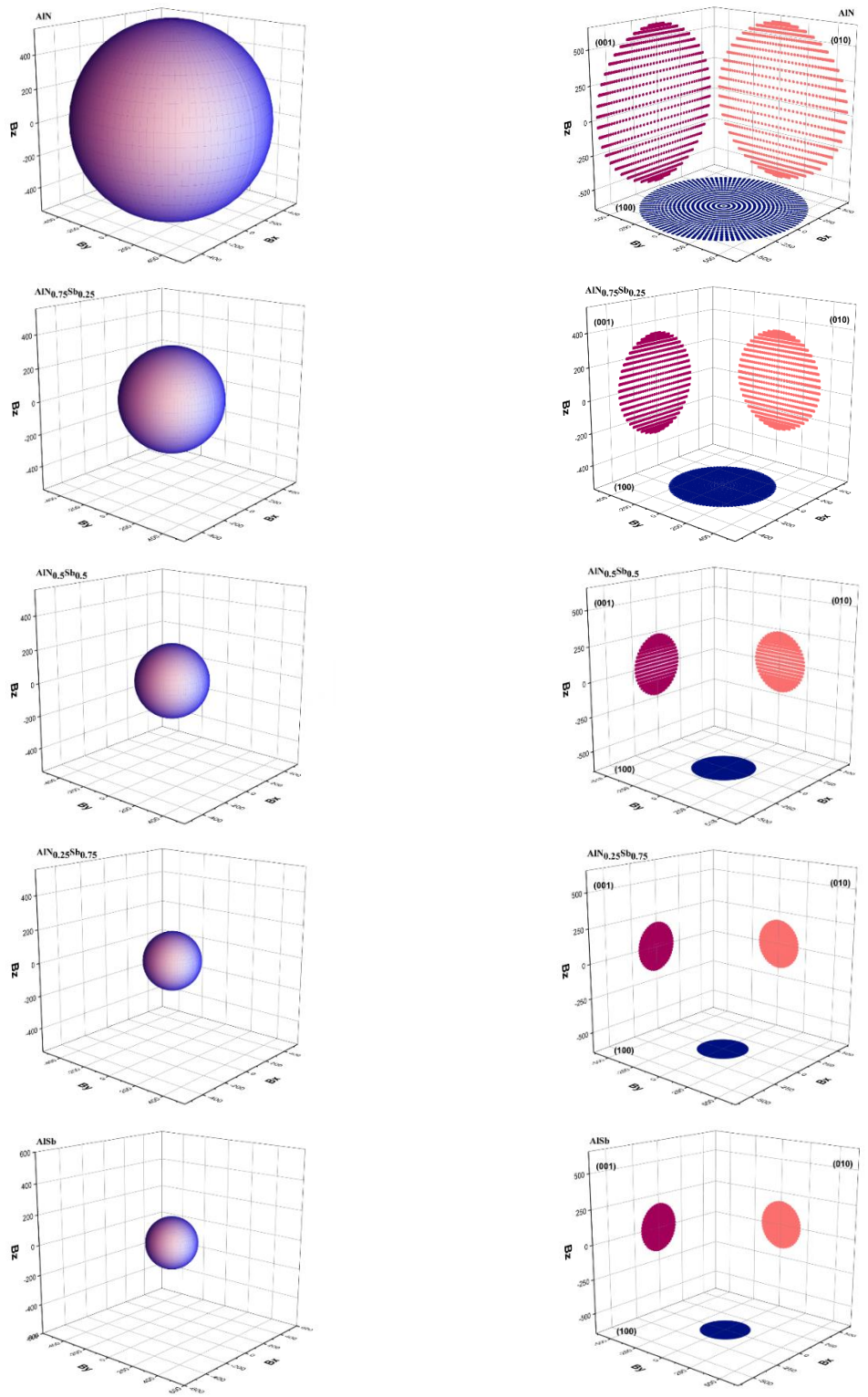


Figure IV. 19: ***3D-directional dependence of the Bulk modulus (B in GPa) accompanied with its projections in different planes for $AlN_{1-x}Sb_x$***

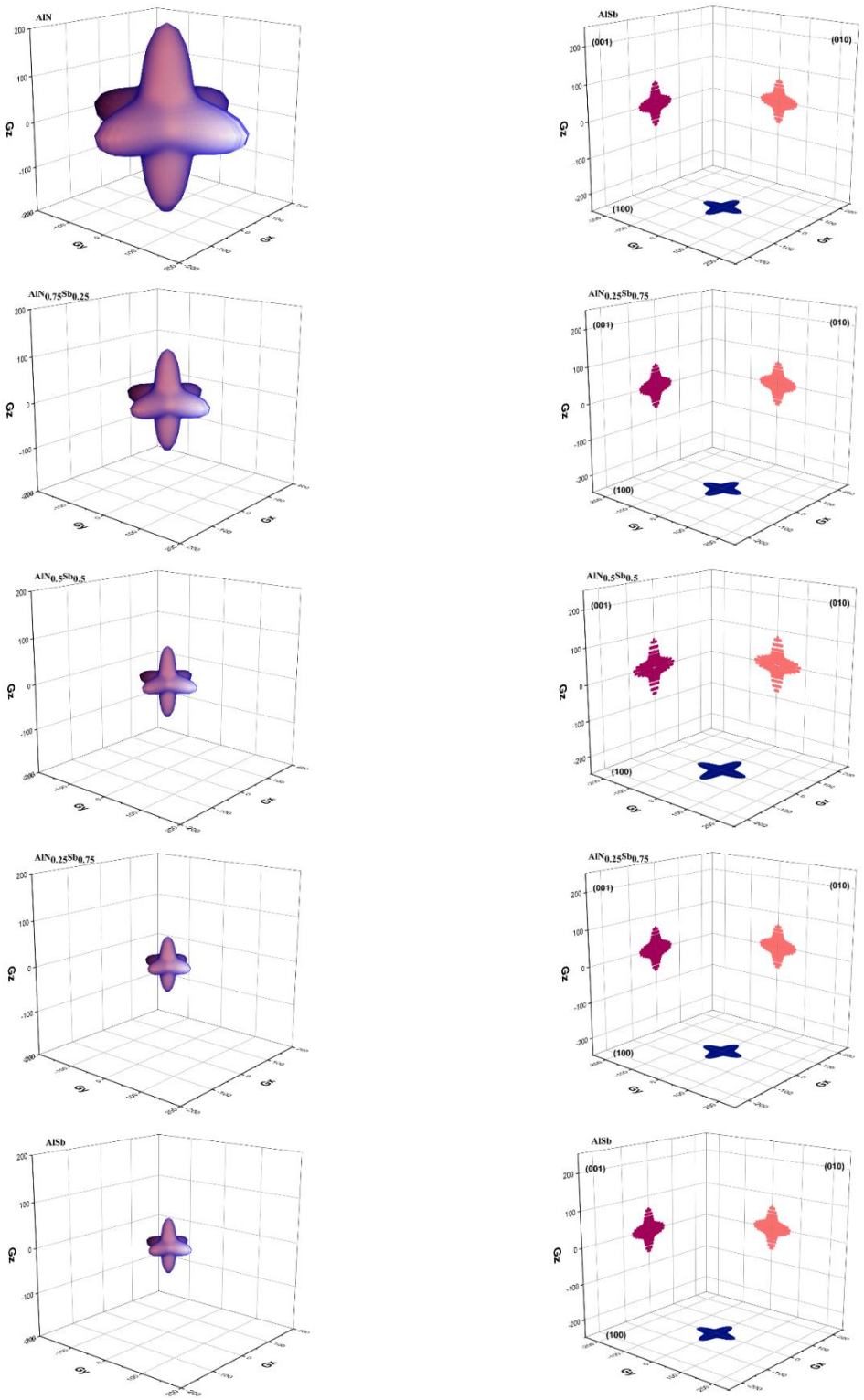


Figure IV. 20: ***3D-directional dependence of the Shear modulus (B in GPa) accompanied with its projections in different planes for $AlN_{1-x}Sb_x$***

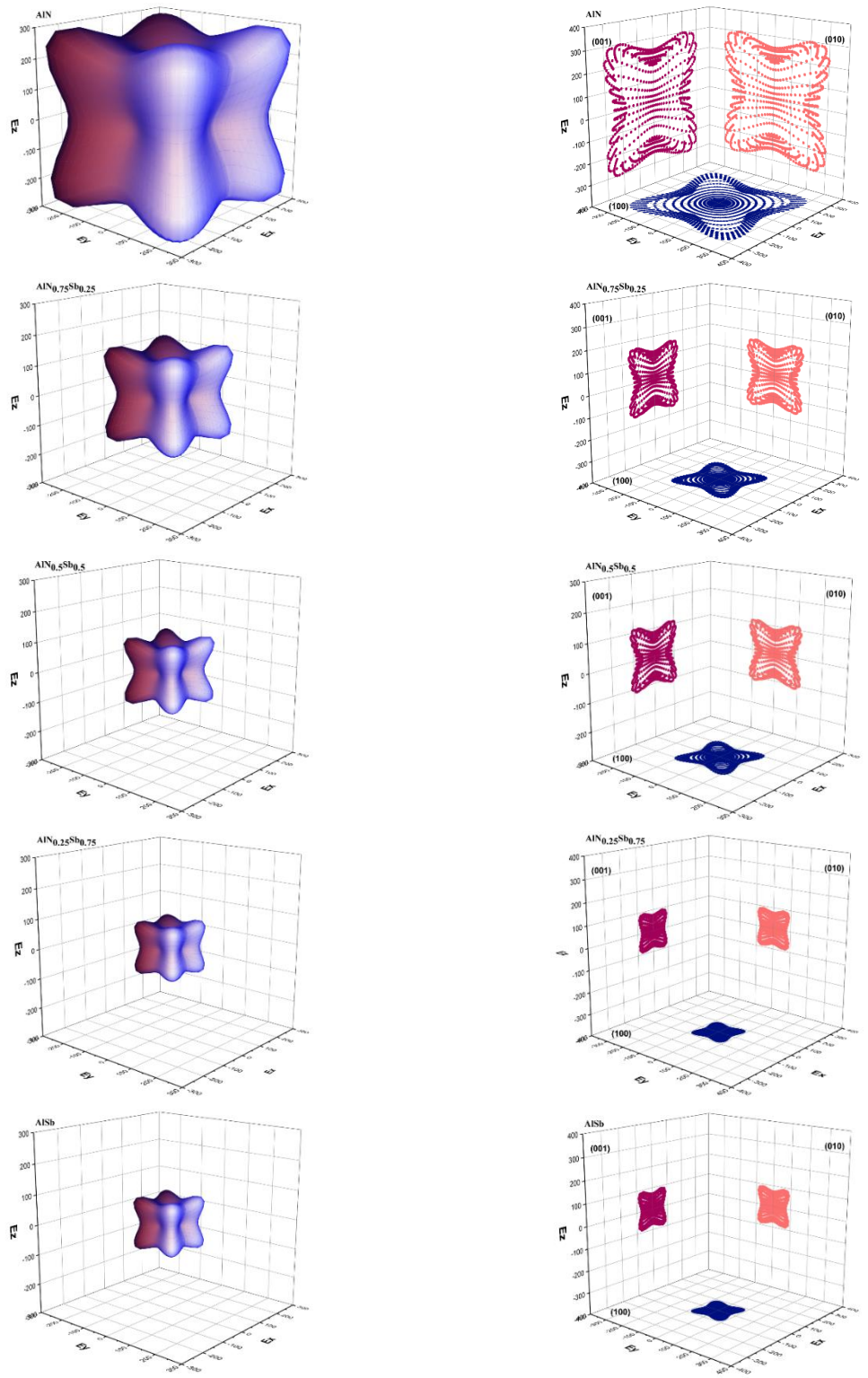


Figure IV. 21: ***3D-directional dependence of the Young modulus (B in GPa) accompanied with its projections in different planes for $AlN_{1-x}Sb_x$***

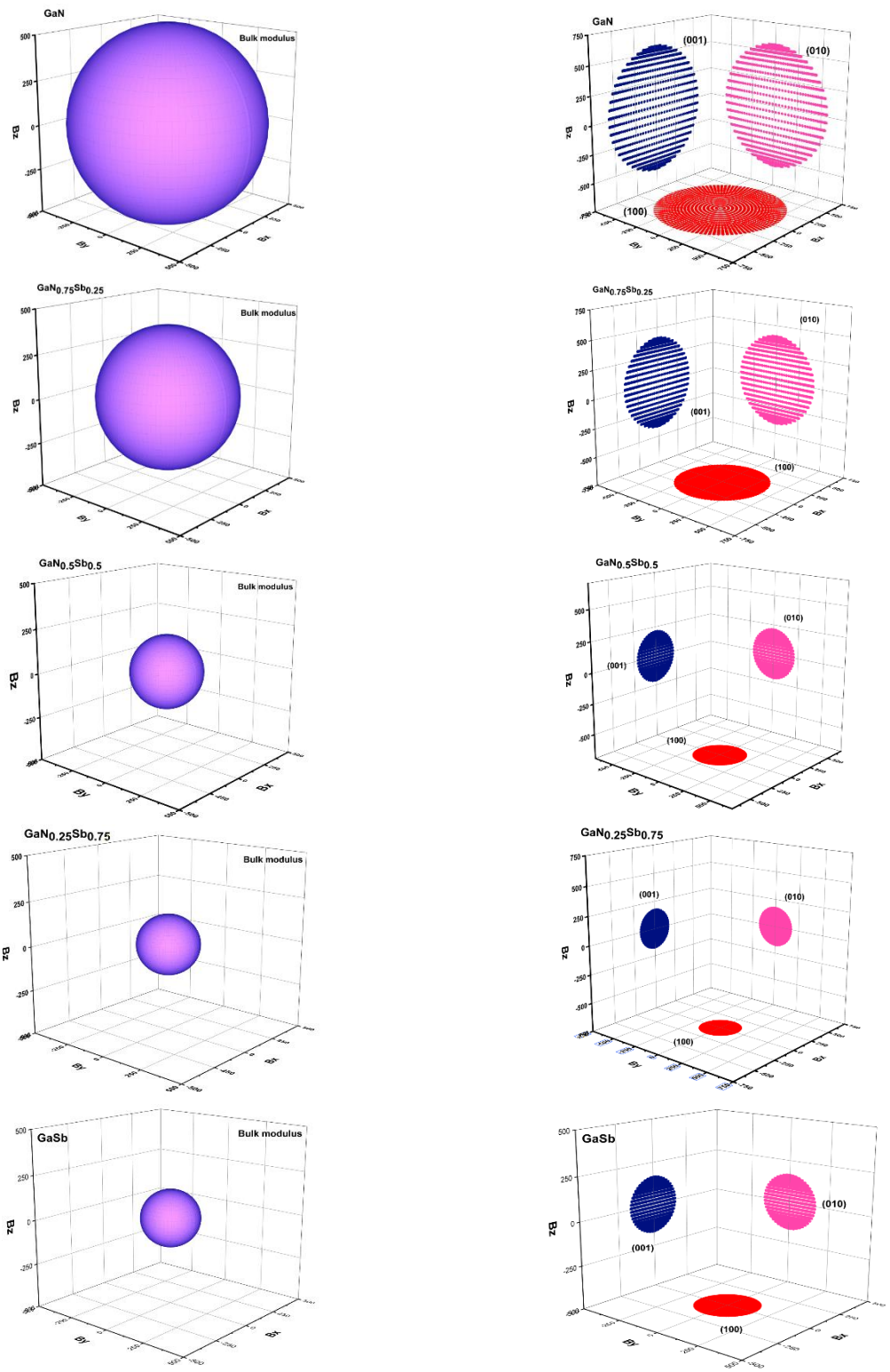


Figure IV. 22: ***3D surface of the bulk modulus in GPa and their 2D projections in (100), (010) and (001) planes for $GaN_{1-x}Sb_x$ with x = (0, 0.25, 0.50, 0.75 and 1).***

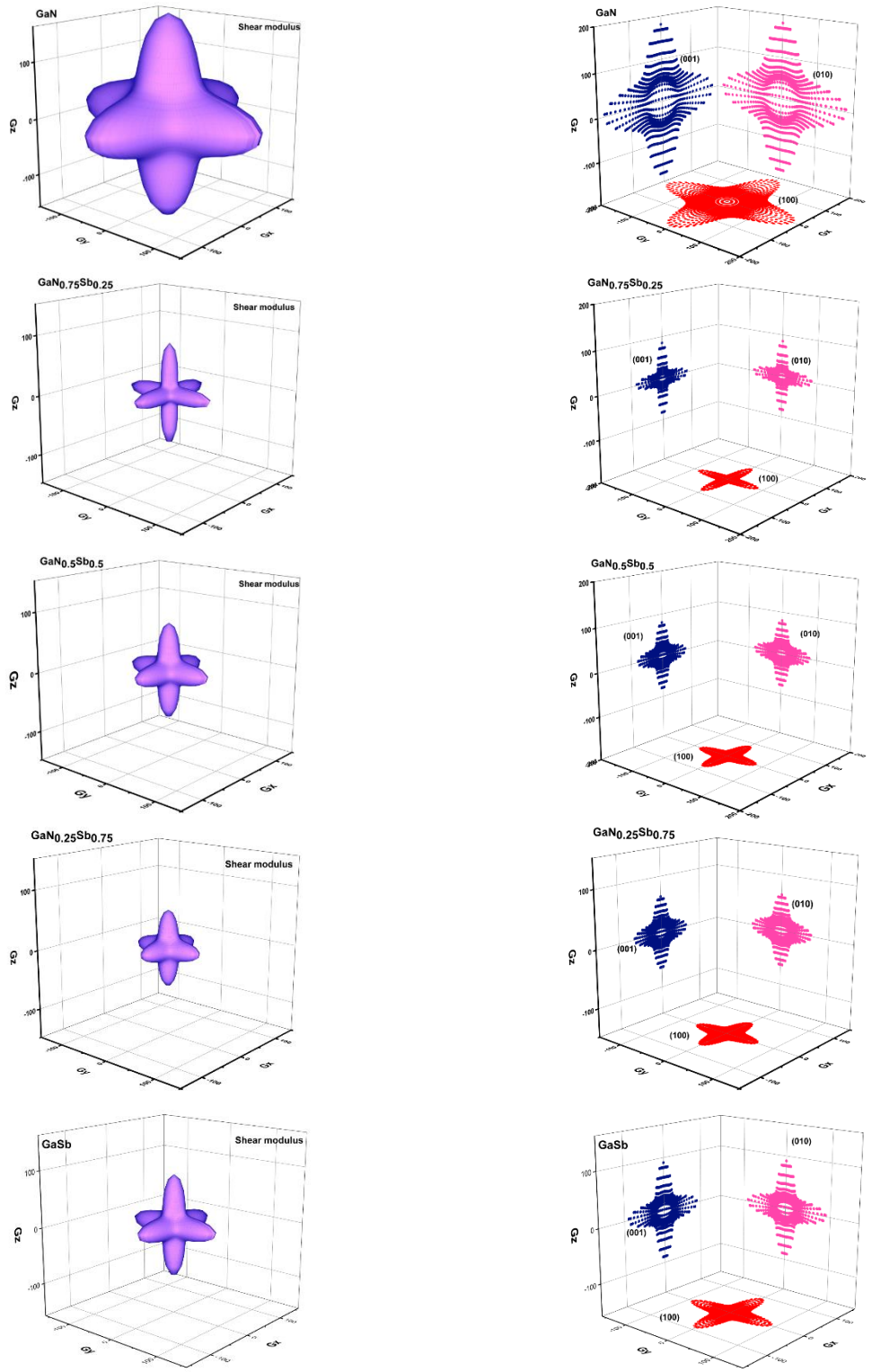


Figure IV. 23: ***3D surface of Shear modulus in GPa and their 2D projections in (100), (010) and (001) planes for $GaN_{1-x}Sb_x$ with x = (0, 0.25, 0.50, 0.75 and 1).***

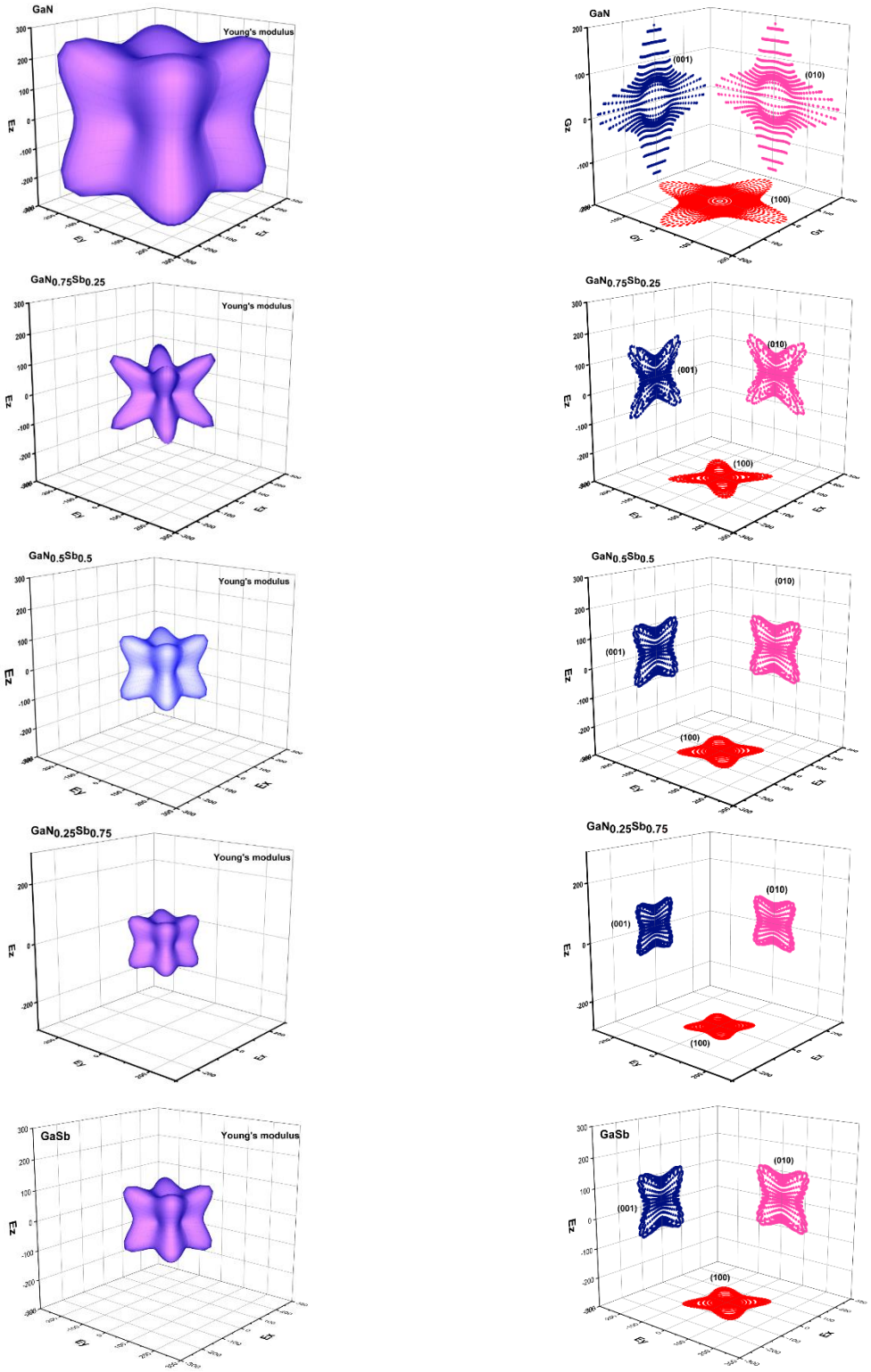


Figure IV. 24: ***3D surface of Young's modulus in GPa and their 2D projections in (100), (010) and (001) planes for $GaN_{1-x}Sb_x$ with x = (0, 0.25, 0.50, 0.75 and 1).***

IV.3.6. Thermal properties

Semiconductors exhibit several important properties associated directly with temperature, like the effect of temperature on lattice parameter and bulk modulus and other thermal properties such as heat capacity(C_V *and* C_P), Debye temperature.

Computational methods for investigating thermal properties suggest the advantage of simulating extreme temperature and pressure conditions that are difficult to achieve experimentally. While reaching such conditions in practice is challenging, these studies are essential for advancing theoretical understanding, predicting material behavior, validating models, and informing future experimental work. The obtained results including the effect of temperature on lattice parameter, bulk modulus, heat capacity C_V, heat capacity C_P and Debye temperature in the temperature range of 0 to 1000 K are displayed in ***Figure IV. 25, Figure IV. 26 and Figure IV. 27*** for $BN_{1-x}Sb_x$, $AlN_{1-x}Sb_x$ and $GaN_{1-x}Sb_x$., respectively.

Based on ***Figure IV. 25(a)***, ***Figure IV. 26(a)*** and ***Figure IV. 27(a)***, lattice parameters of all alloys in $YN_{1-x}Sb_x$ (Y=B, Al and Ga) system are increasing while temperature increase. A marginal increase is observed by about 0.2°A in spite of the increase in temperature by 1000 K for both of $BN_{1-x}Sb_x$ and $AlN_{1-x}Sb_x$ systems, while a noticeable decrease compared to of $BN_{1-x}Sb_x$ and $AlN_{1-x}Sb_x$ systems, yet it remains small for $GaN_{1-x}Sb_x$ system especially for binary compounds. $YN_{1-x}Sb_x$ (Y=B, Al and Ga) alloys with a higher covalent character thus reduces thermal contraction compared to alloys with more ionic or metallic character, in which alloys with stronger bonds and higher stiffness expanded less with increasing temperature.

Temperature have opposite effect on bulk modulus displayed in ***Figure IV. 25(b)***, ***Figure IV. 26(b)*** and ***Figure IV. 27(b),*** increasing of temperature cause an increase in volume as a result the atoms of studied alloy vibrate more, due to increased interatomic spacing. This caused reduction in $YN_{1-x}Sb_x$ alloys resistance to compression, resulting in a lower bulk modulus. The decrement of bulk modulus for $GaN_{1-x}Sb_x$ system is more observed compared with those obtained for $BN_{1-x}Sb_x$ and $AlN_{1-x}Sb_x$.

Based on ***Figure IV. 25(c)***, ***Figure IV. 26(c)*** and ***Figure IV. 27(c)*** presents the changes in isochoric heat capacity C_V as function of temperature at fixed pressure. at T = 0 K the heat capacity tends to 0,for temperature bellow 200K an evident increase in heat capacity

C_V noted due to the exponential increase in the number of excited phonon modes in this temperature range as a result follows the Debye T^3 law [133]. However, for temperature above $200K$ the heat capacityC_V increase slowly and at higher temperature follow the well-known Dulong-Petit limit [134]. The calculated value of specific isochoric heat capacity for binary compounds is about 50J/mol K, however, for ternary alloys it's 199 J/molK. Remarkably, the values of C_V for ternary alloys at composition 0.25, 0.5 and 0.75 is four times than that of the binary alloys because of the heat capacity is proportional to the number of atoms.

The variation of the isobaric heat capacity C_p as a function of temperature is shown in ***Figure IV. 25(d)***, ***Figure IV. 26(d)*** and ***Figure IV. 27(d)*** . In the range of 0 to 200 K, C_p is identical to the isochoric heat capacity C_V. From 200 to 100 K, the rate of increase of C_p slows down and does not converge to a constant value.

Figure IV. 25(e), ***Figure IV. 26(e)*** and ***Figure IV. 27(e)*** represent the variation of Debye temperature as function of temperature, this parameter corresponds to the temperature at which all possible vibrational (phonon) modes of the solid become fully activated.

A marginal decrease for values of Debye temperature for $BN_{1-x}Sb_x$ and $AlN_{1-x}Sb_x$ systems. For $GaN_{1-x}Sb_x$ system, the values of Debye temperature are relatively constant for temperature range of 0 – 100 K and after that, a clear reduced with increasing temperature is noted. A decrease in the Debye temperature values for $YN_{1-x}Sb_x$ (Y=B, Al and Ga) alloys with increasing Sb concentration, also a diminution in which with increasing temperature at fixed pressures, thus, cause expansive distortions of the structure as a result decrease of the vibrational frequencies noted, therefore, Debye temperature decreases.

The table below (***Table IV. 10***) represent the values of lattice parameter a_0, bulk modulus B_0, the isochoric heat capacity C_V, isobaric heat capacity C_P and Debye temperature $\theta(K)$ at ambient conditions (P = 0 and T = 300 K) accompanied with available experimental and theoretical data.

Table IV. 10: *Lattice parameter a_0, bulk modulus B_0, isochoric heat capacity C_V, isobaric heat capacity C_P and Debye temperature $\theta(K)$ at ambient conditions for $YN_{1-x}Sb_x$ (Y=B, Al and Ga) systems*

Alloys	x		$a_0(°A)$	$B_0(GPa)$	C_V(J /mol K)	C_P(J /mol K)	$\theta(K)$
$BN_{1-x}Sb_x$	0.0	Our work	3.63	379.56	19.51	19.63	1444.61
	0.25	Our work	4.31	192.76	145.67	147.96	778.81
	0.5	Our work	4.75	133.90	169.57	173.74	550.9
	0.75	Our work	5.04	113.70	178.62	183.35	451.9
	1	Our work	5.25	103.62	45.84	47.02	393.75
		Other calc.					377.5[135] 456.07[136]
$AlN_{1-x}Sb_x$	0.0	Our work	4.40	194.98	33.23	33.74	893.92
	0.25	Our work	5.08	93.11	172.78	177.62	517.04
	0.5	Our work	5.57	70.36	182.95	188.85	398.95
	0.75	Our work	5.93	57.06	188.14	194.27	327.57
	1	Our work	6.19	50.88	47.68	49.29	286.28
		Other calc.		52.50[137]	46.33[137]		367.77[137] 370[138]
$GaN_{1-x}Sb_x$	0.0	Our work	4.52	185.30	41.31	40.62	621.83
	0.25	Our work	5.14	89.24	195.10	183.13	396.75
	0.5	Our work	5.59	66.21	194.78	188.49	322.28
	0.75	Our work	5.93	52.19	203.61	191.78	268.37
	1	Our work	6.15	49.47	50.07	48.22	247.77

Despite the lack of references about thermal parameters at ambiante condition, the available results are in good accordance with obtained values.

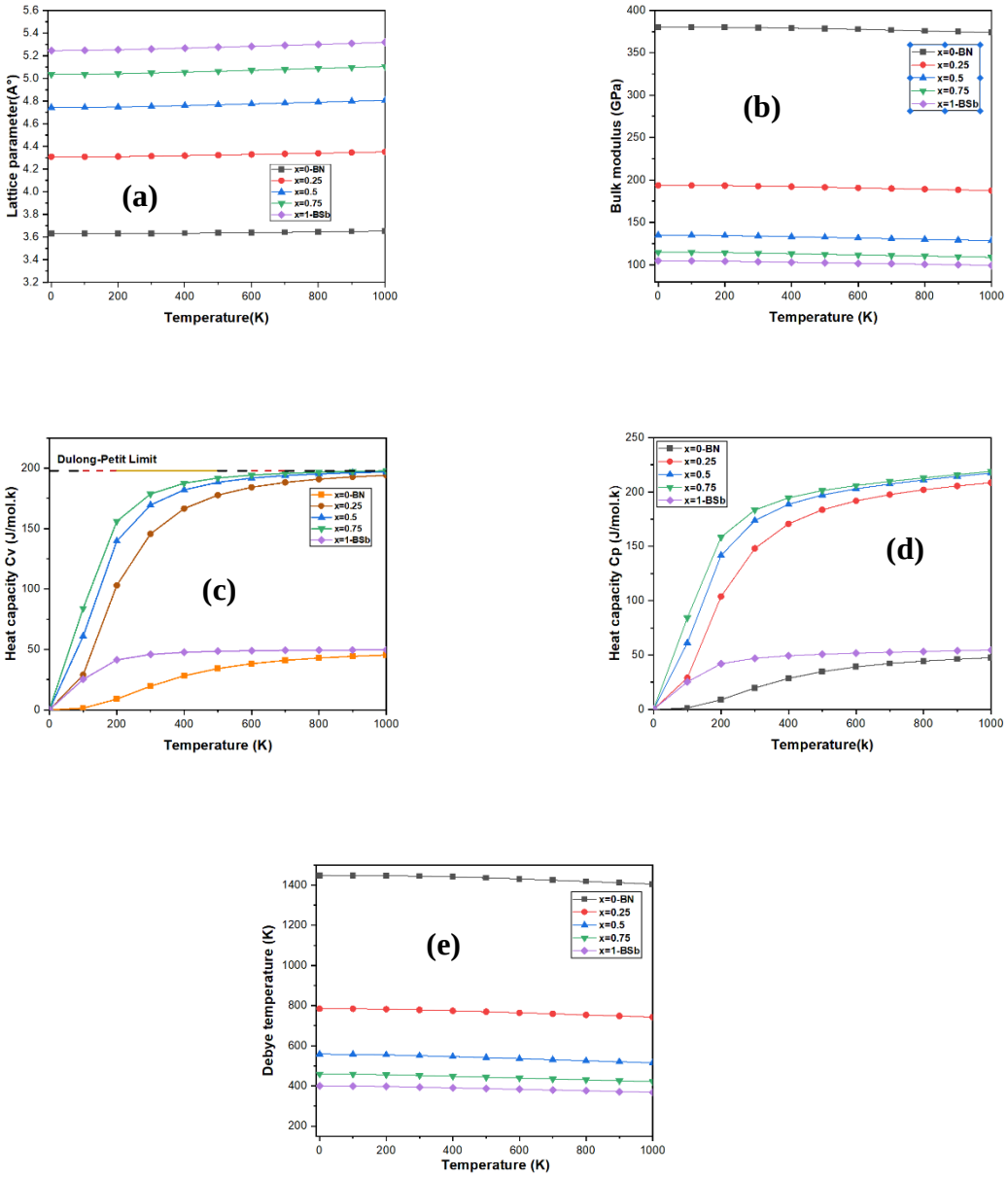


Figure IV. 25: ***variation of lattice parameter, bulk modulus, isochoric heat capacity C_V , isobaric heat capacity C_P and Debye temperature as function of temperature for $BN_{1-x}Sb_x$ alloys***

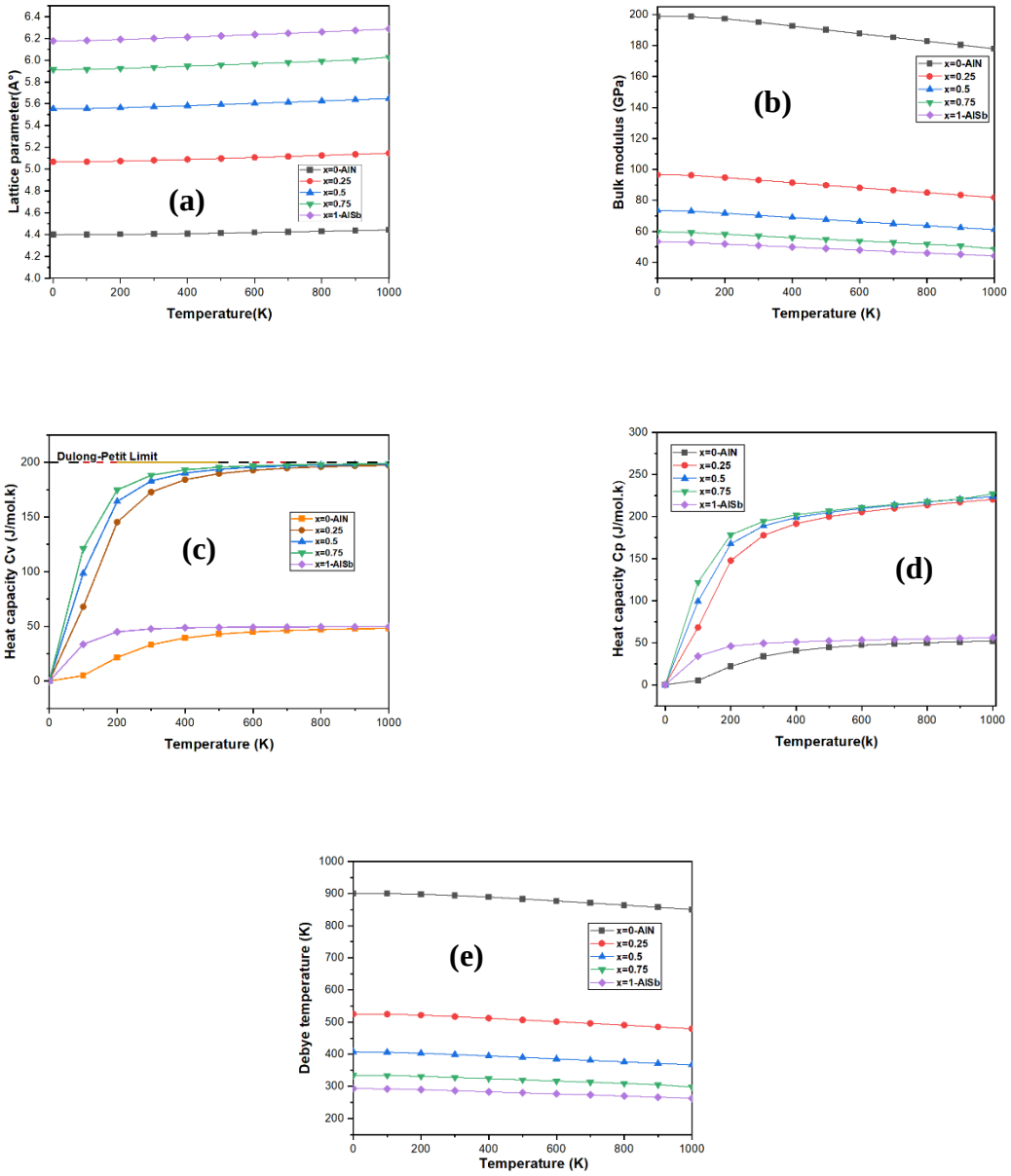


Figure IV. 26: ***variation of lattice parameter, bulk modulus, isochoric heat capacity C_V, isobaric heat capacity C_P and Debye temperature as function of temperature for $AlN_{1-x}Sb_x$ alloys***

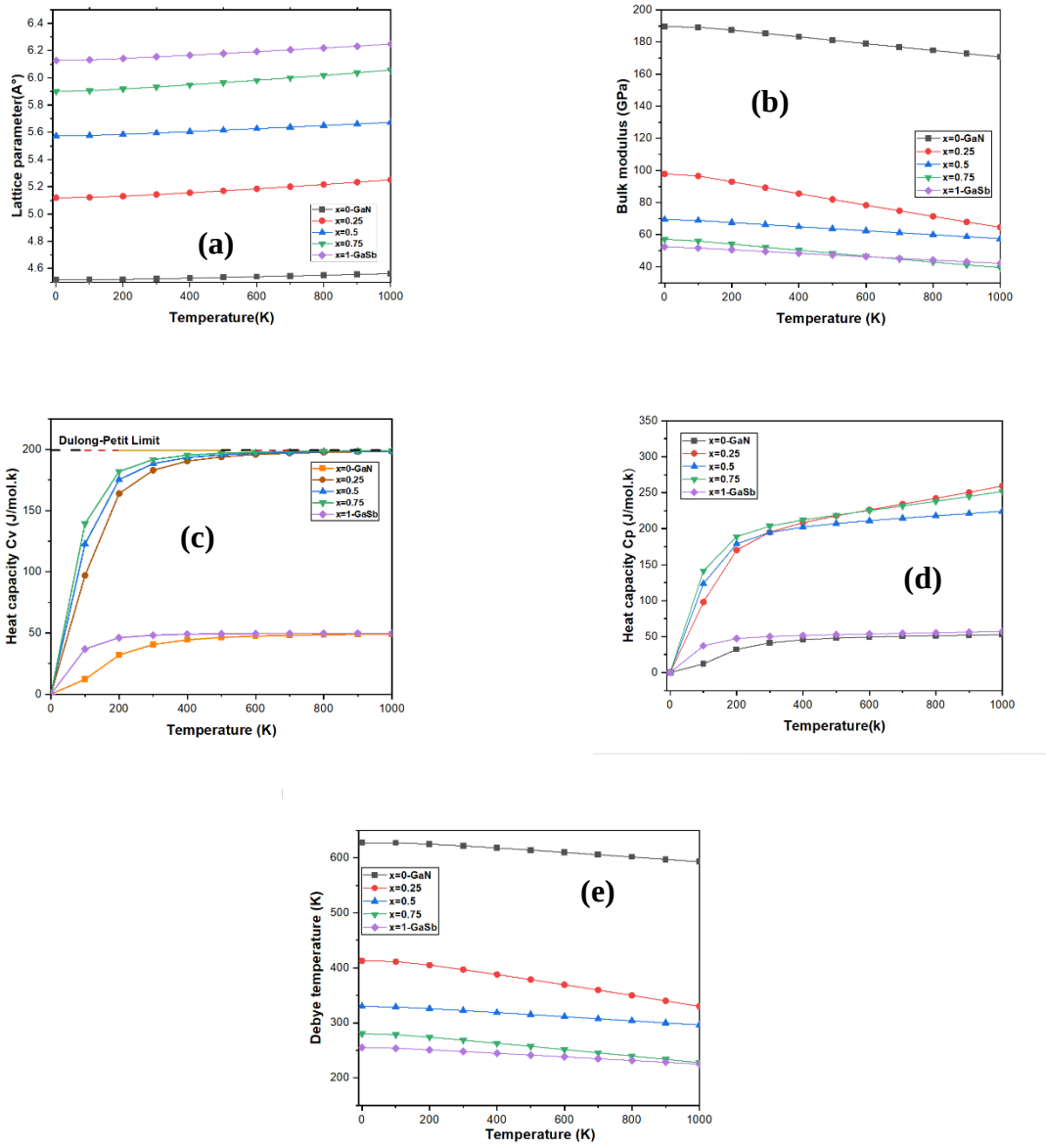


Figure IV. 27: ***variation of lattice parameter, bulk modulus, isochoric heat capacity C_V , isobaric heat capacity C_P and Debye temperature as function of temperature for $GaN_{1-x}Sb_x$ alloys***

IV.4. Properties of Sr_2NaXO_6 (X = Cl, Br and I) Double Perovskite semiconductors

IV.4.1. Structural properties

Sr_2NaXO_6 (X = Cl, Br and I) double perovskites are an interesting group of materials where slight changes in the halide ions can have a significant impact on both structural stability and bonding behavior. It crystallize in a cubic lattice corresponding to the Fm-3m space group [139]. The starting point of this work involves analyzing the ground-state structural features of the oxide double perovskites Sr_2NaXO_6 (X = Cl, Br and I), which obtained by evaluating the total energy $E\ (Ry)$ versus the unit cell volume $V\ (a.u.)^3$.

The calculated $E = f\ (V)$ relationships for each compound are illustrated in ***Figure IV. 28***. The fundamental structural parameters, including the lattice parameter (a_0), bulk modulus (B_0), its first derivative (B_0'), and the ground-state energy (E_0), were obtained by fitting the total energy – volume data to the Birch – Murnaghan equation of state [140], as shown in ***Table IV. 10***.

It is evident that both the lattice parameter and the bulk modulus increase from chlorine to iodine. This trend can be attributed to the increase in atomic radius along the halogen series. The calculated lattice parameter and bulk modulus for Sr_2NaIO_6 are in close agreement with the values reported by J.K. Bairwa and al. [141] (8.31 Å and 130.31 GPa), with deviations of less than 5% and 2%, respectively. However, the results obtained by A. Aziz and al. [142] using CASTEP (5.88 Å and 81.62 GPa) exhibit a notable discrepancy compared to our findings.

It is important to highlight that Sr_2NaClO_6 and Sr_2NaBrO_6 have not been previously investigated either theoretically or experimentally, making our results a useful reference for future studies.

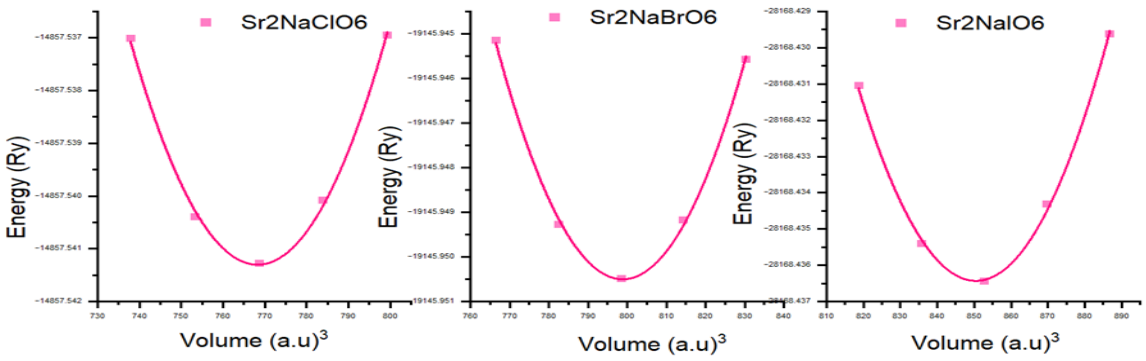


Figure IV. 28: ***The total energy plotted as function of volume for Sr_2NaXO_6(X=Cl, Br and I) oxide double perovskites.***

In order to assess the stability and determine the stable crystal structure of Sr_2NaXO_6 (X = Cl, Br and I), the formation energy (E_F), Goldschmidt's tolerance factor (τ) [143], and octahedral factor (μ) w

As shown in ***Table IV. 11***, the negative values of formation energy demonstrate the chemical stability of Sr_2NaClO_6, Sr_2NaBrO_6, and Sr_2NaIO_6, suggesting that these compounds can potentially be synthesized experimentally.

The tolerance factor (τ) for Sr_2NaXO_6 (X = Cl, Br and I) falls within 0.9 – 1.05, implying the formation of an ideal cubic structure. Additionally, the octahedral factor (μ), according to Goldschmidt, is in the range 0.416 – 0.896, which is further indicating that the studied double perovskites are structurally stable.

Table IV. 11: *Fundamental structural parameters* $(a_0,\ B_0,\ B'_0,\ E_0)$*, formation energy* (E_F)*, Goldschmidt's tolerance factor* (τ)*and octahedral factor* (μ) *for Sr2NaXO6(X=Cl, Br and I)*

Compounds		Sr_2NaClO_6	Sr_2NaBrO_6	Sr_2NaIO_6
Lattice parameter a_0 (°A)	Present	7.689	7.7910	7.95552
	Other Calc.			8.31[141], 5.88[142]
Bulk modulus B_0 (GPa)	Present	103.830	118.275	133.0449
	Other Calc.			130.31[141],81.62[142]
First derivative of bulk modulus B'_0 (GPa)	Present	5.358	4.8398	5.0423
Ground-state total energy E_0 (Ry)	Present	-14857.5413	-19145.9504	-28168.4364
Formation energy (E_F (eV/atom))	Present	-2.948	-3.206	-3.409
Tolerance factor (τ)	Present	0.981	0.954	0.923
Octahedral factor (τ)	Present	0.460	0.503	0.553

IV.4.2. Electronic properties

The analysis of electronic behavior is crucial for the development of material based devices, enhancing performance, efficiency, and identifying in potential optoelectronic applications. Consequently, the electronic band structures of Sr_2NaXO_6 (X = Cl, Br and I) were calculated using the TB - mBJ and KTB - mBJ potential methods. As illustrated in ***Figure IV. 29***, all three

compounds Sr_2NaClO_6, Sr_2NaBrO_6, and Sr_2NaIO_6 exhibit semiconducting properties, with energy band gaps listed in ***Table IV. 12***.

***Table IV. 12**: Energy gap values (eV) of Sr2NaXO6($X = Cl, Br$ and I)*			
Compounds	TB-mBJ	KTB-mBJ	Other calc.
Sr2NaClO6	0.9996	1.3538	
Sr2NaBrO6	1.5324	1.8073	
Sr2NaIO6	3.3605	3.5202	1.57[142] ,0.263[141]

As illustrated in ***Figure IV. 29***, the studied double perovskite compounds exhibit direct band gaps at the Γ point of the Brillouin zone. The valence bands (VB) are more densely packed than the conduction bands (CB), indicating p-type semiconducting behavior with holes as the majority carriers for Sr_2NaXO_6 (X = Cl, Br and I). The calculated band gaps show that the values obtained using the KTB-mBJ approximation are larger than those from the TB-mBJ method by approximately 26%, 15%, and 4% for Sr_2NaClO_6, Sr_2NaBrO_6, and Sr_2NaIO_6, respectively. Moreover, the band gap increases progressively from Sr_2NaClO_6 to Sr_2NaIO_6.

For further validation, our results were compared with those for Sr_2NaIO_6 reported in references [141,142]. The observed discrepancies arise primarily from the different computational schemes and software utilized in the studies.

To explore the contributions of individual atoms to the electronic structure of Sr_2NaXO_6 (X = Cl, Br and I) and the origin of the energy bands, total (T) and partial (P) densities of states (DOS) were calculated using the KTB-mBJ approach and are presented in ***Figure IV. 30***.

For all studied compounds, the DOS exhibits three separate regions: the lower valence band (LVB), the upper valence band (UVB), and the conduction band (CB), which indicates semiconducting behavior.

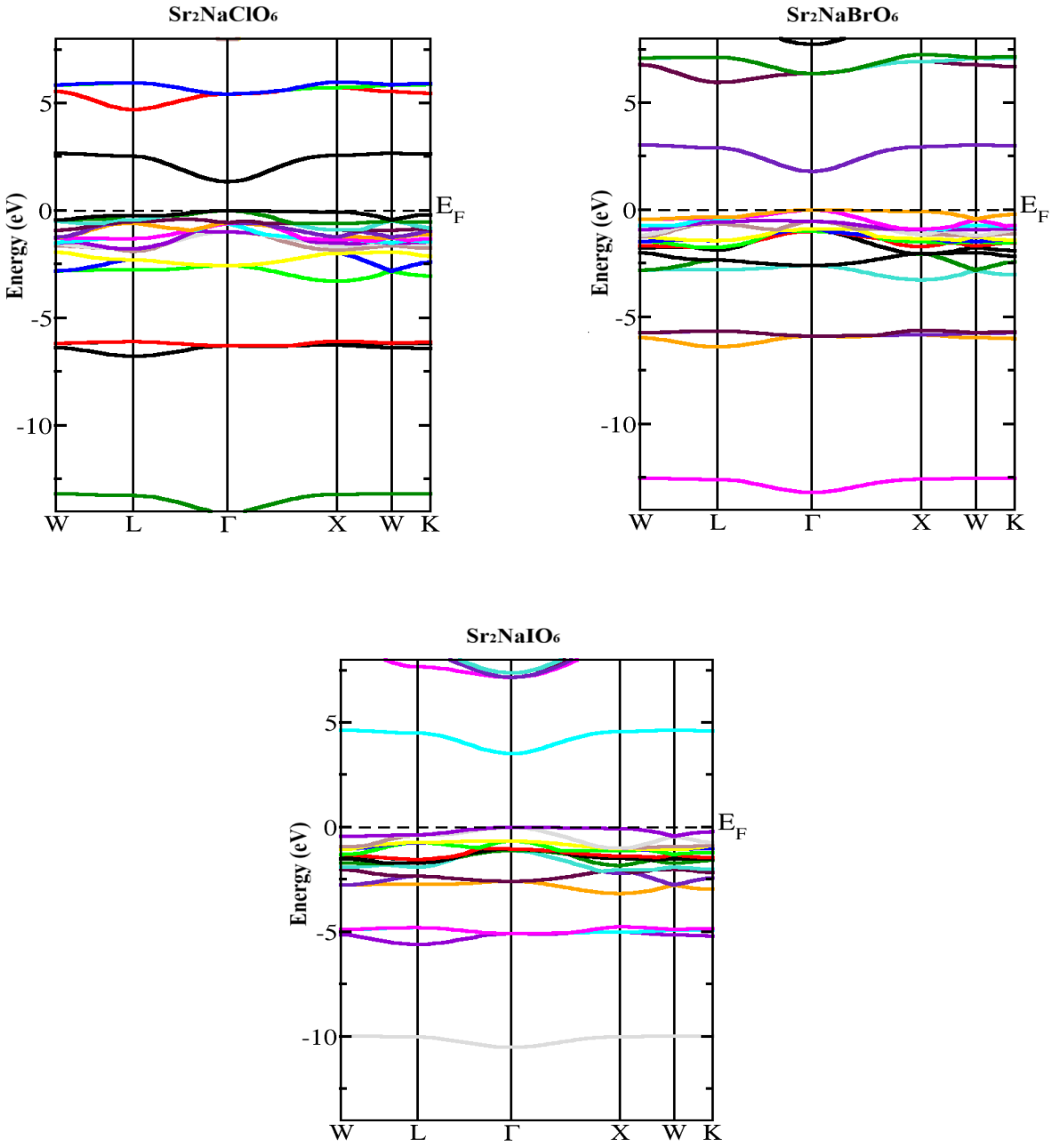


Figure IV. 29: The simulated band structures for Sr_2NaXO_6 (X = Cl, Br and I) using KTB-mBJ approximation.

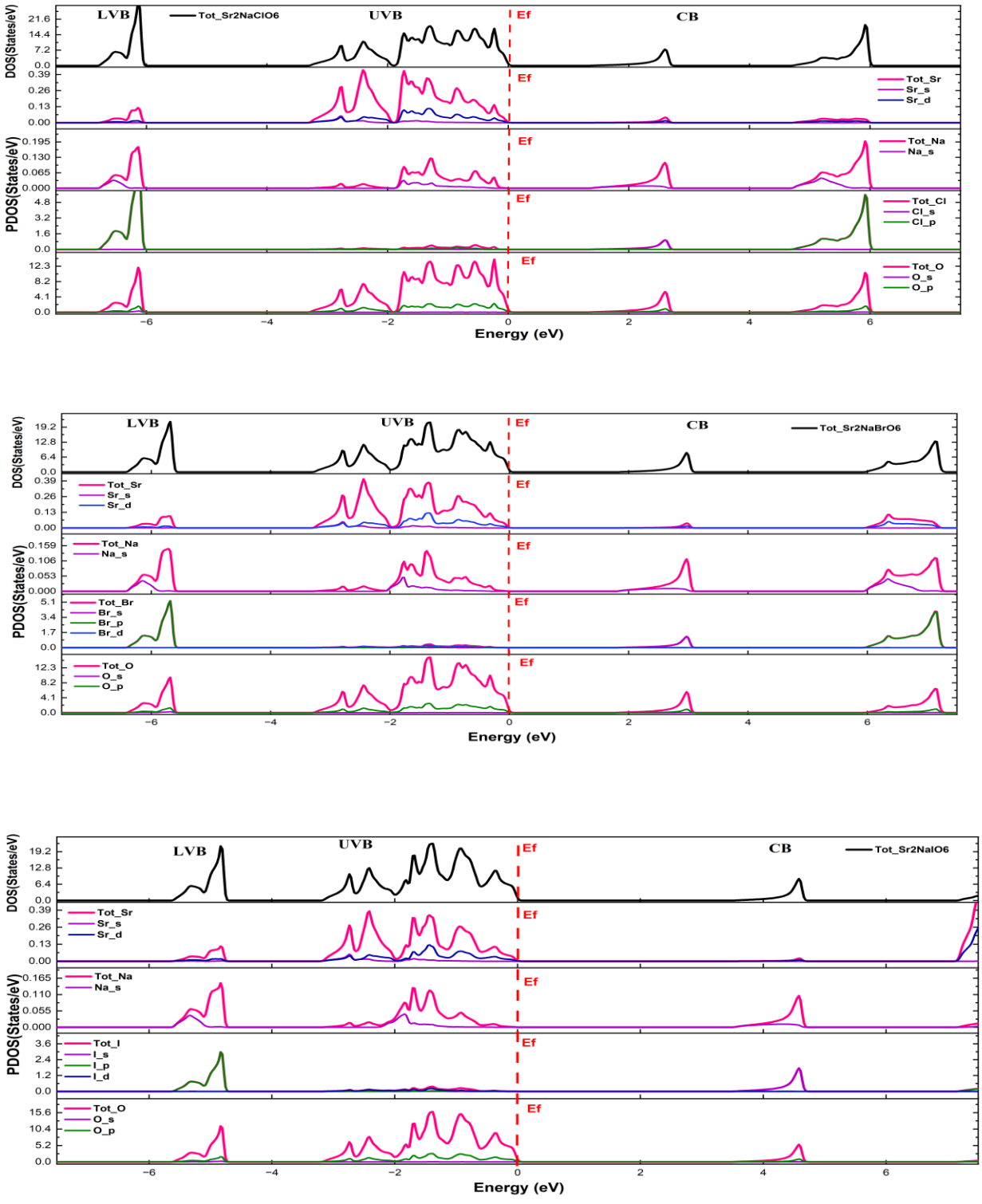


Figure IV. 30: ***TDOS and PDOS for Sr_2NaXO_6 (X = Cl, Br and I) using KTB-mBJ potential scheme***

Figure IV. 30 shows that the lower valence band (LVB) originates primarily from the p-orbital electrons of oxygen atoms and halide ions. The upper valence band (UVB) is dominated by contributions from the p-orbitals of oxygen, with only minor input from the p-orbitals of Sr atoms. However, the CB is mainly contributed by the p-electrons of oxygen. In contrast, the contributions from the s-orbitals of Sr, Na, and halide ions, as well as the d-orbitals of Sr and other electrons of oxygen, are negligible.

It is also evident from Figure 30 that Near the Fermi level, the CB of Sr_2NaClO_6 and Sr_2NaBrO_6 features two prominent peaks at 2.60 and 5.92 eV, and 2.97 and 7.13 eV, respectively. However, Sr_2NaIO_6 displays only one peak at 4.58 eV. The initial conduction band peak in Sr_2NaXO_6(X = Cl, Br and I) is largely influenced by the X-s orbitals, with contributions of 1.00, 1.17, and 1.65 states/eV from Cl, Br, and I, respectively, while the O-p orbitals contribute 0.76, 1.15, and 0.89 states/eV. For both Sr_2NaClO_6 and Sr_2NaBrO_6, the second peak in the conduction band is determined mainly by the halogen p-orbitals, which contribute states/eV 5.51 and 4.02 states/eV, and the O-p orbitals, which contribute 1.53 and 0.89 states/eV, respectively. For Sr_2NaXO_6 (X = Cl, Br and I), the UVB consists of consecutive peaks between approximately −3.3 eV and 0 eV, suggesting a similar electronic structure across the series near the Fermi energy. The LVB is concentrated in a high-intensity peak at energies below about −4.5 eV.

IV.4.3. Optical properties

Optical characteristics such as absorption, emission, refractive index, and reflectivity are directly influenced by the interactions between electrons and holes in a material. These interactions are fundamental for applications in lasers, LEDs, and solar cells.

To understand and optimize these properties, we investigated the complex dielectric function, absorption coefficient, and refractive index of Sr_2NaXO_6 (X = Cl, Br and I) double perovskites in the 0 – 13.5 eV energy range using the KTB-mBJ potential method.

- **Dielectric Function**

The complex dielectric function, ε (ω), is a fundamental tool for explaining a material's optical response, capturing how it interacts with electromagnetic waves. From this function, critical optical properties such as absorption, refractive index, and extinction coefficient can be derived, which are essential for understanding light material interactions.

Figure IV. 31 illustrates the energy-dependent real and imaginary components of the dielectric function, $\varepsilon_1(\omega)$ and $\varepsilon_2(\omega)$, for the Sr_2NaXO_6 (X = Cl, Br and I) double perovskite systems. The real dielectric function, $\varepsilon_1(\omega)$, indicates the polarization response of the materials. From ***Figure IV. 31***, it is evident that $\varepsilon_1(\omega)$rises to its first prominent peak in the UV range at 5.21 eV (6.77), 6.40 eV (6.43) and 8.53 eV (5.38) for Sr_2NaClO_6, $Sr_{22}NaBrO_6$, and Sr_2NaIO_6 respectively. This is followed by a secondary peak at slightly higher energies of 5.91 eV (6.0), 7.25 eV (6.1), and 9.10 eV (4.72), after which the dielectric function drops sharply.

Figure IV. 31 also indicates that the maximum values of $\varepsilon_1(\omega)$ decrease as the halide changes from Cl to I in Sr_2NaXO_6. This trend can be attributed to the increasing atomic size of the halide and the corresponding differences in the energy bandgap among the compounds.

Anomalous dispersion is confirmed by the negative values of the real dielectric constant $\varepsilon_1(\omega)$, implying metallic behavior. Specifically, Sr_2NaClO_6 exhibits this metallic nature within the energy intervals of 6.39 – 7.69 eV, 8.82 – 9.30 eV, and beyond 11 eV. Furthermore, Sr_2NaBrO_6 exhibits metallic behavior within the energy interval of 8.58 – 9.56 eV and again at energies exceeding 10.32 eV. In contrast, Sr_2NaIO_6 shows metallic characteristics only beyond 9.78 eV. This response originates from the strong reflection of incident photons at the material surface, indicating that these double perovskites act as optical conductors in the high-energy region.

The attenuation of electromagnetic radiation in these materials is described by the imaginary dielectric function $\varepsilon_2(\omega)$. As shown in ***Figure IV. 31,*** the onset of absorption occurs at critical energies of 1.8 eV, 2.1 eV, and 4.0 eV for Sr_2NaClO_6, Sr_2NaBrO_6, and Sr_2NaIO_6, respectively. Strong optical absorption is evidenced by the dominant peaks in the $\varepsilon_2(\omega)$ curves, appearing at 6.16 eV, 8.61 eV, and 9.42 eV for Sr_2NaClO_6, Sr_2NaBrO_6, and Sr_2NaIO_6, respectively. The observed disparity in peak magnitudes arises from variations in electronic transition processes.

At zero photon energy, the dielectric response of the material is governed by the static dielectric function. The calculated static dielectric constants $\varepsilon_1(0)$ are 3.55 for Sr_2NaClO_6, 3.05 for Sr_2NaBrO_6, and 2.50 for Sr_2NaIO_6. A systematic reduction in the $\varepsilon_1(\omega)$ and $\varepsilon_2(\omega)$ peaks is noted as Cl is replaced by Br and subsequently by I, which can be explained by the variation in band-gap energies across Sr_2NaClO_6, Sr_2NaBrO_6, and Sr_2NaIO_6.

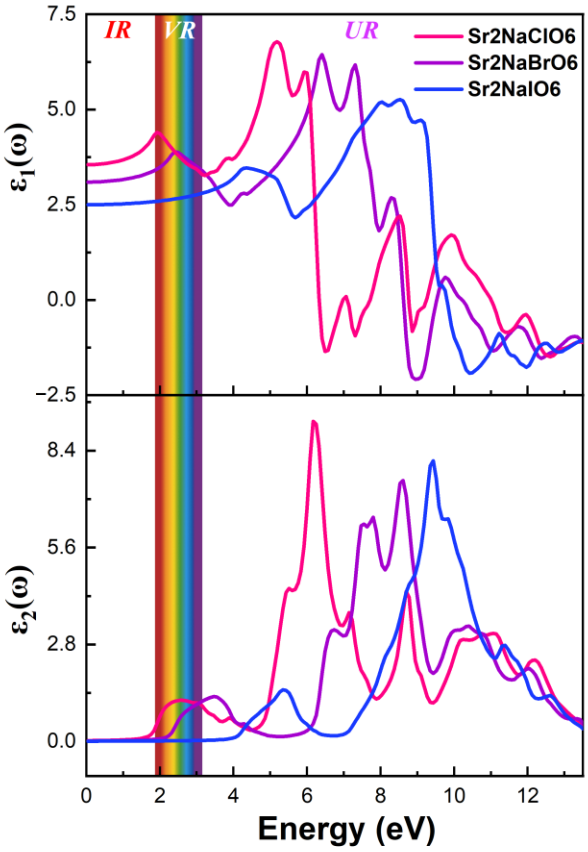


Figure IV. 31: ***The energy dependence on the parts of dielectric function ($\varepsilon_1(\omega)$ and $\varepsilon_2(\omega)$) for Sr_2NaXO_6(X=Cl, Br and I) oxide double perovskites.***

- **Absorption Coefficient**

The absorption coefficient quantifies the ability of a material to absorb electromagnetic radiation during its propagation. The energy-dependent absorption coefficient of the Sr_2NaXO_6 compounds is presented in ***Figure IV. 32***. As observed, Sr_2NaClO_6 and Sr_2NaBrO_6 exhibit absorption onsets in the visible range, whereas Sr_2NaIO_6 shows an absorption edge in the ultraviolet region at approximately 2.25 eV, 2.57 eV, and 4.30 eV, respectively.

The absorption coefficient spectra of the studied compounds exhibit several prominent peaks in the ultraviolet region. For Sr_2NaClO_6, three major peaks are located at 6.40 eV, 8.77 eV, and 12.49 eV; for Sr_2NaBrO_6, they appear at 8.77 eV, 10.97 eV, and 12.28 eV; while for Sr_2NaIO_6, the peaks are observed at 9.51 eV, 10.32 eV, and 11.79 eV. Overall, the Sr_2NaXO_6 (X = Cl, Br and I) double perovskites demonstrate strong ultraviolet absorption. The present findings confirm the

suitability of these materials for use in solar cell devices, ultraviolet photodetectors [144,145], UV-blocking optical coatings, and advanced photovoltaic and optoelectronic technologies [146,147].

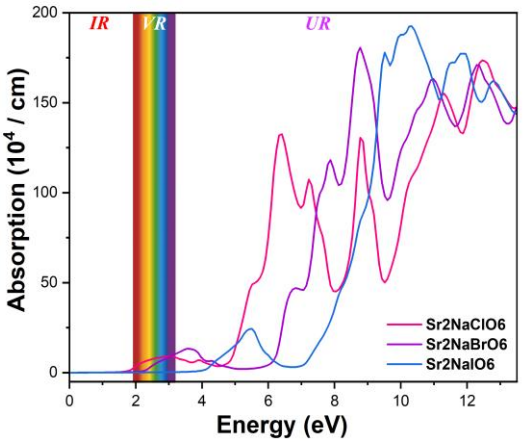


***Figure IV. 32:* Variation of absorption coefficient as function of energy for Sr_2NaXO_6 (X = Cl, Br and I) oxide double perovskites**

- **refractive index and extinction coefficient $K(\omega)$**

By incorporating the phase velocity of light and its absorption, refractive index provides a complete description of light–material interactions. The propagation of light through a material is described by the refractive index $n(\omega)$, while the extinction coefficient $K(\omega)$ represents the extinction of light due to combined absorption and scattering effects.

The real and imaginary components of refractive index for Sr_2NaXO_6 (X = Cl, Br and I) double perovskites are plotted as a function of incident photon energy, as illustrated in ***Figure IV. 33***.

It is observed that as photon energy increases, the calculated refractive index rises rapidly and then gradually decreases, with notable peaks in the ultraviolet region. For Sr_2NaClO_6, Sr_2NaBrO_6, and Sr_2NaIO_6, the highest peaks appear at 6.05 eV, 7.35 eV, and 9.26 eV, with values of 2.73, 2.60, and 2.94, respectively. Conversely, the decrease in the refractive index coincides with the maximum values of the extinction coefficient, measured at 2.04, 2.01, and 1.85 for Sr_2NaClO_6, Sr_2NaBrO_6, and Sr_2NaIO_6 at energies of 6.33 eV, 9.75 eV, and 9.94 eV, respectively, indicating that the extinction coefficient generally takes lower values than the refractive index.

On other hand, by applying the conventional formula for the static refractive index, the values obtained are 1.88, 1.74, and 1.58 for Sr_2NaClO_6, Sr_2NaBrO_6, and Sr_2NaIO_6 respectively.

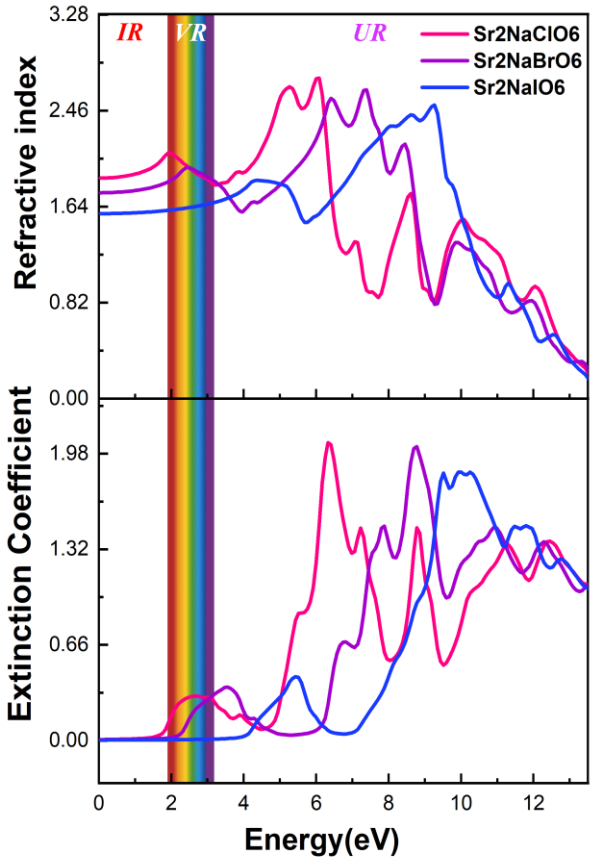


Figure IV. 33: ***Refractive index and Extinction coefficient as function of energy for Sr_2NaXO_6(X=Cl, Br and I) oxide double perovskites***

IV.4.4. Elastic properties

The elastic characteristics of a material define its ability to deform under stress and return to its initial configuration once the stress is released. For the cubic double perovskite compounds under investigation, only three elastic constants, C_{11},C_{12} and C_{44} are needed to describe their elastic response due to structural symmetry.

The elastic constants C_{ij} offer important information about a crystal's structural stability, bonding characteristics, mechanical properties, and anisotropic behavior. The computed constants at ambient conditions using PBEsol are presented in ***Table IV. 13***.

Table IV. 13: *Elastic constants $C_{ij}(GPa)$, Elastic compliance constants $S_{ij}(GPa^{-1})$, Kleinman's parameter ξ and Cauchy pressure C'' (GPa) for Sr2NaXO6(X=Cl, Br and I) oxide double perovskites*

Compounds	Elastic constants (GPa)			Elastic compliance constants (GPa^{-1})			Kleinman's parameter ξ	Cauchy pressure C'' (GPa)
	C_{11}	C_{12}	C_{44}	S_{11}	S_{12}	S_{44}		
Sr_2NaClO_6	199.59	66.94	99.79	0.00603	-0.00151	0.01002	0.582	-32.85
Sr_2NaBrO_6	241.01	59.27	101.51	0.00460	-0.00091	0.00985	0.456	-42.24
Sr_2NaIO_6	279.44	54.18	90.39	0.00382	-0.00062	0.01106	0.386	-39.21

Mechanical stability of cubic structures as determined by the Born – Huang conditions [126,127] are ($C_{11} - C_{12} > 0$, $C_{11} + 2C_{12} > 0$ and $C_{44} > 0$).

The obtained elastic constants serve as a basis for evaluating the mechanical stability of Sr_2NaClO_6, Sr_2NaBrO_6, and Sr_2NaIO_6. From Table 13, it can be observed that the Sr_2NaXO_6 compounds follow $C_{11} > C_{44} > C_{12}$which signifies that these materials are more resistant to axial compressive forces compared to shear and volumetric stress. As also presented in ***Table IV. 13,*** C_{11} exhibits an increasing trend from Sr_2NaClO_6 to Sr_2NaIO_6, in contrast to C_{12} which decreases. However, the shear constant C_{44} is lowest for Sr_2NaIO_6 and highest for Sr_2NaBrO_6. The elastic compliance constants have also been determined. The values of the elastic compliance constants are listed in Table 3, demonstrate that S_{11} and S_{44} are positive, while S_{12} assumes a negative value.

The internal strain parameter ξ named as Kleinman's parameter [148] assesses the impact of internal stresses on a material's stability and deformation characteristics by analyzing the relative tendencies for bond bending and bond stretching. The obtained Kleinman's parameters are within the interval $0 \leq \xi \leq 1$, where $\xi = 0$ corresponds to bond stretching being the main deformation mode, and $\xi = 1$ indicates bond bending as the dominant mechanism.

Approaching the boundaries of 0 and 1, the parameter reflects a dominance of bond stretching at the lower limit and bond bending at the upper limit. The calculated ξ value for

Sr_2NaClO_6 is closer to 1, whereas for Sr_2NaBrO_6, and Sr_2NaIO_6 it is nearer to 0. This suggests that the bonding in Sr_2NaClO_6 is primarily governed by bond bending, while in Sr_2NaBrO_6, and Sr_2NaIO_6, bond stretching dominates over bending.

Cauchy pressure $(C'' = C_{12} - C_{44})$ [148] is the difference between C_{12} and C_{44} can indeed be either positive or negative indicating ductile or brittle nature [149], respectively depending on the specific material properties. For Sr_2NaXO_6 (X = Cl, Br and I), the calculated Cauchy pressures are negative, with values of -32.85 GPa, -42.24 GPa, and -39.21 GPa, suggesting that the compounds are mechanically brittle.

To describe the mechanical properties of materials, the Voigt, Reuss, and Hill (VRH) approximations are used, where the moduli are calculated using the elastic constants.

According to Voigt [129], the strain is uniform throughout the crystal, whereas Reuss [130] assumes uniform stress, which ensures static compatibility of stress fields but leads to a loss of kinematic compatibility. Furthermore, Hill [131] proposed a model that takes into consideration both uniform stress and uniform strain, achieving a more balanced estimation by averaging the Voigt and Reuss moduli.

The mechanical behavior of Sr_2NaXO_6 (X = Cl, Br and I) compounds under different applied forces, and their capacity to return to the original shape after stress, was assessed by computing bulk modulus (B), shear modulus (G), Young's modulus (E), P-wave modulus (M), and Poisson's ratio (υ) through the VRH model. The calculated values are listed in ***Table IV. 14:***

Table IV. 14: *Mechanical modulus (GPa) for Sr2NaXO6(X=Cl, Br and I) oxide double perovskites*

compounds	Sr_2NaClO_6			Sr_2NaBrO_6			Sr_2NaIO_6		
Mechanical properties	Voigt	Reuss	Hill	Voigt	Reuss	Hill	Voigt	Reuss	Hill
Bulk modulus (GPa)	111.158	111.158	111.158	119.855	119.855	119.855	129.269	129.269	129.269
Shear modulus (GPa)	86.404	83.033	84.719	97.254	96.968	97.111	99.289	98.144	98.716
Young modulus (GPa)	205.871	199.440	202.668	229.647	229.116	229.382	237.149	234.968	236.060
P-wave modulus (GPa)	226.364	221.868	224.116	249.527	249.146	249.336	261.654	260.128	260.891
Poisson's ratio	0.191	0.201	0.196	0.181	0.181	0.181	0.194	0.197	0.196

Data show that the bulk modulus is independent of the selected model for Sr_2NaXO_6 (X = Cl, Br and I), while Poisson's coefficient remains stable only in Sr_2NaBrO_6. Furthermore, the rising values of bulk, shear, Young's, and P-wave moduli from Sr_2NaClO_6 to Sr_2NaIO_6 suggest increased resistance to compression and shear, higher tensile rigidity, and lower volumetric strain. The calculated Poisson's ratio values are below 0.26, indicating that the studied compounds exhibit brittle behavior. This brittleness is further confirmed by the evaluation of Pugh's ratio (B/G). The calculated Pugh's ratio for Sr_2NaClO_6, Sr_2NaBrO_6, and Sr_2NaIO_6 are 1.312, 1.234, and 1.309, respectively. These outcomes reflect the mechanical characteristics of these double perovskites.

The resistance of chemical bonds to deformation is captured by the Vickers hardness H_v [150] Using Chen's revised formula, H_v is 16.538 GPa for Sr_2NaClO_6, 19.733 GPa for Sr_2NaBrO_6, and 18.41 GPa for Sr_2NaIO_6, with Sr_2NaBrO_6 demonstrating the highest hardness among them.

The directional variation of elastic properties under applied stress or strain is described by elastic anisotropy. It is quantified using several indices, such as the universal anisotropy index [151], Zener anisotropy factor [152], compression anisotropy [153], shear anisotropy (Chung–Buessem index) [151], and Kube's log-Euclidean parameter [154]. The elastic anisotropy parameters are presented in ***Table IV. 15:***

Table IV. 15: *The elastic anisotropy parameters(A^U, A, A_G, A_B, A_L) for Sr2NaXO6(X=Cl, Br and I) oxide double perovskites*

compounds	A^U	A	A_G	A_B	A_L
Sr_2NaClO_6	0.2030	1.5045	0.0199	0	0.0890
Sr_2NaBrO_6	0.0147	1.1171	0.0015	0	0.0066
Sr_2NaIO_6	0.0583	0.8026	0.0058	0	0.0259

If the values of A^U, A_B or A_G equal to zero, the material is elastically isotropic. However, any deviations from zero signify anisotropic elastic properties [155]. For complete isotropy, the value of A should be 1; any values greater than 1 indicate maximum rigidity along the <111> cubic diagonal, while values less than 1 indicate maximum rigidity along the <100> cubic axes [155].

Our analysis shows that A^U and A_G are nearly zero, confirming that Sr_2NaXO_6 (X = Cl, Br and I) double perovskites are approximately isotropic materials, and the zero value of A_B signifies total isotropy in compressibility. The Zener anisotropy factor A exceeds one for Sr_2NaClO_6 and

Sr_2NaBrO_6, indicating maximum rigidity along the <111> cubic diagonal, whereas for Sr_2NaIO_6, A<1 showing that the highest stiffness occurs along the <100> cubic axes.

The elastic isotropy of the studied compounds can also be examined using 3D surface plots of the elastic parameters. A perfectly spherical 3D shape corresponds to isotropic behavior, whereas deviations from sphericity indicate anisotropy. As shown in ***Figure IV. 34***, ***Figure IV. 35***, and ***Figure IV. 36***, which depict the 3D surfaces of the bulk modulus, Young's modulus, shear modulus, Poisson's ratio, Pugh's ratio, and hardness, only the bulk modulus exhibits a nearly spherical shape, demonstrating isotropic behavior, while the remaining elastic parameters display anisotropic characteristics.

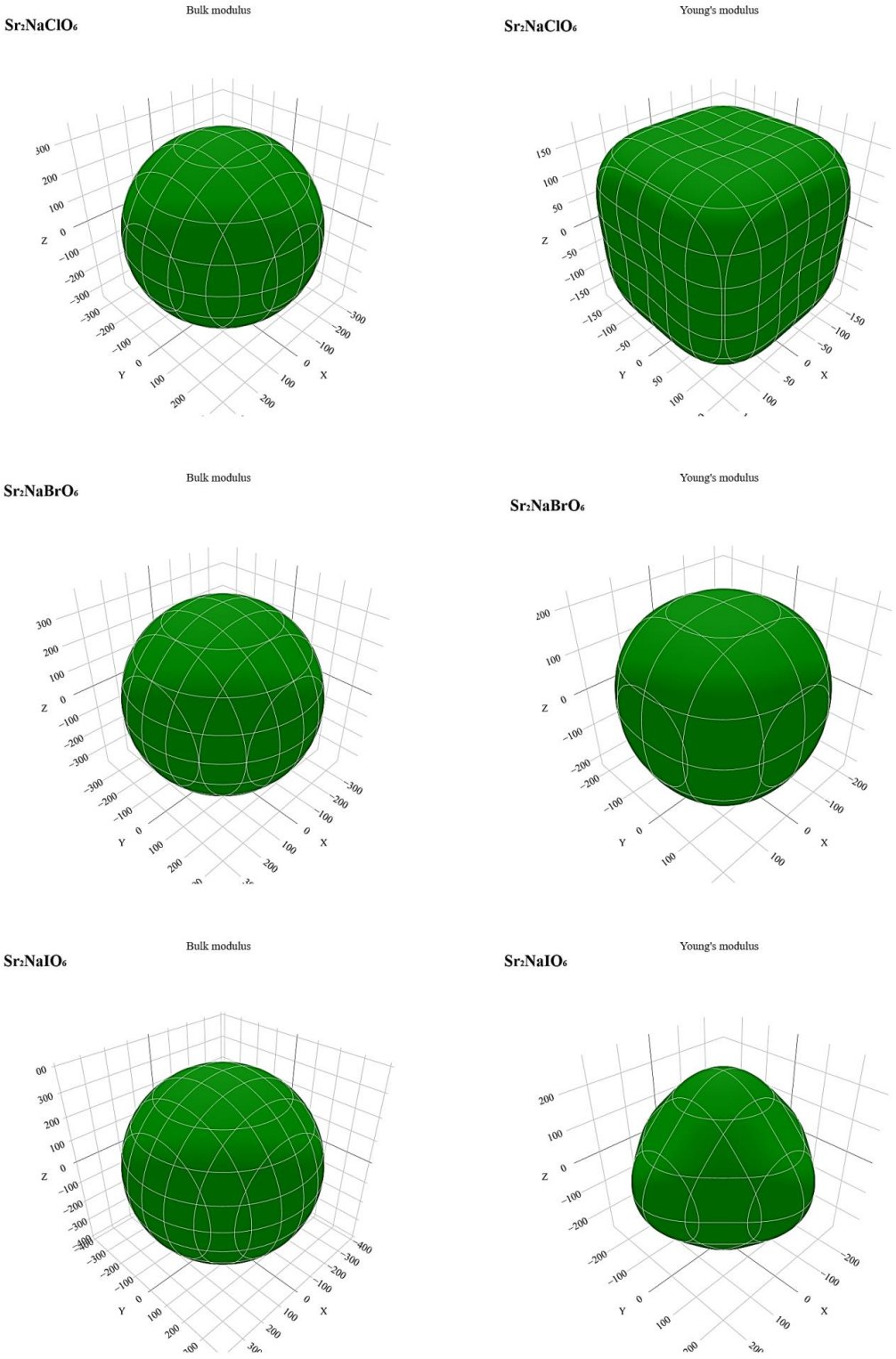


Figure IV. 34: ***3D plotted of Bulk modulus and Young's modulus for Sr_2NaXO_6(X=Cl, Br and I)oxide double Perovskites***

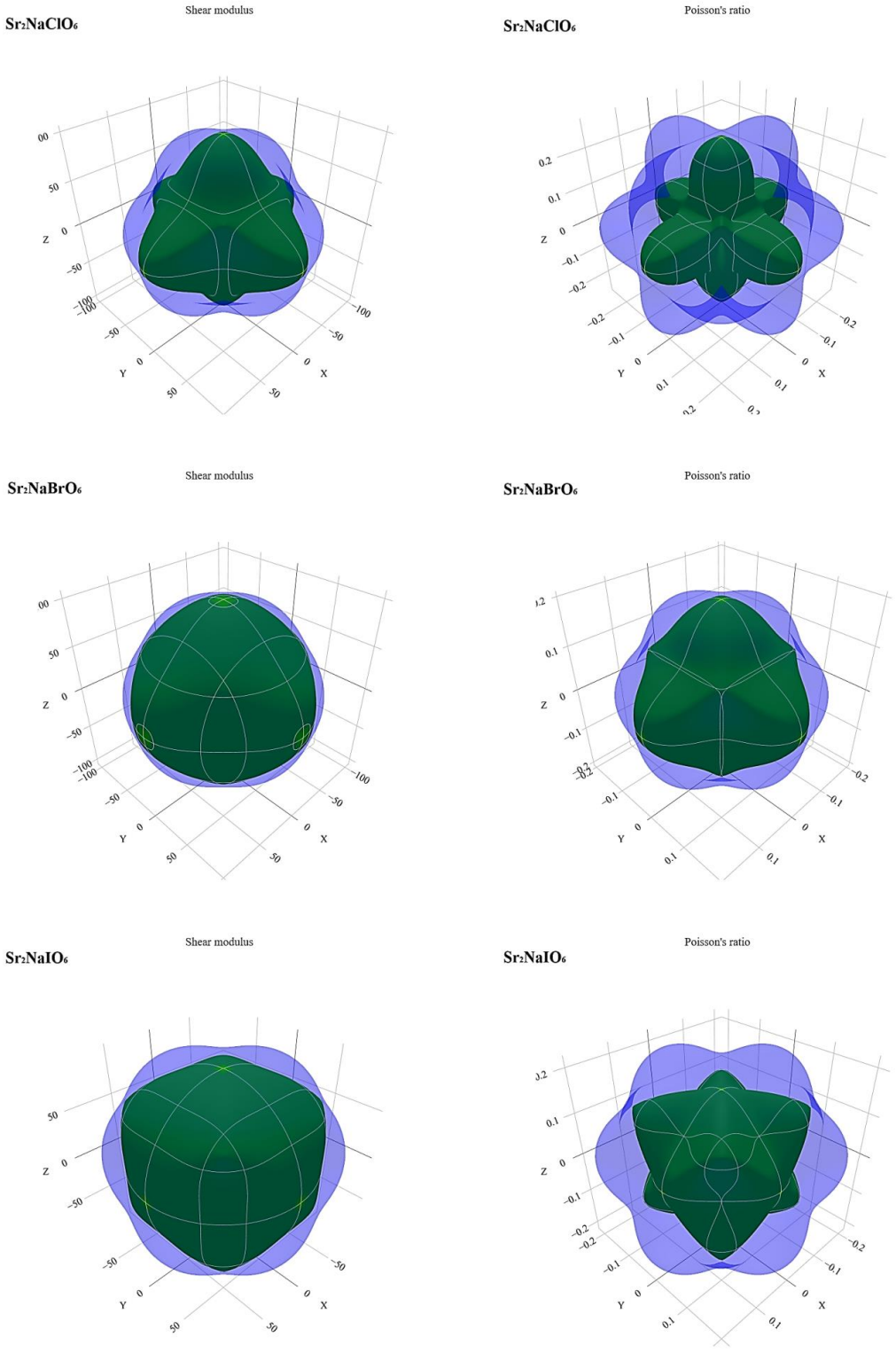


Figure IV. 35: 3D plotted of Shear modulus and Poisson's ratio for Sr_2NaXO_6(X=Cl, Br and I) oxide double Perovskites

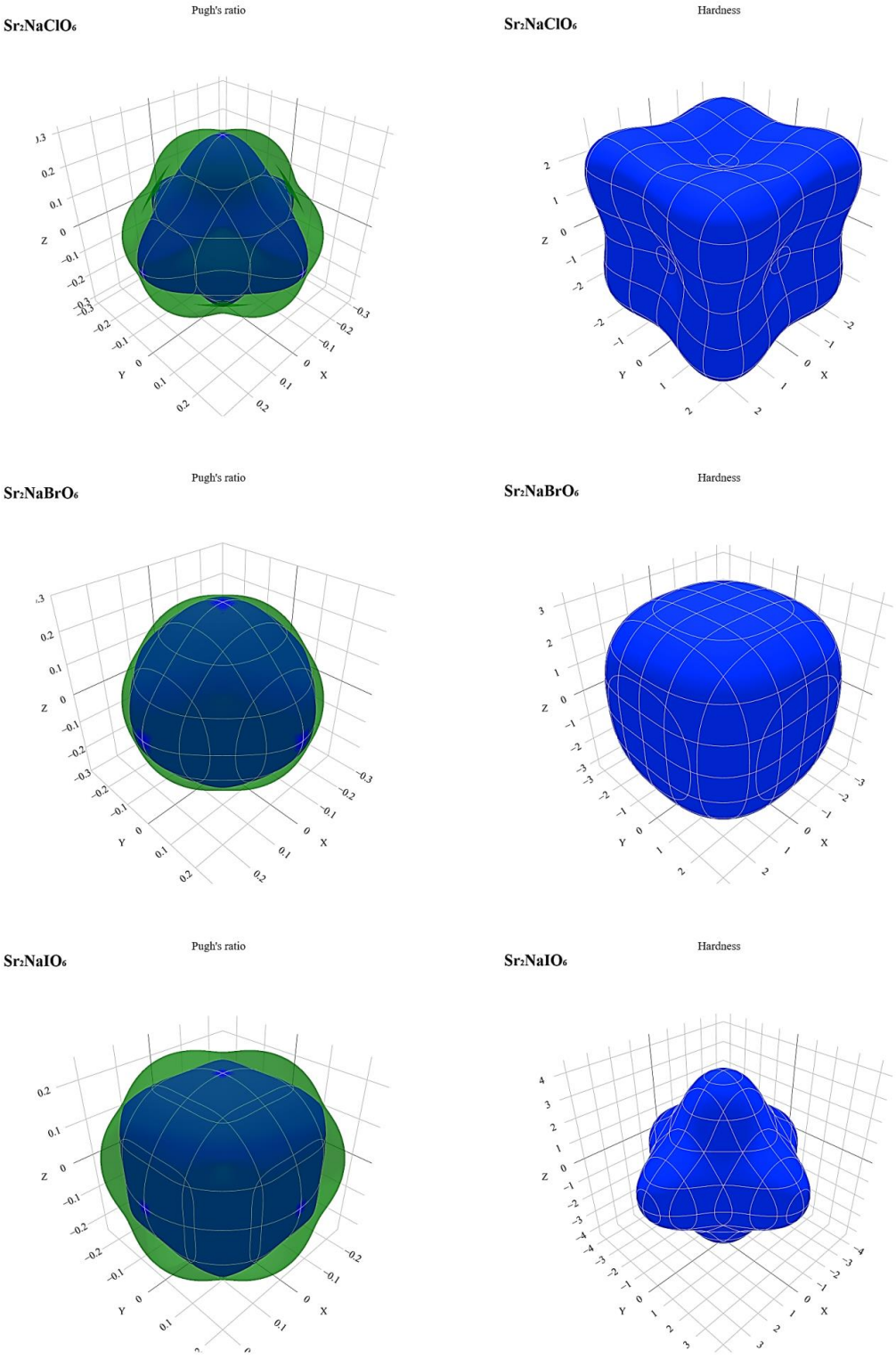


Figure IV. 36: 3D plotted of Pugh's ratio and Hardness for Sr_2NaXO_6 (X=Cl, Br and I) oxide double Perovskites

IV.4.5. Thermoelectric properties

The thermoelectric properties are the characteristics that define the ability of a material to directly transform thermal energy into electric energy, and in the converse manner, to create a temperature gradient when it is subjected to an external electric field. The above-mentioned physical processes are the basis of the thermoelectric devices that are used to produce electric power, refrigerate, regulate temperatures, and create environmentally friendly methods of energy production. In this context, oxide double perovskites are being increasingly recognized because of their chemical stability and the ability to function at high temperatures.

In the present work, the thermoelectric behavior of the oxide double perovskites Sr_2NaXO_6 (X = Cl, Br and I) is systematically investigated in the temperature interval ranging from 50 K to 1000 K. The transport coefficients close to the Fermi energy including the Seebeck coefficient (S), electrical conductivity (σ), power factor (PF), electronic thermal conductivity (k_e), and dimensionless figure of merit (ZT) are evaluated using the semi-classical Boltzmann transport formalism [156]. The lattice thermal conductivity (k_l), which cannot be directly obtained from electronic transport calculations, is estimated independently using Slack's model [157–159]. The resulting integrated theoretical framework provides a reliable description of thermoelectric performance and offers significant guidance for future experimental verification and optimization of devices.

- **Seebeck Coefficient**

The Seebeck effect refers to the generation of an electric potential difference (ΔV) in response to an applied temperature gradient (ΔT) across a material [160]. Its magnitude and sign are highly sensitive to the electronic structure and dominant charge carriers of the system. To quantify this effect in Sr_2NaXO_6 (X = Cl, Br and I).

The calculated Seebeck coefficients, as depicted in ***Figure IV. 37***, show that they remain positive over the full range of temperatures for all the compounds. This confirms that holes transport is predominant. This p-type behavior is fully consistent with that described in the calculated electronic density of states near the Fermi level.

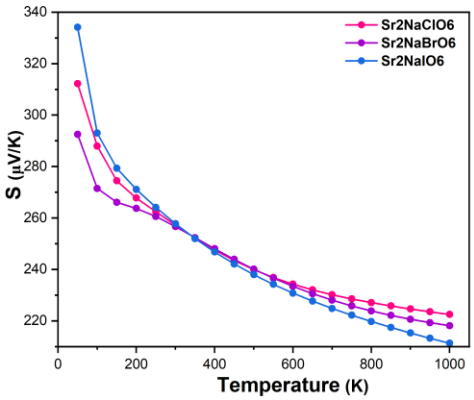


Figure IV. 37: ***The variations of Seebeck coefficient as function of temperature for Sr_2NaXO_6(X=Cl, Br and I) oxide double perovskitse.***

As the temperature increases from 50 K to 1000 K, S decreases gradually. In other words, S decreases from 312.227 μV/K, 292.504 μV/K, and 334.152 μV/K at low temperatures to 222.512 μV/K, 218.127 μV/K, and 211.307 μV/K at high temperatures for Sr_2NaClO_6, Sr_2NaBrO_6, and $Sr2NaIO_6$, respectively. This phenomenon occurs as a result of an increase in thermally excited charge carriers with temperature, leading to a reduction in their mobility as a consequence of enhanced scattering mechanisms [162]. Amongst these compounds, $Sr2NaIO_6$ has a slightly higher rate of decrease in S compared to the other compounds. Interestingly enough, all three compounds have an identical Seebeck coefficient equal to 253.18 μV/K at a temperature equal to 336.8 K.

- **Electrical and Thermal Conductivities**

The variation of electrical conductivity per relaxation time (σ/τ) as a function of temperature for Sr_2NaXO_6 (X = Cl, Br and I) is presented in ***Figure IV. 38***.

In these calculations, the relaxation time τ is assumed to be constant. The results reveal a pronounced increase in σ/τ with rising temperature, a characteristic behavior of semiconducting materials and distinctly different from metallic systems [163].

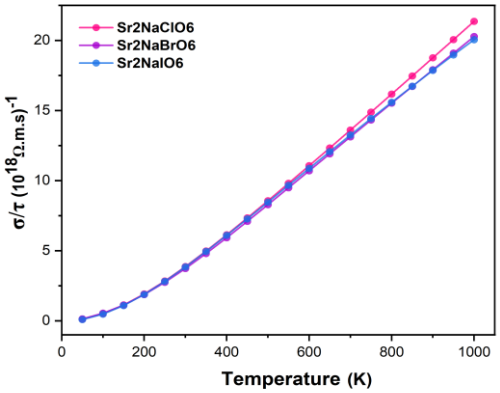


Figure IV. 38: ***The variations of electronic conductivity per relaxation time as function of temperature for Sr_2NaXO_6(X = Cl, Br and I) oxide double perovskites***

Within the temperature interval of 50 – 550 K, all three compounds show nearly identical conductivity trends. Beyond this range, a slight deviation becomes apparent, particularly for Sr_2NaClO_6, whose conductivity marginally diverges from those of Sr_2NaBrO_6 and Sr_2NaIO_6. The overall enhancement of σ with temperature is associated with bond breaking and increased carrier mobility resulting from higher kinetic energy. At room temperature, the electrical conductivity per relaxation time reaches approximately 3.80×10^{-18} $(\Omega \cdot m \cdot s)^{-1}$ for all studied compounds.

The total thermal conductivity (k) consists of both electronic and lattice contributions in which $(k = k_e + k_l)$

Figure IV. 39 presents the temperature dependence of k/τ, k_e/τ, and k_l/τ. The total thermal conductivity decreases initially with rising temperature, reaching minimum values of 1.97, 2.73, and 3.00 $(10^{14}\ W/m \cdot K^2 \cdot s)^{-1}$ at 250 K, 350 K, and 300 K for Sr_2NaClO_6, Sr_2NaBrO_6, and Sr_2NaIO_6, respectively. Beyond these points, the conductivity begins to increase again at higher temperatures. The electronic component, k_e/τ, increases monotonically and exhibits a behavior consistent with its proportionality to the electrical conductivity.

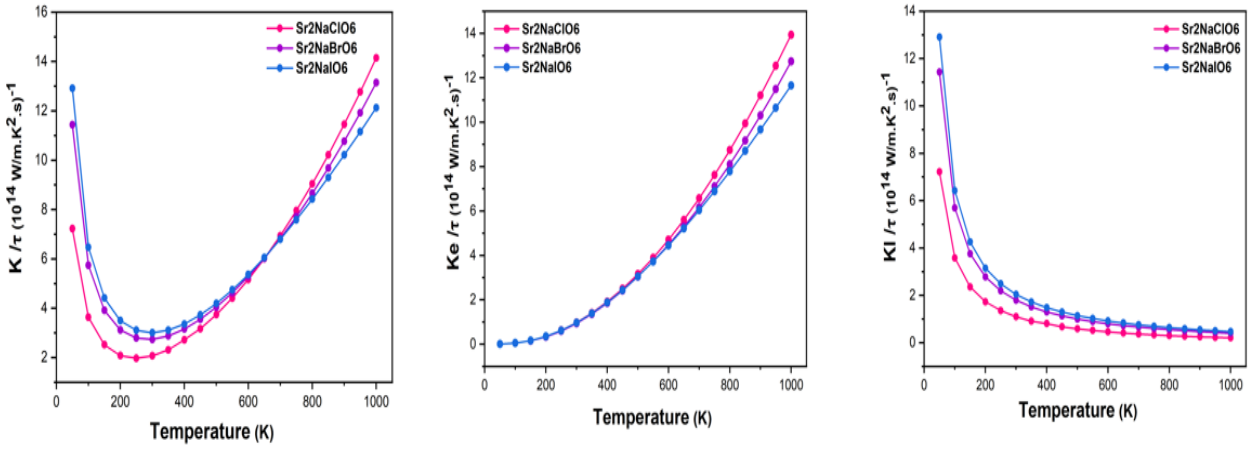


Figure IV. 39*: *The thermal conductivity, the electronic thermal conductivity and the lattice thermal conductivity per relaxation for Sr_2NaXO_6(X=Cl, Br and I) oxide double perovskites

At 300 K, the electronic thermal conductivity k_e/τ attains a value of 0.89×10^{-14} $(W/m\cdot K^2\cdot s)^{-1}$ for all three compounds. In contrast, the lattice contribution k_l/τ decreases progressively with rising temperatures and exhibits only a modest temperature dependence at higher temperatures. This reduced sensitivity is largely associated with the intensification of phonon–phonon scattering processes, which increasingly hinder lattice heat transport as the temperature rises [165]. At room temperature, the corresponding k_l/τ values are 1.088, 1.75, and $2.06 \times (10^{14}$ $W/m\cdot K^2\cdot s)^{-1}$ for Sr_2NaClO_6, Sr_2NaBrO_6, and Sr_2NaIO_6, respectively.

- **Power Factor and Figure of Merit**

The overall thermoelectric efficiency of a material is commonly evaluated using the dimensionless figure of merit; the high thermoelectric performance requires a large Seebeck coefficient and electrical conductivity, combined with low thermal conductivity.

Figure IV. 40 presents the temperature dependence of the power factor per relaxation time (PF/τ) for Sr_2NaXO_6 (X = Cl, Br and I). The PF increases almost linearly with temperature for all compounds, indicating continuous improvement in power output capability. A minor divergence between the curves becomes noticeable above 600 K. At 300 K, the PF/τ value is approximately 2.51×10^{11} $W/m\cdot K^2\cdot s$ for all systems.

The maximum PF values are achieved at 1000 K, reaching 10.57394×10^{11}, 9.6441×10^{11}, and 8.95205×10^{11} $W/m\cdot K^2\cdot s$ for Sr_2NaClO_6, Sr_2NaBrO_6, and Sr_2NaIO_6, respectively.

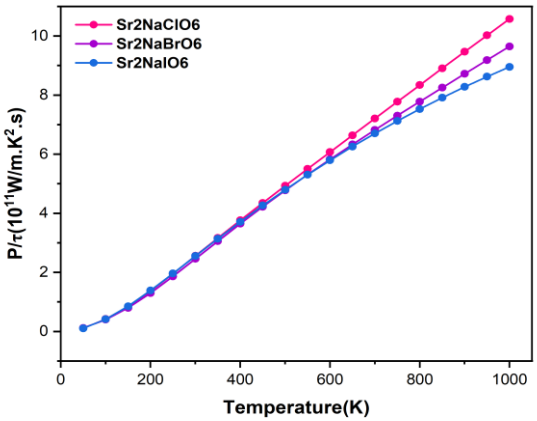


Figure IV. 40: ***The variations of power factor per relaxation time as function of temperature for Sr_2NaXO_6(X=Cl, Br and I) oxide double perovskites***

The figure of merit ZT in terms of temperature as depicted in ***Figure IV. 41*** shows a fast increase at low temperatures pursued by an inclination toward saturation at higher temperatures. At 1000 K, ZT reaches values of 0.747 for Sr_2NaClO_6, 0.734 for Sr_2NaBrO_6, and 0.738 for Sr_2NaIO_6, demonstrating that all three compounds exhibit promising thermoelectric performance in the high-temperature regime.

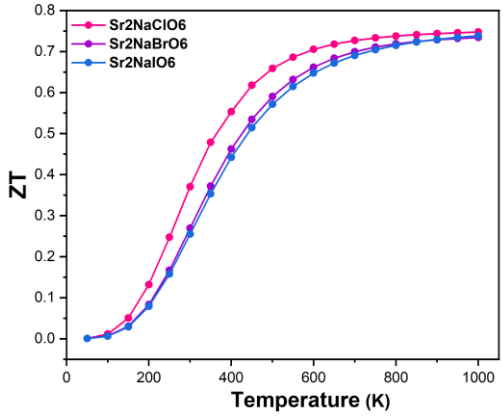


Figure IV. 41: ***The variations of figure of merit as temperature changes for Sr_2NaXO_6(X=Cl, Br and I) oxide double perovskitse***

References:

[1] F. Tran, WIEN2k: an augmented plane wave plus local orbitals program for calculating crystal properties, (2018).
[2] P. Hohenberg, W. Kohn, Inhomogeneous electron gas, Physical Review 136 (1964) B864.
[3] W. Kohn, L.J. Sham, Self-consistent equations including exchange and correlation effects, Physical Review 140 (1965) A1133.
[4] P. Blaha, K. Schwarz, F. Tran, R. Laskowski, G.K. Madsen, L.D. Marks, WIEN2k: An APW+ lo program for calculating the properties of solids, The Journal of Chemical Physics 152 (2020).
[5] P. Blaha, K. Schwarz, P. Sorantin, S.B. Trickey, Full-potential, linearized augmented plane wave programs for crystalline systems, Computer Physics Communications 59 (1990) 399–415.
[6] K. Schwarz, P. Blaha, Solid state calculations using WIEN2k, Computational Materials Science 28 (2003) 259–273.
[7] W. Kohn, L.J. Sham, Self-Consistent Equations Including Exchange and Correlation Effects, Phys. Rev. 140 (1965) A1133–A1138. https://doi.org/10.1103/PhysRev.140.A1133.
[8] Z. Wu, R.E. Cohen, More accurate generalized gradient approximation for solids, Phys. Rev. B 73 (2006) 235116. https://doi.org/10.1103/PhysRevB.73.235116.
[9] J.P. Perdew, A. Ruzsinszky, G.I. Csonka, O.A. Vydrov, G.E. Scuseria, L.A. Constantin, X. Zhou, K. Burke, Restoring the Density-Gradient Expansion for Exchange in Solids and Surfaces, Phys. Rev. Lett. 100 (2008) 136406. https://doi.org/10.1103/PhysRevLett.100.136406.
[10] A.D. Becke, E.R. Johnson, A simple effective potential for exchange, The Journal of Chemical Physics 124 (2006) 221101. https://doi.org/10.1063/1.2213970.
[11] F. Tran, P. Blaha, Accurate Band Gaps of Semiconductors and Insulators with a Semilocal Exchange-Correlation Potential, Phys. Rev. Lett. 102 (2009) 226401. https://doi.org/10.1103/PhysRevLett.102.226401.
[12] D. Koller, F. Tran, P. Blaha, Improving the modified Becke-Johnson exchange potential, Phys. Rev. B 85 (2012) 155109. https://doi.org/10.1103/PhysRevB.85.155109.
[13] A. Otero-De-La-Roza, D. Abbasi-Pérez, V. Luaña, Gibbs2: A new version of the quasiharmonic model code. II. Models for solid-state thermodynamics, features and implementation, Computer Physics Communications 182 (2011) 2232–2248.
[14] M.A. Blanco, E. Francisco, V. Luana, GIBBS: isothermal-isobaric thermodynamics of solids from energy curves using a quasi-harmonic Debye model, Computer Physics Communications 158 (2004) 57–72.
[15] R.J. Guerrero-Moreno, N. Takeuchi, First principles calculations of the ground-state properties and structural phase transformation in CdO, Physical Review B 66 (2002) 205205.
[16] A. Schleife, F. Fuchs, J. Furthmüller, F. Bechstedt, First-principles study of ground-and excited-state properties of MgO, ZnO, and CdO polymorphs, Physical Review B—Condensed Matter and Materials Physics 73 (2006) 245212.
[17] G. Will, G. Nover, J. Von Der Gönna, New Experimental Results on the Phase Diagram of Boron Nitride, Journal of Solid State Chemistry 154 (2000) 280–285. https://doi.org/10.1006/jssc.2000.8850.
[18] C. Cazorla, T. Gould, Polymorphism of bulk boron nitride, Science Advances 5 (2019) eaau5832.

[19] S. Daoud, N. Bioud, N. Lebgaa, L. Belagraa, R. Mezouar, Pressure effect on structural, elastic and electronic properties of (B3) BSb compound, Indian J Phys 87 (2013) 355–362. https://doi.org/10.1007/s12648-012-0231-y.
[20] M. Benchehima, H. Abid, Effects of phosphorus incorporation on the structural and optoelectronic properties of BSb binary compound: A first principle investigation, Computational Condensed Matter (2018). https://doi.org/10.1016/j.cocom.2018.01.011.
[21] A. Siegel, K. Parlinski, U.D. Wdowik, Ab initio calculation of structural phase transitions in AlN crystal, Phys. Rev. B 74 (2006) 104116. https://doi.org/10.1103/PhysRevB.74.104116.
[22] K. Karch, F. Bechstedt, Ab initio lattice dynamics of BN and AlN: Covalent versus ionic forces, Physical Review B 56 (1997) 7404.
[23] P. Rodríguez-Hernández, A. Muãoz, A. Mujica, High Pressure Phases of AlSb from ab-initio Theory, Physica Status Solidi (b) 198 (1996) 455–459.
[24] A. Bendahah, D. Bensaid, A. Yhaia, M. Khadidja, M. Noureddine, D. Bendouma, Y. Al-Douri, First-principles calculations to investigate structural, electronic, piezoelectric and optical properties of Sc-Doped GaN, Emergent Materials 7 (2024) 2787–2795.
[25] E.-E. Castaño-González, N. Seña, V. Mendoza-Estrada, R. González-Hernández, A. Dussan, F. Mesa, First-principles calculations of the electronic and structural properties of GaSb, Semiconductors 50 (2016) 1280–1286.
[26] F. Oumelaz, O. Nemiri, A. Boumaza, S. Ghemid, H. Meradji, S. Bin Omran, F. El Haj Hassan, D.P. Rai, R. Khenata, Theoretical investigation of the structural stabilities, optoelectronic properties and thermodynamic characteristics of GaPxSb1− x ternary alloys, Indian Journal of Physics 92 (2018) 705–714.
[27] F.D. Murnaghan, The compressibility of media under extreme pressures, Proceedings of the National Academy of Sciences 30 (1944) 244–247.
[28] E. Knittle, R.M. Wentzcovitch, R. Jeanloz, M.L. Cohen, Experimental and theoretical equation of state of cubic boron nitride, Nature 337 (1989) 349–352. https://doi.org/10.1038/337349a0.
[29] H. Pedersen, B. Alling, H. Högberg, A. Ektarawong, Thermodynamic stability of hexagonal and rhombohedral boron nitride under chemical vapor deposition conditions from van der Waals corrected first principles calculations, Journal of Vacuum Science & Technology A 37 (2019).
[30] W.J. Yu, W.M. Lau, S.P. Chan, Z.F. Liu, Q.Q. Zheng, Ab initio study of phase transformations in boron nitride, Physical Review B 67 (2003) 014108.
[31] D. Bouragba, M. Benchehima, H. Abid, A. Djili, Optical response functions and thermodynamic stability of BSb1-xNx ternary alloys in zinc blende structure, Optik 222 (2020) 165472. https://doi.org/10.1016/j.ijleo.2020.165472.
[32] M. Guemou, A. Abdiche, R. Riane, R. Khenata, Ab initio study of the structural, electronic and optical properties of BAs and BN compounds and BNxAs1− x alloys, Physica B: Condensed Matter 436 (2014) 33–40.
[33] S. Das, R. Bhunia, S. Hussain, R. Bhar, B.R. Chakraborty, A.K. Pal, Synthesis and characterization of boron antimonide films by pulsed laser deposition technique, Applied Surface Science 353 (2015) 439–448. https://doi.org/10.1016/j.apsusc.2015.06.157.
[34] M. Benchehima, H. Abid, Effects of phosphorus incorporation on the structural and optoelectronic properties of BSb binary compound: A first principle investigation, Computational Condensed Matter 14 (2018) 114–124. https://doi.org/10.1016/j.cocom.2018.01.011.

[35] V. Tiwari, I. Mal, S.K. Agnihotri, D.P. Samajdar, First principle studies on the structural and optoelectronic properties of boron antimonide: A promising candidate for photovoltaic applications, Materials Science in Semiconductor Processing 122 (2021) 105505. https://doi.org/10.1016/j.mssp.2020.105505.

[36] R. Moussa, A. Abdiche, R. Khenata, X.T. Wang, D. Varshney, X.W. Sun, S.B. Omran, A. Bouhemadou, D.P. Rai, Structural, electronic, optical, thermodynamic and elastic properties of the zinc-blende Al x In 1-x N ternary alloys: A first principles calculations, Journal of Physics and Chemistry of Solids 119 (2018) 36–49. https://doi.org/10.1016/j.jpcs.2018.03.035.

[37] M. Mbarki, R. Alaya, A. Rebey, Ab initio investigation of structural and electronic properties of zinc blende AlN1−xBix alloys, Solid State Communications 155 (2013) 12–15. https://doi.org/10.1016/j.ssc.2012.10.031.

[38] K. Kim, W.R.L. Lambrecht, B. Segall, Elastic constants and related properties of tetrahedrally bonded BN, AlN, GaN, and InN, Phys. Rev. B 53 (1996) 16310–16326. https://doi.org/10.1103/PhysRevB.53.16310.

[39] Ab initio calculations of structural properties of ScxGa1−xN | Journal of Applied Physics | AIP Publishing, (n.d.). https://pubs.aip.org/aip/jap/article-abstract/103/6/063510/284301/Ab-initio-calculations-of-structural-properties-of?redirectedFrom=fulltext (accessed February 3, 2026).

[40] S. Louhibi-Fasla, H. Achour, K. Kefif, Y. Ghalem, First-principles Study of High-pressure Phases of AlN, Physics Procedia 55 (2014) 324–328. https://doi.org/10.1016/j.phpro.2014.07.047.

[41] I. Vurgaftman, J.R. Meyer, L.R. Ram-Mohan, Band parameters for III–V compound semiconductors and their alloys, Journal of Applied Physics 89 (2001) 5815–5875. https://doi.org/10.1063/1.1368156.

[42] R.K. Willardson, A.C. Beer, A.E. Middleton, Electrical properties of semiconducting AlSb, Journal of The Electrochemical Society 101 (1954) 354.

[43] H. Salehi, H.A. Badehian, M. Farbod, First principle study of the physical properties of semiconducting binary antimonide compounds under hydrostatic pressures, Materials Science in Semiconductor Processing 26 (2014) 477–490. https://doi.org/10.1016/j.mssp.2014.05.020.

[44] S. Nabi, A.W. Anwar, M. Ahmad, N.U. Haq, R. Waqas, M. Tayyab, M. Moin, A. Ali, M. Afzal, K. Nabi, Computational Correlation analysis of In-doped Aluminium Antimonide Alloy for Optoelectronic Applications: A First Principle Study, (2023). https://doi.org/10.21203/rs.3.rs-2051905/v2.

[45] N. Devi, S. Sharma, U.P. Verma, Ab-initio study of Al_{1-x} Ga_x Sb compound, Zeitschrift Für Kristallographie 226 (2011) 83–88. https://doi.org/10.1524/zkri.2011.1335.

[46] H. Hirano, S. Uehara, A. Mori, A. Onodera, K. Takemura, O. Shimomura, Y. Akahama, H. Kawamura, High-pressure phase transitions in AlSb, Journal of Physics and Chemistry of Solids 62 (2001) 941–949. https://doi.org/10.1016/S0022-3697(00)00260-2.

[47] H. Harima, Properties of GaN and related compounds studied by means of Ramanscattering, Journal of Physics: Condensed Matter 14 (2002) R967.

[48] M. Abu-Jafar, A.I. Al-Sharif, A. Qteish, FP-LAPW and pseudopotential calculations of the structural phase transformations of GaN under high-pressure, Solid State Communications 116 (2000) 389–393.

[49] A. Janotti, S.-H. Wei, S.B. Zhang, Theoretical study of the effects of isovalent coalloying of Bi and N in GaAs, Physical Review B 65 (2002) 115203.
[50] B.K. Agrawal, S. Agrawal, P.S. Yadav, S. Kumar, Ab initio calculation of electronic properties of alloys, Journal of Physics: Condensed Matter 9 (1997) 1763.
[51] O. Madelung, Semiconductors—basic data, Springer Science & Business Media, 2012.
[52] Y. Al-Douri, H. Abid, H. Aourag, Empirical formula relating the bulk modulus to the lattice constant in tetrahedral semiconductors, Materials Chemistry and Physics 87 (2004) 14–17.
[53] M.L. Cohen, Calculation of bulk moduli of diamond and zinc-blende solids, Physical Review B 32 (1985) 7988.
[54] K. Kim, W.R.L. Lambrecht, B. Segall, Elastic constants and related properties of tetrahedrally bonded BN, AlN, GaN, and InN, Physical Review B (1996). https://doi.org/10.1103/PhysRevB.53.16310.
[55] F. El Haj Hassan, First-principles study of $BN_x Sb_{1-x}$, $BP_x Sb_{1-x}$ and $BAs_x Sb_{1-x}$ alloys, Physica Status Solidi (b) 242 (2005) 3129–3137. https://doi.org/10.1002/pssb.200441157.
[56] L. Vegard, The constitution of the mixed crystals and the filling of space of the atoms, Zeitschrift Fur Physik 5 (1921) 17–26.
[57] Qing Xia, Hui Xia, A.L. Ruoff, New high pressure phases of the III-V compounds AlN, GaN, InN, in: AIP Conference Proceedings, AIP, Colorado Springs, Colorado (USA), 1994: pp. 307–310. https://doi.org/10.1063/1.46334.
[58] M. Ueno, A. Onodera, O. Shimomura, K. Takemura, X-ray observation of the structural phase transition of aluminum nitride under high pressure, Phys. Rev. B 45 (1992) 10123–10126. https://doi.org/10.1103/PhysRevB.45.10123.
[59] M.B. Kanoun, A.E. Merad, G. Merad, J. Cibert, H. Aourag, Prediction study of elastic properties under pressure effect for zincblende BN, AlN, GaN and InN, Solid-State Electronics 48 (2004) 1601–1606. https://doi.org/10.1016/j.sse.2004.03.007.
[60] F. Peng, D. Chen, H. Fu, X. Cheng, The phase transition and the elastic and thermodynamic properties of AlN: First principles, Physica B: Condensed Matter 403 (2008) 4259–4263. https://doi.org/10.1016/j.physb.2008.09.013.
[61] N.E. Christensen, I. Gorczyca, Optical and structural properties of III-V nitrides under pressure, Phys. Rev. B 50 (1994) 4397–4415. https://doi.org/10.1103/PhysRevB.50.4397.
[62] I. Gorczyca, N.E. Christensen, P. Perlin, I. Grzegory, J. Jun, M. Bockowski, High pressure phase transition in aluminium nitride, Solid State Communications 79 (1991) 1033–1034. https://doi.org/10.1016/0038-1098(91)90004-F.
[63] A.J. Wang, S.L. Shang, Y. Du, Y. Kong, L.J. Zhang, L. Chen, D.D. Zhao, Z.K. Liu, Structural and elastic properties of cubic and hexagonal TiN and AlN from first-principles calculations, Computational Materials Science 48 (2010) 705–709. https://doi.org/10.1016/j.commatsci.2010.03.014.
[64] S.C. Yu, I.L. Spain, E.F. Skelton, High pressure phase transitions in tetrahedrally coordinated semiconducting compounds, Solid State Communications 25 (1978) 49–52.
[65] R.K. Singh, S. Singh, High-pressure phase transition and elastic behavior of aluminum compound semiconductors, Phys. Rev. B 45 (1992) 1019–1022. https://doi.org/10.1103/PhysRevB.45.1019.
[66] F. Series, Wiley Series in Materials for Electronic & Optoelectronic Applications, (n.d.).
[67] S.B. Zhang, M.L. Cohen, High-pressure phases of III-V zinc-blende semiconductors, Phys. Rev. B 35 (1987) 7604–7610. https://doi.org/10.1103/PhysRevB.35.7604.

[68] D. Varshney, G. Joshi, M. Varshney, S. Shriya, Pressure induced structural phase transition and elastic properties in BSb, AlSb, GaSb and InSb compounds, Physica B: Condensed Matter 405 (2010) 1663–1676. https://doi.org/10.1016/j.physb.2009.12.064.
[69] L. Salmi, H. Meradji, S. Ghemid, O. Nemiri, F. Oumelaz, R. Khenata, Phase stability, pressure-induced phase transition and electronic properties of AlX (X = P, As and Sb) compounds from first principle calculations., Phase Transitions 93 (2020) 843–855. https://doi.org/10.1080/01411594.2020.1795858.
[70] H. Xia, Q. Xia, A.L. Ruoff, High-pressure structure of gallium nitride: Wurtzite-to-rocksalt phase transition, Physical Review B 47 (1993) 12925.
[71] B. DAOUDI, A. BOUKRAA, The structural and electronic properties of GaN under high pressure, (2010).
[72] P. Pawar, V.A. Shukoor, S. Singh, Study of effect of temperature on phase transition pressure of GaAs and GaSb, in: IOP Conference Series: Materials Science and Engineering, IOP Publishing, 2018: p. 012060.
[73] R.K. Singh, S. Singh, Structural phase transition and high-pressure elastic behavior of III-V semiconductors, Physical Review B 39 (1989) 671.
[74] C. He, L. Sun, C. Zhang, X. Peng, A. Et., Z-BN: a novel superhard boron nitride phase, Physical Chemistry Chemical Physics (2012). https://doi.org/10.1039/c2cp41368j.
[75] W.J. Yu, W.M. Lau, S.P. Chan, Z.F. Liu, Q.Q. Zheng, *Ab initio* study of phase transformations in boron nitride, Phys. Rev. B 67 (2003) 014108. https://doi.org/10.1103/PhysRevB.67.014108.
[76] A. Zaoui, F.E.H. Hassan, Full potential linearized augmented plane wave calculations of structuraland electronic properties of BN, BP, BAs and BSb, Journal of Physics: Condensed Matter 13 (2001) 253.
[77] R.M. Wentzcovitch, K.J. Chang, M.L. Cohen, Electronic and structural properties of BN and BP, Physical Review B (1986). https://doi.org/10.1103/PhysRevB.34.1071.
[78] E. Deligoz, K. Colakoglu, Y.O. Ciftci, The first principles study on the Boron antimony compound, Journal of Physics and Chemistry of Solids 68 (2007) 482–489.
[79] F.E.H. Hassan, H. Akbarzadeh, M. Zoaeter, Structural properties of boron compounds at high pressure, Journal of Physics: Condensed Matter 16 (2004) 293.
[80] V.A. Fomichev, M.A. Rumsh, Investigation of X-ray spectra of hexagonal and cubic boron nitride, Journal of Physics and Chemistry of Solids 29 (1968) 1015–1024.
[81] R.M. Chrenko, Ultraviolet and infrared spectra of cubic boron nitride, Solid State Communications 14 (1974) 511–515.
[82] M. Ferhat, B. Bouhafs, A. Zaoui, H. Aourag, First-principles study of structural and electronic properties of BSb, J. Phys.: Condens. Matter 10 (1998) 7995. https://doi.org/10.1088/0953-8984/10/36/010.
[83] M. Röppischer, R. Goldhahn, G. Rossbach, P. Schley, C. Cobet, N. Esser, T. Schupp, K. Lischka, D.J. As, Dielectric function of zinc-blende AlN from 1 to 20 eV: Band gap and van Hove singularities, Journal of Applied Physics 106 (2009) 076104. https://doi.org/10.1063/1.3239516.
[84] C. Alibert, A. Joullié, A.M. Joullié, C. Ance, Modulation-spectroscopy study of the Ga 1 − x Al x Sb band structure, Phys. Rev. B 27 (1983) 4946–4954. https://doi.org/10.1103/PhysRevB.27.4946.
[85] F. Annane, H. Meradji, S. Ghemid, H. Bendjeddou, F.E.H. Hassan, V. Srivastava, R. Khenata, Ab-initio study of ordered III–V antimony-based semiconductor alloys

$$\mathbf{GaP }_{1-x}{} \mathbf{Sb} _{x} \mathbf{and} AlP _{1-x}{} \mathbf{Sb} _{x}$$, Pramana - J Phys 94 (2020) 107. https://doi.org/10.1007/s12043-020-01966-1.

[86] K. Nakano, T. Sakai, Assessing the performance of the Tran–Blaha modified Becke–Johnson exchange potential for optical constants of semiconductors in the ultraviolet–visible light region, Journal of Applied Physics 123 (2018) 015104. https://doi.org/10.1063/1.5006170.

[87] J.H. Edgar, Properties of group III nitrides, (No Title) (1994).

[88] A. Rubio, J.L. Corkill, M.L. Cohen, E.L. Shirley, S.G. Louie, Quasiparticle band structure of AlN and GaN, Physical Review B 48 (1993) 11810.

[89] D. Vogel, P. Krüger, J. Pollmann, Structural and electronic properties of group-III nitrides, Physical Review B 55 (1997) 12836.

[90] C. Stampfl, C.G. Van de Walle, Density-functional calculations for III-V nitrides using the local-density approximation and the generalized gradient approximation, Physical Review B 59 (1999) 5521.

[91] J. Grim, V. Holý, J. Kubena, A.A. Darhuber, S. Zerlauth, G. Bauer, X-ray reflection from self-organized interfaces in an SiGe/Si multilayer, Semiconductor Science and Technology 14 (1999) 32.

[92] M.B. Kanoun, First-principles study of structural, elastic and electronic properties of AlN and GaN semiconductors under pressure effect and magnetism in AlN: Mn and GaN: Mn systems, Université de Tlemcen, 2004.

[93] F.E.H. Hassan, A. Breidi, S. Ghemid, B. Amrani, H. Meradji, O. Pagès, First-principles study of the ternary semiconductor alloys (Ga, Al)(As, Sb), Journal of Alloys and Compounds 499 (2010) 80–89.

[94] K. Ogawa, R. Abe, A. Walsh, Band Gap Narrowing by Suppressed Lone-Pair Activity of Bi3+, J. Am. Chem. Soc. 146 (2024) 5806–5810. https://doi.org/10.1021/jacs.4c00150.

[95] S.-Y. Shin, J.M. Choi, J. Seo, H.-W. Ahn, Y.G. Choi, B. Cheong, S. Lee, The effect of doping Sb on the electronic structure and the device characteristics of Ovonic Threshold Switches based on Ge-Se, Sci Rep 4 (2014) 7099. https://doi.org/10.1038/srep07099.

[96] P. Dufek, P. Blaha, K. Schwarz, Applications of Engel and Vosko's generalized gradient approximation in solids, Physical Review B 50 (1994) 7279.

[97] M.P. Surh, S.G. Louie, M.L. Cohen, Quasiparticle energies for cubic BN, BP, and BAs, Physical Review B 43 (1991) 9126.

[98] F. Tran, P. Blaha, Accurate Band Gaps of Semiconductors and Insulators with a Semilocal Exchange-Correlation Potential, Phys. Rev. Lett. 102 (2009) 226401. https://doi.org/10.1103/PhysRevLett.102.226401.

[99] D. Koller, F. Tran, P. Blaha, Improving the modified Becke-Johnson exchange potential, Phys. Rev. B 85 (2012) 155109. https://doi.org/10.1103/PhysRevB.85.155109.

[100] A. Kafi, F. Driss Khodja, F. Saadaoui, S. Chibani, A. Bentayeb, M. Driss Khodja, An ab initio study of the structural and optoelectronic properties of AlxGa1−xN (x = 0, 0.125, 0.375, 0.625, 0.875, and 1) semiconductors, J Comput Electron 19 (2020) 26–37. https://doi.org/10.1007/s10825-019-01423-2.

[101] D. Li, X. Zhang, Z. Zhu, H. Zhang, First-principles calculation of structural, electronic, and optical properties of zinc-blende AlxGa1−xN alloys, Solid State Sciences 13 (2011) 1731–1734. https://doi.org/10.1016/j.solidstatesciences.2011.06.027.

[102] P.J. Gielisse, S.S. Mitra, J.N. Plendl, R.D. Griffis, A. Et., Lattice Infrared Spectra of Boron Nitride and Boron Monophosphide, Physical Review (1967). https://doi.org/10.1103/PhysRev.155.1039.

[103] S. Loughin, R.H. French, L.K.D. Noyer, W.-Y. Ching, Y.-N. Xu, Critical point analysis of the interband transition strength of electrons, J. Phys. D: Appl. Phys. 29 (1996) 1740–1750. https://doi.org/10.1088/0022-3727/29/7/009.

[104] R. Alaya, S. Slama, M. Hashassi, M. Mbarki, A. Rebey, S. Alaya, Theoretical Predictions of Structural, Electronic, and Optical Properties of Dilute Bismide AlN1−x Bi x in Zinc-Blend Structures, Journal of Elec Materi 46 (2017) 1977–1983. https://doi.org/10.1007/s11664-017-5318-y.

[105] Y.W. Jung, T.H. Ghong, J.S. Byun, Y.D. Kim, H.J. Kim, Y.C. Chang, S.H. Shin, J.D. Song, Dielectric response of AlSb from 0.7 to 5.0 eV determined by *in situ* ellipsometry, Applied Physics Letters 94 (2009) 231913. https://doi.org/10.1063/1.3153127.

[106] M. Benchehima, H. Abid, A.C. Chaouche, A. Resfa, Structural and optoelectronic properties of $B_x Al_{1-x} Sb$ ternary alloys: first principles calculations, Eur. Phys. J. Appl. Phys. 77 (2017) 30101. https://doi.org/10.1051/epjap/2017160319.

[107] S. Zollner, C. Lin, E. Schönherr, A. Böhringer, M. Cardona, The dielectric function of AlSb from 1.4 to 5.8 eV determined by spectroscopic ellipsometry, Journal of Applied Physics 66 (1989) 383–387. https://doi.org/10.1063/1.343888.

[108] S.K. Tripathy, A. Pattanaik, Optical and electronic properties of some binary semiconductors from energy gaps, Optical Materials 53 (2016) 123–133. https://doi.org/10.1016/j.optmat.2016.01.012.

[109] M.S. Al-Assiri, N. Bouarissa, Electronic band structure and derived properties of AlAsxSb1−x alloys, Superlattices and Microstructures 59 (2013) 144–154. https://doi.org/10.1016/j.spmi.2013.04.007.

[110] G. Theodorou, G. Tsegas, Theory of electronic and optical properties of bulk AlSb and InAs and InAsÕAlSb superlattices, (n.d.).

[111] M. Feneberg, M. Röppischer, C. Cobet, N. Esser, J. Schörmann, T. Schupp, D.J. As, F. Hörich, J. Bläsing, A. Krost, Optical properties of cubic GaN from 1 to 20 eV, Physical Review B—Condensed Matter and Materials Physics 85 (2012) 155207.

[112] Y. Du, B. Chang, X. Fu, X. Wang, M. Wang, Electronic structure and optical properties of zinc-blende GaN, Optik 123 (2012) 2208–2212.

[113] R. Riane, A. Zaoui, S.F. Matar, A. Abdiche, Pressure dependence of electronic and optical properties of Zinc-blende GaN, BN and their B0.25Ga0.75N alloy, Physica B: Condensed Matter 405 (2010) 985–989. https://doi.org/10.1016/j.physb.2009.10.038.

[114] N.M. Ravindra, P. Ganapathy, J. Choi, Energy gap–refractive index relations in semiconductors – An overview, Infrared Physics & Technology 50 (2007) 21–29. https://doi.org/10.1016/j.infrared.2006.04.001.

[115] M. Steube, K. Reimann, O. Brandt, H. Yang, K.H. Plogg, High pressure luminescence of zincblende and wurtzite GaN, Physica Status Solidi (b) 211 (1999) 57–61.

[116] Y. Yan, Q. Wang, H. Ma, First principles calculations of electronic and optical properties of GaN1− xBix alloys, Journal of Semiconductors 35 (2014) 122002.

[117] S. Gagui, S. Ghemid, H. Meradji, B. Zaidi, B. Amimour, S.A. Tahir, R. Ahmed, B. Chouial, B. Hadjoudja, A.K. Kushwaha, Ab-initio study on the phase transition, elastic, optoelectronic, and thermodynamic properties of GaAs1-xSbx, Optik 219 (2020) 165253. https://doi.org/10.1016/j.ijleo.2020.165253.

[118] D.E. Aspnes, A.A. Studna, Dielectric functions and optical parameters of Si, Ge, GaP, GaAs, GaSb, InP, InAs, and InSb from 1.5 to 6.0 eV, Phys. Rev. B 27 (1983) 985–1009. https://doi.org/10.1103/PhysRevB.27.985.

[119] M. Grimsditch, E.S. Zouboulis, A. Polian, Elastic constants of boron nitride, Journal of Applied Physics (1994). https://doi.org/10.1063/1.357757.
[120] M. Ferhat, A. Zaoui, M. Certier, H. Aourag, Electronic structure of BN, BP and BAs, Physica B: Condensed Matter 252 (1998) 229–236.
[121] S.Q. Wang, H.Q. Ye, First-principles study on elastic properties and phase stability of III–V compounds, Physica Status Solidi (b) 240 (2003) 45–54.
[122] A.F. Wright, Elastic properties of zinc-blende and wurtzite AlN, GaN, and InN, Journal of Applied Physics 82 (1997) 2833–2839. https://doi.org/10.1063/1.366114.
[123] R. Weil, Correction to the elastic constants of AISb, Journal of Applied Physics 43 (1972) 4271–4271. https://doi.org/10.1063/1.1660914.
[124] K. Shimada, T. Sota, K. Suzuki, First-principles study on electronic and elastic properties of BN, AlN, and GaN, Journal of Applied Physics 84 (1998) 4951–4958. https://doi.org/10.1063/1.368739.
[125] N. Bouarissa, Elastic constants and acoustical phonon properties of GaAsxSb1−x, Materials Chemistry and Physics 100 (2006) 41–47. https://doi.org/10.1016/j.matchemphys.2005.12.004.
[126] Z. Zhou, B. Joós, Stability criteria for homogeneously stressed materials and the calculation of elastic constants, Phys. Rev. B 54 (1996) 3841–3850. https://doi.org/10.1103/PhysRevB.54.3841.
[127] J. Wang, S. Yip, S.R. Phillpot, D. Wolf, Crystal instabilities at finite strain, Phys. Rev. Lett. 71 (1993) 4182–4185. https://doi.org/10.1103/PhysRevLett.71.4182.
[128] M.I. Naher, S.H. Naqib, An ab-initio study on structural, elastic, electronic, bonding, thermal, and optical properties of topological Weyl semimetal TaX (X = P, As), Sci Rep 11 (2021) 5592. https://doi.org/10.1038/s41598-021-85074-z.
[129] W. Voigt, Theoretische studien über die elasticitätsverhältnisse der krystalle, Königliche Gesellschaft der Wissenschaften zu Göttingen, 1887.
[130] A. Reuss, Berechnung der Fließgrenze von Mischkristallen auf Grund der Plastizitätsbedingung für Einkristalle ., Z Angew Math Mech 9 (1929) 49–58. https://doi.org/10.1002/zamm.19290090104.
[131] R. Hill, The Elastic Behaviour of a Crystalline Aggregate, Proc. Phys. Soc. A 65 (1952) 349–354. https://doi.org/10.1088/0370-1298/65/5/307.
[132] D.G. Pettifor, Theoretical predictions of structure and related properties of intermetallics, 8 (1992).
[133] B.M. Askerov, M. Cankurtaran, Isobaric Specific Heat and Thermal Expansion of Solids in the Debye Approximation, Physica Status Solidi (b) 185 (1994) 341–348. https://doi.org/10.1002/pssb.2221850204.
[134] R. Piazza, The strange case of Dr. Petit and Mr. Dulong, (2018). https://doi.org/10.48550/arXiv.1807.02270.
[135] N. Bioud, X.-W. Sun, S. Daoud, T. Song, A. Et., Structural stability and thermodynamic properties of BSb under high pressure and temperature, Materials Research Express (2018). https://doi.org/10.1088/2053-1591/aad3a5.
[136] S. Daoud, Sound velocities and thermal properties of BX (X= As, Sb) compounds, International Journal of Scientific World 3 (2015) 43–48.
[137] W. Gouasmia, D. Boudjaadar, F. Oumelaz, O. Nemiri, H. Meradji, S. Ghemid, A. Boumaza, S. Bin Omran, D. Singh, R. Khenata, First-principles assessment of the structural,

phase transition, electronic, elastic and thermal properties of the semiconductor alloys AlSb1–x Bi x (x= 0, 0.25, 0.5, 0.75, 1), The European Physical Journal B 98 (2025) 85.

[138] S. Adachi, Properties of Group-IV, III-V and II-VI Semiconductors, 1st ed., Wiley, 2005. https://doi.org/10.1002/0470090340.

[139] S.E. O'Sullivan, E. Montoya, S.-K. Sun, J. George, C. Kirk, M.C. Dixon Wilkins, P.F. Weck, E. Kim, K.S. Knight, N.C. Hyatt, Crystal and Electronic Structures of A_2 $NaIO_6$ Periodate Double Perovskites (A = Sr, Ca, Ba): Candidate Wasteforms for I-129 Immobilization, Inorg. Chem. 59 (2020) 18407–18419. https://doi.org/10.1021/acs.inorgchem.0c03044.

[140] F.D. Murnaghan, The compressibility of media under extreme pressures, Proceedings of the National Academy of Sciences 30 (1944) 244–247.

[141] J.K. Bairwa, M. Rani, P.K. Kamlesh, R. Singh, U. Rani, S. Al-Qaisi, T. Kumar, S. Kumari, A.S. Verma, Modeling and simulation of multifaceted properties of X2NaIO6 (X = Ca and Sr) double perovskite oxides for advanced technological applications, J Mol Model 29 (2023) 379. https://doi.org/10.1007/s00894-023-05786-z.

[142] A. Aziz, N. Bibi, M. Usman, S. Noreen, First-Principles evaluation of Lead-Free X2NaIO6 (X=Sr, Ba) Double-Perovskite: For optoelectronic and solar cell applications, Chemical Physics 586 (2024) 112405. https://doi.org/10.1016/j.chemphys.2024.112405.

[143] V.M. Goldschmidt, Die Gesetze der Krystallochemie, Naturwissenschaften 14 (1926) 477–485. https://doi.org/10.1007/BF01507527.

[144] C.-Y. Lu, S.-P. Chang, S.-J. Chang, C.-L. Hsu, Y.-Z. Chiou, I.-C. Chen, ZnO Nanowire-Based UV Photodetector, J. Nanosci. Nanotech. 10 (2010) 1135–1138. https://doi.org/10.1166/jnn.2010.1862.

[145] K.-T. Lam, Y.-J. Hsiao, L.-W. Ji, T.-H. Fang, K.-H. Hsiao, T.-T. Chu, High-Sensitive Ultraviolet Photodetectors Based on ZnO Nanorods/CdS Heterostructures, Nanoscale Res Lett 12 (2017) 31. https://doi.org/10.1186/s11671-016-1818-6.

[146] B. Shi, B. Liu, J. Luo, Y. Li, C. Zheng, X. Yao, L. Fan, J. Liang, Y. Ding, C. Wei, D. Zhang, Y. Zhao, X. Zhang, Enhanced light absorption of thin perovskite solar cells using textured substrates, Solar Energy Materials and Solar Cells 168 (2017) 214–220. https://doi.org/10.1016/j.solmat.2017.04.038.

[147] M.A. Green, Y. Hishikawa, W. Warta, E.D. Dunlop, D.H. Levi, J. Hohl-Ebinger, A.W.H. Ho-Baillie, Solar cell efficiency tables (version 50), Progress in Photovoltaics 25 (2017) 668–676. https://doi.org/10.1002/pip.2909.

[148] M.I. Naher, S.H. Naqib, An ab-initio study on structural, elastic, electronic, bonding, thermal, and optical properties of topological Weyl semimetal TaX (X = P, As), Sci Rep 11 (2021) 5592. https://doi.org/10.1038/s41598-021-85074-z.

[149] W. Feng, S. Cui, Mechanical and electronic properties of Ti_2 AlN and Ti_4 AlN_3 : a first-principles study, Can. J. Phys. 92 (2014) 1652–1657. https://doi.org/10.1139/cjp-2013-0746.

[150] M. Mukherjee, H. Sahu, M.D. Losego, W.R. Gutekunst, R. Ramprasad, Informatics-Driven Design of Superhard B–C–O Compounds, ACS Appl Mater Interfaces 16 (2024) 10372–10379. https://doi.org/10.1021/acsami.3c18105.

[151] S.I. Ranganathan, M. Ostoja-Starzewski, Universal Elastic Anisotropy Index, Phys. Rev. Lett. 101 (2008) 055504. https://doi.org/10.1103/PhysRevLett.101.055504.

[152] I.C. Dragomir, T. Ungár, The dislocations contrast factors of cubic crystals in the Zener constant range between zero and unity, Powder Diffr. 17 (2002) 104–111. https://doi.org/10.1154/1.1471520.

[153] G.E. Green, D.E. Reades, Boundary conditions, anisotropy and sample shape effects onthe stress-strain behaviour of sand in triaxial compression and plane strain, Géotechnique 25 (1975) 333–356. https://doi.org/10.1680/geot.1975.25.2.333.

[154] C.M. Kube, M. De Jong, Elastic constants of polycrystals with generally anisotropic crystals, Journal of Applied Physics 120 (2016) 165105. https://doi.org/10.1063/1.4965867.

[155] A. Boumaza, S. Ghemid, H. Meradji, O. Nemiri, R. Belghit, F. Oumelaz, L. Hamioud, M.H. Gous, R. Khenata, S.B. Omran, X. Wang, DFT-Based Calculations of the Structural Stability, Electronic and Elastic Characteristics of BBi1-xSbx Ternary Ordered Alloys, Journal of Elec Materi 50 (2021) 598–612. https://doi.org/10.1007/s11664-020-08576-y.

[156] C.L. Julian, Theory of Heat Conduction in Rare-Gas Crystals, Phys. Rev. 137 (1965) A128–A137. https://doi.org/10.1103/PhysRev.137.A128.

[157] Yu.G. Gurevich, J.E. Velazquez-Perez, Peltier Effect in Semiconductors, in: J.G. Webster (Ed.), Wiley Encyclopedia of Electrical and Electronics Engineering, 1st ed., Wiley, 2014: pp. 1–21. https://doi.org/10.1002/047134608X.W8206.

[158] D.T. Morelli, G.A. Slack, High Lattice Thermal Conductivity Solids, in: S.L. Shindé, J.S. Goela (Eds.), High Thermal Conductivity Materials, Springer-Verlag, New York, 2006: pp. 37–68. https://doi.org/10.1007/0-387-25100-6_2.

[159] S. Hébert, La recherche de nouveaux matériaux thermoélectriques, Reflets phys. (2014) 18–22. https://doi.org/10.1051/refdp/201441018.

[160] B. Ul Haq, R. Ahmed, S. AlFaify, F.K. Butt, A. Shaari, A. Laref, Exploring thermoelectric materials for renewable energy applications: The case of highly mismatched alloys based on AlBi1-xSbx and InBi1-xSbx, Intermetallics 93 (2018) 235–243. https://doi.org/10.1016/j.intermet.2017.09.017.

[161] G. Nazir, Q. Mahmood, M. Hassan, M.M. AL-Anazy, N.A. Kattan, N. Sfina, M.A. Amin, A. Mera, H.H. Somaily, Tuning of band gap by anions (Cl, Br, I) of double perovskites Rb_2AgAsX_6 (Cl, Br, I) for solar cells and thermoelectric applications, Phys. Scr. 98 (2023) 025811. https://doi.org/10.1088/1402-4896/acaec1.

[162] L.R.V. Buizza, A.D. Wright, G. Longo, H.C. Sansom, C.Q. Xia, M.J. Rosseinsky, M.B. Johnston, H.J. Snaith, L.M. Herz, Charge-Carrier Mobility and Localization in Semiconducting Cu2AgBiI6 for Photovoltaic Applications, ACS Energy Lett. 6 (2021) 1729–1739. https://doi.org/10.1021/acsenergylett.1c00458.

[163] G.A. Slack, R.A. Tanzilli, R.O. Pohl, J.W. Vandersande, The intrinsic thermal conductivity of AIN, Journal of Physics and Chemistry of Solids 48 (1987) 641–647. https://doi.org/10.1016/0022-3697(87)90153-3.

[164] P. Kumari, V. Srivastava, R. Sharma, N. Kaur, H. Ullah, Unveiling the thermoelectric, optical and mechanical performances of Hafnium and Zirconium based Beryllium oxide perovskite, Materials Today Communications 40 (2024) 109571. https://doi.org/10.1016/j.mtcomm.2024.109571.

[165] S. Charef, A. Assali, A. Boukortt, Optoelectronic and thermoelectric properties of novel double halide perovskites Na2AgAsX6 (X = Cl, Br) for efficient green solar cells, Materials Today Communications 38 (2024) 108065. https://doi.org/10.1016/j.mtcomm.2024.108065.

General Conclusion

This study presents a rigorous first-principles investigation of $YN_{1-x}Sb_x$ (Y: B, Al and Ga) ternary alloys while x is the Sb concentration (x=0, 0.25, 0.5, 0.75 and 1), in addition to Sr_2NaXO_6 (X = Cl, Br, and I) double perovskites. For which no prior comprehensive theoretical or experimental reports are available to the best of our knowledge. A detailed analysis for structural, electronic, optical, elastic and thermal properties in addition to thermoelectric properties for double oxide perovskites has been carried out within the framework of Density Functional Theory (DFT). Structural optimization, transition phase, and elastic constant calculations were performed using the WC-GGA for $YN_{1-x}Sb_x$ternary alloys and PBEsol exchange–correlation functional forSr_2NaXO_6 (X = Cl, Br, and I) double perovskites. The electronic, thermoelectric, and optical properties were accurately computed by using the KTB-mBJ potential. Furthermore, the WC-GGA and TB-mBJ schemes were applied to validate and refine the electronic band-structure analysis.

For $YN_{1-x}Sb_x$ (Y=B, Al and Ga) alloys (x=0, 0.25, 0.50, 0.75 and 1), the $BN_{1-x}Sb_x$ system, $AlN_{1-x}Sb_x$ (x= 0.25, 0.50, 0.75 and 1) alloys and $GaN_{1-x}Sb_x$ (x= 0.25, 0.50, 0.75 and 1) exhibited stable phase in the zinc blende, while both AlN and GaN found stable in the wurtzite structure. The estimated measurements of lattice constants and bulk modulus display inverse relationship with increasing antimony 'Sb' composition; lattice constant shown an increment while bulk modulus shown a decrement. On the other hand, the lattice parameter exhibits a systematic increase from BN to AlN and GaN, as well as from BSb to AlSb and GaSb, the opposite is true for bulk modulus. The transition pressure has been calculated. The computed band structure represents an indirect band gap at X – Γ points for binary compounds BN BSb, AlN and AlSb, and direct band gap at Γ – Γ points for GaN, GaSb and for the ternary alloys of $YN_{1-x}Sb_x$ (Y = B, Al and Ga) (x=0.25, 0.50 and 0.75) systems. The energy gap exhibits a monotonic decrease from BN to AlN and GaN, as well as from BSb to AlSb and GaSb, this effect arises from the increased lattice parameter and the resulting reduction in orbital overlap, and weakening of cation – anion bonding. Furthermore, Sb - based compounds display significantly smaller band gaps compared to nitrides due to the larger atomic size, lower electronegativity with increasing Sb concentration across all $BN_{1-x}Sb_x$, $AlN_{1-x}Sb_x$ and $GaN_{1-x}Sb_x$ systems. The investigation of optical properties proves that the $YN_{1-x}Sb_x$ (Y=B, Al and Ga) alloys exhibit a composition-dependent optical response, allowing continuous tuning of

the band gap from the ultraviolet to the infrared regions as the Sb concentration increases. This tunability, combined with strong optical absorption and dielectric response, makes these alloys promising candidates for a broad range of optoelectronic applications, including UV photodetectors, visible-light emitters, infrared sensing and communication devices. The values of elastic constants indicate a mechanical stability for the studied systems. The resistance to volume change, shape change and hardness decrease from YN to YSb in each system. Cauchy pressure, Poisson ratio and Pugh ratio implies brittle nature, whereas; isotropic nature for bulk modulus and anisotropic for both Shear modulus and Young modulus have been demonstrated using elastic anisotropy parameters, also the acoustic behavior has been determined. The obtained thermal property results, including the effect of temperature on lattice parameter and bulk modulus, and the variation of heat capacity C_V, heat capacity C_P and Debye temperature in the temperature range of 0 to $1000\ K$ shown lattice parameter increasing, bulk modulus and Debye temperature decreasing and increases in specific heat as temperature increase.

The properties investigation of Sr_2NaXO_6 (X = Cl, Br, and I) double perovskites prove its crystallization in a stable ideal cubic double perovskite structure, satisfying all mechanical stability criteria. This structural stability strongly suggests that these materials are viable candidates for experimental synthesis. Electronic structure calculations reveal that all studied compounds exhibit semiconducting behavior with direct band gap located at the Γ point. The calculated band gap values range from 0.99 to 3.36 eV using the TB-mBJ approach, while slightly larger values ranging from 1.35 to 3.52 eV are obtained with the KTB-mBJ scheme, confirming the reliability and consistency of the adopted computational methods. The optical properties were investigated through key optical parameters such as the complex dielectric function, absorption coefficient, and complex refractive index. The obtained spectra exhibit pronounced optical activity and strong absorption in the ultraviolet region, indicating that Sr_2NaXO_6 (X = Cl, Br, and I) compounds are highly suitable for ultraviolet (UV) optoelectronic and photonic applications. Elastic property analysis confirms the mechanical stability of the studied systems. The negative Cauchy pressure values, together with the evaluated Poisson's ratio and Pugh's ratio, consistently indicate a brittle mechanical nature dominated by directional bonding. Furthermore, the mechanical moduli were calculated, and a detailed assessment of the isotropic and anisotropic elastic behavior was carried out, providing

deeper insight into the mechanical response of these materials. A comprehensive evaluations of thermoelectric transport properties, including Seebeck coefficient, electrical conductivity, electronic thermal conductivity, lattice thermal conductivity, power factor, and dimensionless figure of merit, reveal well suited for thermoelectric performance. Remarkably, high ZT values of 0.747, 0.734, and 0.738 at 1000 K are achieved for Sr_2NaClO_6, Sr_2NaBrO_6, and Sr_2NaIO_6, respectively. These results highlight the strong potential of these oxide double perovskites for hightemperature thermoelectric applications and efficient energy conversion devices.

Our work demonstrates a high consistency between our calculated results and both available experimental data and previous theoretical studies. Therefore, we expect this research to represent a significant scientific contribution and serve as a key reference for future studies, while also motivating and supporting future experimental investigations.